

Control over Dimensionality and Magnetic Properties in Metal Complexes formed with Substituted Salicyl Ligands

Zur Erlangung des akademischen Grades eines
DOKTORS DER NATURWISSENSCHAFTEN

(Dr. rer. nat.)

von der Fakultät für Chemie und Biowissenschaften
der Universität Karlsruhe (TH)

angenommene

DISSERTATION

von

Sudarshana Mukherjee

aus Varanasi, India

Dekan: Prof. Dr. S. Bräse

Referent: Prof. Dr. A. K. Powell

Korreferent: Prof. Dr. P. Roesky

Tag der mündlichen Prüfung: 21.10.2008

In the memory of my Grandma

This thesis was completed in the period from Feb 2006 until September 2008 in the Institut für Anorganische Chemie der Universität Karlsruhe (TH) under the supervision of Prof. Dr. A. K. Powell.

Contents

Chapter 1	Introduction	1
1.1	Overview of some relevant compounds formed with the ligands	5
1.1.1	Complexes with salicylate-type ligands	5
1.1.1.1	A nonanuclear mixed-valence manganese (III,II) complex	5
1.1.1.2	An infinite chain of mixed-valence manganese complex	6
1.1.1.3	A linear trinuclear complex and related mixed valent infinite chain	7
1.1.2	Complexes with Schiff base ligands	8
1.1.2.1	A dimeric manganese Schiff base complex as single molecule magnet	8
1.1.2.2	Mn ₄ complexes with SMM behaviour	9
1.1.2.3	A record barrier for a single molecule magnet	10
1.1.2.4	A dinuclear Mn(III)-Cu(II) single molecule magnet	10
1.1.2.5	A heterometallic single molecule magnet of [Mn ^{III} ₂ Ni ^{II} ₂ Cl ₂ (salpa) ₂]	11
1.2	Synthetic strategy	12
1.3	Characterisation of the synthesised ligands by NMR spectroscopy	14
1.4	Introduction to Magnetochemistry	17
1.4.1	Magnetic Susceptibility	17
1.4.2	Different kinds of magnetic behaviour	18
1.4.3	Determination of the magnetic behaviour	19
1.5	Single molecule magnet behaviour	21
1.6	Thesis overview	24
Chapter 2	Research objectives	25
Chapter 3	Structure and magnetic properties of 1D and 3D compounds with substituted salicylates	27
3.1	Homometallic 1D and 3D compounds	28
3.1.1	Structure and magnetic behaviour of 3D MOF, [Mn ^{III} ₂ Mn ^{II} (3-Me-sal) ₄ (py) ₄], 1	29
3.1.2	Structure and magnetic behaviour of 3D MOF, [Mn ^{III} ₂ Mn ^{II} (4-Me-sal) ₄ (py) ₄ (MeOH)]·H ₂ O, 2	35
3.1.3	Structure and magnetic behaviour of 3D MOF, [Mn ^{III} ₂ Mn ^{II} (5-Me-sal) ₄ (py) ₄ (H ₂ O) ₂]·(MeOH), 3	38

3.1.4	Structure and magnetic behaviour of 3D MOF, [Mn ^{III} ₂ Mn ^{II} (3-Me-sal) ₄ (4-Me-py) ₄], 4	42
3.1.5	Structure and magnetic behaviour of 1D polymer [Mn ^{III} (4-Me-sal) ₂ (4-Me-py) ₂ Mn ^{II} (OH ₂) ₂ (MeOH) ₂][Mn ^{III} (4-Me-sal) ₂ (4-Me-pyr) ₂], 5	44
3.1.6	Characterisation of a Mn - (5-Me-salH ₂) - (4-Me-py) product, 6	50
3.2	Heterometallic 1D compounds	50
3.2.1	Structure of [MnNa ₂ (3-MeO-sal) ₂ (MeOH) ₂], 7	50
3.2.2	Structure and magnetic behaviour of 1D polymer, [Fe ₂ Pr(4-Me-sal) ₄ (2,2'-bipy) ₂ (OH ₂) ₆](NO ₃)·2MeOH·1.5H ₂ O, 8	52
3.2.3	Structure and magnetic behaviour of 1D polymer, [Fe ₂ Gd(4-Me-sal) ₄ (2,2'-bipy) ₂ (OH ₂) ₅]Cl _{1/2} (NO ₃) _{1/2} ·5H ₂ O, 9	55
3.2.4	Structure and magnetic behaviour of 1D polymer, [Fe ₂ Dy(4-Me-sal) ₄ (2,2'-bipy) ₂ (OH ₂) ₅]Cl _{1/2} (NO ₃) _{1/2} ·5H ₂ O, 10	58
3.3	Summary	60
Chapter 4	Structure and magnetic properties of discrete compounds obtained with substituted salicylates	62
4.1	Structure of (NHEt ₃)[Mn ^{III} (3-MeOsal) ₂ (MeOH)(H ₂ O)], 11	63
4.2	Structure of (NHEt ₃) ₂ [Fe ^{III} (3-MeOsal) ₂ (OAc)], 12	65
4.3	Structure and magnetic behaviour of [Mn ^{II} Mn ^{III} ₂ (3-MeOsal) ₄ (py) ₆ (H ₂ O) ₂]·4H ₂ O, 13	66
4.4	Structure and magnetic behaviour of [Mn ^{III} ₂ Mn ^{II} (3-MeO-sal) ₄ (py) ₄ (H ₂ O) ₄]·4MeOH, 14	69
4.5	Structure and magnetic behaviour of [Mn ^{III} ₂ Mn ^{II} (3-MeO-sal) ₄ (2,2'-bipy)(H ₂ O) ₃ (MeOH) ₂]·3MeOH, 15	73
4.6	Structure and magnetic behaviour of [Cu ₃ (3-MeO-salH) ₂ (3-MeO-sal) ₂ (2,2'-bipy) ₂], 16	77
4.7	Summary	81
Chapter 5	Structure and magnetic properties of Schiff base complexes obtained using substituted salicylaldehydes	83
5.1	Characterisation of the Schiff base ligands	85
5.2	Metal complexes obtained with the Schiff base ligands	90
5.2.1	Structure and magnetic behaviour of [Mn ^{III} ₂ Mn ^{II} (L ¹) ₂ (μ-OAc) ₂ (μ-OMe) ₂ (MeOH) ₂]·2MeOH, 17	90

5.2.2	Structure and magnetic behaviour of [Mn ^{III} ₂ Mn ^{II} (L ³) ₂ (μ-OAc) ₂ (μ-OMe) ₂], 18	94
5.2.3	Structure and magnetic behaviour of [Mn ^{III} ₂ Mn ^{II} (L ⁷) ₂ (OAc) ₄ (OH ₂) ₂]·MeOH, 19	97
5.2.4	Structure and magnetic behaviour of [Mn ^{III} ₃ (μ ₃ -O)(L ¹¹) ₃ (MeOH) ₃](ClO ₄), 20	100
5.2.5	Structure and magnetic behaviour of [Mn ₂ ^{III} Ni ₂ ^{II} (L ¹⁴) ₄](X) ₂ , {X= CH ₃ COO ⁻ (21), X= Cl ⁻ (22)}	102
5.3	Summary	113
Chapter 6	Conclusions	115
Chapter 7	Experimental	119
7.1	NMR spectroscopy	119
7.2	Elemental analysis	119
7.3	Infra-red spectroscopy	119
7.4	X-ray powder diffraction (PXRD)	120
7.5	X-ray single crystal measurement	120
7.6	Magnetic Measurements	121
7.7	Syntheses	121
7.7.1	Ligand Syntheses	121
7.7.1.1	Preparation of 3-methoxysalicylidene-2-aminophenol (H₂L¹)	121
7.7.1.2	Preparation of 3-ethoxysalicylidene-2-aminophenol (H₂L²)	122
7.7.1.3	Preparation of 3-methoxysalicylidene-(2-amino-4-methylphenol) (H₂L³)	122
7.7.1.4	Preparation of 3-ethoxysalicylidene-(2-amino-4-methylphenol) (H₂L⁴)	122
7.7.1.5	Preparation of 3-hydroxysalicylidene-2-aminophenol (H₂L⁵)	122
7.7.1.6	Preparation of 3-hydroxysalicylidene-(2-amino-4-methylphenol) (H₂L⁶)	123
7.7.2	Inorganic Syntheses	123
7.7.2.1	Preparation of [Mn ^{III} ₂ Mn ^{II} (3-Me-sal) ₄ (py) ₄], 1	123
7.7.2.2	Preparation of [Mn ^{III} ₂ Mn ^{II} (4-Me-sal) ₄ (py) ₄ (MeOH)]·H ₂ O, 2	123
7.7.2.3	Preparation of [Mn ^{III} ₂ Mn ^{II} (5-Me-sal) ₄ (py) ₄ (H ₂ O) ₂](MeOH), 3	124
7.7.2.4	Preparation of [Mn ^{III} ₂ Mn ^{II} (3-Me-sal) ₄ (4-Me-py) ₄], 4	124
7.7.2.5	Preparation of [Mn ^{III} (4-Me-sal) ₂ (4-Me-py) ₂ Mn ^{II} (OH ₂) ₂ (MeOH) ₂] [Mn ^{III} (4-Me-sal) ₂ (4-Me-py) ₂], 5	124

7.7.2.6 Preparation of product 6	125
7.7.2.7 Preparation of [(3-MeO-sal) ₂ MnNa ₂ ·MeOH], 7	125
7.7.2.8 Preparation of [Fe ₂ Pr(4-Me-sal) ₄ (2,2'-bipy) ₂ (OH ₂) ₆](NO ₃)·2MeOH·1.5 H ₂ O, 8	126
7.7.2.9 Preparation of [Fe ^{III} ₂ Gd ^{III} (4-Me-sal) ₄ (2,2'-bipy) ₂ (OH ₂) ₅]Cl _{1/2} (NO ₃) _{1/2} ·5H ₂ O, 9	126
7.7.2.10 Preparation of [Fe ₂ Dy(4-Me-sal) ₄ (2,2'-bipy) ₂ (OH ₂) ₅] Cl _{1/2} (NO ₃) _{1/2} ·5H ₂ O, 10	126
7.7.2.11 Preparation of (NH ₄) ₃ [Mn ^{III} (3-MeO-sal) ₂ (MeOH)(H ₂ O)], 11	126
7.7.2.12 Preparation of (NH ₄) ₂ [Fe ^{III} (3-MeO-sal) ₂ (OAc)], 12	127
7.7.2.13 Preparation of [Mn ^{II} Mn ^{III} ₂ (3-MeO-sal) ₄ (py) ₆ (H ₂ O) ₂]·4H ₂ O, 13	127
7.7.2.14 Preparation of [Mn ^{III} ₂ Mn ^{II} (3-MeO-sal) ₄ (py) ₄ (H ₂ O) ₄]·4MeOH, 14	128
7.7.2.15 Preparation of [Mn ^{III} ₂ Mn ^{II} (3-MeO-sal) ₄ (2,2'-bipy)(H ₂ O) ₃ (MeOH) ₂]·3MeOH, 15	128
7.7.2.16 Preparation of [Cu ₃ (3-MeO-salH) ₂ (3-MeO-sal) ₂ (2,2'-bipy) ₂], 16	128
7.7.2.17 Preparation of [Mn ^{III} ₂ Mn ^{II} (L ¹) ₂ (μ-OAc) ₂ (μ-OMe) ₂ (MeOH) ₂]·2MeOH, 17	129
7.7.2.18 Preparation of [Mn ^{III} ₂ Mn ^{II} (L ³) ₂ (μ-OAc) ₂ (μ-OMe) ₂], 18	129
7.7.2.19 Preparation of [Mn ^{III} ₂ Mn ^{II} (L ⁷) ₂ (OAc) ₄ (OH ₂) ₂]·MeOH, 19	130
7.7.2.20 Preparation of [Mn ^{III} ₃ (μ ₃ -O) (L ¹¹) ₃ (MeOH) ₃] (ClO ₄), 20	130
7.7.2.21 Preparation of [Mn ₂ ^{III} Ni ₂ ^{II} (L ¹⁴) ₄](CH ₃ COO) ₂ , 21	131
7.7.2.22 Preparation of [Mn ₂ ^{III} Ni ₂ ^{II} (L ¹⁴) ₄](Cl) ₂ , 22	131
Chapter 8 Crystallographic data	132
Chapter 9 Bibliography	137
Appendix A List of compounds	144
Appendix B List of organic compounds	145
Appendix C List of abbreviations	146
Appendix D List of figures	147
Appendix E List of schemes	152
Appendix F List of tables	152

Chapter 1: Introduction

In the last few years, major scientific achievements have been made at the atomic, molecular and macromolecular levels. This involves a length scale range of 1-100 nm. The goal has been to create systems with novel properties that can be controlled and manipulated. Among various properties that may be possessed by these systems, magnetism is certainly important because it may be applied to information storage technology and it may allow investigations into the coexistence of quantum and classical effects.

Molecule-based magnets possess properties comparable to traditional magnets; they, however, have many advantages, such as low temperature fabrication, low density, transparency and electrical insulation.¹ They are composed of paramagnetic building blocks which are molecular. These building blocks often have transition or lanthanide metal ions with unpaired spins, which provide the magnetic moment, and organic groups to mediate magnetic interactions between these metal centres. This has produced magnetic materials of various dimensions, and some with long-range magnetic ordering.² They not only have the potential use as functional materials, but also exhibit fascinating structural diversity. As a result, there has been an increasing interest in designing 1D, 2D and 3D magnetic systems which can provide a better understanding of magneto-structural relationships.³ These systems have been found to exhibit diverse magnetic properties.⁴ The molecular approach offers a unique opportunity because the properties of the precursors and magnetic bridges can be chosen beforehand in order to obtain magnets with desired physical properties.

An exciting development was the discovery of single molecule magnets (SMM), which are magnetic molecular clusters. These molecules exhibit slow relaxation of magnetisation at low temperatures, and thus represent a molecular approach to nanomagnets. Their special characteristics arise from purely molecular properties. These molecules should possess a spin ground state (S), where $S \geq \frac{1}{2}$, and a uniaxial magnetoanisotropy, where $D < 0$. The combination of these properties can lead to an energy barrier to the thermal relaxation of

the magnetisation. The magnetic bistability arising from this energy barrier indicates potential applications for these materials in information storage devices, whereby a single molecule could act as the smallest possible unit of magnetic memory. They have many important advantages over conventional nanoscale magnetic particles composed of metals, metal alloys or metal oxides because of their uniform size, solubility in organic solvents and readily alterable peripheral ligands. In the hope of producing new SMMs, polynuclear metal compounds which contain interacting metal centres held together by bridging units, such as oxides, hydroxides, alkoxides and carboxylates, have been synthesised. Much effort has been applied in the design and synthesis of such compounds and in the investigation of their magnetic properties. Many different types of molecular magnets are now known.⁵⁻²⁵ Recently, SMM clusters have also been used as building blocks in the assembly of more complicated architectures.²⁶ Extended networks of magnetically coupled SMMs led to new magnetic behaviour induced by the intrinsic properties of the magnetic units, such as a high-spin state, an Ising-type anisotropy and quantum effects.

Another key development was the discovery that one-dimensional compounds may also show slow relaxation of the magnetisation at low temperature. These new systems are called single chain magnets (SCM).²⁷⁻³⁵ SCMs are expected to exhibit slow relaxation at higher temperatures than SMMs. To be a SCM, a compound requires large uniaxial anisotropy, strong intrachain magnetic interactions between the high-spin magnetic units, and good isolation of the chains.

In this research, the goal was to synthesise and study a range of compounds starting from discrete molecules to extended solids. A variety of magnetic properties, such as SMM behaviour and long-range magnetic ordering, was expected from these compounds. In this way, a comprehensive study on different kinds of magnetic behaviour in different systems can be achieved. To synthesise such compounds, a commonly used strategy is to employ appropriate bridging ligands that can bind several metal centres and transmit magnetic

interactions. In this context, substituted salicylic acids and salicylaldimines were used as ligands with different metal ions under various reaction conditions. It has been observed that heterometallic complexes can have interesting magnetic properties; therefore, more than one type of metal ion was used to obtain compounds containing two different transition metal ions (3*d*-3*d*) or of transition and lanthanide metal ions (3*d*-4*f*). The effect of ligand modifications on the structure and properties of the complexes was also investigated.

The inspiration for this work was the observation that the ligand *o*-vanillin (3-methoxysalicylaldehyde) enabled the formation of triangular dysprosium compounds which exhibited SMM behaviour.³⁶ By using the carboxylic acid analogue of *o*-vanillin, 3-methoxy salicylic acid, the coordination chemistry and magnetism of another promising system could be explored (Figure 1.01). Carboxylate moieties are one of the most studied multibridging groups in inorganic chemistry. They can undergo self-assembly complexation reactions with metal ions to produce polynuclear metal compounds, in which they can assume various coordination modes and can bridge many metal centres. In addition, phenoxo group of salicylic acids can provide another binding site for the metal ions. Varying the type of substituents (such as 3-methyl salicylic acid) and their position can play a key role in the formation of different compounds. Substituents with coordinating functional groups increase the number of donor atoms and can significantly change the properties of the ligand. Altering the position of the substituents can affect steric and electronic factors, and consequently, can modify both the structure and magnetic properties of any subsequent clusters.

Additionally, Schiff bases synthesised from *o*-vanillin gave interesting complexes, such as a Mn₄Ca cluster³⁷ and a 3*d*-4*f* mixed-metal (Cu-Gd) cluster.³⁸ A Schiff base forms when an aldehyde or ketone condenses with a primary or secondary amine forming an imine. These ligands with additional alkoxo groups can afford various multinuclear metal clusters and some of them have been shown to possess SMM properties.³⁹ Several Schiff base ligands were synthesised by the condensation of substituted salicylaldehydes with aromatic or

aliphatic amines containing mono-, di- or tri- alkoxy groups. These ligands were complexed with different metal ions. Functionalising the side chains of the aliphatic amines can modify the donor properties of the ligating group, enabling them to coordinate more metal centres. A number of systems was investigated by slightly modifying the ligands and by observing the effects on the structure and magnetic behaviour of the metal complexes produced by them.

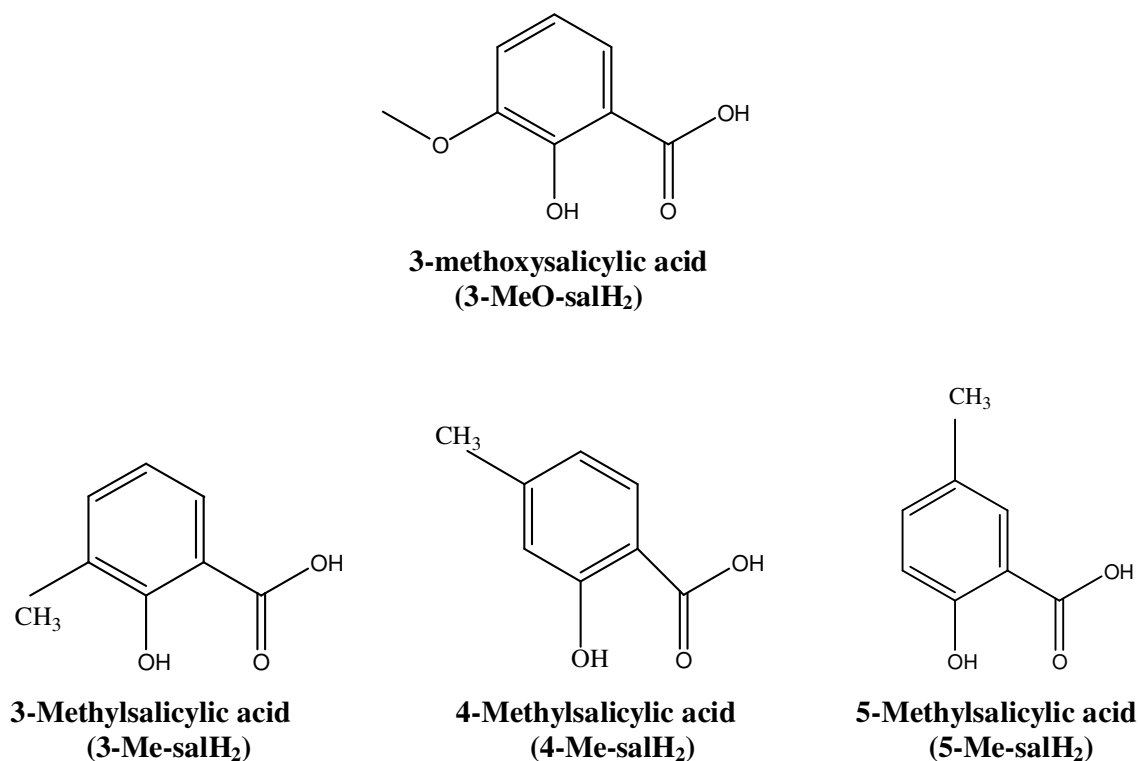


Figure 1.01 Substituted Salicylic acids used as ligands.

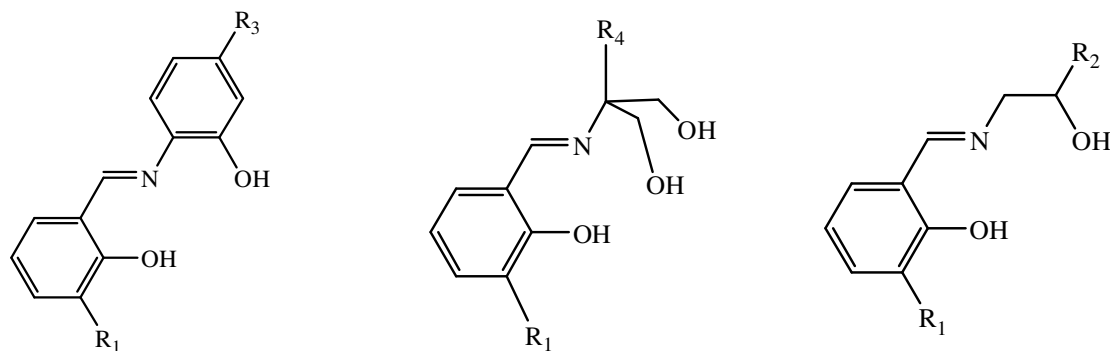


Figure 1.02 Salicylaldehyde (Schiff base) ligands used in this research, where R₁ = H, OCH₃, OC₂H₅, OH; R₂ = H, CH₃; R₃ = H, CH₃; and R₄ = CH₃, CH₂OH.

1.1 Overview of some relevant compounds formed with the ligands

As discussed previously, substituted salicylates and salicylaldehydes with many donor atoms are interesting ligands for coordination compounds. Some previously reported work with these ligands is summarised here to demonstrate features of their chemistry and to provide examples for comparison with the results in the following chapters. A detailed description of the types of magnetic behaviour possible in such systems is given in section 1.4.

1.1.1 Complexes with salicylate-type ligands

1.1.1.1 A nonanuclear mixed-valence manganese (III,II) complex

A mixed-valence nonanuclear manganese complex, $[\text{Mn}_9\text{O}_4(\text{OOCPh})_8(\text{sal})_4(\text{salH})_2(\text{py})_4]$, where $\text{salH}_2 = \text{salicylate}$, $\text{PhCOO} = \text{benzoate}$ and $\text{py} = \text{pyridine}$, was reported by George Christou's group in 1988.⁴⁰ There is a central Mn(II) ion surrounded by two butterfly-

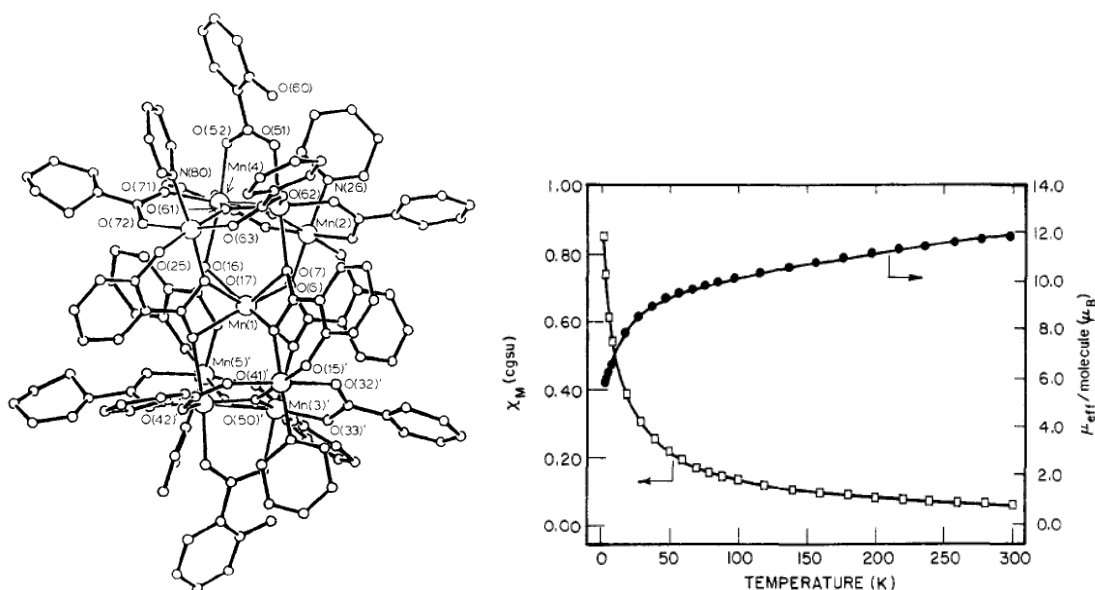


Figure 1.03 Structure of $[\text{Mn}_9\text{O}_4(\text{OOCPh})_8(\text{sal})_4(\text{salH})_2(\text{py})_4]$. Plots of molar susceptibility (χ_m) and effective magnetic moment (μ_{eff}) versus temperature.⁴⁰

like $\text{Mn(III)}_4(\mu_2\text{-O})_2$ units (Figure 1.03). The salicylate groups link the Mn(II) and $[\text{Mn}_4\text{O}_2]$ units with a $\mu_3\text{-}\eta^3$ -bridging mode; peripheral ligation to the complete molecule is provided by pyridine, μ_2 -benzoate and μ_2 -salicylate groups. Each carboxylate oxygen atom of the salicylic

acid ligand has μ_2 -bridging mode, while the phenoxide oxygen atoms bind in a terminal fashion. Magnetic measurements revealed very weak antiferromagnetic interaction between the central Mn(II) and each of the eight Mn(III) ions ($J_1 = -0.97 \text{ cm}^{-1}$) and stronger antiferromagnetic interactions ($J_2 = -11.12 \text{ cm}^{-1}$ and $J_3 = -26.2 \text{ cm}^{-1}$) in the two Mn_4 butterfly units. This gave rise to a spin ground state of $3/2$ for this complex.

1.1.1.2 An infinite chain of mixed-valence manganese complex

In 1995, X. S. Tan *et al.* synthesised an infinite chain of the mixed-valence manganese complex, $[\text{Mn}_4(\text{sal})_4(\text{H}_2\text{O})_4(\text{py})_8][\text{salH}]_2 \cdot 4\text{py}$.⁴¹ The repeat unit has alternating Mn(II) and Mn(III) centres. All the manganese ions are six-coordinate, and adjacent pairs of manganese ions are bridged by carboxylate groups in *syn-anti* configuration. The phenolate oxygen atom of the salicylate is coordinated to the Mn(III) centres in *syn* configuration (Figure 1.04). The sal^{2-} ligands linking the Mn(III) and Mn(II) ions have a $\mu\text{-}\eta^3$ -bridging mode. Magnetic studies showed that the mixed-valence chain is weakly antiferromagnetically coupled and that there are very weak inter-chain antiferromagnetic interactions.

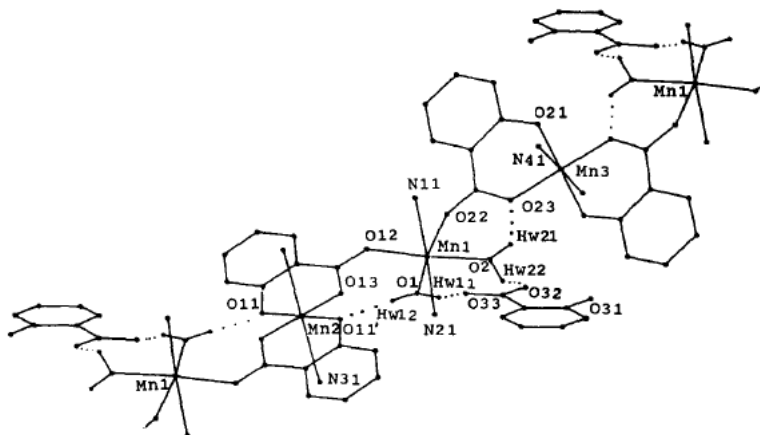


Figure 1.04 Structure of the infinite chain of $[\text{Mn}_4(\text{sal})_4(\text{H}_2\text{O})_4(\text{py})_8][\text{salH}]_2 \cdot 4\text{py}$.⁴¹

1.1.1.3 A linear trinuclear complex and a related infinite mixed-valence chain

Two mixed-valence manganese salicylate complexes were synthesised in 1997 by W. X. Tang and coworkers.⁴² The first compound, $[\text{Mn}_3(\text{sal})_2(\text{salH}_2)_2(\text{H}_2\text{O})_4(4\text{-Me-Py})_6]$ $[\text{Mn}(\text{sal})_2(4\text{-Me-Py})_2] \cdot 2(4\text{-Me-Py})$, is composed of a linear trinuclear Mn(II)-Mn(III)-Mn(II) cationic complex with bridging salicylate carboxylates and a mononuclear Mn(III) complex as an anionic unit (Figure 1.05). The second compound, $[\text{Mn}_2(\text{sal})_2(\text{im})_2(\text{CH}_3\text{OH})_2]$ $[\text{Mn}(\text{sal})_2(\text{Py})_2]$, (im = imidazole) consists of two distinct ionic units. The cation is a binuclear mixed-valence Mn(III)-Mn(II) unit coordinated by imidazole (im) and bridging salicylate (sal^{2-}) ligands. These units form a polymeric chain. The anionic unit is a mononuclear Mn(III) complex with sal^{2-} and py ligands (Figure 1.06). The carboxylate bridges mediate a weak antiferromagnetic exchange interaction in both the complexes.

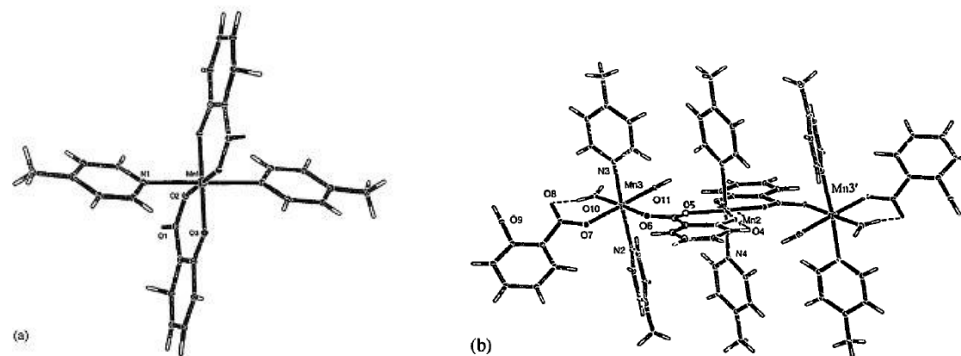


Figure 1.05 Structure of (a) the mononuclear anion, $[\text{Mn}(\text{sal})_2(4\text{-Me-Py})_2]$ (b) the trinuclear cation, $[\text{Mn}_3(\text{sal})_2(\text{salH}_2)_2(\text{H}_2\text{O})_4(4\text{-Me-Py})_6]$.⁴²

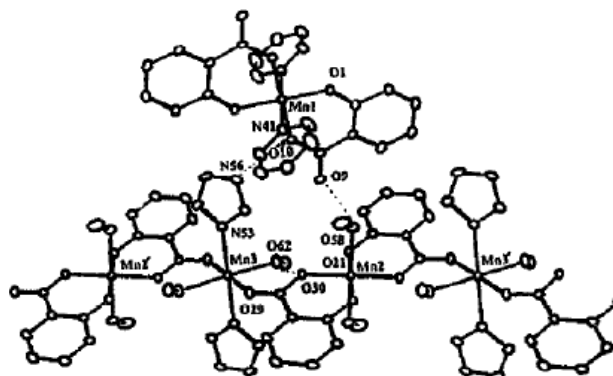


Figure 1.06 Structure of $[\text{Mn}_2(\text{sal})_2(\text{im})_2(\text{CH}_3\text{OH})_2]$ $[\text{Mn}(\text{sal})_2(\text{Py})_2]$, an infinite chain.⁴²

1.1.2 Complexes with Schiff base ligands

Schiff bases are an important class of ligands, and a large amount of work has been done with them.³⁹ This section summarizes some previously reported homo- and heterometallic compounds that exhibit SMM behaviour.

1.1.2.1 A dimeric manganese Schiff base complex as single molecule magnet

A dimeric manganese complex, $[\text{Mn}_2(\text{saltmen})_2(\text{ReO}_4)_2]$, was prepared using a tetradentate Schiff base ligand, *N, N'*-(1,1,2,2-tetramethylethylene)bis(salicylideneiminato) (saltmen^{2-}), by Hitoshi Miyasaka *et al.* in 2004.⁴³ The $[\text{Mn}_2(\text{saltmen})_2]^{2+}$ motif lies on an inversion centre, and the asymmetric unit contains only one Mn(III) site. Mn(III) is coordinated by N_2O_2 atoms from the Schiff base ligand and by two oxygen atoms from $(\text{ReO}_4)^-$. Magnetic measurements show the presence of ferromagnetic interactions between the Mn(III) centres and a spin ground state of $S = 4$. A single relaxation process was observed in the in-phase and out-of-phase components of the ac susceptibility measurements, indicating that this compound is a SMM. From the relaxation time, the energy barrier of 16 K was estimated.

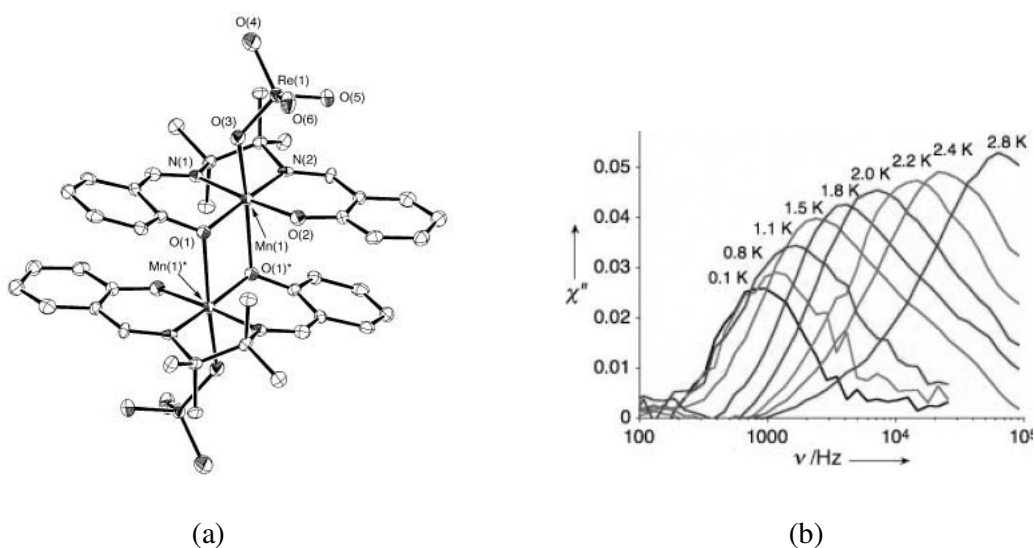


Figure 1.07 (a) Dinuclear manganese complex, $[\text{Mn}_2(\text{saltmen})_2(\text{ReO}_4)_2]$, (b) Plot of out-of-phase ac susceptibility versus frequency.⁴³

1.1.2.2 Mn₄ complexes with SMM behaviour

A family of tetranuclear Mn complexes [Mn₄X₄L₄], where L = salicylidene-2-ethanolamine (**A**, **B**) or 4-tert-butyl-salicylidene-2-ethanolamine (**C**) and X = Cl (**A**, **C**) or Br (**B**) have been synthesised and studied by C. Boskovic *et al.* in 2003.⁴⁴ These complexes possess a square-shaped core (Figure 1.08) with ferromagnetic exchange interactions between the four Mn(III) centres resulting in an $S = 8$ spin ground state, and an anisotropy-induced energy barrier to magnetisation reversal. The effective energy barrier was determined to be 7.7 and 7.9 K, for **A** and **B**, respectively. Detailed magnetic measurements revealed that relatively strong intermolecular interactions are present in all of the compounds. The intermolecular interactions were found to be antiferromagnetic for **A** and **B**, and ferromagnetic for **C**. This last system approaches a ferromagnetic phase transition with a critical temperature of ~ 1 K, which is coincident with the onset of slow relaxation of the magnetisation. It was found that the intermolecular interactions have a significant effect on the manifestation of slow relaxation of the magnetisation, and thus these complexes represent a family of “exchange-biased single molecule magnets”.

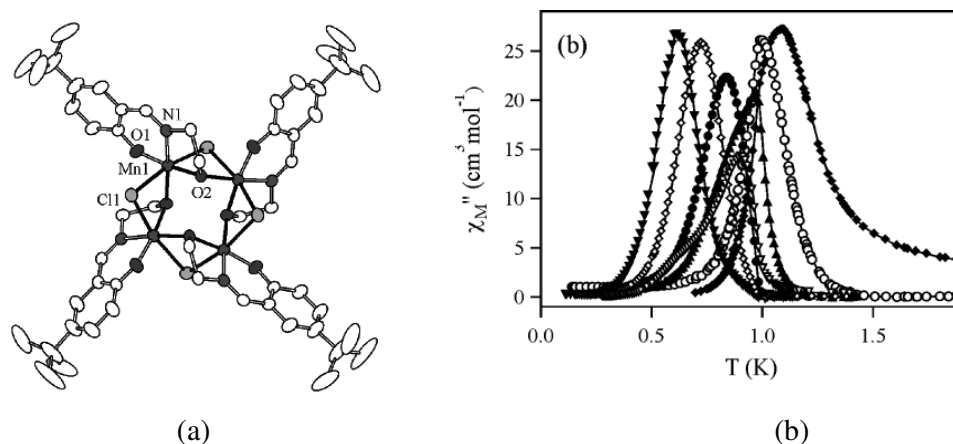


Figure 1.08 (a) Tetranuclear manganese complex, [Mn₄X₄L₄], (b) Plot of out-of-phase susceptibility versus temperature for **C**.⁴⁴

1.1.2.3 A record barrier for a single molecule magnet

A series of hexanuclear Mn complexes using salicylaldehyde or its bulkier derivatives and different carboxylic acid ligands have been reported by the groups of G. Christou and E. K. Brechin.⁴⁵ The basic structure (Figure 1.09) is comprised of a non-planar Mn₆ unit of two off-set stacked triangular [Mn(III)₃(μ₃-O)]⁷⁺ subunits linked by two central oximate oxygen atoms.

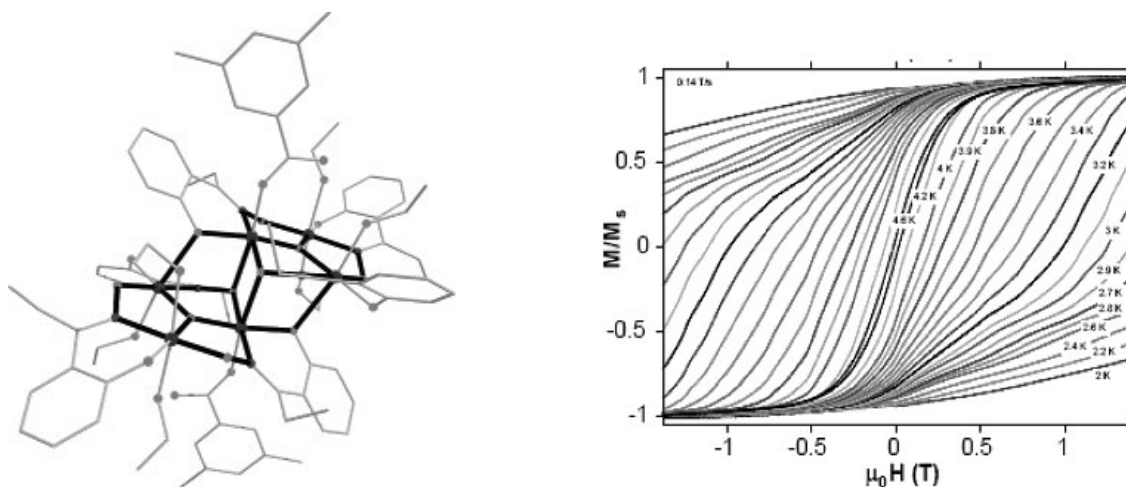


Figure 1.09 Molecular structure of [Mn^{III}₆O₂(Et-sao)₆(O₂CPh(Me)₂)₂(EtOH)₆].⁴⁵

It was observed that the deliberate structural distortion of the core by using bulkier ligands changes the magnetic exchange interactions between the metal centres from antiferromagnetic to ferromagnetic resulting in a molecule with $S = 12$, $D = -0.43 \text{ cm}^{-1}$ and an effective barrier to magnetisation reversal of 86.4 K. The frequency-dependent out-of-phase ac susceptibility signals and the steplike hysteresis loops indicate that this compound is a SMM.

1.1.2.4 A dinuclear Mn(III)-Cu(II) single molecule magnet

A dinuclear mixed-metal SMM, [Mn^{III}Cu^{II}Cl(5-Br-sap)₂(MeOH)], was synthesised in 2005 by H. Oshio *et al.*, where 5-Br-sapH₂ is the Schiff base, 5-bromo-2-salicylideneamino-1-

propanol.⁴⁶ The complex has an alkoxo-bridged dinuclear core of Mn(III) and Cu(II) ions (Figure 1.10), which have elongated octahedral and square-planar coordination geometries, respectively. Dc magnetic susceptibility measurements showed that the χT values increased as the temperature was lowered, followed by a sudden decrease below 20 K. The initial increase indicates the presence of intramolecular ferromagnetic interactions, and fitting the data indicated an $S = 5/2$ spin ground state. In the ac magnetic susceptibility measurements, frequency-dependent in-phase (χ') and out-of-phase (χ'') signals were observed supporting the conclusion that this compound is a single molecule magnet with a calculated energy barrier of 10.5 K.

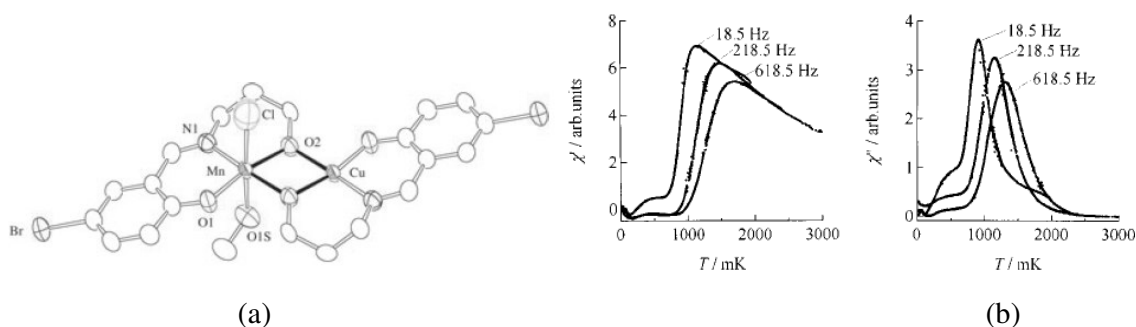


Figure 1.10 (a) Structure of $[\text{Mn}^{\text{III}}\text{Cu}^{\text{II}}\text{Cl}(\text{5-Br-sap})_2(\text{MeOH})]$, (b) Plot of in-phase and out-of-phase ac susceptibility versus temperature.⁴⁶

1.1.2.5 A heterometallic single molecule magnet of $[\text{Mn}^{\text{III}}_2\text{Ni}^{\text{II}}_2\text{Cl}_2(\text{salpa})_2]$

A new heterometallic SMM of $[\text{Mn}^{\text{III}}_2\text{Ni}^{\text{II}}_2\text{Cl}_2(\text{salpa})_2]$ (salpa = *N*-(2-hydroxybenzyl)-3-amino-1-propanol) was synthesised by H. Oshio *et al.* in 2005.⁴⁷ The structure consists of an incomplete face-sharing double cube that is composed of two Mn(III) and two Ni(II) ions (Figure 1.11). The Mn(III) and Ni(II) ions are doubly bridged by two oxygen atoms forming a dinuclear unit. They are bridged by phenoxo and alkoxo groups in μ_2 and μ_3 fashions, respectively. Mn(III) is five-coordinate with a square pyramidal geometry and Ni(II) is octahedral. Dc magnetic susceptibility measurements indicated that there are dominant ferromagnetic interactions in the complex. Magnetisation data showed a steplike hysteresis

loop, indicating that the molecule is a SMM. It possesses an $S = 6$ spin ground state with a negative D value (-0.70 cm^{-1}), and a magnetisation reversal barrier of 36 cm^{-1} .

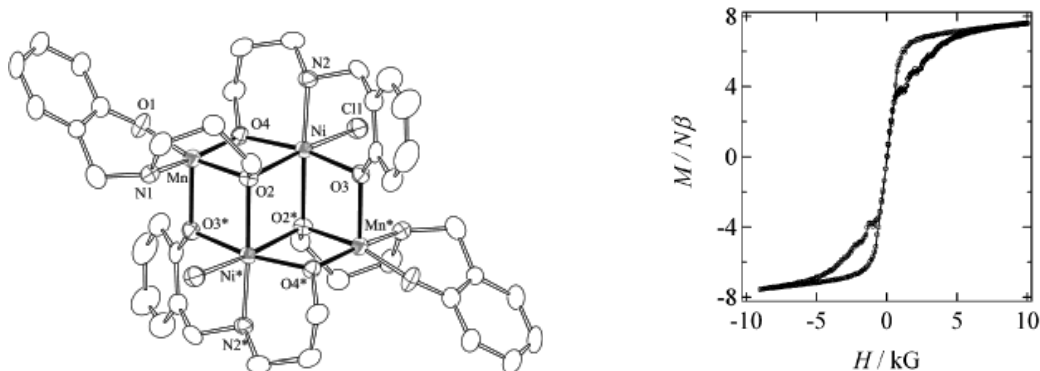


Figure 1.11 Structure of $[\text{Mn}^{\text{III}}_2\text{Ni}^{\text{II}}_2\text{Cl}_2(\text{salpa})_2]$ and hysteresis loop at 0.55 K .⁴⁷

This shows that these ligands are suitable for synthesising both extended and molecular systems. This can thus give a scope to study a wide range of magnetic behaviours.

1.2 Synthetic Strategy

The salicylic acid ligands used in the syntheses were polydentate with oxygen donor atoms where carboxylate or hydroxyl groups can coordinate to more than one metal centre. In order to have N-donor atoms, several coligands such as pyridine, 4-Me-pyridine and 2,2'-bipyridyl were used along with the salicylic acid ligands. The Schiff base ligands have both nitrogen and oxygen-donor sites, and they can be tri-, tetra- and pentadentate. The synthetic approach targeted oxygen-bridged molecular aggregates by solvolysis reactions of the ligands with different metal ions, in varying solvents. By controlling the ratios of ligand, metal and base, different complexes can be obtained. The compounds formed revealed information about the coordination ability and binding modes of the ligand. Different coligands can also be used in the above mentioned procedure. Varying the coligand by increasing the number of donor groups might lead to the incorporation of more metal centres. When alcohol-based

solvents (ROH or H₂O) were employed, hydrolysis reactions of the solvents can be expected, forming hydroxy or oxo ligands. One further possible variation is to add bridging species like acetate or azide, which can act as additional linkers between the metal ions, or can fill any empty coordination sites on the metal centres.

Another approach was to use two types of metal ions, so that heterometallic complexes could be obtained. The presence of two types of metal centres can give rise to interesting magnetic properties and can allow further investigation of the exchange interaction between two different metal ions. This was pursued using two different transition metals or a combination of transition and lanthanide metal ions. The lanthanide ions behave as hard acids preferring oxygen (O-) rather than nitrogen (N-) donors, while d-block metal ions are borderline acids, having a tendency to coordinate to N-donors as well as O- donors. Consequently, a typical approach in constructing *3d-4f* complexes is by self-assembly of different metal ions with ligands containing both O- and N-donors. With this in mind, substituted salicylic acid with O-donors and coligands with N-donors were complexed with metal ions. The Schiff base ligands, however, possess both types of donors, so they are suitable for the synthesis of mixed-metal clusters.

The transition metal ions used in the following chapters were Mn(II), Cu(II), Ni(II) and Fe(III). With O- and N- donors, Mn(II) has five unpaired electrons in its high-spin state which can give large ground state spins on aggregates. It can be easily oxidized to Mn(III), which is anisotropic in octahedral geometry, and can give rise to high zero-field splitting values (*D*) leading to a significant barrier to magnetisation reversal (*U*). As a result, mixed-valence manganese compounds are likely to have a combination of both high spin and high anisotropy. Cu(II) ions have one unpaired electron, making the interpretation of magnetic interactions relatively straightforward. Fe(III) with five unpaired electrons in its high-spin state can give rise to large ground state spins. It also has a zero-field splitting which can be useful for synthesising SMMs. Ni(II) has two unpaired electrons in octahedral coordination

environments, and is anisotropic with significant zero-field splitting. This can impart interesting magnetic properties to the complexes.

Lanthanides (Ln) have the advantages that they can have a large number of unpaired f -electrons and considerable single-ion anisotropy. The origin of SMM behaviour in lanthanide containing compounds is, however, more complicated than that of d -block transition metal ions since there is likely to be a significant orbital component. The effect of spin-orbit coupling increases as the atomic number increases, with the exception of the $4f^7$ configuration, which has no first-order angular momentum. As a result, it is useful to synthesise Gd analogues of Ln complexes in order to interpret the magnetic properties. The magnetic interactions between $4f$ electrons on different metal centres are expected to be much weaker than the interactions between $3d$ electrons in transition metal complexes because the overlap between the $4f$ orbital and the orbital of the bridging ligand is small. Recently, slow relaxation of magnetisation has been observed in some lanthanide containing compounds.^[34,37] Thus, there is much interest in identifying further magnetically unusual Ln compounds. In addition, series of analogous Ln-M compounds can be synthesised, enabling investigation into the variation of structure and magnetic properties.

1.3 Characterisation of the synthesised ligands by NMR spectroscopy

Nuclear magnetic resonance (*NMR*) spectroscopy is an important tool for the chemist as it can give information about the number of hydrogen and carbon atoms, their connectivity, and the type of functional groups present in a molecule. NMR spectroscopy involves transitions between nuclear spin states. Important examples are the nucleus of hydrogen (^1H) and the nucleus of the ^{13}C isotope of carbon. In the presence of an applied external magnetic field, these nuclei exist in two nuclear spin states of different energy. In the NMR spectrum, peaks appear at the positions of absorption, also called the positions of resonance, or *precession frequencies*, for different nuclei in the molecule.

The frequency of absorption for a nucleus of interest relative to the frequency of absorption of a molecular standard is called the **chemical shift** of the nucleus. The chemical shift of a particular nucleus in a molecule gives us information about the environment of the atom to which the nucleus is bonded. The height of the peak is proportional to the number of ^1H nuclei in the molecule with the same chemical shift. The intensity of a ^{13}C resonance is, however, not proportional to the number of carbons.

In a 1D NMR spectrum, some of the most useful information for structure determination comes from the J -coupling between NMR active nuclei. This coupling arises from the interaction of different spin states through the chemical bonds of a molecule and results in the splitting of NMR signals known as **spin-spin splitting**. This coupling provides detailed insight into the connectivity of atoms in a molecule. The splitting arises between protons on adjacent or on the same atoms, and the splitting occurs only between nuclei with different chemical shifts. This is due to coupling interactions between proton neighbours and is related to the number of possible spin orientations that these neighbours can adopt. The number of peaks into which a proton signal is split equals to one more than the number of equivalent neighbouring protons n ($n+1$ rule).

Two-dimensional NMR spectra provide more information about a molecule, and are especially useful in determining the structure of a molecule. The 2D NMR spectra have two frequency axes and one intensity axis. The most commonly used 2D NMR is ^1H - ^1H correlation spectroscopy (**COSY**) in which both frequency axes show ^1H chemical shifts. COSY identifies pairs of proton which are coupled to each other. A 2D NMR experiment involves a series of one-dimensional experiments. Each experiment consists of a sequence of radio frequency pulses with delay periods in between them. During some of the delays, the nuclear spins are allowed to freely precess (rotate) for a determined length of time known as the evolution time. The frequencies of the nuclei are detected after the final pulse. By

incrementing the evolution time in successive experiments, a two-dimensional data set is generated.

A typical spectrum is shown in Figure 1.12. The spectrum is interpreted starting from the diagonal, which consists of a series of peaks that occur when both frequency axes have peaks representing the same nuclei. The peaks that appear off of the diagonal are called cross-peaks. The cross-peaks are symmetrical on either side of the diagonal and indicate which hydrogen atoms are spin-spin coupled to each other. To determine which protons are on neighbouring carbons, the centre of a cross-peak is matched with the centre of each of the two corresponding diagonal peaks.

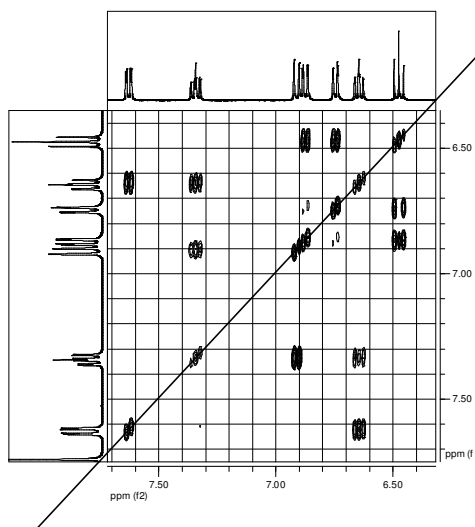


Figure 1.12 An example of 2D ^1H - ^1H COSY spectra.

Two dimensional NMR spectra which show ^{13}C - ^1H shift correlations are termed **HETCOR** (from heteronuclear coorelation). These are used to detect directly-bonded ^{13}C - ^1H atoms. These 2D techniques can be very useful in characterising the ligands and in comparing the effects of ligand modifications. It can thus be predicted that the changes in the electronic structure of the ligands can lead to changes in the structure of the metal complexes they form.

1.4 Introduction to Magnetochemistry

Magnetochemistry is the study of the interrelationship between the structure of a compound and its magnetic properties. Magnetic measurements can give information about the electronic structure and magnetic exchange interactions in metal complexes. This section provides a brief overview of how magnetic measurements can be applied to this area of inorganic chemistry. More detailed accounts are given in standard texts by Mabbs and Machin,⁴⁸ O'Connor,⁴⁹ Carlin,⁵⁰ Kahn,⁵¹ and Kittel.⁵²

1.4.1 Magnetic Susceptibility

The magnetic moment of a free atom is due to the spins of its electrons, their orbital angular momentum around the nucleus, and the change in the orbital moment induced by an applied magnetic field. The magnetic susceptibility, χ , is the degree to which a material can be magnetised in an external magnetic field, and the magnetisation, M , is defined as the magnetic moment per unit volume. The magnetic susceptibility per unit volume is then:

$$\chi = M/H \text{ (cgs)} \quad \text{or} \quad \chi = \mu_0 M/H \text{ (SI)} \quad \text{Eq. 1.1}$$

where H is the macroscopic magnetic field intensity in Oersted, Gauss or Tesla. It is sometimes convenient to refer to M/H as susceptibility without specifying the system units. Susceptibility is often referred to as per unit mass or per mole of the substance, and thus, the molar susceptibility is designated as χ_M , and the magnetic moment per gram is sometimes written as σ .⁵²

In general χ is the algebraic sum of two contributions:

$$\chi = \chi^D + \chi^P \quad \text{Eq. 1.2}$$

where χ^D and χ^P represent the diamagnetic and paramagnetic susceptibilities, respectively. The former is negative and the latter is positive. When χ^D dominates, the sample is called diamagnetic with the magnetisation in opposition to the applied magnetic field. When χ^P is the leading contribution, the sample is said to be paramagnetic with the magnetisation in the direction of the applied field.⁵¹

1.4.2 Different kinds of magnetic behaviour

The origin of magnetism lies in the orbital and spin motion of electrons, and in the interaction of these electrons with one another. The best way to introduce different kinds of magnetism is to describe the response of materials to magnetic fields. The main distinction is that in some materials there is no collective interaction of atomic magnetic moments, whereas in some there is a very strong interaction between atomic moments.

The interaction of the magnetic field with the motion of the electrons in their orbitals leads to diamagnetism. In this case, magnetic susceptibility is usually independent of the temperature and the strength of the applied field. When this is the only magnetic response, these substances are composed of atoms which have no net magnetic moments because all the orbitals are filled. When exposed to a magnetic field, a negative magnetisation is produced, and the susceptibility is negative. It is a fundamental property of all matter and is usually very weak.

Any atom, ion or molecule that has one or more unpaired electrons is paramagnetic and possesses a net magnetic moment. These substances are attracted to the magnetic field due to partial alignment of the atomic magnetic moments in the direction of the field, resulting in a net positive magnetisation and positive susceptibility. The individual magnetic moments, however, do not interact magnetically. Paramagnets do not retain any magnetisation in the absence of an externally applied magnetic field because thermal motion causes the spins to become randomly oriented.

Substances which have magnetic interaction between the neighbouring paramagnetic centres leading to an increase in the magnetic moment are designated as ferromagnets. In this case, the individual moments are perfectly aligned parallel to each other. A ferromagnetic substance usually divides into domains to minimise its total free energy, a spontaneous magnetisation arises in each domain even in the absence of a magnetic field. The saturation of

magnetisation corresponds to the complete alignments of all magnetic domains. Its magnetic susceptibility is positive and very large.

When the magnetic interaction between paramagnetic centres lead to an antiparallel alignment of the moments the substance is known as an antiferromagnet. There is complete cancellation of the magnetic moment and it does not have any spontaneous magnetisation.

Substances where the magnetic moments are aligned antiparallel but there is an incomplete cancellation of the spins are termed ferrimagnets. They exhibit spontaneous magnetisation as in the case of ferromagnets. This may occur in molecules with unequal numbers of spin centres. In the case of extended systems this might be due to two or more magnetic species possessing different magnitudes of magnetic moment. These species may be two different valence states of the same ion or two different elements or even a combination of an ion and a free radical. Spontaneous magnetisation is the consequence of a lack of cancellation of the magnetisation.

1.4.3 Determination of the magnetic behaviour

It was shown by Pierre Curie that for most paramagnetic substances with isolated magnetic sites, the magnetic susceptibility varies inversely with temperature. The magnetisation of paramagnets follows Curie's law to a good approximation:

$$M = C \cdot H / T \quad \text{Eq 1.3}$$

where M is the resulting magnetisation, H is the applied field and C is the Curie constant where $C = Ng^2\mu_B^2/(4k_B)$.

Since the magnetic susceptibility is $\chi = M/H$, in this case:

$$\chi = C/T \quad \text{Eq 1.4}$$

When the paramagnetic ions or atoms interact this law is no longer valid, and the magnetic exchange between spin carriers then needs to be included in the model. As a result, in ferromagnets and antiferromagnets Curie-Weiss law is applicable, which is:

$$M = C \frac{H}{T - \theta} \quad \text{with} \quad C = \frac{Ng^2\mu_B^2}{4k_B} \quad \theta = \frac{zJ}{2k_B}, \quad \text{Eq 1.5}$$

where θ is the Weiss constant, and the magnetic susceptibility is:

$$\chi = C / T - \theta. \quad \text{Eq 1.6}$$

There are three ways to plot the temperature dependence of the magnetic susceptibility, and these are shown in the Figures 1.13 and 1.14. These plots give information about the kind of magnetic interactions present in a compound.

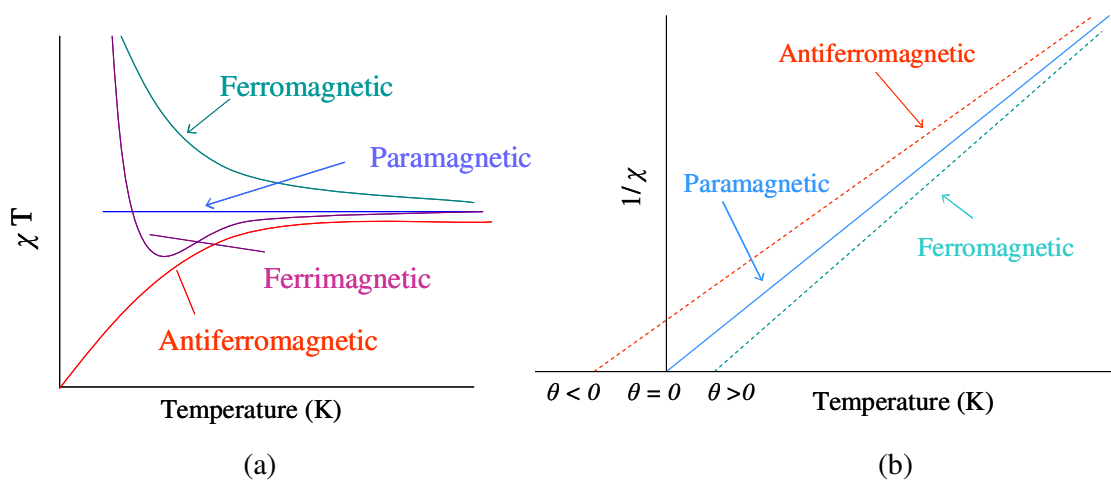


Figure 1.13 (a) The plot of χT and (b) the plot of $1/\chi$, as a function of temperature for paramagnetic, ferromagnetic, antiferromagnetic and ferrimagnetic materials.

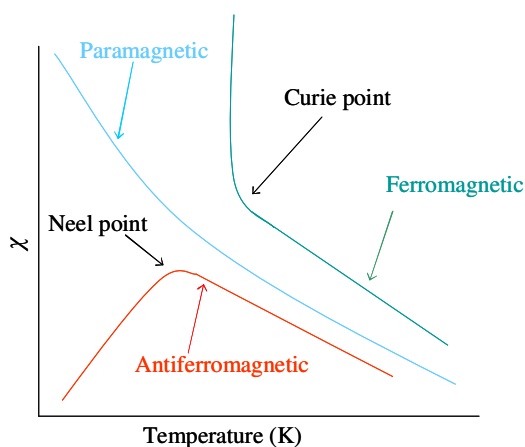


Figure 1.14 The plot of magnetic susceptibility as a function of temperature for paramagnetic, ferromagnetic, antiferromagnetic and ferrimagnetic materials.

When the Weiss constant is negative, a decrease in the χT versus T plot is observed, which indicates the presence of antiferromagnetic interactions. The value of θ can be obtained directly by plotting a $1/\chi$ versus T plot, where θ is the negative intercept on the temperature axis. When the Weiss constant is positive, there is an increase of the χT versus T curve. This indicates the presence of ferromagnetic interactions. The value of θ can be obtained directly by plotting a $1/\chi$ versus T plot, where θ is now the positive intercept on the temperature axis.

In a ferromagnet, even though electronic exchange forces are very large, thermal energy eventually overcomes the exchange and produces a randomising effect. This occurs at a particular temperature called the Curie temperature (T_C), shown in the χ versus T plot (Figure 1.14). Above T_C an ideal ferromagnet becomes a paramagnet that obeys the Curie-Weiss law,⁵⁴ but below this temperature, its magnetic susceptibility increases rapidly. An exchange integral, J , is used to define the degree of coupling at any temperature and is given in units of cm^{-1} or K, where $1 \text{ cm}^{-1} = 1.43877 \text{ K}$. For ferromagnetic coupling, J is positive. In an antiferromagnet, above a critical temperature, known as the Néel temperature, T_N , thermal agitation destroys magnetic ordering and a material becomes a paramagnet, but below this temperature, its magnetic susceptibility decreases with decreasing temperature. A negative J value implies antiferromagnetic coupling. Ferrimagnets, like ferromagnets, hold a spontaneous magnetisation below the Curie temperature, and show no magnetic order (are paramagnetic) above this temperature.

1.5 Single molecule magnet behaviour

Single molecule magnets (SMMs) are molecules with a large barrier to magnetisation relaxation, and consequently display hysteresis loops at low temperatures in magnetisation versus applied-field plots. This is the diagnostic property of a magnet. They possess a negative zero-field splitting due to magnetic anisotropy and a significant spin ground state (S). The negative axial anisotropy ($D < 0$) removes the degeneracy in the M_s levels of the ground

spin state, placing higher magnitude levels lower in energy. The selection rule $\Delta M_s = \pm 1$ for allowed transitions, results in an energy barrier U separating the two lowest energy levels of $M_s = \pm S$. The spin reversal energy barrier will be $U = S^2|D|$ for integral spin states, while $U = (S^2 - 1/4)|D|$ for half-integral spin states. A positive D value would result in $M_s = 0$ level being lowest in energy, such that there is no energy cost for losing direction of the spin (i.e. in going from $M_s = +S$ to $M_s = 0$). This means that for a molecule to behave as SMM, it should have a negative D value.

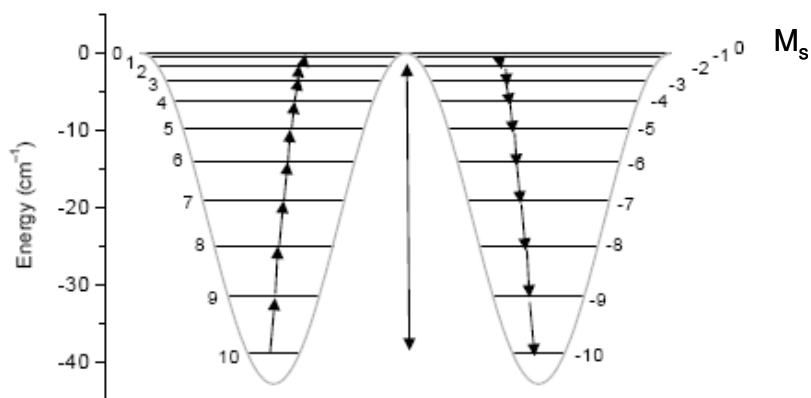


Figure 1.15 Plot of energies of the microstates in a $S = 10$ system.

As the energy barrier is intrinsic to the ground state, the magnetisation can be pinned along one direction as is shown in Figure 1.15, leading to slow relaxation at a very low temperature. This effect is readily probed through ac magnetic susceptibility measurements, which provide a direct means of gauging the relaxation rate. Here the magnetic susceptibility of a sample is measured using a weak magnetic field that switches direction at a fixed frequency. If the effective barrier to magnetisation relaxation is significant in comparison to the thermal energy (kT), then the measured susceptibility referred to as the in-phase or real component (χ') of the ac susceptibility begins to diminish. Accordingly, the portion of the susceptibility that cannot keep up with the switching field, the out-of-phase or imaginary component of the ac

susceptibility, χ'' , increases. When a magnetisation reversal barrier exists, then χ' and χ'' are also frequency-dependent. If the net magnetisation relaxes fast enough to keep up with the oscillating ac field, then there is no imaginary (out-of-phase) susceptibility (χ''), and the real (in-phase) susceptibility (χ') is equal to the dc susceptibility.

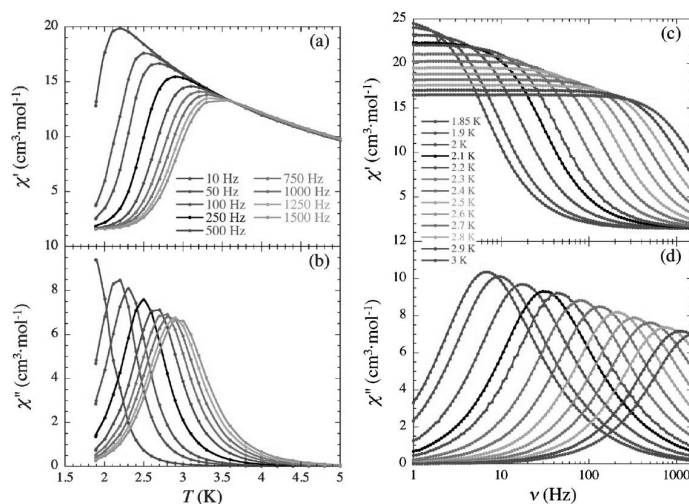


Figure 1.16 An example of ac susceptibility measurements as a function of temperature at different frequencies, and as a function of frequency at different temperatures (a, c) in-phase and (b, d) out-of-phase signals.

If just a single relaxation process is operational, then a plot of χ'' versus temperature will display a peak with a maximum at the temperature where the switching of the magnetic field matches the relaxation rate, $1/\tau$. Furthermore, since $1/\tau$ increases with temperature, this peak should shift to higher temperature when the switching frequency is increased. The relaxation time for the magnetisation in a single molecule magnet can be expected to follow an Arrhenius relationship:

$$\tau = \tau_0 \cdot e^{(U_{eff}/kBT)}$$

where the pre-exponential term τ_0 can be thought of as the relaxation attempt frequency. A plot of $\ln \tau$ versus $1/T$ should be linear, with the slope and intercept permitting evaluation of U_{eff} and τ_0 .

It has also been recognised that there can be additional influences on the SMM behaviour such as quantum effects⁵⁵ or inter-complex magnetic interactions.⁵⁶ Indeed at low enough temperature, quantum relaxation of the magnetisation can be experimentally observed as it becomes faster than the thermally activated relaxation induced by U_{eff} . When two M_S microstates on the either side of the energy barrier have similar energies, then there is a increased probability of quantum tunnelling of the magnetisation (QTM). SMM complexes appear to be unique systems for studying fundamental phenomena such as quantum spin tunneling and quantum interference. These may be used for future applications in molecular electronics.

1.6 Thesis overview

The following chapters will discuss the synthesis, structure and properties of the coordination compounds obtained using substituted salicylic acid and Schiff base ligands. Homometallic mixed-valence manganese and heterometallic Fe-Ln coordination polymers from substituted salicylic acids and different coligands are presented in chapter 3. Discrete oligomeric complexes of Mn, Cu and Fe with salicylic acid ligands are described in chapter 4. Detailed NMR studies of the synthesised Schiff base ligands are shown in chapter 5. It also includes a comparison of the structure and properties of the resulting homo- and heterometallic complexes using Mn(II) and Ni(II) ions. Various types of magnetic systems encompassing long-range magnetic ordering and single molecule magnet behaviour were studied in detail.

Chapter 2: Research objectives

The goal of this research work was to design and synthesise molecule-based materials, and characterise their magnetic behaviour. An important concept in synthesising such compounds is the use of molecular building blocks to create systems of different dimensionalities, ranging from discrete to extended systems. A variety of strategic methods were developed to achieve this. A further aim of this work was to investigate the influence of ligands, coligands, metal salts, bases, solvents and the ratios of these components, on the formation of polymeric networks or metal aggregates.

In recent years, the use of crystal engineering concepts has produced a variety of metal organic frameworks (MOFs),⁵⁷ many of which exhibit unusual and fascinating modes of entanglement of individual motifs.⁵⁸ There is an increasing interest in these species not only for their potential properties, but also for their intriguing architectures and topologies such as molecular grids, herringbones, bricks, ladders, rings, boxes and honeycombs. They have been produced utilizing organic ligands as linkers and metal centres as nodes. One of our research goals was to construct extended systems, including MOFs, possessing novel structural motifs and interesting magnetic properties.

The complexes of *3d* transition metal ions and substituted salicylic acids have received less attention than systems with other aromatic carboxylic acids.⁵⁹ In Chapter 3, coordination polymers synthesised *via* the solvolysis reaction of paramagnetic metal ions, substituted salicylic acid ligands and different coligands are discussed.

The design of supramolecular architectures with novel spin-carrier topologies is of current interest in the field of molecular magnetism. This has led to the syntheses of heterometallic complexes, such as *3d-4f* metal systems. Although a number of *3d-4f* heterometallic complexes with discrete structures has been obtained by conventional self-assembly reactions in solution,⁶⁰⁻⁶⁴ the syntheses of polymeric compounds has been relatively rare.⁶⁵ Our objective was to synthesise heterometallic coordination polymers of transition and

lanthanide metal ions using substituted salicylic acids (O-donors) and several coligands (N-donors). Chapter 3 also describes the syntheses and properties of certain heterometallic coordination polymers.

In order to understand the behaviour that might be expected in such extended structures, it is useful to synthesise and study analogous systems of mononuclear or trinuclear units. These units may act as building blocks of the extended structures and can help to explain the behaviour observed in such systems. This is described in Chapter 4, where oligomeric structures obtained from salicylic ligands are reported.

The term SMM (single molecule magnet) has been coined to describe well-defined molecular entities which behave as single-domain magnetic particles below a certain blocking temperature in the same way as the less structurally precise superparamagnetic nanoscale particles are known to do. An attractive feature of SMMs is that they can be assembled and manipulated using synthetic chemistry principles at the molecular level. In this context, several salicylaldimine (Schiff base) ligands, with diverse slight modifications, were complexed with metal ions. In this way, the effect of structural or electronic variation on the magnetic properties was investigated. These kind of ligands have multiple coordination sites, in which each coordination site possesses a different affinity for different metal ions, and they have the potential to afford heterometallic clusters by facile one-pot reactions. In Chapter 5, the structural and magnetic properties of some homo- and heterometallic complexes obtained by these ligands are examined in detail.

Chapter 3: Structure and magnetic properties of 1D and 3D compounds with substituted salicylates

Carboxylate bridges can mediate magnetic interaction in coordination compounds, thus it is very interesting to study how different kinds of carboxylate ligands and their various bridging modes can modulate the overall magnetic behaviour of compounds. The tri- and tetradentate ligands used were 3-methylsalicylic acid (3-Me-salH₂), 4-methylsalicylic acid (4-Me-salH₂), 5-methylsalicylic acid (5-Me-salH₂) and 3-methoxysalicylic acid (3-MeO-salH₂) (Figure 3.01). Another interest was to investigate the effect of ligand substituents on the structure and magnetic properties of resulting compounds. The presence of the substituent at different positions (*ortho*, *meta* or *para*) on the benzene ring of the salicylic acid can help to understand the role of steric and electronic factors on the coordination chemistry of salicylic acids.

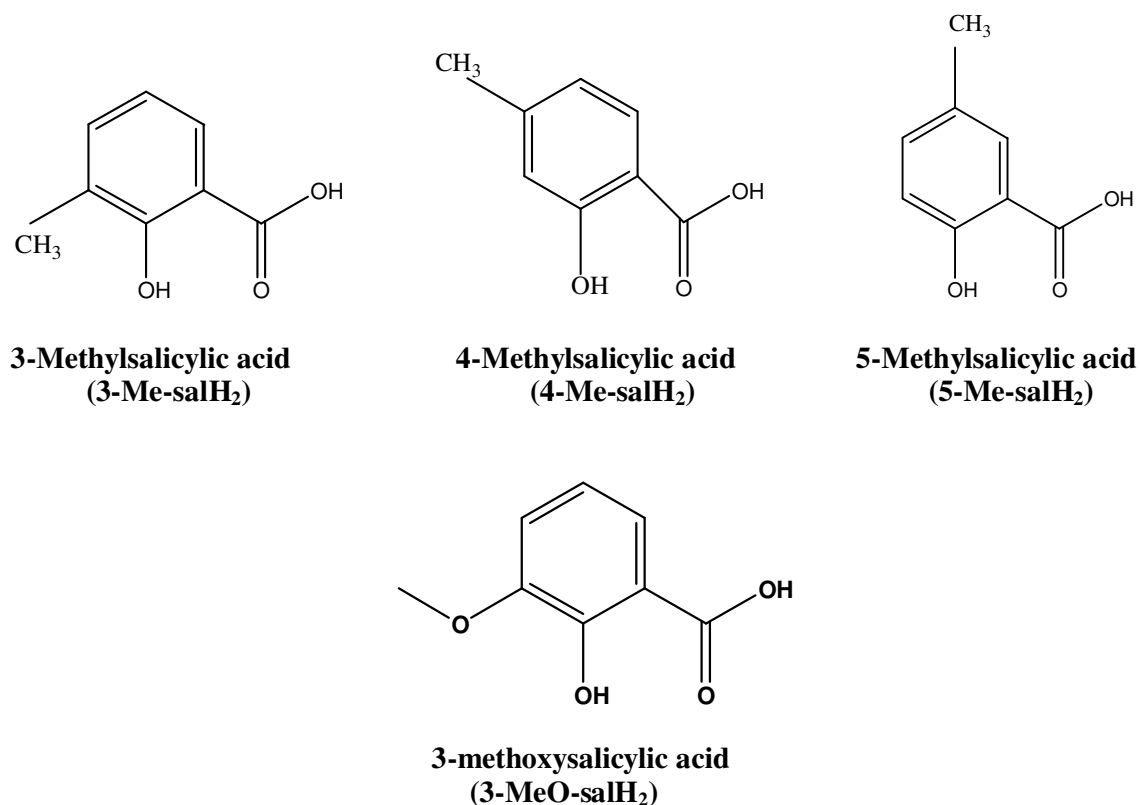


Figure 3.01 Structure of the different salicylic acid ligands.

Coligands were employed to increase the number and type of donor groups. The following coligands were used: pyridine (py), 4-methylpyridine (4-Me-py) and 2,2'-bipyridyl (2,2'-bipy) (Figure 3.02). Using coligands with varying steric effects can have significant results on the structure of the products.

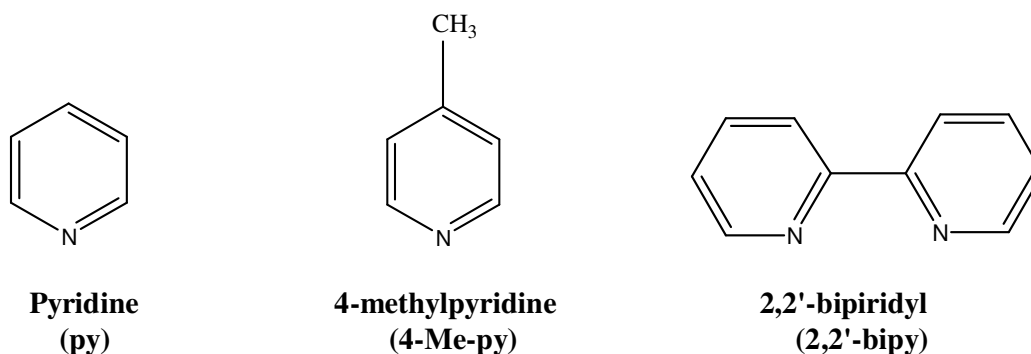


Figure 3.02 Structure of the various coligands.

During the investigation, new 1D and 3D mixed-valence manganese compounds were obtained. It was possible to understand how the arrangement of ligands and coligands in these systems gave rise to different dimensionalities. In addition, the relationship between structure and magnetic behaviour was deduced by studying the effect of structural changes on the magnetic properties. The attempt to introduce different metal centres in these extended systems was also successful, and heterometallic 1D Fe(III)-Ln(III) coordination polymers were obtained. Magnetic studies gave insight into the kind of interactions mediated by salicylic acid ligands between the metal centres. It was evident that by using selected ligands, coligands and metal salts, a significant degree of control over the structure and magnetic behaviour can be obtained.

3.1 Homometallic 1D and 3D compounds

Compounds were obtained by room temperature syntheses in methanol using the selected substituted salicylic acid, py or 4-Me-py, and a Mn(II) salt. The base used to oxidise Mn(II) to Mn(III) was triethylamine.

3.1.1 Structure and magnetic behaviour of $[\text{Mn}^{\text{III}}_2\text{Mn}^{\text{II}}(\text{3-Me-sal})_4(\text{py})_4]$, **1**

The reaction of 3-Me-salH₂ and py with Mn(II) in methanol gave $[\text{Mn}^{\text{III}}_2\text{Mn}^{\text{II}}(\text{3-Me-sal})_4(\text{py})_4]$, **1**. The structure of compound **1** is an infinite 3D network that crystallizes in the tetragonal space group, $P4_3$. The asymmetric unit contains one Mn(II) and two Mn(III) ions, four 3-Me-sal²⁻ ligands and four pyridine coligands (Figure 3.03).

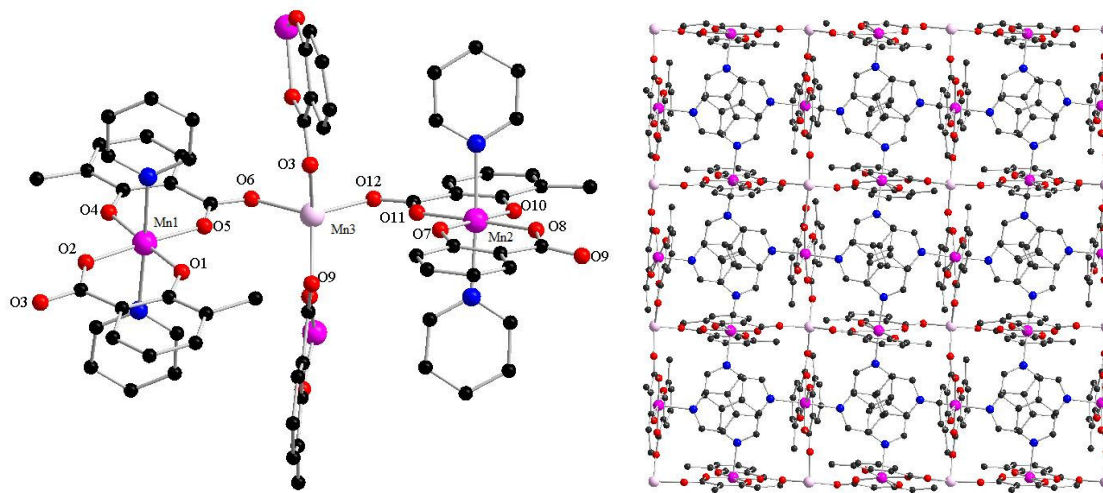


Figure 3.03 The asymmetric unit of $[\text{Mn}^{\text{III}}_2\text{Mn}^{\text{II}}(\text{3-Me-sal})_4(\text{py})_4]$, **1** and its packing diagram. Colour code: Mn(III), purple; Mn(II), pink; C, black; O, red and N, blue. Hydrogen atoms are omitted for clarity.

The two Mn(III) centres, Mn1 and Mn2, are each chelated (through phenoxo and carboxylate oxygen atoms) by two different 3-Me-sal²⁻ ligands (arranged in a *trans* position) forming an equatorial plane with Mn–O bond lengths in the range of 1.847–2.035 Å. They are further ligated by two pyridine nitrogen atoms which define the Jahn-Teller axes, with Mn–N bond lengths in the range of 2.204–2.271 Å. In this way, a building unit $[\text{Mn}^{\text{III}}(\text{3-Me-sal})_2(\text{py})_2]^-$ can be defined. The Mn(II) centre, Mn3, is coordinated by four carboxylate oxygen atoms (O3, O6, O9, O12) from four bridging 3-Me-sal²⁻ ligands. The geometry about Mn3 is close to tetrahedral, with Mn3–O bond lengths in the range of 2.051–2.095 Å, and the O–Mn–O angles 100.22–114.73°. The Mn3–O distances correspond to the Mn(II)–O distances

previously reported in the literature.⁶⁶ Bond Valence Sum (BVS) analysis further confirms the oxidation states of the metals.⁶⁷

The network can be described in terms of distorted tetrahedral four-fold Mn(II) nodes. They are bridged by $\{\text{Mn}^{\text{III}}(3\text{-Me-sal})_2(\text{py})_2\}^-$ spacers, giving a diamondoid network (Figure 3.04), which is compressed along the tetragonal four-fold axis. Alternatively, four-fold Mn(II) nodes and two-fold *quasi*-linear Mn(III) nodes (in the ratio of 1:2) can be considered as linked by 3-Me-sal^{2-} spacers. In either description, the carboxylate groups form *syn-anti* bridges between Mn(II) and Mn(III) cations. The four carboxylate bridges about each Mn(II) are crystallographically independent, resulting in four different Mn(III)–Mn(II) distances, 4.612(0) Å, 5.025(0) Å, 5.054(0) Å and 5.381(1) Å. Topological analysis of this framework with the TOPOS software reveals a *heterogeneous* four-fold diamond-type network with the total Schläfli symbol of $[6^6]$.⁶⁸ Each Mn(II) node is linked to four other Mn(II) nodes *via* Mn(III) two-fold nodes, such that each Mn(II) participates in six six-membered $\{\text{Mn}^{\text{II}}\}_6$ rings, with distances between the Mn(II) nodes of 9.615 Å and 10.415 Å.

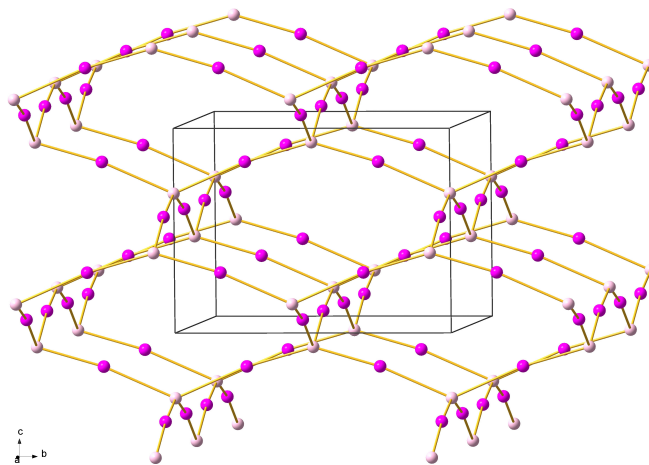


Figure 3.04 A diagram of the diamondoid network motif for compound **1**. Four-fold Mn(II) nodes are shown as pink spheres, two-fold Mn(III) nodes are shown in purple.

The magnetic susceptibility of **1** was studied from 300 K to 1.8 K at 1000 Oe and 10000 Oe (Figure 3.05). At room temperature, the χT product at 1000 Oe is 9.6 cm³K/mol which is in agreement with the expected value (10.4 cm³K/mol) for the presence of one Mn(II) and two Mn(III) metal ions. Upon cooling, the χT product steadily decreases to reach a minimum value of 4.4 cm³K/mol around 10 K, then increases rapidly to reach a maximum value of 37.5 cm³K/mol at 6 K, and afterwards, abruptly drops down to 14.0 cm³K/mol at 1.8 K. The initial decrease down to 10 K is indicative of dominant antiferromagnetic interactions between Mn(II) and Mn(III) metal ions through the two different but very similar *syn-anti* carboxylate bridges. The ground state of the system should correspond to a ferrimagnetic arrangement of spins. The χT values start to deviate from normal paramagnetic behaviour at about 10 K. This strongly suggests the appearance of a magnetically ordered phase with a spontaneous magnetisation. The plot of χ versus T at different fields is shown in Figure 3.06.

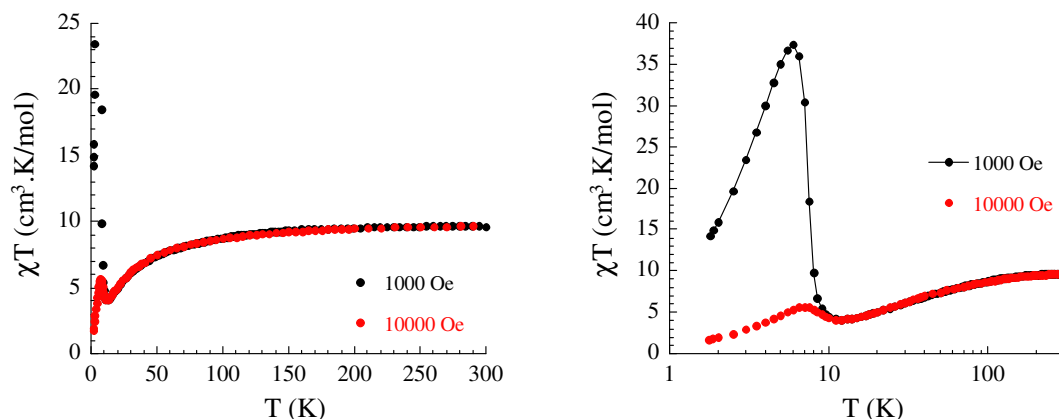


Figure 3.05 Temperature dependence of the χT product for **1** at 1000 Oe and 10000 Oe, from 0 to 300 K (left side) and from 1 to 100 K (right side).

The magnetisation as a function of field at low temperatures has been measured up to a field of 7 T (Figure 3.07). At low fields, there is an abrupt increase up to 1.4 μ_B at 250 Oe. When the field is further increased, the magnetisation gradually reaches 3.8 μ_B at 7 T without saturation. The curve has a weak sigmoidal shape. It is worth noting that already above 5 T,

the magnetisation is higher than the expected value ($3 \mu_B$) for a ferrimagnetic system with two $S = 2$ Mn(III) and one $S = 5/2$ Mn(II) spin units. This shows, that the Mn(II)-Mn(III) antiferromagnetic interactions are clearly overcome by the applied dc field, and that the magnetisation is expected to saturate at $13 \mu_B$ well above 7 T. The M vs H data at 2 K reveals the existence of hysteresis with a small coercive field (about 60 Oe), indicating that this material is a very soft magnet.

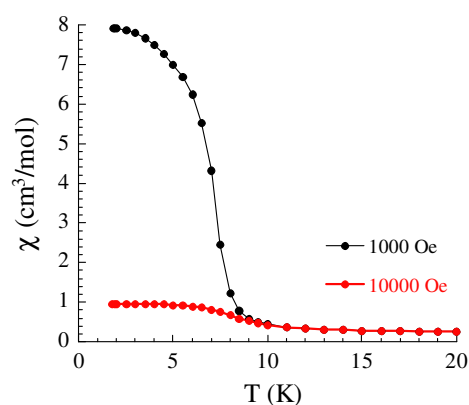


Figure 3.06 Temperature dependence of χ for **1** at 1000 Oe and 10000 Oe.

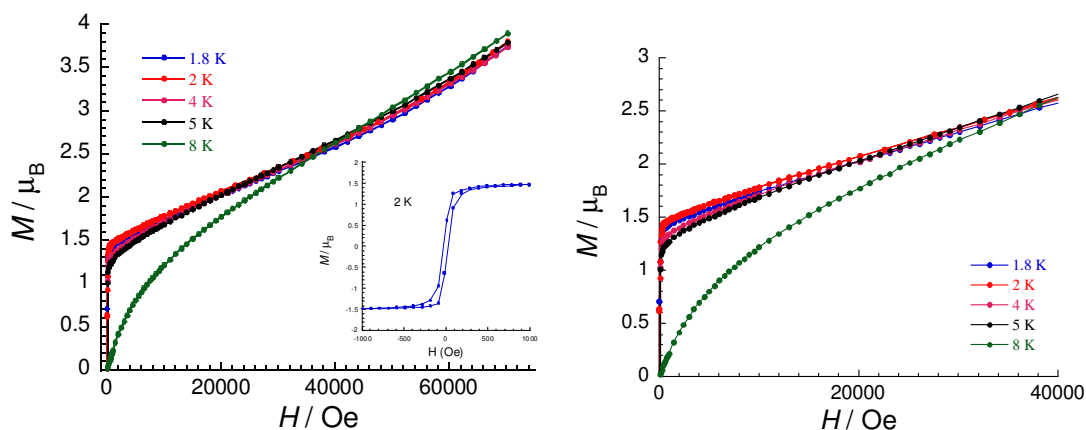


Figure 3.07 Field dependence of the magnetisation (left side up to 60000 Oe and right side up to 40000 Oe) for **1** from 1.8 to 8 K; hysteresis loop at 2 K (left, inset).

The in-phase ac magnetic susceptibility (χ') exhibits a peak located around 7 K and the out-of-phase ac susceptibility (χ'') deviates from zero at 7.4 K (Figure 3.08). This behaviour

was found to be almost perfectly frequency-independent, indicating the presence of a true three-dimensional ferrimagnetic order below 7.4 K.

The Mn(II) and Mn(III) interactions can be evaluated using the mean field theory, and the experimental critical temperature. The main idea of mean field theory (MFT) is to use an average or effective interaction for a multi-body system with many interactions. MFT is used for higher dimensionality system, when the Hamiltonian includes long-range forces. This method can easily help in understanding the behaviour of the system.

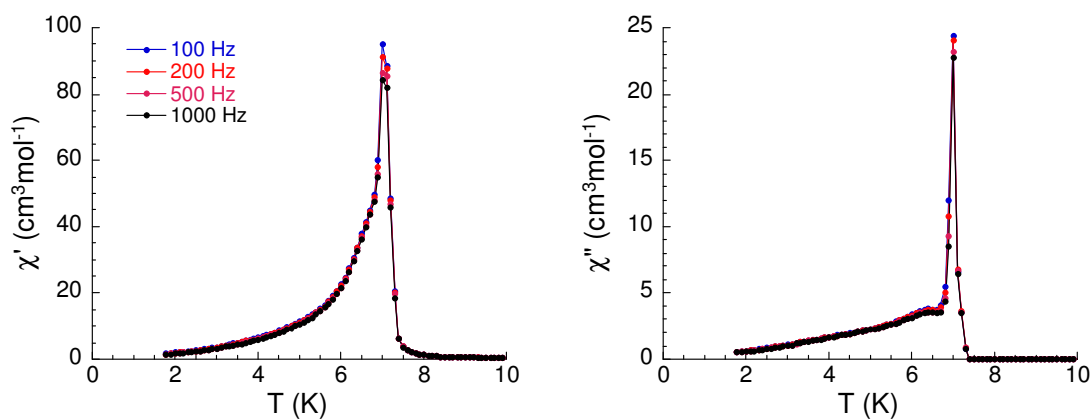


Figure 3.08 Temperature dependence of χ' and χ'' for **1** from 100 to 1000 Hz.

There are two different types of metal sites in the structure, Mn(II) and Mn(III). The Mn(II) ions are linked to four Mn(III) ions, and each Mn(III) ion is linked to two Mn(II) ions. The exchange field therefore is:

$$H_{S_1} = -\frac{8J}{g\mu_B} \langle S_2 \rangle \quad 1(a)$$

$$H_{S_2} = -\frac{4J}{g\mu_B} \langle S_1 \rangle \quad 1(b)$$

where $\langle S_1 \rangle$ and $\langle S_2 \rangle$ are the magnetisations of the Mn(II) and Mn(III) sites, respectively. In the presence of an applied dc field, the magnetisation on each site is:

$$\langle S_1 \rangle = \frac{S_1(S_1+1)g\mu_B}{3k_B T} (H + H_{S_1}) \quad 2(a)$$

$$\langle S_2 \rangle = \frac{S_2(S_2+1)g\mu_B}{3k_B T} (H + H_{S_2}) \quad 2(b)$$

if we consider: $C_{S_1} = \frac{S_1(S_1+1)g\mu_B}{3k_B}$ and $C_{S_2} = \frac{S_2(S_2+1)g\mu_B}{3k_B}$.

At $T = T_C$ and under $H = 0$, the equations 2(a) and 2(b) can be simplified as:

$$\langle S_1 \rangle = \frac{C_{S_1}}{T_C} H_{S_1} = \frac{8C_{S_1}|J|}{g\mu_B T_C} \langle S_2 \rangle \quad 3(a)$$

$$\langle S_2 \rangle = \frac{C_{S_2}}{T_C} H_{S_2} = \frac{4C_{S_2}|J|}{g\mu_B T_C} \langle S_1 \rangle \quad 3(b)$$

by replacing $\langle S_1 \rangle$ in the equation 3(b) by equation 3(a). The expression of T_C as a function of C_{S_1} , C_{S_2} , g , J , is deduced:

$$T_C^2 = 32J^2 \frac{C_{S_1} C_{S_2}}{g^2 \mu_B^2} \quad 4$$

Considering the expressions of C_{S_1} and C_{S_2} as :

$$C_{S_1} = \frac{35g\mu_B}{12k_B} \text{ and } C_{S_2} = \frac{2g\mu_B}{k_B}, \quad 5$$

the expression of T_C can be deduced as a function of J/k_B :

$$T_C = \frac{4\sqrt{35}|J|}{\sqrt{3}k_B} . \quad 6$$

Considering a T_C of 7.4 K, J/k_B is estimated to be -0.54 K. This average J parameter is comparable with similar Mn(III)-Mn(II) interactions reported in the literature.⁶⁹

Compounds	T_c (K)	J (K)
1	7.4	-0.54
2	4.6	-0.34
3	3	-0.22
4	7.7	-0.56

Table 3.01 Critical temperature (T_c), coupling constant (J) between Mn(II) and Mn(III) and coercive field (H_c), for compounds **1**, **2**, **3** and **4**.

3.1.2 Structure and magnetic behaviour of $[\text{Mn}^{\text{III}}_2\text{Mn}^{\text{II}}(4\text{-Me-sal})_4(\text{py})_4(\text{MeOH})]\cdot\text{H}_2\text{O}$, **2**

The reaction of 4-Me-salH₂ and py with Mn(II) in methanol gave $[\text{Mn}^{\text{III}}_2\text{Mn}^{\text{II}}(4\text{-Me-sal})_4(\text{py})_4(\text{MeOH})]\cdot\text{H}_2\text{O}$, **2**. The structure of **2** is an infinite 3D network that crystallizes in the tetragonal space group, $I4_1$. The structure is closely related to that of **1**, but with additional symmetry elements resulting from the lattice centring. The asymmetric unit contains half of a Mn(II) cation (situated on a crystallographic two-fold axis), one Mn(III) cation, two 4-Me-sal²⁻ ligands, two pyridine molecules and half of a methanol molecule, which is disordered about the two-fold axis (Figure 3.09).

In an analogous manner to that seen in **1**, Mn1 forms $[\text{Mn}^{\text{III}}(4\text{-Me-sal})_2(\text{py})_2]^-$ building block, which is linked to the Mn(II) centres by two *syn-anti* carboxylate bridges. The two 4-Me-sal²⁻ ligands on each Mn(III) are mutually *trans* coordinated. Mn2 is coordinated to four carboxylate oxygen atoms (O3, O3', O6, O6') of four bridging 4-Me-sal²⁻ ligands in the equatorial plane and to the disordered methanol molecule (O7) in the apical position. This causes a distortion of the tetrahedral geometry about Mn2, pushing apart O3 and O3' to give an O3-Mn2-O3' angle of 146.5(1)°, and pushing together O6 and O6' to give a O6-Mn2-O6' angle of 96.5(1)°. The Mn2–O3 and Mn2–O6 bond lengths are 2.037(1) and 2.119(1) Å, respectively, while the Mn2–O7 bond length is longer, at 2.277(1) Å. The additional coordination from the methanol ligand has, as would be expected, weakened the Mn2–O(carboxylate) bonding.

Topological analysis of this framework with the TOPOS software⁶⁸ reveals a *homogeneous* four-fold non-interpenetrating diamond-type network with a total Schläfli symbol of $[6^6]$. Each Mn(II) metal centre-node is linked to four others as shown in Figure 3.10, forming six six-membered rings at each metal atom. The Mn^{II}⋯Mn^{II} distances are all identical (10.102 Å) as a result of the higher crystal symmetry.

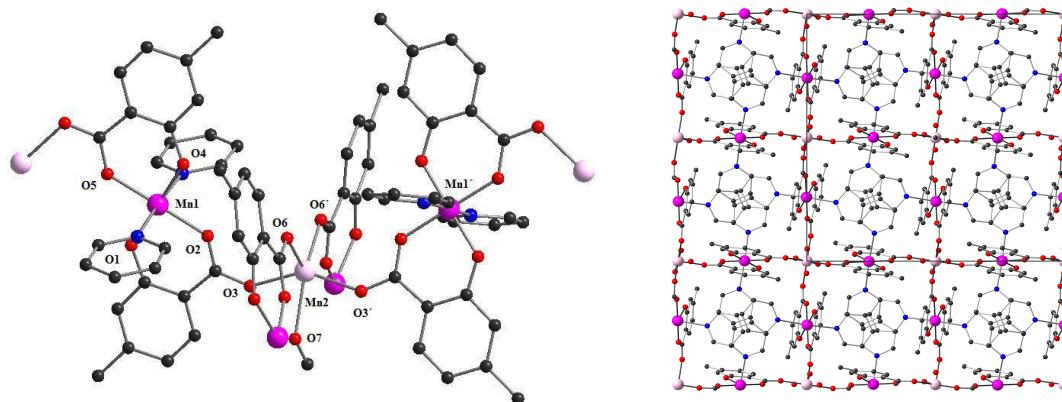


Figure 3.09 The asymmetric unit of $[\text{Mn}^{\text{III}}_2\text{Mn}^{\text{II}}(4\text{-Me-sal})_4(\text{py})_4(\text{MeOH})]\cdot\text{H}_2\text{O}$, **2** and its packing diagram. Colour code: Mn(III), purple; Mn(II), Pink; C, black; O, red and N, blue. Hydrogen atoms are omitted for clarity.

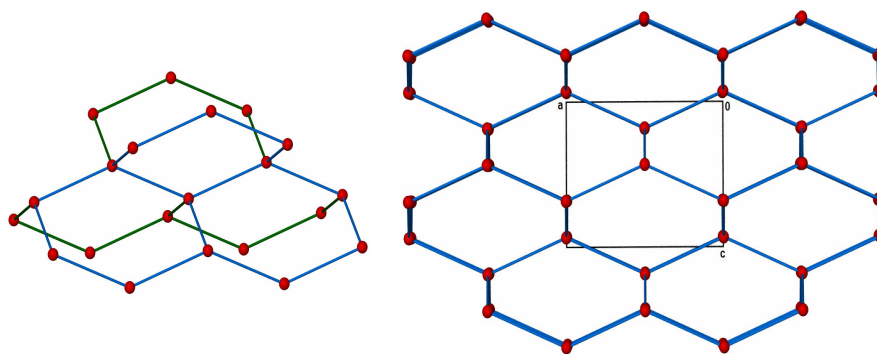


Figure 3.10 The diamond fragment (left) and the network (right) of compound **2**.

This compound shows very similar magnetic behaviour as in **1**. Figures 3.11-3.14 show all the graphs related to the magnetic properties of compound **2**. The χT values start to deviate from the normal paramagnetic behaviour close to 5 K, and the out-of-phase ac

susceptibility (χ'') deviates from zero at 4.6 K. The magnetisation at 7 T is higher for this compound ($5.5 \mu_B$) than in **1** ($3.8 \mu_B$), indicating weaker antiferromagnetic interactions in this case. The hysteresis effect is observed at low temperature with a small coercive field (30 Oe). The approach developed to deduce the Mn(II) and Mn(III) interactions in compound **1** was also applied here, and by considering a T_C of 4.6 K, J/k_B is estimated to be of -0.34 K (Table 3.01).

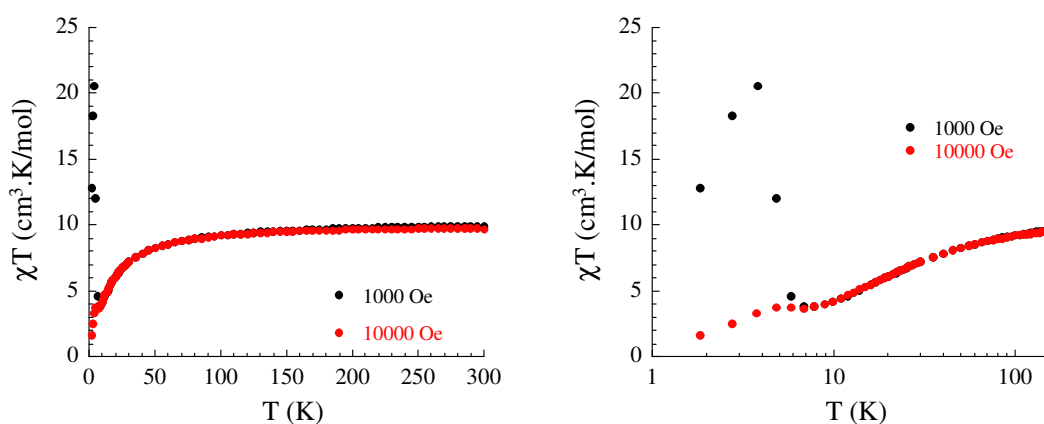


Figure 3.11 Temperature dependence of the χT product for **2** at 1000 Oe and 10000 Oe, from 0 to 300 K (left side) and from 1 to 100 K (right side).

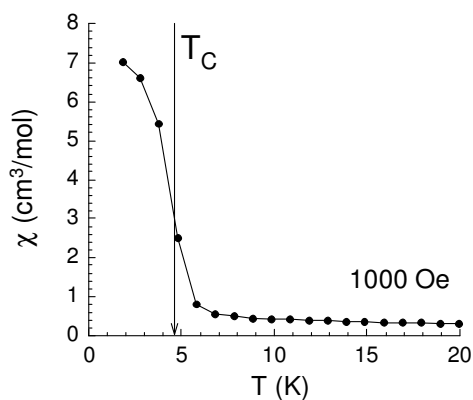


Figure 3.12 Temperature dependence of χ for **2** at 1000 Oe and 10000 Oe.

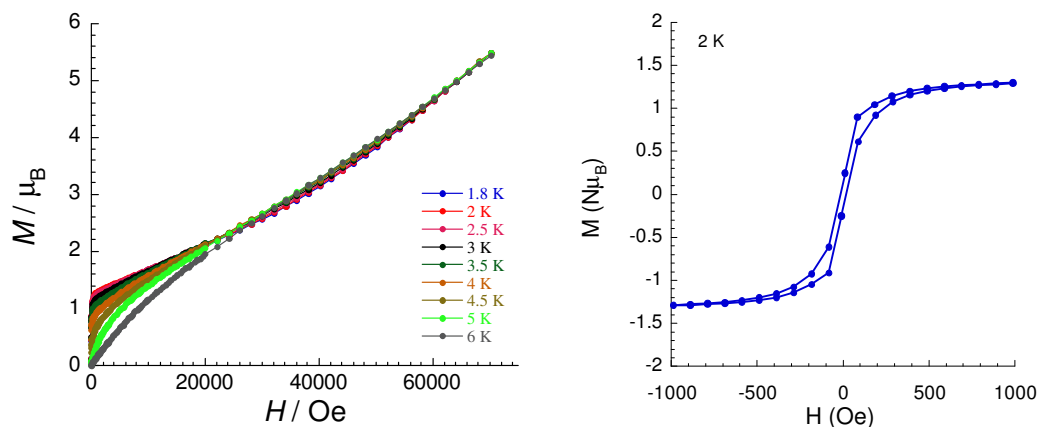


Figure 3.13 Field dependence of the magnetisation from 1.8 to 7 K (left) and hysteresis loop at 2 K (right).

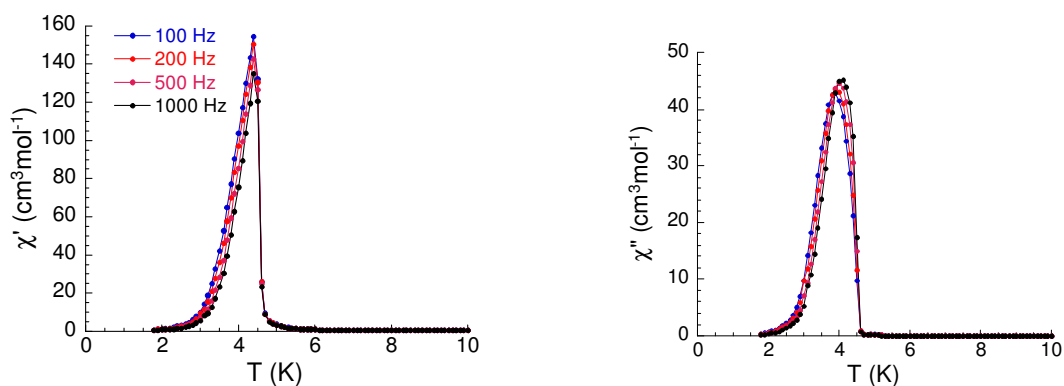


Figure 3.14 Temperature dependence of χ' and χ'' for **2** from 100 to 1000 Hz.

3.1.3 Structure and magnetic behaviour of $[\text{Mn}^{\text{III}}_2\text{Mn}^{\text{II}}(\text{5-Me-sal})_4(\text{py})_4(\text{H}_2\text{O})_2] \cdot (\text{MeOH})$,

3

The reaction of 5-Me-salH₂ and py with Mn(II) in methanol gave $[\text{Mn}^{\text{III}}_2\text{Mn}^{\text{II}}(\text{5-Me-sal})_4(\text{py})_4(\text{H}_2\text{O})_2] \cdot (\text{MeOH})$, **3**. Complex **3** crystallizes in the monoclinic space group, $P2_1/c$, as an infinite 3D network that is structurally related to those in **1** and **2** (Figure 3.15). Consideration of the unit cell parameters (see Chapter 8) shows that the unit cell is derived from that of **1** by loss of the tetragonal four-fold symmetry. The tetragonal four-fold c -axis has now become the monoclinic b -axis; the a - and c -axes now have similar but different

lengths, and the angle between them no longer 90° . The crystal structure of **3** can therefore be regarded as derived from that of **1** by a shear deformation. The structure of **3**, however, is built up in a similar manner to that of **1** and **2**. The asymmetric unit contains one Mn(II), one complete and two half Mn(III) cations (the half cations lie on inversion centres), four 5-Me-sal²⁻ ligands, four pyridine ligands, two water ligands and one solvating methanol molecule.

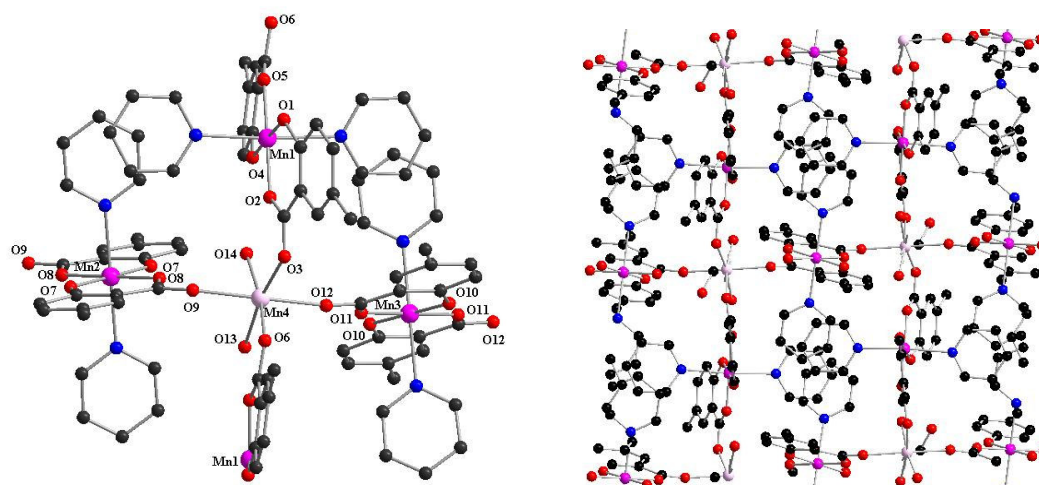


Figure 3.15 The asymmetric unit of $[\text{Mn}^{\text{III}}_2\text{Mn}^{\text{II}}(5\text{-Me-sal})_4(\text{py})_4(\text{H}_2\text{O})_2]\cdot(\text{MeOH})$, **3** and its packing diagram. Colour code: Mn(III), purple; Mn(II), pink; C, black; O, red and N, blue. Hydrogen atoms are omitted for clarity.

The three crystallographically independent Mn(III) cations, Mn1, Mn2 and Mn3, form $[\text{Mn}^{\text{III}}(5\text{-Me-sal})_2(\text{py})_2]^-$ linking units, in the same way as in **1** and **2**, and these form *syn-anti* carboxylate bridges to the Mn(II) centres, Mn4. The Mn4 ion has a rather regular octahedral geometry. Two water ligands are coordinated in a *cis* configuration, while the remaining four sites are occupied by carboxylate oxygen atoms from four different $[\text{Mn}^{\text{III}}(5\text{-Me-sal})_2(\text{py})_2]^-$ units. The two Mn4–OH₂ bond lengths are 2.205(9) and 2.242(1) Å, while the four Mn4–O (carboxylate) distances are now in the range of 2.165–2.192 Å. The trend observed in **1** and **2** continues, the two additional non-carboxylate oxygen atoms coordinated to Mn4 have weakened the Mn(II)–O (carboxylate) bond further. The mean Mn(II)–O bond lengths

increases in the series: 2.067 Å (four-coordinate Mn(II), **1**), 2.078 Å (five-coordinate Mn(II), **2**) to 2.173 Å (six-coordinate Mn(II), **3**). Topological analysis of this framework again reveals a *heterogeneous* four-fold diamondoid network (Figure 3.16) with a total Schläfli symbol of $[6^6]$. This diamondoid network is flattened compared to those in **1** and **2**, as might be expected due to the two *cis*-orientated aqua ligands on Mn4. Of the four Mn^{II}...Mn^{II} internodal distances, two are equivalent at 10.031 Å, while the other two are 10.995 and 11.363 Å. The three networks are, however, still closely related, and this gives the opportunity to see how the change in Mn(II)-O (carboxylate) bonding might affect the magnetic properties of the networks.

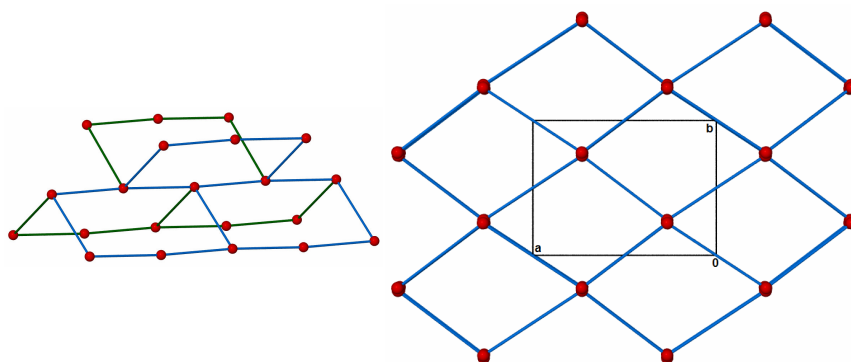


Figure 3.16 The flatter diamond fragment (left) and the network (right) of compound **3**.

The magnetic behaviour of this compound is very similar to that in **1** and **2**. Figures 3.17-3.19 show all the graphs related to the magnetic properties of compound **3**. The χT values start to deviate from normal paramagnetic behaviour at about 3 K. This is consistent with ac susceptibility measurement, and the out-of-phase ac susceptibility (χ'') deviates from zero at 3 K. The magnetisation at 7 T is higher for this compound ($10.9 \mu_B$) than in **2** ($5.5 \mu_B$), indicating even weaker antiferromagnetic interactions in this case than in complex **2**. The hysteresis effect is observed at low temperature with a coercive field (100 Oe). The approach used in compound **1** for evaluating the Mn(II) and Mn(III) interactions can also be used here (Table 3.01), and by considering a T_C of 3 K, J/k_B is estimated to be -0.22 K.

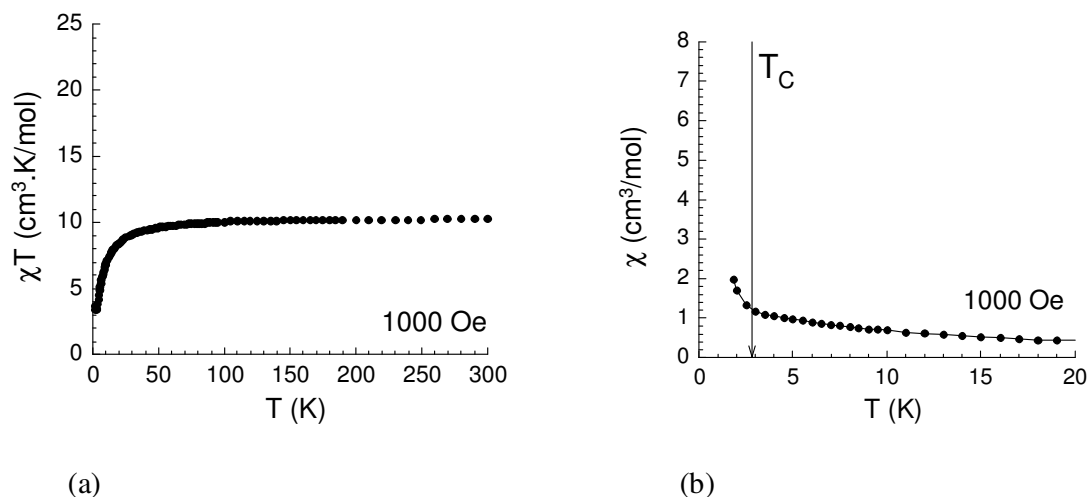


Figure 3.17 (a) Temperature dependence of the χT product for **3** at 1000 Oe.
 (b) Temperature dependence of χ for **3** at 1000 Oe.

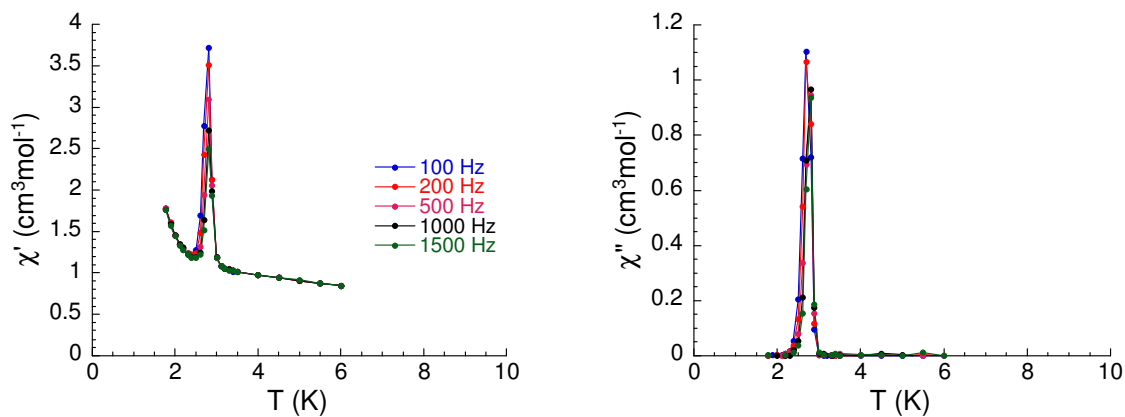


Figure 3.18 Temperature dependence of χ' and χ'' for **3** from 100 to 1500 Hz.

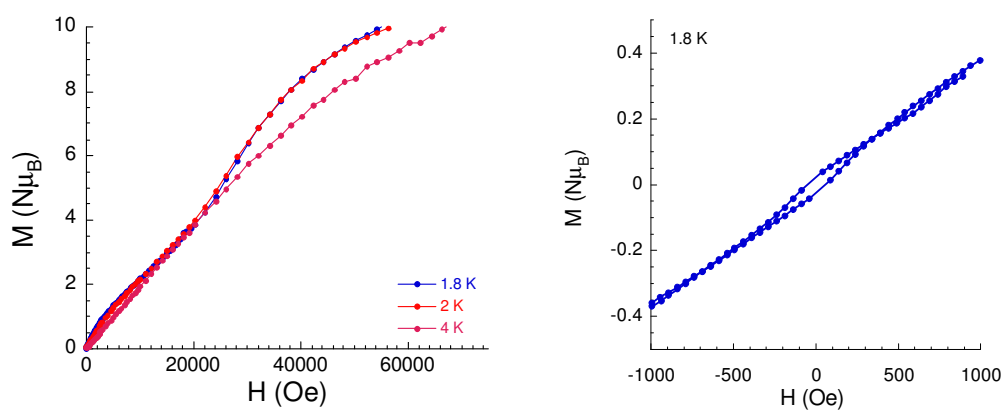


Figure 3.19 Field dependence of the magnetisation from 1.8 to 4 K (left), and hysteresis loop at 1.8 K (right), for **3**.

3.1.4 Structure and magnetic behaviour of $[\text{Mn}^{\text{III}}_2\text{Mn}^{\text{II}}(\text{3-Me-sal})_4(\text{4-Me-py})_4]$, **4**

Compound **4**, like **1**, crystallizes in the space group $P4_3$, with a similar, but slightly larger unit cell (see Chapter 8). The tetragonal space group show that the packing is isostructural with **1**. Due to disorder among the Mn(II) ions, the structure of compound **4** could not be satisfactorily refined. There may also be disorder of ligands. Consideration of the structure of **1**, indicates that the steric requirements of the 4-methyl substituent on the pyridine ligand in **4** are likely to force the 4-methylpyridine ligands to bend up or down. Since these can be considered as occupying separate “compartments” in the lattice, it is assumed that the deviation of these ligands may not be subject to long-range order, resulting in the refinement problems. However, X-ray powder diffraction measurements support (Figure 3.20) a structural motif similar to the 3D diamondoid networks seen in **1**, **2** and **3**. The powder pattern of this compound appears to be more similar to that of compounds **1** and **2**. Additionally, the molecular formula, $[\text{Mn}_3(\text{3-Me-sal})_4(\text{4-Me-py})_4]$, is supported by the microanalytical data.

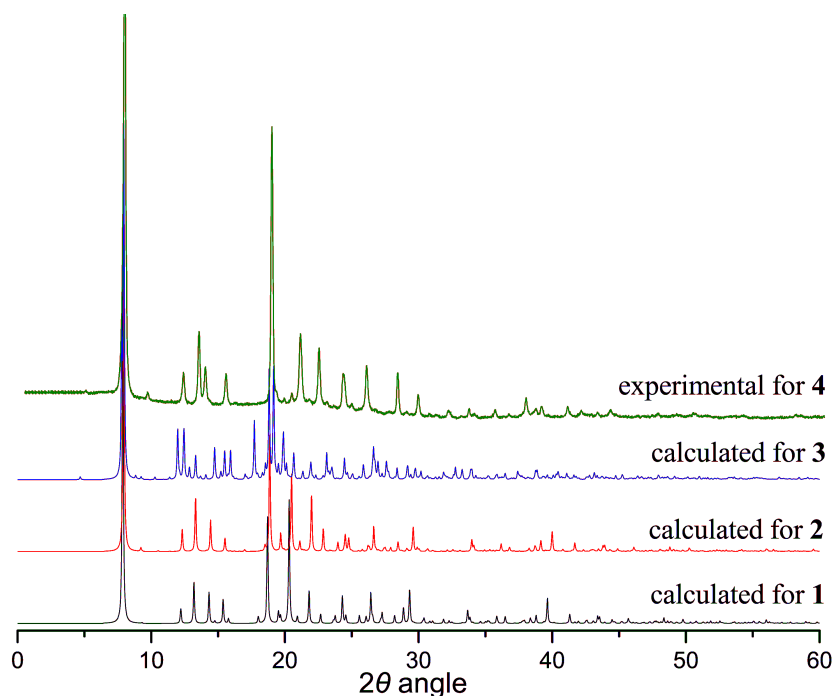


Figure 3.20 Powder pattern for **1-4**, black line is **1**, red is **2**, blue is **3** and olive is **4**.

This compound also has magnetic behaviour similar to that of **1**, **2**, and **3**. Figures 3.21-3.23 show all the graphs related to the magnetic properties of compound **4**. In this case, the χT values start to deviate from normal paramagnetic behaviour close to 7.5 K.

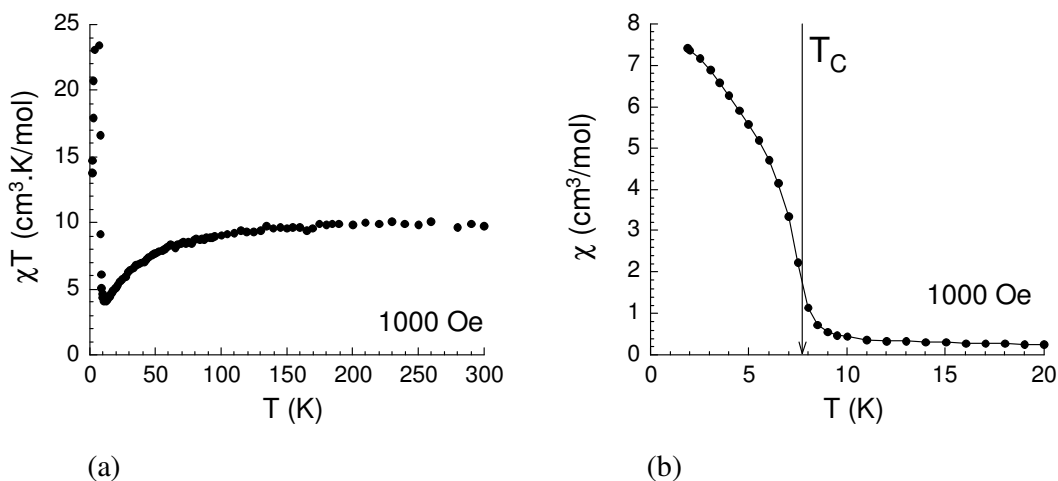


Figure 3.21 (a) Temperature dependence of the χT product for **4** at 1000 Oe.
(b) Temperature dependence of χ for **4** at 1000 Oe.

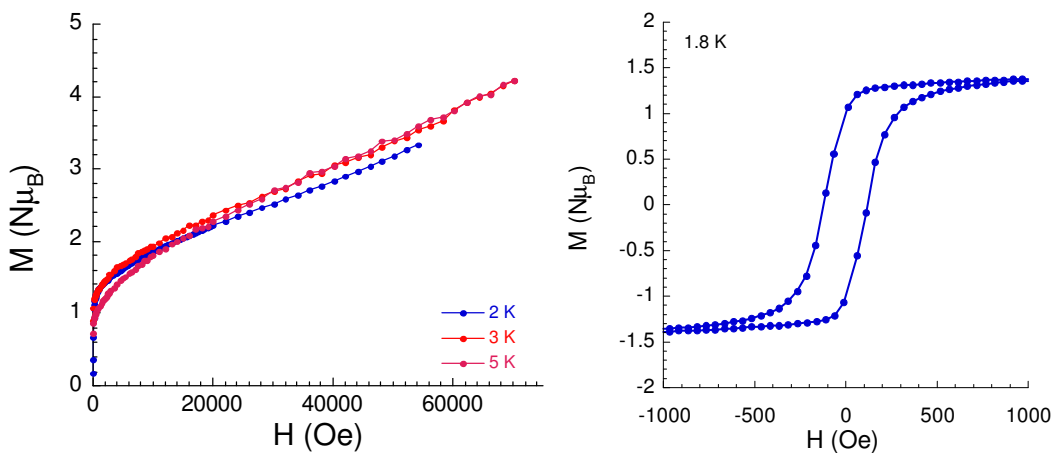


Figure 3.22 Field dependence of the magnetisation from 2 to 5 K (left), and hysteresis loop at 1.8 K (right), for **3**.

The out-of-phase ac susceptibility (χ'') deviates from zero at 7.7 K. The ordering temperature of this compound is close to that (7.4 K) observed in **1**. This implies that

antiferromagnetic interactions are stronger in **1** and **4**, than in **2** and **3**. The hysteresis effect is observed at low temperature with a coercive field of 250 Oe. The Mn(II) and Mn(III) interactions were evaluated using the same approach used for compound **1** (Table 3.01), and by considering a T_C of 7.7 K, J/k_B is estimated to be -0.56 K.

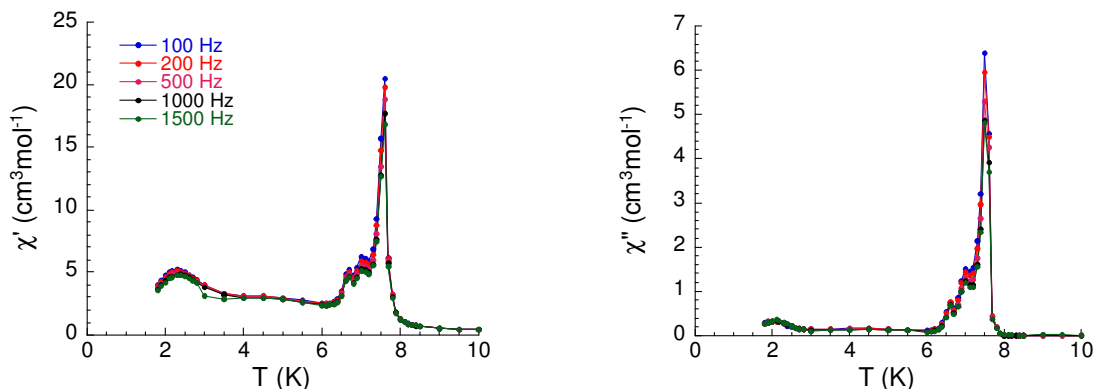
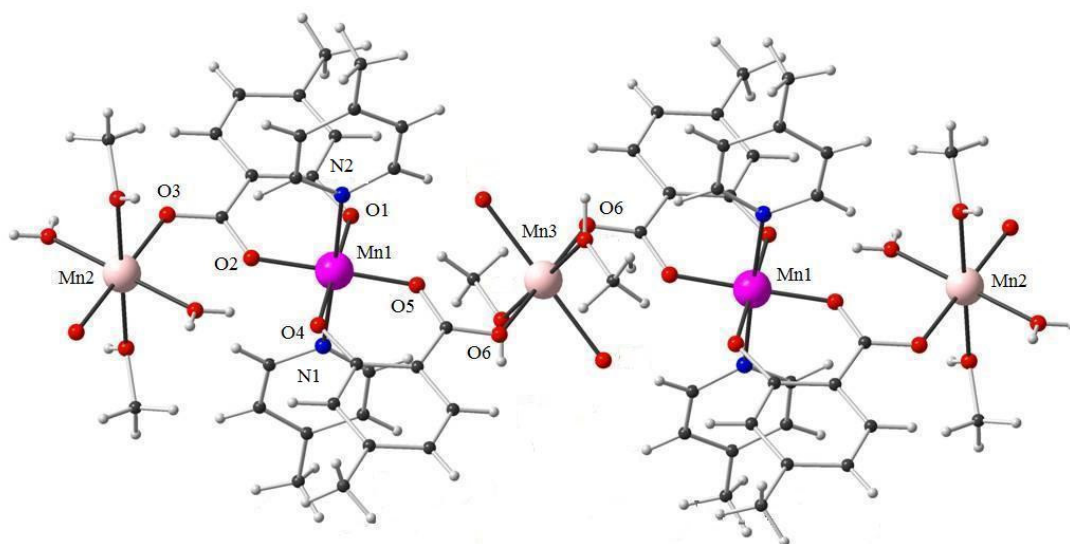


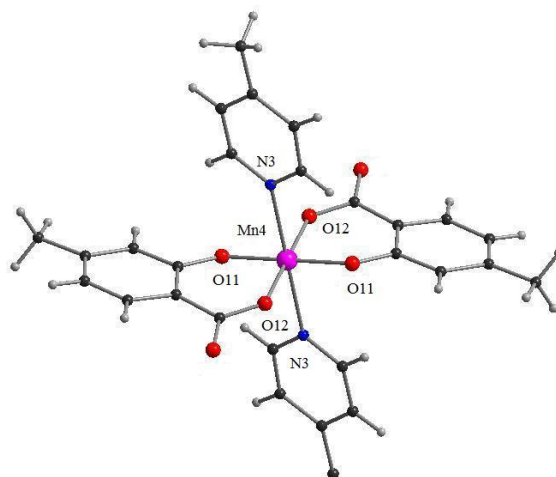
Figure 3.23 Temperature dependence of χ' and χ'' for **4** from 100 to 1500 Hz.

3.1.5 Structure and magnetic behaviour of $[\text{Mn}^{\text{III}}(\text{4-Me-sal})_2(\text{4-Me-py})_2\text{Mn}^{\text{II}}(\text{OH}_2)_2(\text{MeOH})_2][\text{Mn}^{\text{III}}(\text{4-Me-sal})_2(\text{4-Me-pyr})_2]$, **5**

The reaction of 4-Me-salH₂ and 4-Me-py with Mn(II) in methanol gave $[\text{Mn}^{\text{III}}(\text{4-Me-sal})_2(\text{4-Me-py})_2\text{Mn}^{\text{II}}(\text{H}_2\text{O})_2(\text{MeOH})_2][\text{Mn}^{\text{III}}(\text{4-Me-sal})_2(\text{4-Me-py})_2]$, **5**. Compound **5** is composed of 1D linear chains that are a polymer of the monocationic $[\text{Mn}^{\text{III}}(\text{4-Me-sal})_2(\text{4-Me-py})_2\text{Mn}^{\text{II}}(\text{H}_2\text{O})_2(\text{MeOH})_2]^+$ building block, which interact with monoanionic mononuclear complexes $[\text{Mn}^{\text{III}}(\text{4-Me-sal})_2(\text{4-Me-pyr})_2]^-$ through hydrogen bonds and π -stacking interactions to form a 3D supramolecular network. It crystallizes in the triclinic space group, *P*-1. As shown in Figure 3.24, the asymmetric unit contains one Mn(III) and two half Mn(II) cations (the latter is on inversion centre), which form the polymer, and two half Mn(III) ions which build up the centrosymmetric mononuclear counteranions.



(a)



(b)

Figure 3.24 (a) Structure of the chain, $[\text{Mn}^{\text{III}}(4\text{-Me-sal})_2(4\text{-Me-py})_2\text{Mn}^{\text{II}}(\text{H}_2\text{O})_2(\text{MeOH})_2]^+$, and (b) Structure of the mononuclear anion, $[\text{Mn}^{\text{III}}(4\text{-Me-sal})_2(4\text{-Me-py})_2]^-$, in **5**. Colour code: Mn^{III} , purple; Mn^{II} , pink; C, black; O, red and N, blue.

The cationic 1D chain is mixed-valence, with alternating Mn(III) and Mn(II) centres. Mn1 has a distorted octahedral geometry and is coordinated by four oxygen atoms (O1, O2, O4, O5) of two bidentate 4-Me-sal²⁻ ligands in the equatorial plane with Mn–O bond lengths in the range of 1.879–1.897 Å. The two axial sites have two 4-Me-py nitrogen atoms (N1, N2) which define the Jahn-Teller axes, with Mn–N bond lengths in the range of 2.179–2.272 Å.

This Mn(III) centre, Mn1, forms $\{\text{Mn}^{\text{III}}(4\text{-Me-sal})_2(4\text{-Me-py})_2\}^-$ units analogous to those found in **1-3**, and these form *syn-anti* carboxylate bridges to the Mn(II) centres, Mn2 and Mn3. According to the crystal symmetry, each of the Mn2 and Mn3 is coordinated by two carboxylate oxygen atoms in a strictly *trans* arrangement, with additional coordination from two water and two methanol molecules at an equatorial plane. The average Mn2–O bond length (2.183 Å) is similar to the Mn(II)–O distances (2.175 Å) previously reported in literature.⁶⁶

In the anionic mononuclear complex, $[\text{Mn}^{\text{III}}(4\text{-Me-sal})_2(4\text{-Me-py})_2]$, the Mn(III) centre, Mn4, is coordinated by two bidentate 4-Me-sal²⁻ ligands in the equatorial plane and by two 4-Me-py in the axial sites. Mn3 has an elongated octahedral geometry. The average Mn–O bond length (1.898 Å) is similar to reported Mn(III)–O bond lengths.⁶⁶

In compound **5**, two different coordination modes can be found for the 4-Me-sal²⁻ ligands. In the first, the 4-Me-sal²⁻ ion utilizes the two carboxylate oxygen atoms in a *syn-anti* configuration to bridge the Mn(III) and Mn(II) centres. The second crystallographically independent ligand is chelated to Mn4 through one of its carboxylate oxygen atom (O12) and the oxygen atom of hydroxyl group (O11). The mean Mn(III)···Mn(II) separation is 4.888 Å. The Mn(III)-Mn(II)-Mn(III) angle is 180° by symmetry, while the Mn(II)-Mn(III)-Mn(II) angle is 174.8(2)°, so the polymer is very close to linear; the chains run parallel to the *c* axis. These 1D chains are linked *via* hydrogen bonds formed by the coordinated water and methanol molecules on the Mn(II) centres with the non-coordinated salicylate oxygen atoms of the mononuclear counteranionic complexes. The hydrogen-bonded network forms 2D supramolecular layers parallel to the {1 0 0} direction. The stacked 2D layers are held together with a very complicated arrangement of π - π stacking interactions, resulting in the supramolecular structure shown in Figure 3.25. The shortest distance between the planes of the two parallel aromatic rings is 3.693(4) Å, which is within the common range for stacking interactions between two aryl rings.⁷⁰

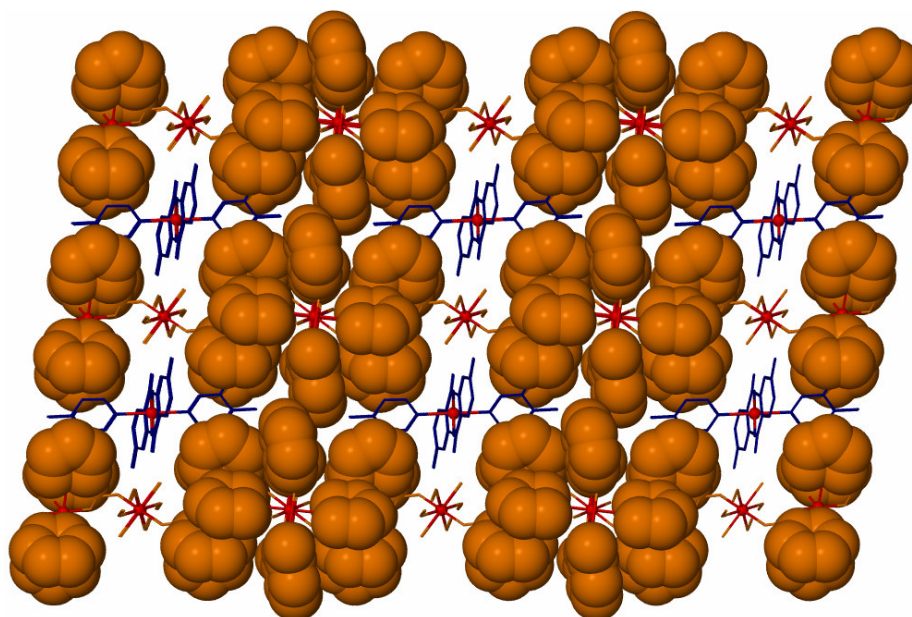


Figure 3.25 A view along the [1 0 0] direction of the unit cell of the 3D supramolecular network in **5**. The atoms of the 1D cationic chain (orange) are the space-filling spheres. The skeleton represents mononuclear anions (blue) and Mn ions (red).

The magnetic susceptibility of **1** was studied from 300 K to 1.8 K at 1000 Oe and 10000 Oe (in Figure 3.26). At room temperature, the χT value at 1000 Oe is 10.6 cm³K/mol which is close to the expected value (10.2 cm³K/mol) for two Mn(III) and one Mn(II) ions. On decreasing the temperature, the χT value steadily decreases until 50 K (10.2 cm³K/mol) and falls rapidly from 40 K, reaching a minimum of 3.75 cm³Kmol⁻¹ at 1.8 K. The initial decrease down to 50 K is indicative of dominant antiferromagnetic interactions within the complex. Above 1.8 K, the Curie-Weiss law leads to a Curie constant (C) of 10.8 cm³K/mol and a Weiss constant (θ) of -3.7 K. The Curie constant is in agreement with the expected value (10.375 cm³K/mol) for one Mn(II) and two Mn(III) metal ions, and the negative Weiss constant further suggests the presence of antiferromagnetic interactions between the spin carriers.

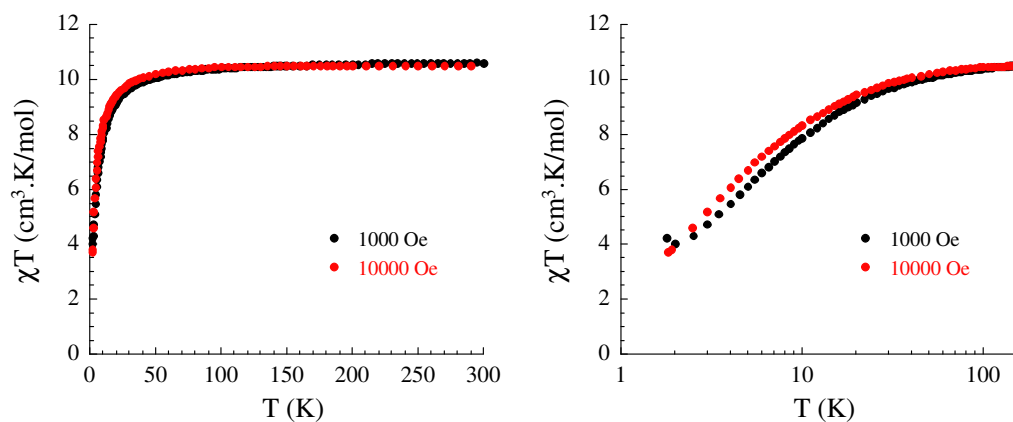


Figure 3.26 Temperature dependence of the χT product for **5** at 1000 Oe and 10000 Oe, from 0 to 300 K (left side) and from 1 to 100 K (right side).

The magnetic properties of this compound were modelled using a regular chain model (one J value) of alternating $s = 2$ and $S = 5/2$ spins, and a Curie contribution for the mononuclear Mn(III) counterion. The chain portion of the model uses the approach developed by Fisher, *et al.*⁷¹ for alternating chains. The method developed by Fisher is used to determine the magnetic susceptibility of a chain compound with a local spin larger than $1/2$. Thus, the following Hamiltonian was used:

$$\hat{H} = -2J \sum_{i=1}^N \mathbf{S}_i \cdot \mathbf{s}_i$$

with $s_i = 2$ and $S_i = 5/2$. Fitting the data, results in $g_{av} = 2.04$ and $J_{ab}/k_B = -0.55$ K, which is expected for a *syn-anti* carboxylate bridge between Mn(II) and Mn(III). This shows that the interactions are antiferromagnetic and weak.⁶⁹ The fitting of the χT plot is shown in the Figure 3.27.

The magnetisation measurements done as a function of the field at low temperatures reveal a gradual increase and the absence of a true saturation of the magnetisation. It reaches $11.4 \mu_B$ at 7 T as shown in Figure 3.28. This behaviour suggests the presence of low-lying excited states that might be populated when a field is applied and is in agreement with the fact that there are only weak antiferromagnetic interactions in the coordination polymer. Indeed, at

high field when the antiferromagnetic interactions are overcome, one would expect a saturation of the magnetisation at $13 \mu_B$ for all parallel spins.

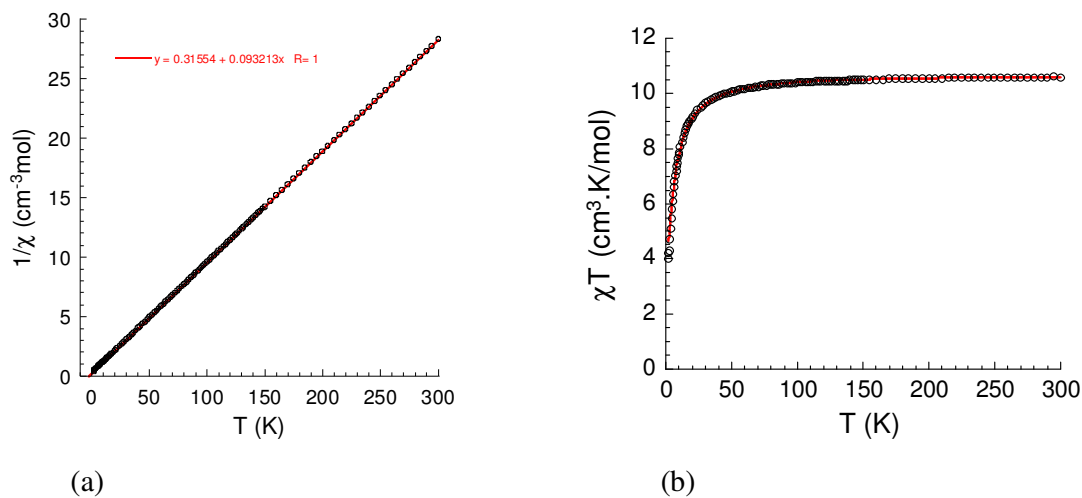


Figure 3.27 (a) The Curie-Weiss plot for **5** in the temperature range of 1.8-300 K. (b) Temperature dependence of the χT product for **5** from 1.8 to 300 K, and the solid line is the fit.

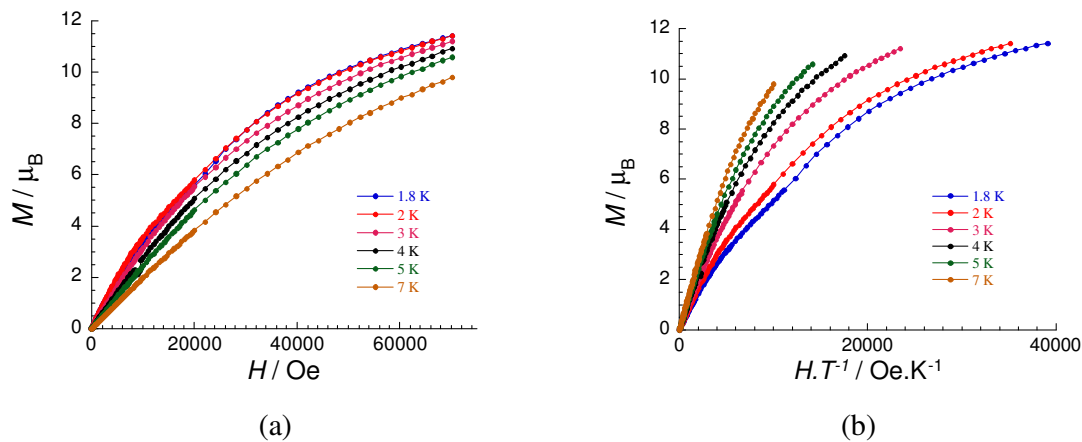


Figure 3.28 (a) Field dependence of the magnetisation for **5** from 1.8 to 7 K. (b) M versus H/T plot for **5** from 1.8 to 7 K.

3.1.6 Characterisation of a Mn - (5-Me-salH₂) - (4-Me-py) product, 6

The reaction of 5-Me-salH₂ and 4-Me-py with Mn(II) in methanol gave compound **6**. The compound was obtained in powder form, therefore single crystal X-ray determination was not possible in this case. The X-ray powder pattern did not reveal much about its structure as there was some similarity with the powder pattern of the 3D complexes but presence of other extra peaks indicated that the compound is not pure. This complex might be a mixture of various structures and thus, predicting its structure is difficult.

In conclusion, four 3D networks and one 1D coordination polymer composed of mixed-valence manganese units have been synthesized using various methyl-substituted salicylic acids and coligands, such as py and 4-Me-Py. The 3D frameworks are based on diamondoid networks and show long-range ferrimagnetic ordering.

3.2 Heterometallic 1D compounds

One of the research efforts was to synthesize mixed-metal coordination polymers using salicylic acid ligands. Compounds were obtained by a room temperature reaction of a substituted salicylic acid and a coligand with more than one type of metal salt. The solvent combination used for all of the syntheses was MeOH and H₂O in a ratio of 4:1, as this favoured the formation of crystals. In some cases, the ether diffusion method was also useful to obtain single crystals. In order to oxidise Mn(II) ions and deprotonate the ligands, triethylamine was used as the base.

3.2.1 Structure of [MnNa₂(3-MeO-sal)₂(MeOH)₂], 7

The reaction of 3-MeO-salH₂ and a Mn(II) salt in the presence of sodium azide gave [MnNa₂(3-MeO-sal)₂(MeOH)₂], **7**. The structure of compound **7** (Figure 3.29) consists of a 1D coordination polymer of manganese and sodium ions arranged in an alternate fashion. They are bridged by two 3-MeO-sal²⁻ ligands.

Mn1 has a distorted octahedral geometry. It is coordinated by two bidentate 3-MeO-sal²⁻ ligands (through μ -phenoxo and carboxylate oxygen atoms) in the equatorial plane. The axial sites are occupied by two methanol molecules. The average Mn–O bond length (1.896 Å) is similar to Mn(III)–O bond lengths reported in the literature.⁶⁶ As expected for a Mn(III) ion, there is a Jahn-Teller elongation with an average axial bond length (2.227 Å) significantly longer than the average equatorial bond length (1.896 Å).

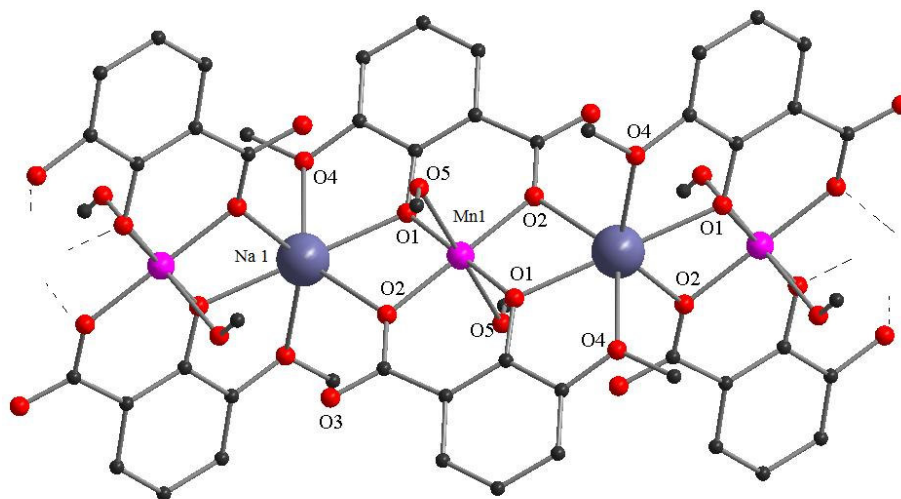


Figure 3.29 Part of the structure of the 1D polymer, $[\text{MnNa}_2(3\text{-MeO-sal})_2(\text{MeOH})_2]$, **7**. Hydrogen atoms are omitted for clarity. Colour code: Mn(III), pink; Na (blue); C, black and O, red.

Na1 is also octahedral and is coordinated by two bidentate 3-MeO-sal²⁻ ligands where phenoxo (O1) and methoxy (O4) oxygen atoms from each ligand are coordinating. The other two sites are occupied by two carboxylate oxygen atoms of two bridging 3-MeO-sal²⁻ ligands. The 3-MeO-sal²⁻ ligands bridge Mn1 and Na1 by a μ -phenoxo (O1) and a μ -carboxylate oxygen (O2) atoms. As a result, a 1D coordination polymer is formed. The distance between the Na and Mn ions is 3.309(3) Å whereas the distance between two Mn(III) ions is 6.066(6) Å. The Mn-O-Na bond angles are 104.57(3)° and 99.11(3)°. The interesting observation is that the oxygen atoms of both the carboxylate and phenoxo groups of the 3-MeO-sal²⁻ ligand

show a μ -bridging mode. In previously reported compounds⁴⁰⁻⁴² from salicylic acid ligands however, only the carboxylate group showed a μ -bridging mode and the phenoxo oxygen coordinated in a terminal fashion. The Na ions are diamagnetic and the magnetic interactions between two Mn(III) centres through the Na ion will be very small.

3.2.2 Structure and magnetic behaviour of $[\text{Fe}_2\text{Pr}(4\text{-Me-sal})_4(2,2'\text{-bipy})_2(\text{OH}_2)_6](\text{NO}_3) \cdot 2\text{MeOH} \cdot 1.5 \text{H}_2\text{O}$, **8**

The reaction of 4-Me-salH₂, 2,2'-bipy, Fe(III) and Pr(III) nitrates (mole ratio 4:1:1:1) in MeOH/H₂O (4:1), gave $[\text{Fe}_2\text{Pr}(4\text{-Me-sal})_4(2,2'\text{-bipy})_2(\text{OH}_2)_6] (\text{NO}_3) \cdot 3\text{MeOH}$, **8**. It is a heterometallic 1D coordination polymer, and crystallizes in the monoclinic space group, $P2_1/c$. The repeating unit comprises of $[\text{Fe}_2\text{Pr}(4\text{-Me-sal})_4(2,2'\text{-bipy})_2(\text{OH}_2)_6]^+$, one nitrate as counteranion, one and a half water and two methanol molecules as lattice solvent (Figure 3.30).

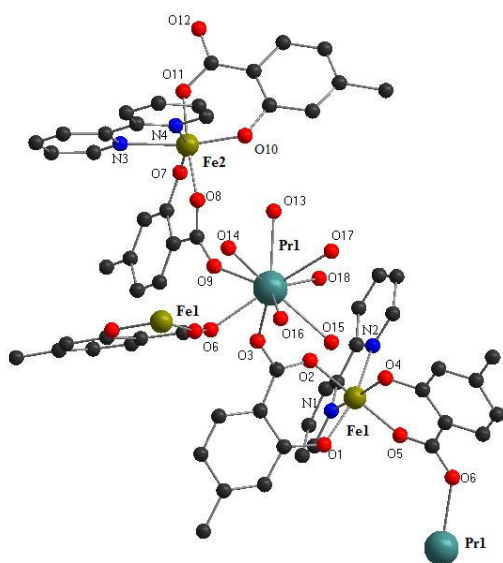


Figure 3.30 The repeating unit, $[\text{Fe}_2\text{Pr}(4\text{-Me-sal})_4(2,2'\text{-bipy})_2(\text{OH}_2)_6](\text{NO}_3) \cdot 3\text{MeOH}$, of the 1D chain in **8**. Hydrogen atoms are omitted for clarity. Colour code: Fe(III), light green; Pr(III), dark green; C, black; O, red and N, blue.

The trinuclear unit consists of one Pr1 linked by carboxylate bridges to two Fe(III) centres, Fe1 and Fe2. The coordination environment for the two Fe centres (Fe1 and Fe2) are similar, and both of them have octahedral geometry. They are each chelated (through phenoxo and carboxylate oxygen atoms) by two different 4-Me-sal²⁻ ligands, and by one bidentate 2,2'-bipy. In this way, two crystallographically independent anionic units, [Fe1(2,2'-bipy)(4-Me-sal)₂]⁻ and [Fe2(2,2'-bipy)(4-Me-sal)₂]⁻, are constructed. Each [Fe2(2,2'-bipy)(4-Me-sal)₂]⁻ is linked to only one Pr1 by a *syn-anti* carboxylate bridge from one 4-Me-sal²⁻ ligand, whereas each [Fe1(2,2'-bipy)(4-Me-sal)₂]⁻ is linked to two Pr1 by *syn-anti* carboxylate bridges from two 4-Me-sal²⁻ ligands.

The Pr1 is nine-coordinate. The coordination environment consists of six water molecules (O13, O14, O15, O16, O17, O18) and three carboxylate oxygen atoms (O3, O6, O9) from three bridging 4-Me-sal²⁻ molecules. As a result, Pr1 is linked to one [Fe2(2,2'-bipy)(4-Me-sal)₂]⁻ and two [Fe1(2,2'-bipy)(4-Me-sal)₂]⁻ units (Figure 3.31). The distances between Pr1 and three carboxylate oxygens are 2.451(4) Å (Pr1–O3), 2.430(6) Å (Pr1–O6) and 2.472(5) Å (Pr1–O9), whereas Pr1–Fe2 distance is 5.877(1) Å and Pr1–Fe1 distance is 5.698(1) Å.

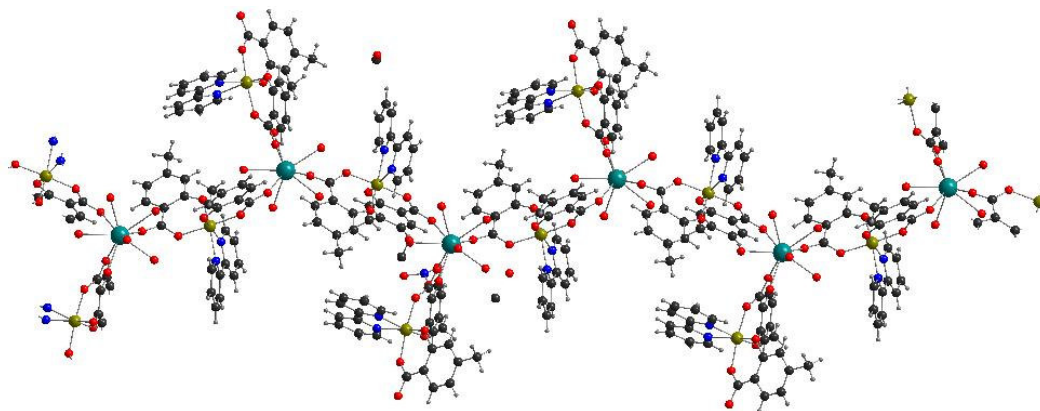


Figure 3.31 Structure of the 1D chain of compound **8**.

As explained above, $[\text{Fe1}(2,2'\text{-bipy})(4\text{-Me-sal})_2]^-$ and hydrated Ln units create an alternate infinite chain, and the $[\text{Fe2}(2,2'\text{-bipy})(4\text{-Me-sal})_2]^-$ are perpendicularly attached to the Ln1 ions of the chain. The 1D chains are connected through hydrogen bonds, giving rise to the formation of a 2D hydrogen-bonded sheet. The hydrogen atoms of the coordinated water molecules on Pr1 form hydrogen bonds with carboxylate oxygen atoms of 4-Me-sal²⁻ ligand, coordinating to the Fe2 of another chain. In addition, the stacked 2D layers are held together by π - π stacking interactions between the aromatic rings of 2,2'-bipyridyl and 4-Me-sal²⁻ ligand, resulting in the supramolecular structure. The closest distance between the planes of two aromatic rings is about 3.49 Å.

The magnetic susceptibility of **8** was studied from 300 K to 1.8 K at 1000 Oe and 10000 Oe. At 300 K, the χT product is 10.5 cm³K/mol (Figure 3.32). This value is in good agreement with the expected value (10.35 cm³ K/mol) for two Fe(III) ions ($S = 5/2$, $g = 2$, $C = 4.375$ cm³K/mol) and one Pr(III) ion ($S = 1$, $L = 3$, $g = 4/5$, $^3\text{H}_4$, $C = 1.60$ cm³K/mol).⁷² On decreasing the temperature, the χT product almost stays constant until about 50 K and then rapidly decreases to reach a minimum value of 8.4 cm³K/mol at 1.8 K. The decrease of χT product below 50 K may be due to antiferromagnetic interactions among the spin carriers or due to the zero-field splitting of Fe(III) ions. Also, with the decrease of temperature, the Stark sublevels of the anisotropic Pr ions are thermally depopulated resulting in a decrease of the χT vs T plot;⁷³ hence, the thermal decrease of the χT product might also partially originate from the spin-orbit coupling of the single ions.

The field dependence of the magnetisation at several low temperatures shows that the magnetisation is smoothly increasing with the applied dc field (Figure 3.33). At 7 T, it reaches a value of 12.0 μ_B . There is no clear saturation of magnetisation, suggesting the presence of magnetic anisotropy and/or the population of low-lying excited states. Also, the plot of M vs H/T at several low temperatures, shows that the curves are not superposed on a single master-curve, further indicating the presence of magnetic anisotropy and/or low-lying excited states.

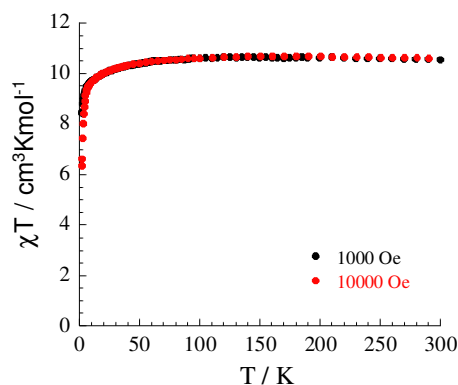


Figure 3.32 Temperature dependence of χT for **8** at 1000 Oe and 10000 Oe.

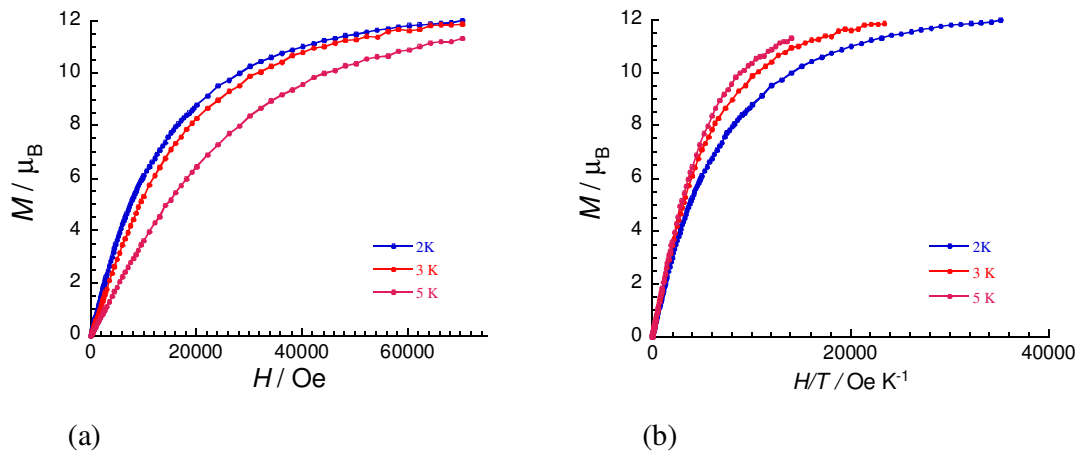


Figure 3.33 (a) Field dependence of magnetisation, (b) M versus H/T , for **8** from 2 to 5 K.

3.2.3 Structure and magnetic behaviour of $[\text{Fe}_2\text{Gd}(\text{4-Me-sal})_4(2,2'\text{-bipy})_2(\text{OH}_2)_5] \text{Cl}_{1/2}(\text{NO}_3)_{1/2} \cdot 5\text{H}_2\text{O}$, **9**

Using Gd(III) nitrates a similar reaction as in compound **8** gave $[\text{Fe}_2\text{Gd}(\text{4-Me-sal})_4(2,2'\text{-bipy})_2(\text{OH}_2)_5] \text{Cl}_{1/2}(\text{NO}_3)_{1/2} \cdot 5\text{H}_2\text{O}$, **9**. Compound **9**, like **8**, is a heterometallic 1D coordination polymer and crystallizes in the same space group, $P2_1/c$. The repeating unit is comprised of $[\text{Fe}_2\text{Gd}(\text{4-Me-sal})_4(2,2'\text{-bipy})_2(\text{OH}_2)_5]^+$, half of a nitrate, half of a chloride and five H_2O molecules as lattice solvent (Figure 3.34).

The trinuclear unit is similar to that of compound **8** and consists of one Gd1 linked to two Fe(III) centres (Fe1, Fe2) by *syn-anti* carboxylate bridges. The Fe2 and Fe1 coordination environment is the same as in compound **8**. Here also, each $[\text{Fe2}(2,2'\text{-bipy})(4\text{-Me-sal})_2]^-$ is linked to only one Gd1 by a carboxylate bridge of one 4-Me-sal^{2-} ligand, whereas each $[\text{Fe1}(2,2'\text{-bipy})(4\text{-Me-sal})_2]^-$ is linked to two Gd1 by the carboxylate bridges of two 4-Me-sal^{2-} ligands.

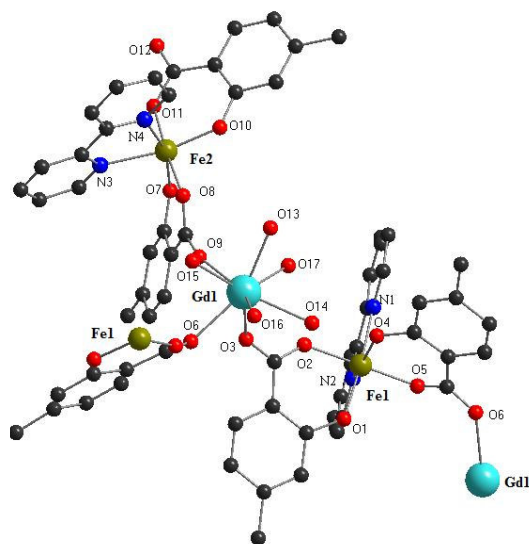


Figure 3.34 The repeating unit, $[\text{Fe}_2\text{Gd}(4\text{-Me-sal})_4(2,2'\text{-bipy})_2(\text{OH}_2)_5]\text{Cl}_{1/2}(\text{NO}_3)_{1/2}\cdot 5\text{H}_2\text{O}$, of the 1D chain in **9**. Hydrogen atoms are omitted for clarity. Colour code: Fe(III), light green; Gd(III), light blue; C, black; O, red and N, blue.

The Gd1 is eight-coordinate whereas the Pr1 in compound **8** was nine-coordinate. This is expected due to the decrease in ionic radius from Pr to Gd, thus decreasing the coordination number. Gd1 is coordinated by five H_2O molecules (O13, O14, O15, O16, O17) and three carboxylate oxygen atoms (O3, O6, O9) from three bridging 4-Me-sal^{2-} ligands. As a result, (Figure 3.35), an infinite chain is formed in a similar manner as observed in compound **8**. The distances between Gd1 and three carboxylate oxygen atoms are 2.345(1) Å (Gd1-O3), 2.369(1) Å (Gd1-O6) and 2.290(1) Å (Gd1-O9). The Gd1-Fe2 distance is 6.221(2) Å and Gd1-Fe1 distance is 5.495(2) Å.

In this case also, the 1D chains are connected through hydrogen bonds forming a 2D hydrogen-bonded sheet. There are π - π stacking interactions in the 2D layer between the aromatic rings of the 2,2'-bipyridyl and the 4-Me-sal²⁻ ligands. The closest distance between the planes of two aromatic rings is about 3.95 Å.

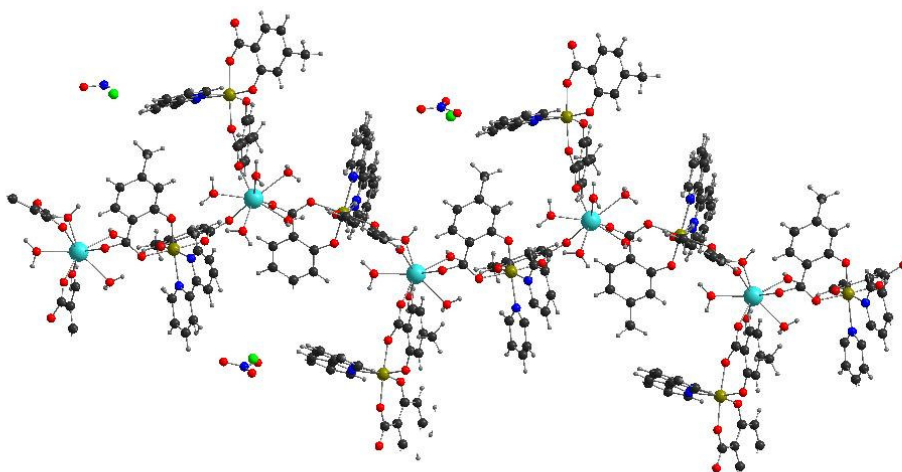


Figure 3.35 Structure of the 1D chain of compound **9**.

The magnetic susceptibility of **9** was studied from 300 K to 1.8 K at 1000 Oe and 10000 Oe. At 300 K, χT product is 15.9 cm³K/mol (Figure 3.36). This value is in good agreement with the expected value (16.6 cm³K/mol) for two Fe(III) ions ($S = 5/2$, $g = 2$, $C = 4.375$ cm³K/mol) and one Gd(III) ion ($S = 7/2$, $L = 0$, $g = 2$, $^8S_{7/2}$, $C = 7.875$ cm³K/mol).⁷² Upon decreasing the temperature, the χT product continuously decreases to reach 11.0 cm³K/mol at 1.8 K. Fitting of the experimental data above 1.8 K to the Curie-Weiss law, leads to the following Curie and Weiss constants, 16.0 cm³K/mol and -0.85 K, respectively. As expected, the Curie constant is close to 16.6 cm³K/mol, for two Fe(III) and one Gd(III) ions.

The field dependence of the magnetisation at low temperatures shows that the magnetisation smoothly increases with the applied dc field (Figure 3.37). At 7 T, it reaches the value of 15.9 μ_B . This magnitude of M is very close to the value of 17 μ_B expected for two Fe(III) ions ($S = 5/2$) and one Gd(III) ion ($S = 7/2$), if the spins are uncoupled.

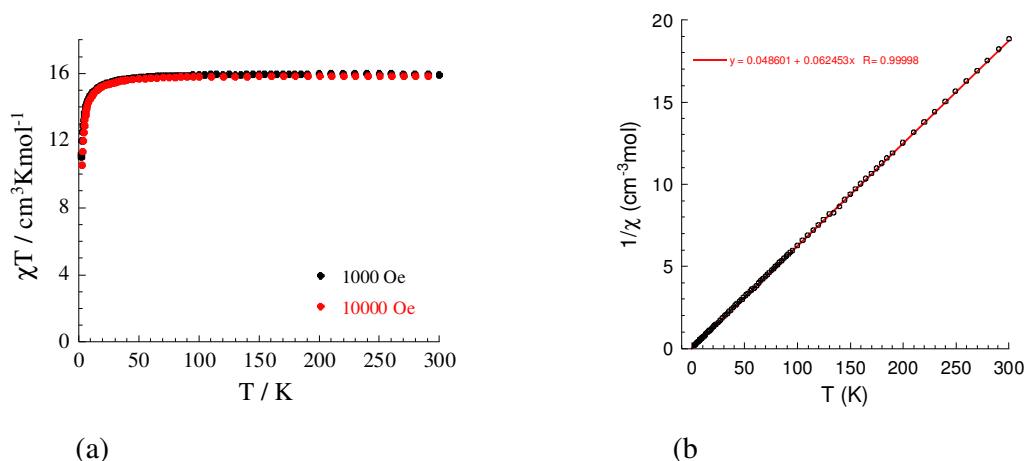


Figure 3.36 (a) Temperature dependence of χT product for **9** at 1000 Oe and 10000 Oe. (b) The Curie-Weiss plot in the temperature range of 1.8-300 K.

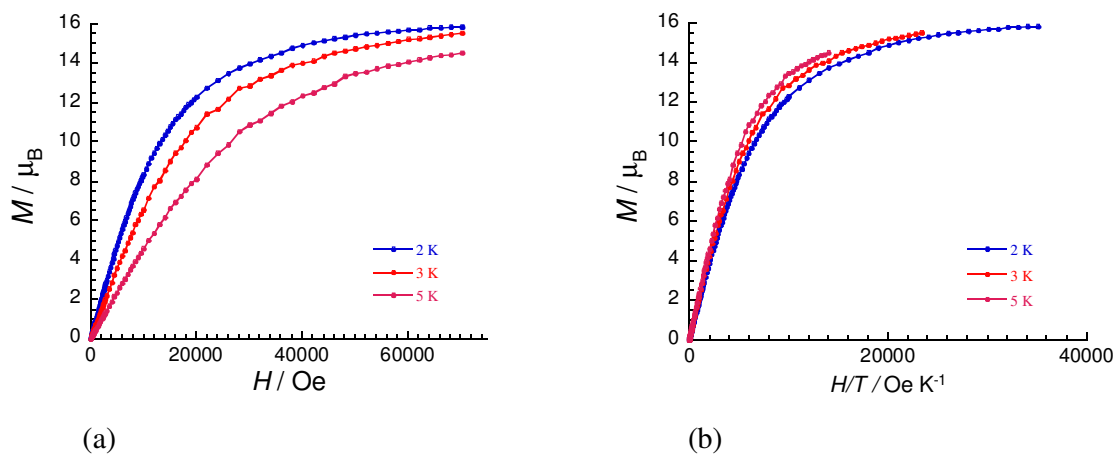


Figure 3.37 (a) Field dependence of magnetisation, (b) M versus H/T , for **9** from 2 to 5 K.

3.2.4 Structure and magnetic behaviour of $[\text{Fe}_2\text{Dy}(\text{4-Me-sal})_4(\text{2,2'-bipy})_2(\text{OH}_2)_5]\text{Cl}_{1/2}(\text{NO}_3)_{1/2} \cdot 5\text{H}_2\text{O}$, **10**

For compound **10**, it was not possible to determine the structure using single crystal X-Ray crystallographic methods, as it was difficult to obtain good single crystals in this case. However, IR and elemental analysis provided useful tools for the elucidation of the structure of compound **10**. The IR of this compound is quite similar to that of compounds **8** and **9**. As observed before, the repeating units in the 1D chain compounds, **8** and **9**, are similar so this

compound is likely to be an isostructural analogue of compound **9**. The elemental analysis indicates a formula similar to **9**. This shows that compound **10** is likely to be a 1D coordination polymer with $[\text{Fe}^{\text{III}}_2\text{Dy}^{\text{III}}(4\text{-Me-sal})_4(2,2'\text{-bipy})_2(\text{H}_2\text{O})_5]^+$ as the repeating unit.

The magnetic susceptibility of **10** was studied from 300 K to 1.8 K at 1000 Oe and 10000 Oe. At 300 K, the χT product is 22.2 $\text{cm}^3\text{K/mol}$ (Figure 3.38). This value is in good agreement with the expected value (22.9 $\text{cm}^3\text{K/mol}$) for two Fe(III) ions ($S = 5/2$, $g = 2$, $C = 4.375\text{ cm}^3\text{K/mol}$) and one Dy(III) ion ($S = 5/2$, $L = 5$, $g = 4/3$, ${}^6\text{H}_{15/2}$, $C = 14.17\text{ cm}^3\text{K/mol}$).⁷² On decreasing the temperature, the χT product almost stays constant until about 50 K and then rapidly decreases to reach a minimum value of 17.6 $\text{cm}^3\text{K/mol}$ at 1.8 K. As mentioned before, the decrease of the χT product may be due to many reasons, thus it is difficult to say whether there is any interaction between the Fe and Ln ions or not. Mössbauer studies were also done for this compound, but it could not reveal much about the kind of interactions between Fe-Ln ions.

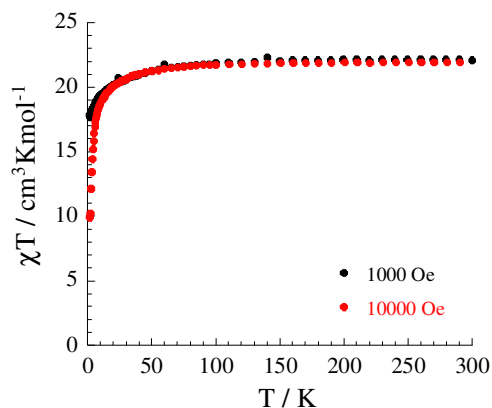


Figure 3.38 Temperature dependence of χT product for **10** at 1000 Oe and 10000 Oe.

The field dependence of the magnetisation at low temperatures shows that the magnetisation smoothly increases with the applied dc field (Figure 3.39). At 7 T, it reaches the value of 15.1 μ_{B} . There is no clear saturation of magnetisation, suggesting the presence of magnetic anisotropy and/or the population of low-lying excited states. The magnetisation

value $15.1 \mu_B$, is in good agreement with the expected value ($15.23 \mu_B$) for all the spins aligned parallel, that is $10 \mu_B$ for two $S = 5/2$ Fe(III) ions and $5.23 \mu_B$ for one Dy(III) ion. The M vs H/T at low temperatures shows that the curves are not superposed on a single master-curve, indicating the presence of magnetic anisotropy and/or low lying excited states.

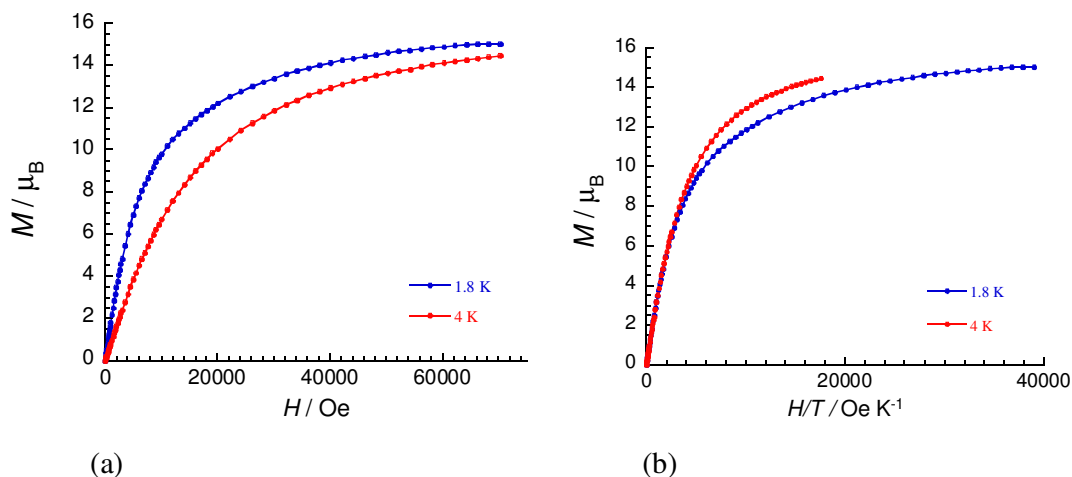


Figure 3.39 (a) Field dependence of magnetisation, (b) M versus H/T , for **10** at 1.8 and 4 K.

3.3 Summary

In this chapter, four novel 3D diamondoid metal organic frameworks $[\text{Mn}^{\text{III}}_2\text{Mn}^{\text{II}}(\text{3-Me-sal})_4(\text{py})_4]$ (**1**), $[\text{Mn}^{\text{III}}_2\text{Mn}^{\text{II}}(\text{4-Me-sal})_4(\text{py})_4(\text{MeOH})] \cdot (\text{H}_2\text{O})$ (**2**), $[\text{Mn}^{\text{III}}_2\text{Mn}^{\text{II}}(\text{5-Me-sal})_4(\text{py})_4(\text{H}_2\text{O})_2] \cdot (\text{MeOH})$ (**3**) and $[\text{Mn}^{\text{III}}_2\text{Mn}^{\text{II}}(\text{3-Me-sal})_4(\text{4-Me-py})_4]$ (**4**) and 1D coordination polymer $[\text{Mn}^{\text{III}}(\text{4-Me-sal})_2(\text{4-Me-py})_2\text{Mn}^{\text{II}}(\text{H}_2\text{O})_2(\text{MeOH})_2][\text{Mn}^{\text{III}}(\text{4-Me-sal})_2(\text{4-Me-py})_2]$ (**5**) have been discussed. These compounds are the first metal organic frameworks synthesized using substituted methylsalicylates and substituted pyridine ligands. In all these compounds, the structure is dictated by the coordination environment of Mn(II). When Mn(II) is four- or five-coordinated, a 3D diamondoid framework is constructed. For coordination number six, the arrangement of the ligands and water molecules induces a change in the structural motif of the final compound. The *cis* arrangement of the two coordinated water molecules in compound **3** results in a 3D diamondoid framework, while a

trans arrangement in **5** leads to the formation of a 1D coordination polymer. The shape of the diamond networks are also affected by the modification of the coordination environment of Mn(II). Magnetic studies show that there are weak antiferromagnetic interactions between Mn(II) and Mn(III) metal ions in the 1D coordination polymer. The 3D networks exhibit long-range ferrimagnetic ordering at 7.4 K (**1**), 4.6 K (**2**) and 3.0 K (**3**) depending on the coordination number (4, 5 or 6) of the Mn(II) centres in the network. The blocking temperature increases as the coordination number of Mn(II) decreases. This shows that there is a decrease in the magnetic interactions with the increase in bond length. The result also reinforces the hypothesis that the structure of **1** ($T_C = 7.4$ K) and **4** ($T_C = 7.7$ K) are similar as suggested by the X-ray analysis, and probably Mn(II) in **4** also has a coordination sphere of four as in **1**. These observations show that the coordination geometry and coordination number of Mn(II) can be varied, giving a possibility to change the dimensionality and tune the magnetic properties. This strategy can be very useful to achieve ferrimagnetic systems that may have higher blocking temperatures.

This synthetic strategy was also applied using more than one type of metal ion to obtain mixed-metal complexes. In compound **7**, the azide added in the reaction does not coordinate, but it act as a base to oxidise the manganese. The sodium cation instead coordinates to the ligand giving a 1D polymer of Na and Mn, where the ligand bridges in a different fashion from what has been observed before for salicylic acid ligands. Heterometallic 3d-4f coordination polymers were synthesised with $[\text{Fe}_2\text{Ln}(4\text{-Me-sal})_4(2,2'\text{-bipy})_2(\text{OH}_2)_x]^+$ (Ln = Pr, Gd, Dy, x = 5 or 6) as repeating units. The chelating 2,2'-bipyridyl coligand blocks further bridging of the Fe(III) centres with Ln(III), and favours the formation of a 1D polymer rather than a 3D extended structure. This shows that the variation of coligands also plays an important role in obtaining different structures. There are only a few examples of Fe-Ln mixed-metal coordination polymers, and these complexes are an addition to these class of compounds described so far.⁷⁴⁻⁷⁵

Chapter 4: Structure and magnetic properties of discrete compounds obtained with substituted salicylates

An important concept for synthesising molecule-based magnetic solids is the use of molecular building blocks to create systems of varying dimensionalities. These systems range from zero-dimensional molecules to extended three-dimensional networks. These materials can be constructed by connecting two paramagnetic metal centres using bridging ligands that act as super-exchange pathways, inducing either parallel or antiparallel spin pairing. In all cases, the magnetic units display properties that originate from the molecular nature of the system. As a result, fine-tuning of these molecular motifs and their magnetic properties may be possible.

During the investigation of the coordination chemistry of salicylic acid ligands, both extended and discrete structures were obtained. In chapter 3, 1D and 3D compounds synthesized from methyl-substituted salicylate ligands were discussed in detail. To understand the interactions in these extended systems, it was important to isolate and investigate the magnetic properties of their repeating units. The interesting observation was that the salicylate ligand, 3-methoxysalicylic acid (3-MeO-salH₂) (Figure 4.01), gave discrete structures. The methyl-substituted salicylic acids, however, produced polymeric networks. This chapter describes the monomeric and oligomeric complexes obtained from 3-MeO-salH₂. It was observed that some of these complexes are similar to the building blocks of the 1D and 3D compounds synthesized from methyl-substituted salicylic acid ligands.

In addition to the Mn(II) and Fe(III) metal ions which have been used before, Cu(II) ions were also used here to compare the affinity of the ligand towards different metal centres. A range of solvents (py, MeOH, MeCN, DMF and H₂O) was used to find out the appropriate reaction conditions for obtaining single crystals. The strategy of varying the coligands was also employed, and coligands such as pyridine (py) and 2,2'-bipyridyl (2,2'- bipy) were used. The coligands can play an important role in modifying the structures of the complexes and

can also trap more metal ions. A stepwise study of the variation of metal centres, bases, coligands, and reaction conditions can be very useful for the purpose of controlling the synthesis as well as investigating any structure-property relationships.

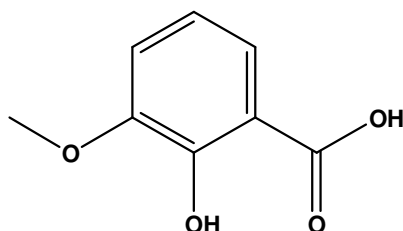


Figure 4.01 The ligand, 3-methoxysalicylic acid (3-MeO-salH₂).

4.1 Structure of (NH₄)⁺[Mn^{III}(3-MeOsal)₂(MeOH)(H₂O)], **11**

The reaction of 3-MeO-salH₂ and manganese perchlorate in the presence of base (triethylamine) using methanol as solvent gave (NH₄)⁺[Mn^{III}(3-MeOsal)₂(MeOH)(H₂O)] (**11**). It is a mononuclear anionic Mn complex with a triethylammonium counter cation (Figure 4.02). The Mn(III) ion has an elongated octahedral geometry. It is coordinated by four oxygen atoms (O1, O2, O5, O6) of the phenoxo and carboxylate groups of the two bidentate 3-MeO-sal²⁻ ligands in the equatorial plane. The axial sites are occupied by methanol and a water molecule. The average Mn–O equatorial bond length (1.899(2) Å) is typical for Mn(III),⁶⁶ and it has a Jahn-Teller axial elongation with an average axial bond length of 2.255(1) Å.

There is intramolecular hydrogen bonding between the hydrogen atom of the triethylammonium cation and the carboxylate oxygen of the ligand (O7...N 2.731(2) Å). There is also intermolecular hydrogen bonding, where hydrogen atoms of the coordinated water molecule form hydrogen bonds with methoxy (O9...O4 2.835(2) Å) and hydroxy (O9...O1 2.982(3) Å) oxygen atoms of the ligand from another mononuclear unit (Figure 4.03). The coordinated methanol molecule also forms hydrogen bond with the non-coordinated

carboxylate oxygen (O10...O3 2.654(2)Å) of the ligand from another mononuclear unit. The adjacent mononuclear units are held together by π - π stacking interactions between benzene rings of two units. The shortest distance between the planes of the two parallel aromatic rings is 3.65(2) Å.

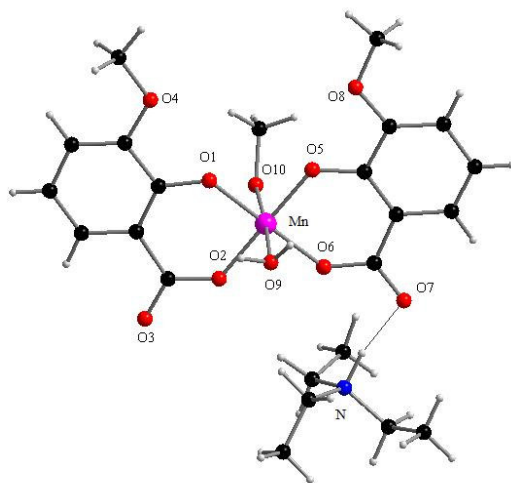


Figure 4.02 Structure of $(\text{NHEt}_3)[\text{Mn}^{\text{III}}(3\text{-MeOsal})_2(\text{MeOH})(\text{H}_2\text{O})]$, **11**. The hydrogen bond is shown by the dotted line. Colour code: Mn^{III} , purple; C, black; O, red; N, blue and H, grey.

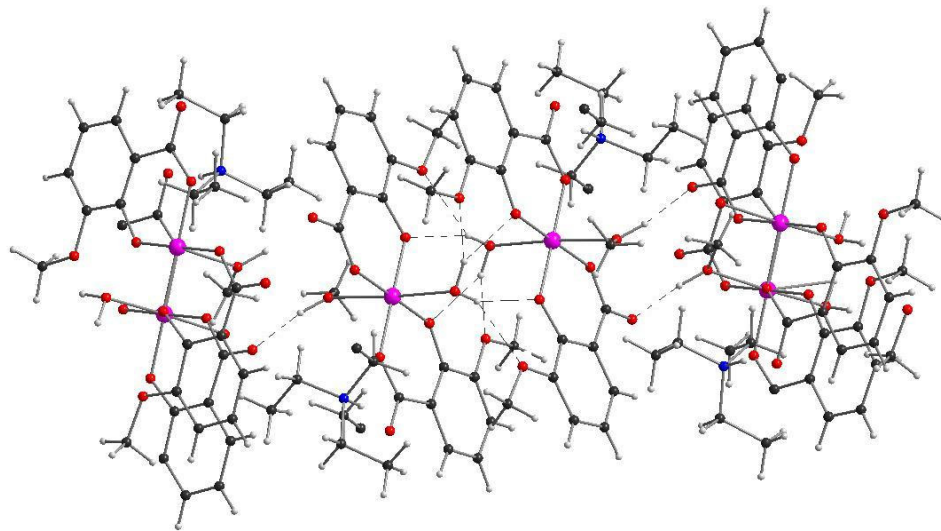


Figure 4.03 Packing diagram of compound **11**. Hydrogen bonds are shown by dotted lines.

4.2 Structure of $(\text{NHET}_3)_2[\text{Fe}^{\text{III}}(\text{3-MeOsal})_2(\text{OAc})]$, **12**

The reaction of preformed $[\text{Fe}_3(\text{OAc})_6(\text{Py})_3](\text{ClO}_4)^{76}$ with 3-MeO-salH₂ in MeCN gave $(\text{NHET}_3)_2[\text{Fe}^{\text{III}}(\text{3-MeOsal})_2(\text{OAc})]$, **12** (Figure 4.04). It is a mononuclear Fe complex with $[\text{Fe}^{\text{III}}(\text{3-MeOsal})_2(\text{OAc})]^{2-}$ as an anionic unit and two $(\text{NHET}_3)^+$ as counter cations.

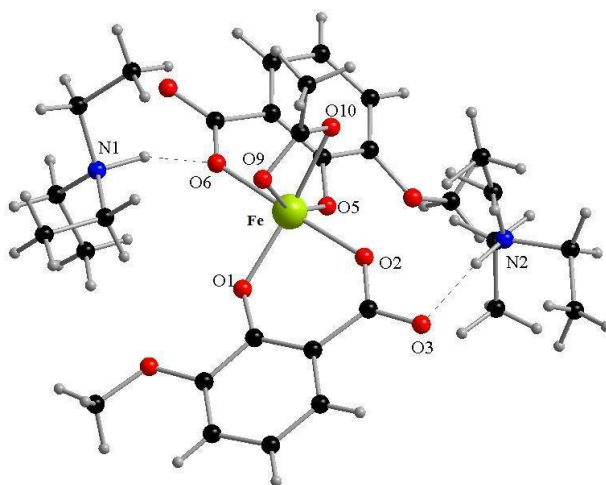


Figure 4.04 Structure of $(\text{NHET}_3)_2[\text{Fe}^{\text{III}}(\text{3-MeOsal})_2(\text{OAc})]$, **12**. Hydrogen bonds are shown as dotted line. Colour code: Fe^{III}, green; C, black; O, red; N, blue and H, grey.

Fe(III) is coordinated by two oxygen atoms (O9, O10) of a bidentate acetate group, and by four oxygen atoms (O1, O2, O5, O6) of two bidentate 3-MeO-sal²⁻ ligand where carboxylate and phenoxy oxygen atoms from each ligand coordinate. The average equatorial Fe–O bond length is 1.951(2) Å, and the average axial bond length is 2.151(1) Å. The Fe(III) centre has a distorted octahedral geometry, and the angles at Fe subtended by *cis* and *trans* ligand atoms are about 87.86° and 156.67°, respectively. The counter cations form intramolecular hydrogen bonds with the carboxylate oxygen atoms of the ligand (O6...N1 2.714(2)Å, O3...N2 is 2.805(2)Å). Similar coordination environments were seen for the Fe(III) centres in the Fe-Ln 1 D compounds (**8**, **9**, **10**) described in chapter 3. The carboxylate groups of the ligand in those compounds, however, were bridging between the Fe and Ln centres to form chains.

4.3 Structure and magnetic behaviour of $[\text{Mn}^{\text{II}}\text{Mn}^{\text{III}}_2(3\text{-MeOsAl})_4(\text{py})_6(\text{H}_2\text{O})_2]\cdot 4\text{H}_2\text{O}$, **13**

The reaction of 3-MeO-salH₂ with manganese acetate in pyridine in the presence of the oxidizing agent (NBu₄MnO₄)⁷⁷ gave $[\text{Mn}^{\text{II}}\text{Mn}^{\text{III}}_2(3\text{-MeOsAl})_4(\text{py})_6(\text{H}_2\text{O})_2]\cdot 4\text{H}_2\text{O}$ (**13**). Crystals were obtained by layering the resulting pyridine solution with an equal volume of petroleum ether. Compound **13** is a linear trinuclear manganese complex with four 3-MeOsAl²⁻, six pyridine and two water ligands. There are also four water molecules present as lattice solvent (Figure 4.05).

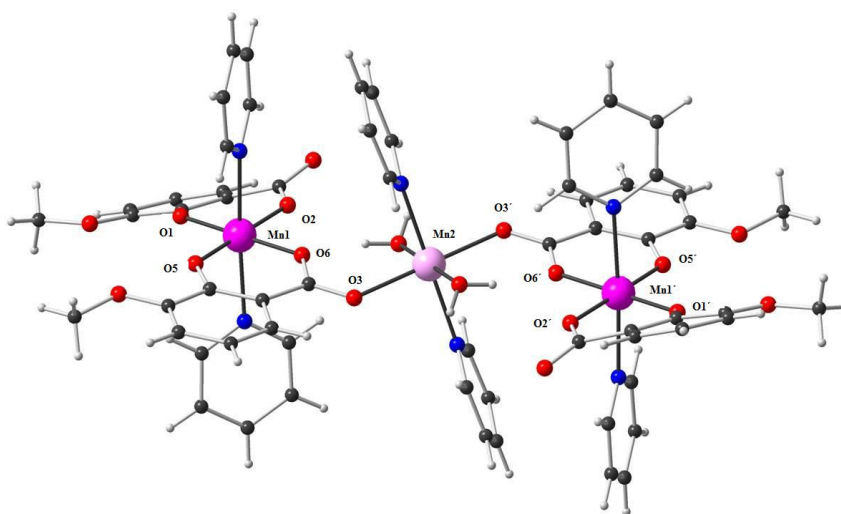


Figure 4.05 Molecular structure of $[\text{Mn}^{\text{II}}\text{Mn}^{\text{III}}_2(3\text{-MeOsAl})_4(\text{py})_6(\text{H}_2\text{O})_2]\cdot 4\text{H}_2\text{O}$, **13**. Colour code: Mn^{III}, purple; Mn^{II}, pink; C, black; O, red; N, blue and H, grey.

All three manganese are six-coordinate, and they are bridged by carboxylate groups in *syn-anti* configuration. The central Mn2 ion is located on a crystallographic inversion centre, and it is flanked by Mn1 and its symmetry equivalent. The Mn2⋯Mn1 separation is 5.134(2) Å. Mn2 has two axial coordination sites occupied by pyridine. The equatorial sites have two water molecules in *cis* configuration, and two carboxylate oxygen atoms (O3, O3') from two bridging 3-MeO-sal²⁻ ligands. Mn1 is coordinated by four oxygen atoms (O1, O2, O5, O6) of two bidentate 3-MeO-sal²⁻ in the equatorial plane, and the two axial sites are occupied by pyridine molecules. The average Mn1–O equatorial bond length (1.897(1) Å) is

typical for Mn(III), whereas the average Mn2–O equatorial bond length (2.180(1) Å) is typical for Mn(II).⁶⁶ Bond valence sum (BVS) analysis also confirms the oxidation states of the metals.⁶⁷ Mn1 shows a Jahn-Teller axial elongation as expected for a Mn(III) ion. The average Mn1–N axial bond length is 2.353(1) Å, and it is significantly longer than the average equatorial bond length of 1.897(1) Å.

The magnetic susceptibility of **13** was studied from 300 K to 1.8 K at 1000 Oe and 10000 Oe (Figure 4.06). At 300 K, the χT product is 9.6 cm³Kmol⁻¹, which is slightly lower than the expected value of 10.4 cm³Kmol⁻¹ (one Mn(II), $S = 5/2$, $g = 2.00$ and two Mn(III), $S = 2$, $g = 2.00$) ions. On decreasing the temperature, the χT product continuously decreases to reach 1.75 cm³Kmol⁻¹ at 1.8 K, indicating dominant antiferromagnetic interactions in the trinuclear complex, compatible with an $S = 3/2$ ground state. The magnetic behaviour follows the Curie-Weiss law in the full temperature range of 1.8-300 K, with a Curie constant (C) of 9.78 cm³K/mol, and a Weiss constant (θ) of -5.62 K (Figure 4.07).

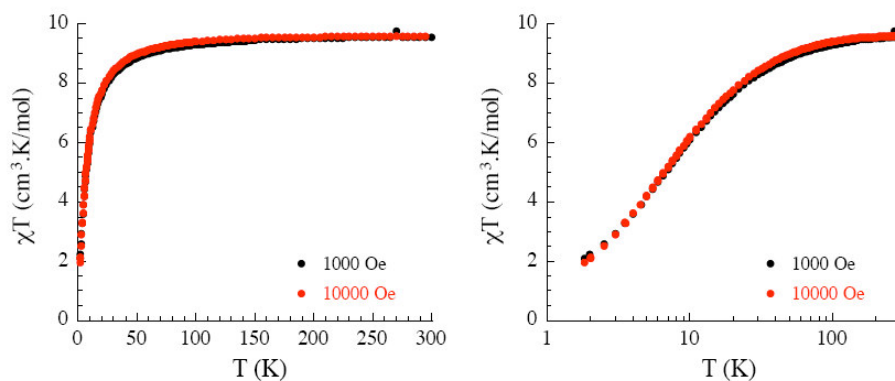


Figure 4.06 Temperature dependence of the χT product from 0 to 300 K (left) and from 1 to 100 K (right) for **13** at 1000 Oe and 10000 Oe.

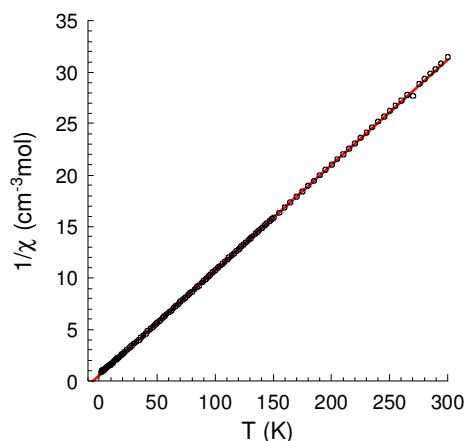


Figure 4.07 The Curie-Weiss Plot for **13**, and solid line (red) is the fit.

The M versus H measurements (Figure 4.08) at 1.8 K as a function of the field reveal a slow increase of the magnetisation, which reaches a value of $9.1 \mu_B$ at 7 T. A true saturation of the magnetisation value was not observed, suggesting the presence of low-lying excited states that might be populated when a field is applied. At higher field when the antiferromagnetic interactions are overcome, there should be a saturation of the magnetisation at $13 \mu_B$ because all spins would be parallel.

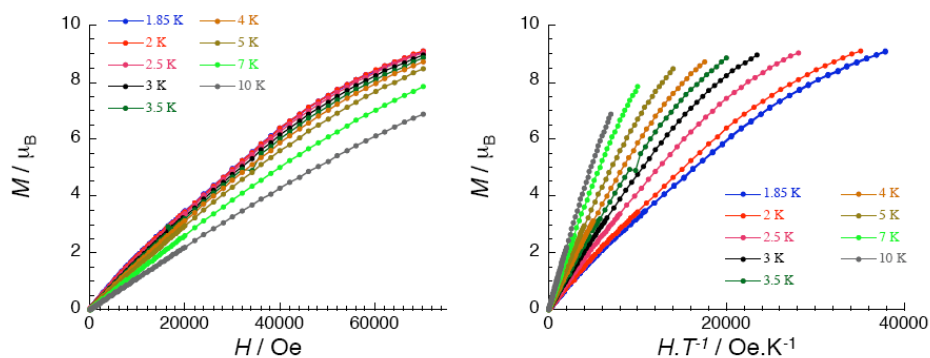


Figure 4.08 Field dependence of the magnetisation (left side up to 60000 Oe and right side up to 40000 Oe) for **13**, from 1.85 K to 10 K.

The high-temperature behaviour of the magnetic susceptibility was modelled by using a simple symmetrical trimer model approach considering the Mn(II)-Mn(III) interactions (J_1)

are identical by symmetry. With this structural motif, the Heisenberg spin Hamiltonian can be written as follows:

$$H = -2J_1(S_{IA}S_2 + S_{IB}S_2)$$

where J_1 is the exchange interactions in the trimer between adjacent Mn(II) and Mn(III) ions, $S_{IA} = S_{IB} = 2$ is for Mn(III), and $S_2 = 5/2$ is for Mn(II).

The application of the Van Vleck equation⁷⁸ to the Kambe's vector coupling scheme⁷⁹ allows a determination of the low-field analytical expression of the magnetic susceptibility.⁸⁰ The experimental data from 300 K to 1.8 K can be very well reproduced by this model (Figure 4.09). The best set of parameters obtained are $J_1/k_B = -0.64(1)$ K and $g = 1.93(1)$. The amplitude of the interaction through *syn-anti* carboxylate bridge between Mn(III) and Mn(II) centres is consistent with previously published data.⁶⁹

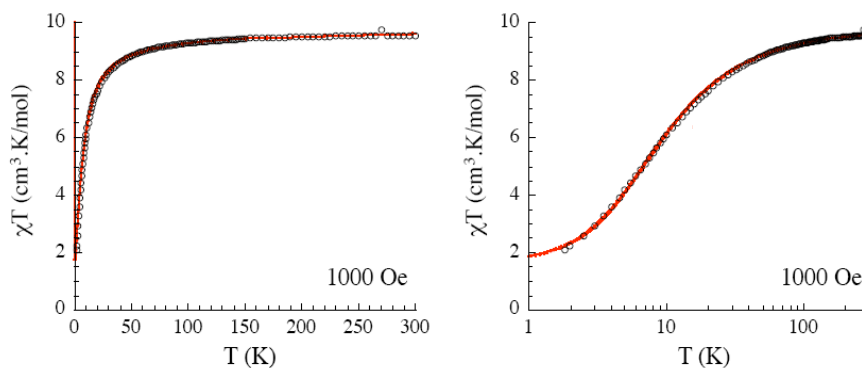


Figure 4.09 Temperature dependence of the χT product (left side from 0 to 300 K and right side from 0 to 100 K) for **13**, at 1000 Oe, and solid line is the best fit.

4.4 Structure and magnetic behaviour of $[\text{Mn}^{\text{III}}_2\text{Mn}^{\text{II}}(\text{3-MeO-sal})_4(\text{py})_4(\text{H}_2\text{O})_4]\cdot 4\text{MeOH}$,

14

The reaction of 3-MeO-salH₂ with manganese chloride in methanol using triethylamine as base gave $[\text{Mn}^{\text{III}}_2\text{Mn}^{\text{II}}(\text{3-MeO-sal})_4(\text{Py})_4(\text{H}_2\text{O})_4]\cdot 4\text{MeOH}$, **14**. The structure of compound **14** is similar to compound **13**, but **14** has only four pyridine ligands while **13**

has six . Each Mn(III) centre in **13** was coordinated by two pyridine molecules, but in **14** one of these pyridine molecules has been replaced by a water molecule (Figure 4.10). The lattice solvents are also different. In this case there are four methanol molecules rather than the four water molecules found in compound **13**.

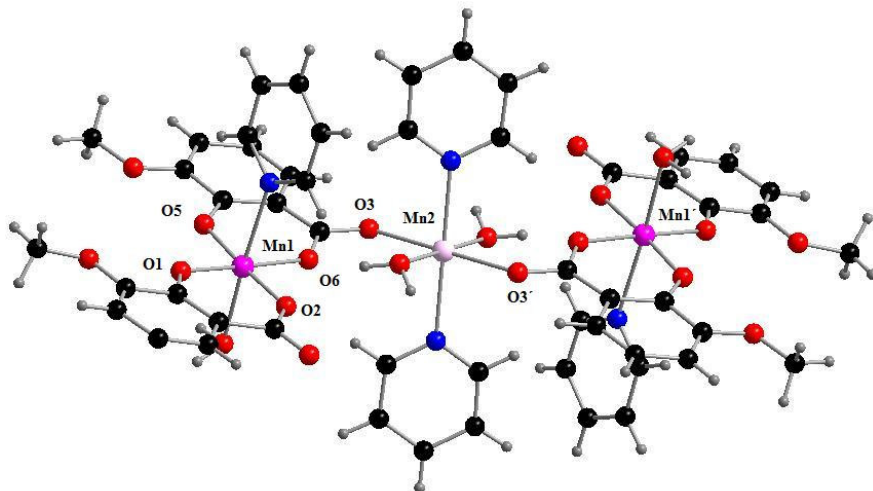


Figure 4.10 Molecular structure of $[\text{Mn}^{\text{III}}_2\text{Mn}^{\text{II}}(\text{3-MeO-sal})_4(\text{Py})_4(\text{H}_2\text{O})_4]\cdot 4\text{MeOH}$, **14**. Colour code: Mn^{III} , purple; Mn^{II} , pink; C, black; O, red and N, blue.

All three manganese are six-coordinate, and are again bridged by carboxylate groups in *syn-anti* configuration. The central Mn2 ion is located on a crystallographic inversion centre, with a $\text{Mn2}\cdots\text{Mn1}$ separation of 5.120(1) Å. The Mn2 coordination environment is identical to that of Mn2 in **13**. Mn1 is, however, coordinated by four oxygen atoms (O1, O2, O5, O6) of two bidentate 3-MeOsal²⁻ in the equatorial plane, and the two axial sites now have one water and one pyridine molecule. The average Mn2–O equatorial bond length (2.198(8) Å), and the average Mn1–O equatorial bond length (1.898(7) Å) are typical for Mn(II) and Mn(III) distances, respectively.⁶⁶ Mn1 has a Jahn-Teller elongation with an average axial bond length of 2.324(7) Å and an average equatorial bond length of 1.898(7) Å.

The coordinated water molecule on Mn1 forms intermolecular hydrogen bonds with the carboxylate oxygen of the 3-MeO-sal²⁻ ligand from another trinuclear unit. As a result,

each trinuclear unit is linked by hydrogen bonding to two other units at both ends making a staircase-like structure, and **14** can be described as hydrogen-bonded 1D chain (Figure 4.11).

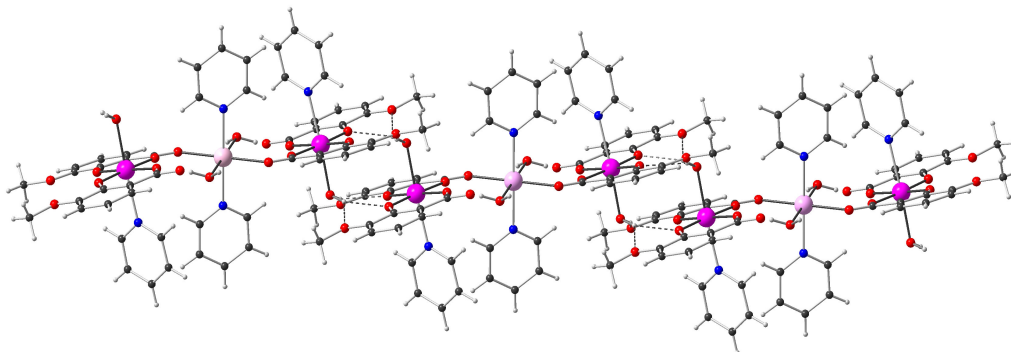


Figure 4.11 Hydrogen-bonded structure of compound **14**.

The magnetic susceptibility of **14** was measured from 300 K to 1.8 K at 1000 Oe and 10000 Oe (Figure 4.12). At 300 K, the χT product at 1000 Oe is 9.87 cm³K/mol. On decreasing the temperature, the χT product continuously decreases to reach 1.7 cm³K/mol at 1.8 K indicating dominant antiferromagnetic interactions in the trinuclear complex. This is compatible with an $S = 3/2$ ground state. Fitting the experimental data to the Curie-Weiss law above 1.8 K leads to the Curie and Weiss constants of 10.9 cm³K/mol and -5.9 K, respectively. The Curie constant is in agreement with the value (10.375 cm³.K/mol) expected for one Mn(II) metal ion ($S = 5/2$, $g = 2$) and two $S = 2$ Mn^{III} ions ($S = 2$, $g = 2$). The negative Weiss constant suggests the presence of antiferromagnetic interactions between the spin carriers.

The temperature dependence of the magnetic susceptibility was analysed using the symmetrical trimer model used for compound **13**. This model can reproduce the experimental data very well from 300 K to 5 K (Figure 4.13). The best set of parameters found were $J_1/k_B = -0.57(1)$ K and $g = 2.00(1)$. The magnitude of the interactions through the *syn-anti* carboxylate bridge between Mn(III) and Mn(II) is comparable with previous data published in

the literature,⁶⁹ and is also similar to compound **13**. Below 5 K, it is noteworthy that the theoretical curve after fitting the data is higher than the experimental values, this might indicate the presence of additional inter-complex antiferromagnetic interactions.

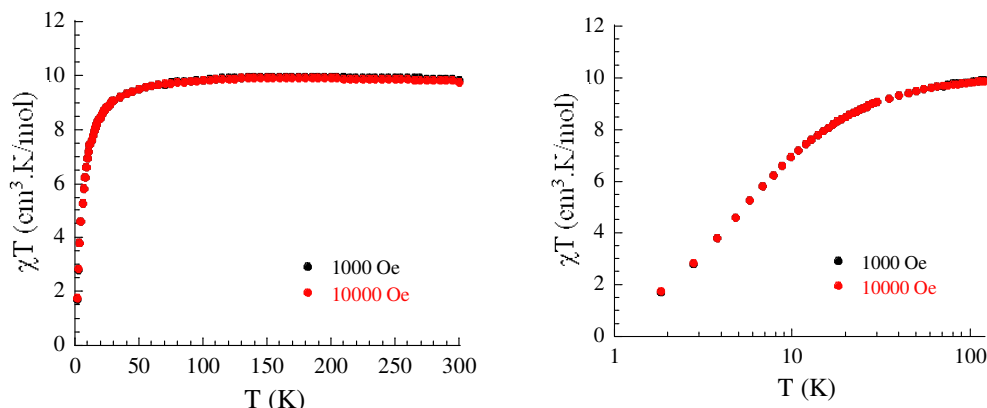


Figure 4.12 Temperature dependence of the χT product (left side from 0 to 300 K and right side from 1 to 100 K) for **14** at 1000 Oe and 10000 Oe.

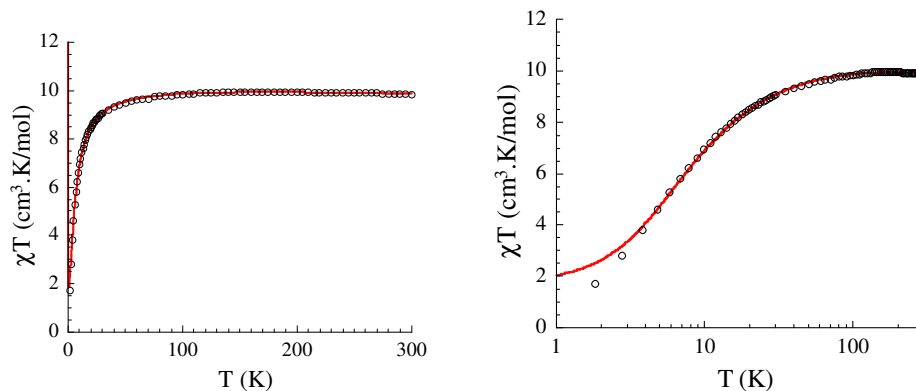


Figure 4.13 Temperature dependence of the χT product (left side from 0 to 300 K and right side from 1 to 100 K) for **14**, at 1000 Oe, and solid line is the best fit.

The M versus H measurements (Figure 4.14) at 1.8 K reveal similar results as seen in compound **13**. There is a slow increase of the magnetisation with an S -shaped curve, and absence of a true saturation of the magnetisation. It reaches a value of $10.5 \mu_B$ at 7 T.

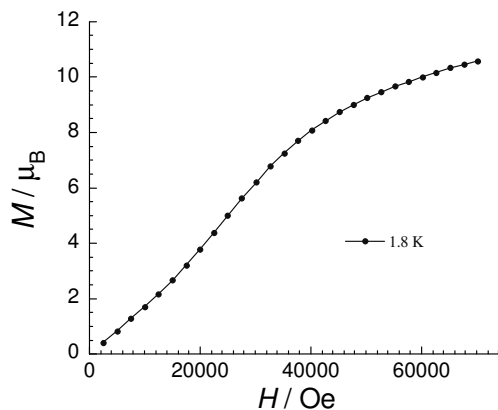


Figure 4.14 Field dependence of the magnetisation for **14** at 1.8 K.

The change of solvent from **13** to **14** does modify the structure to some extent; however, it seems that the trinuclear core is stable, and the magnetic interactions do not change significantly. Similar trinuclear units form the repeating units of the polymeric chain and networks described in chapter 3. It appears that the bulkier methoxy group of 3-MeO-salH₂ prevents further bridging of the Mn(III) centres with Mn(II) centres of another trinuclear unit. The coordination at each Mn(II) is instead completed by two pyridine molecules, favouring the formation of discrete structures. It can also be seen that in these complexes there are antiferromagnetic interactions between the metal centres similar to those observed in the extended systems; however, there is a remanent magnetisation in the 3D networks leading to ferrimagnetic long-range ordering.

4.5 Structure and magnetic behaviour of [Mn^{III}₂Mn^{II}(3-MeO-sal)₄(2,2'-bipy)(H₂O)₃(MeOH)₂]₃MeOH, **15**

The reaction of 3-MeO-salH₂ with manganese acetate in methanol using triethylamine as base produces [Mn^{III}₂Mn^{II}(3-MeO-sal)₄(2,2'-bipy)(H₂O)₃(MeOH)₂]₃MeOH, **15**. It is a trinuclear, mixed-valence manganese complex arranged in a triangular fashion. The metals are

coordinated by four 3-MeO-sal²⁻, one 2,2'-bipy, three water and two methanol molecules. Three methanol molecules are present as lattice solvent (Figure 4.15).

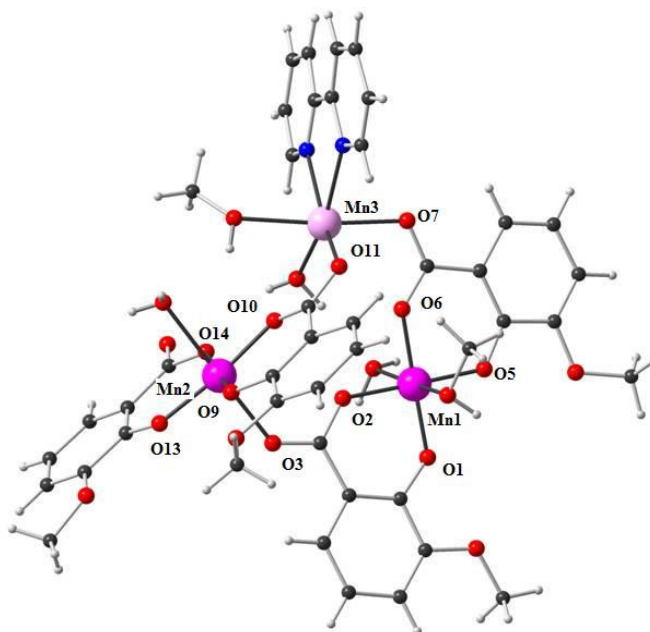


Figure 4.15 Structure of the trinuclear cluster, $[\text{Mn}^{\text{III}}_2\text{Mn}^{\text{II}}(3\text{-MeO-sal})_4(2,2'\text{-bipy})(\text{H}_2\text{O})_3(\text{MeOH})_2]$, in **15**. Colour code: Mn^{III} , purple; Mn^{II} , pink; C, black; O, red; N, blue and H, grey.

All three manganese ions (Mn1, Mn2, Mn3) are six-coordinate, and they are bridged by three carboxylate groups in a *syn-anti* configuration. The Mn1 \cdots Mn2, Mn1 \cdots Mn3 and Mn2 \cdots Mn3 distances are 5.242(3) Å, 4.652(2) Å and 4.687(4) Å, respectively. The coordination environments of the three manganese ions are different. Mn1 has distorted octahedral geometry, and is coordinated by four oxygen atoms (O1, O2, O5, O6) of two bidentate 3-MeO-sal²⁻ ligands in the equatorial plane. The two axial sites are occupied by water and methanol. Mn2 also has distorted octahedral geometry, and is coordinated by four oxygen atoms (O9, O10, O13, O14) of two bidentate 3-MeO-sal²⁻ in the equatorial plane. In the axial sites, Mn2 has one water molecule and one carboxylate oxygen (O3) from a bridging

3-MeO-sal²⁻ ligand, which is also coordinated to Mn1. Mn3 is octahedral, and is coordinated by one bidentate 2,2'-bipy, one water and one carboxylate oxygen (O11) from a bridging 3-MeO-sal²⁻ ligand in the equatorial plane. This 3-MeO-sal²⁻ ligand also coordinates to Mn2. In the axial sites, Mn3 has one methanol and one carboxylate oxygen (O7) from a bridging 3-MeO-sal²⁻ ligand, which is also coordinated to Mn1. All three manganese ions are, thus interconnected forming a triangular structure. The carboxylate groups bridge in a *syn-anti* configuration. The average Mn3 bond length (2.244(1) Å) is significantly longer than the average Mn1 (1.891(1) Å) and Mn2 (1.900(1) Å) bond lengths, indicating that Mn3 is a Mn(II) ion, whereas Mn1 and Mn2 are Mn(III) ions.⁶⁶ Further confirmation of the oxidation states was done by BVS analysis.⁶⁷ Mn1 and Mn2, both have Jahn-Teller axial elongations as expected for Mn(III) ions with the average axial bond lengths (Mn1: 2.273(1) Å and Mn2: 2.285(1) Å) significantly longer than the average equatorial bond lengths (Mn1: 1.891(1) Å and Mn2: 1.900(1) Å). The coligand, 2,2'-bipy, being bidentate and chelating, has to be in cis positions and sterically favours the formation of a triangular structure. The pyridine coligand, however, being monodentate prefer to be in trans positions and favoured the formation of the linear structure in compound **13** and **14**.

The magnetic susceptibility of **15** was studied from 300 K to 1.8 K at 1000 Oe and 10000 Oe (Figure 4.16). At 300 K, the χT product is 10.0 cm³K/mol. This is in agreement with the expected value for the presence of one Mn(II) metal ion ($S = 5/2$, $g = 2$) and two Mn(III) ions ($S = 2$, $g = 2$). On decreasing the temperature, the χT product continuously decreases to reach 1.7 cm³K/mol at 1.8 K indicating dominant antiferromagnetic interactions in the trinuclear complex, which would be compatible with an $S = 3/2$ ground state.

The M versus H measurements at 1.8 K reveal (Figure 4.17) similar magnetic behaviour as compounds **13** and **14**. The magnetisation reaches a value of 9.6 μ_B at 7 T.

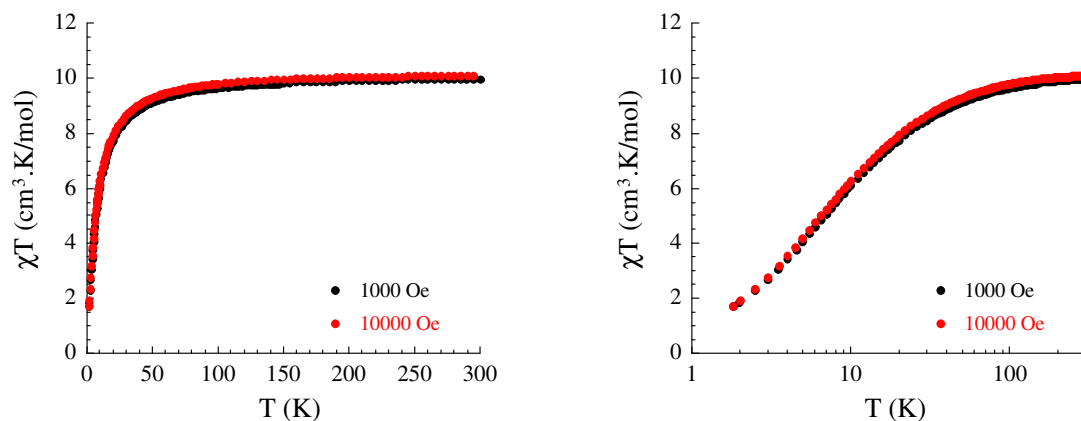


Figure 4.16 Temperature dependence of the χT product from 0 to 300 K (left) and from 1 to 100 K (right) for **15** at 1000 Oe and 10000 Oe.

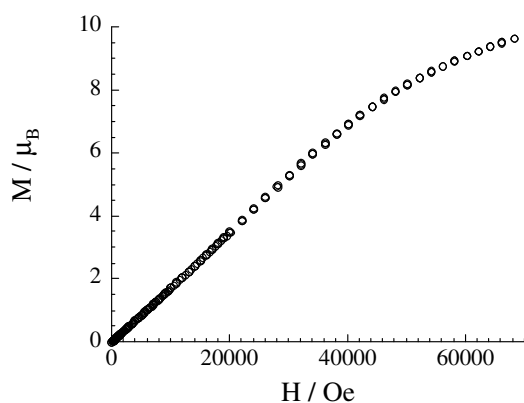


Figure 4.17 Field dependence of the magnetisation for **15** at 1.8 K.

The high temperature behaviour of the magnetic susceptibility was treated with the symmetrical trimer model, and the Mn(II)-Mn(III) interactions (J_i) were considered equivalent even if by symmetry this is not the case. It is a good approximation considering that the *syn-anti* carboxylate bridges are very similar. With this structural motif, the Heisenberg spin Hamiltonian can be written as follows:

$$H = -2J_1(S_{1A}S_2 + S_{1B}S_2) - 2J_2S_{1A}S_{1B}$$

where J_1 and J_2 are the exchange interactions in the trimer between Mn(II) and Mn(III) ions and between two Mn(III) ions, respectively. $S_{IA} = S_{IB} = 2$ is for Mn(III) and $S_2 = 5/2$ is for Mn(II) centres.

This model can reproduce the experimental data very well from 300 K to 1.8 K (Figure 4.18). The best set of parameters found are $J_1/k_B = -0.63(1)$ K, $J_2/k_B = -0.50(3)$ K and $g = 1.98(1)$. The magnitude of the interactions through the *syn-anti* carboxylate bridges between Mn(II) and Mn(III) or between two Mn(III) ions, are comparable with previous published data.⁶⁹

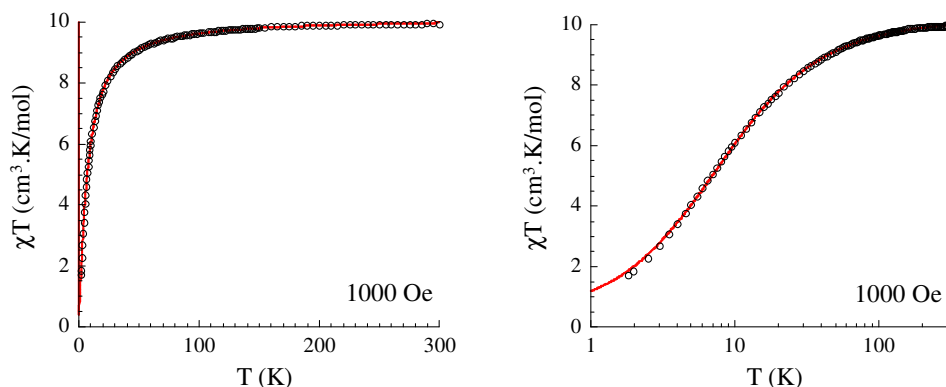


Figure 4.18 Temperature dependence of the χT product (left side from 0 to 300 K and right side from 1 to 100 K) for **15** at 1000 Oe, and solid line is the best fit.

4.6 Structure and magnetic behaviour of $[\text{Cu}_3(3\text{-MeO-salH})_2(3\text{-MeO-sal})_2(2,2'\text{-bipy})_2]$, **16**

The solvolysis reaction of a Cu(II) salt, 3-MeO-salH₂ and 2,2'-bipy in methanol gave a green precipitate of the copper complex, which was partially soluble in DMF. To obtain single crystals, the solvent diffusion method was used. Layering copper acetate in H₂O with 3-MeO-salH₂ in DMF and then with 2,2'-bipyridyl in MeOH gave $[\text{Cu}_3(3\text{-MeO-salH})_2(3\text{-MeO-sal})_2(2,2'\text{-bipy})_2]$ (**16**). Compound **16** is a linear trinuclear copper complex bridged by carboxylate and phenoxy oxygen atoms of two fully deprotonated 3-MeO-sal²⁻ and two

monodeprotonated 3-MeO-salH ligands (Figure 4.19). All the copper ions are six-coordinate with a Cu1...Cu2 separation of 3.009(2) Å. The central Cu1 ion is located on a crystallographic inversion centre. The carboxylate group of the 3-MeO-salH ligand bridges between two copper ions in a *syn-syn* configuration (O6, O7), and the 3-MeO-sal²⁻ ligands uses only one of its carboxylate oxygen (O2) as a donor to bridge between two copper ions (Figure 4.20).

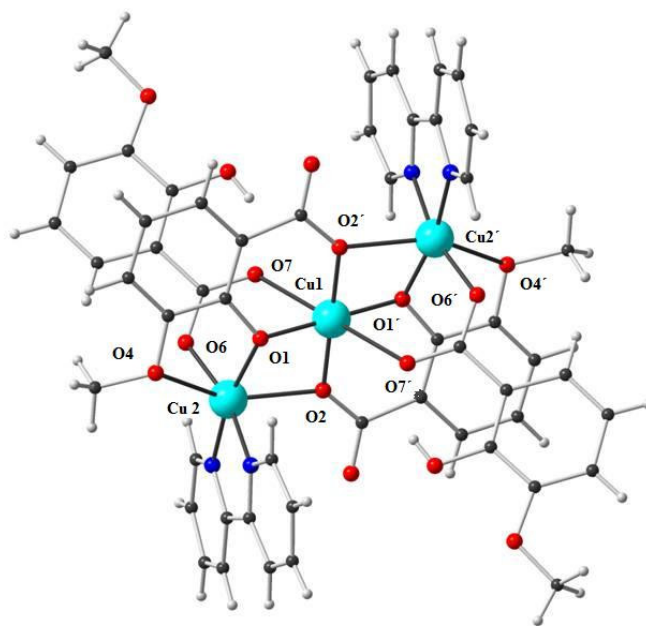


Figure 4.19 Molecular structure of $[\text{Cu}_3(3\text{-MeO-salH})_2(3\text{-MeO-sal})_2(2,2'\text{-bipy})_2]$, **16**. Colour code: Cu^{II}, light blue; C, black; O, red; N, blue and H, grey.

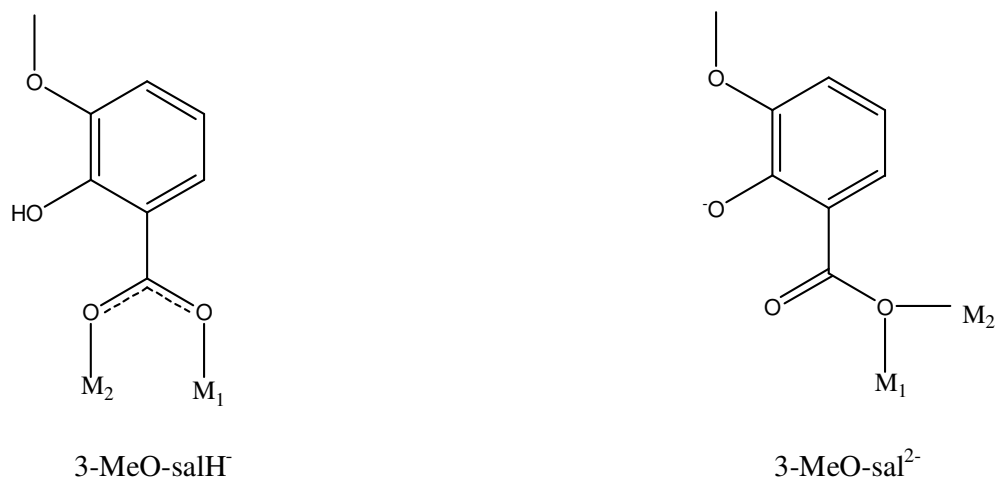


Figure 4.20 The two carboxylate bridging modes in compound **16**.

Cu2 has a distorted octahedral coordination environment created by a bidentate 2,2'-bipy, by two oxygen atoms from the methoxy (O4) and the μ -phenoxy group (O1) of a 3-MeO-sal²⁻ ligand, and by carboxylate oxygen atoms from additional 3-MeO-salH⁻ (O6) and 3-MeO-sal²⁻ (O2) ligands. Cu1 has distorted octahedral geometry with two bidentate 3-MeO-sal²⁻ ligands in the equatorial plane, where phenoxy (O1) and carboxylate oxygen (O2) from each ligand has coordinated. The axial sites are occupied by two carboxylate oxygen atoms (O7 and O7') from two bridging 3-MeO-salH⁻ ligands. The Cu1-O1-Cu2 angle is 99.30(4)°, and the Cu1-O2-Cu2 angle is 91.99(3)°. Cu1 bond lengths are in the range of 1.887-2.564 Å, and Cu2 bond lengths are in the range of 1.938-2.503 Å. BVS analysis showed that all three Cu ions exist in the +2 oxidation state.

The magnetic susceptibility of **16** was studied from 300 K to 1.8 K at 1000 Oe and 10000 Oe. At room temperature, the χT product is 1.18 cm³K/mol, which is slightly larger than the value (1.125 cm³K/mol) expected for three magnetically isolated Cu(II) ions with $S = \frac{1}{2}$ and $g = 2.0$. The χT value increases with decrease of temperature and reaches a maximum of 1.90 cm³K/mol at 6 K, and then drops down to 1.60 cm³K/mol at 1.8 K (Figure 4.21). The initial increase of the curve indicates ferromagnetic coupling between the Cu(II) centres in the complex. This is expected for a linear Cu(II)₃ unit like **16** with average Cu...Cu distance of 3.009 Å(2) and average Cu-O-Cu angle of 95.65°. The average Cu-O-Cu angle in this case is lower than 97.5°, which is considered to be reasonable for the ferromagnetic coupling.⁸¹

Fitting the experimental data was done using the following Heisenberg spin Hamiltonian⁸²:

$$H = -2J(S_1S_2 + S_1S_2')$$

where J is the exchange interaction between adjacent Cu(II) ions in the trimer, and S_i is the spin operator for each $S = 1/2$ Cu(II). The expression of the susceptibility is given below:

$$\chi_{trimer}(T) = \frac{Ng^2\mu_B^2}{4k_B T} \left\{ \frac{1 + \exp(2J/k_B T) + 10\exp(3J/k_B T)}{1 + \exp(2J/k_B T) + 2\exp(3J/k_B T)} \right\}$$

In order to fit the decrease of the χT product at low temperature, the inter-trimer interaction is introduced within the frame of the mean field approximation. In this approximation, the magnetic susceptibility expression becomes:

$$\chi = \frac{\chi_{trimer}}{1 - \frac{2zJ'}{Ng^2\mu_B^2} \chi_{trimer}}$$

where J' is the inter-trimer interactions and z is the number of neighbouring Cu_3 complexes. This model satisfactorily reproduces the experimental data in the temperature range of 300 K to 1.8 K. Fitting the data gave $J/k_B = 16.8$ K, $g = 2.08(1)$ and $zJ/k_B = -0.023(1)$ K (Figure 4.22).

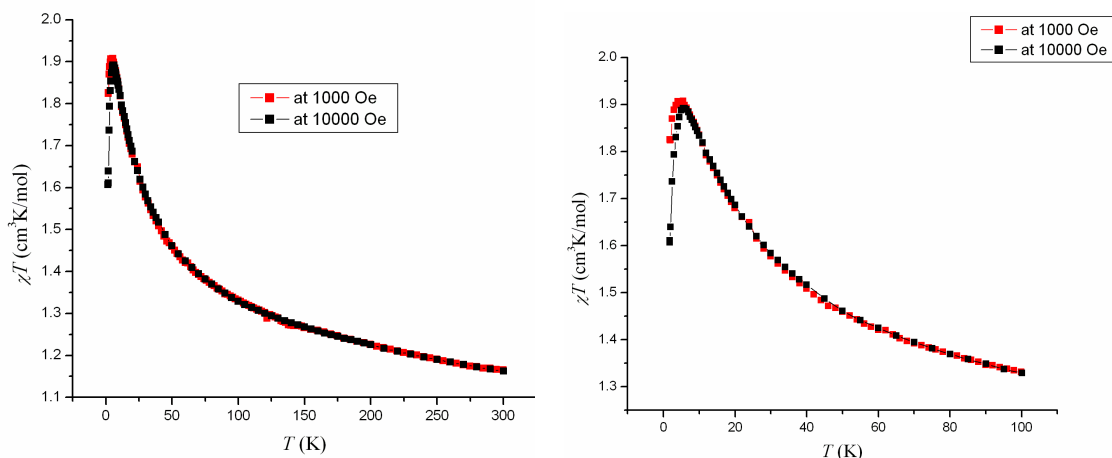


Figure 4.21 Temperature dependence of the χT product from 0 to 300 K (left) and from 1 to 100 K (right) for **16** at 1000 Oe and 10000 Oe.

The field dependence of the magnetisation at 1.8 K and 3 K is shown in Figure 4.23. There is a slow increase of the magnetisation, and it reaches a value of $3.03 \mu_B$ at 7 T. This is compatible with an $S = 3/2$ ground state, which is expected for three ferromagnetically coupled Cu(II) ions. Fitting the M versus H data with a simple $S = 3/2$ Brillouin function leads to a good agreement with the experimental results considering $g = 2.04(2)$. It is worth noting

that the g factor obtained by this fitting is consistent with the calculated value from the fitting of the χT product

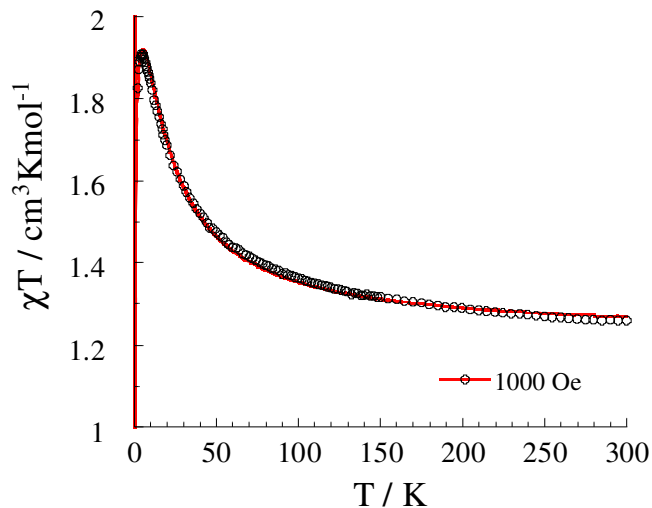


Figure 4.22 Temperature dependence of the χT product, and solid line is the fit.

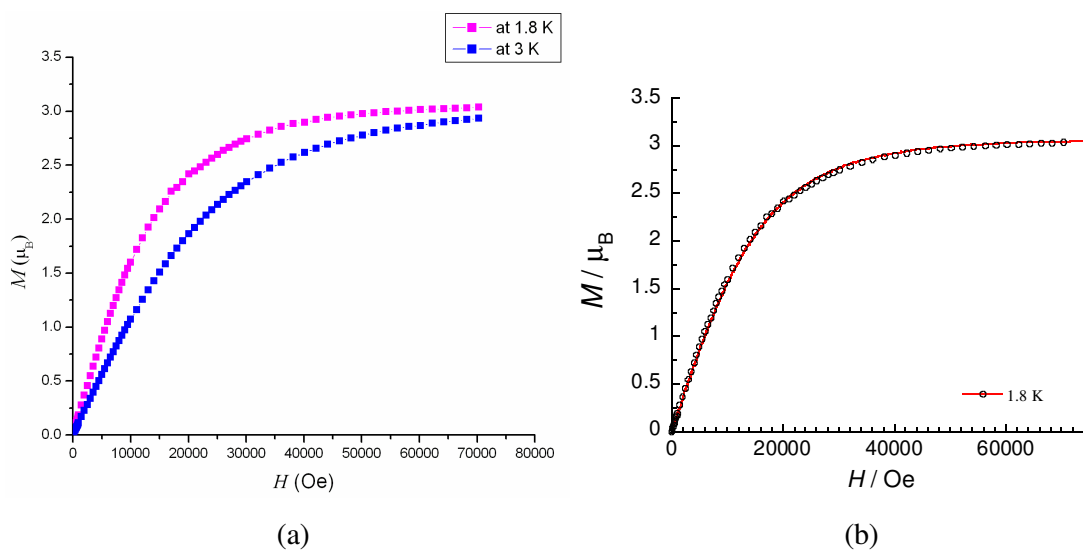


Figure 4.23 (a) Field dependence of the magnetisation for **16** at 1.8 K and 3 K.
(b) The plot of M versus H with the fitting and solid line is the fit.

4.7 Summary

The results demonstrate that different types of structures can be obtained using a combination of metal ions and coligands with 3-MeO-salH₂. In the trinuclear manganese compounds, the

carboxylate group was bridging in a *syn-anti* fashion, and mediated antiferromagnetic interactions between the metal centres. It was inferred that the addition of coligand helped to bind more metal centres, but it also changed the structure of the products. Variation of the solvent affected the structure of the complexes. When pyridine was used, a well-isolated trinuclear mixed-valence manganese complex (**13**) was obtained. The same reaction in methanol (**14**) replaced two of the coordinated pyridine molecules by water in the trinuclear Mn complex, and led to the formation of hydrogen bonds between the trinuclear units. Magnetic studies of compounds **13** and **14**, show that there are antiferromagnetic interactions between the metal centres. In compound **14**, however, there are additional intermolecular antiferromagnetic interactions between the trinuclear units. These trinuclear complexes are similar to the repeating units of the mixed-valence manganese coordination polymers synthesised from methyl-substituted salicylic acids described in chapter 3. These results indicate that the methoxy-substituted salicylic acid (3-MeO-salH₂) favours discrete and oligomeric structures probably as a result of steric effects.

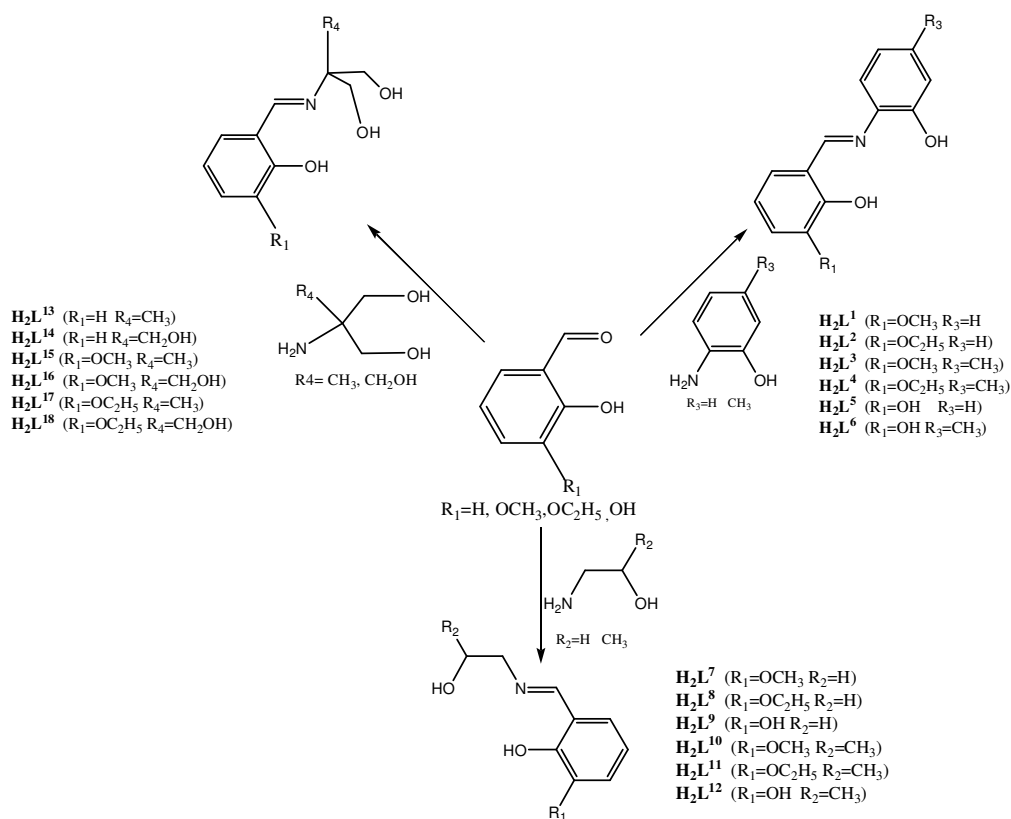
The use of the chelating and bidentate coligand, 2,2'-bipyridyl, along with 3-MeO-salH₂ and Mn(II) ions, favoured the formation of a triangular structure in **15**. This shows that under similar reaction conditions variation of the coligand can influence the structure. The same coligand with Cu(II) ions and 3-MeO-salH₂ gave a linear structure, with μ -oxo bridges from both carboxylate and phenoxy groups. The methoxy group of the ligand (3-MeO-salH₂) did not coordinate in the Mn complexes (**13**, **14**, **15**), but did coordinate with Cu(II) ions in complex **16**. The ferromagnetic coupling in the Cu₃ complex (**16**) is well-supported⁸¹ by the structural parameters, and this shows that the bridging modes of carboxylates in this complex favour ferromagnetic interactions. The strategy of varying the metal ions, coligands, solvents and reaction conditions made it possible to obtain a series of compounds which provide a system useful for understanding the coordination chemistry of salicylic acid ligands.

Chapter 5: Structure and magnetic properties of Schiff base complexes obtained using substituted salicylaldehydes

Molecules that can function as nanoscale magnets have potential applications in data storage devices. These molecules, called single molecule magnets (SMMs),⁸³ exhibit the classical properties of a macroscopic magnet below their blocking temperature,^{84,85} which is currently limited to about 5 K. They show slow relaxation of the spin reorientation along an axis because they have a high-spin ground state and an uniaxial magnetic anisotropy (D). The first discovered SMM, the Mn_{12} -acetate molecule, with a D value of -0.46 cm^{-1} (-0.66 K , $1 \text{ Kelvin} = 0.695 \text{ cm}^{-1}$) and $S = 10$ ground state, has an energy barrier of about 46 cm^{-1} (66 K).⁸⁶ After this discovery, a number of complexes have been classified as SMMs. These include derivatives of the original Mn_{12} species and other polynuclear complexes containing Mn, Fe, Ni, Co or lanthanides ions, such as Tb, Dy, Ho and Er.⁸⁷⁻⁹⁵ To understand the SMM behaviour better, the complexes that exist in structurally related families are of particular interest because the effect of structural variations on the magnetic properties can be investigated. With this in mind, ligand systems derived from Schiff-type condensations of various substituted salicylaldehydes with aromatic or aliphatic amines were used (Scheme 5.01). Deprotonation of these ligands affords tri-, tetra- and pentadentate species possessing the potential to bridge and chelate metal ions, increasing the stability of any resultant metal complex.

Schiff bases obtained from aromatic amines were synthesised, isolated in crystalline form and then characterised. Complexation reactions using the resultant ligands and transition metal ions were then pursued. Reactions using aliphatic amines led to Schiff base ligands in the form of oils. In this case, ligand synthesis and metal complexation was achieved in a one step reaction. The ligands can be modified in several ways. The aromatic and aliphatic amines containing hydroxyl groups were chosen in order to provide more donor atoms on the ligand. The number of alcohol arms on aliphatic amines can be increased, making the Schiff base ligand potentially polydentate. Different substituents on the benzene ring of salicylaldehyde

or on the aromatic amines can change the electronic environment of the ligand, thus modifying the structure, and the magnetic properties of the complexes. NMR spectra of the synthesised ligands were compared in order to determine the conformational structure of the ligand. This study helped to predict whether ligand modifications might affect the structure of the resulting metal complexes.



Scheme 5.01 Schematic representations of the reactions to produce the Schiff base ligands.

Several homometallic complexes were synthesised from the Schiff base ligands and Mn(II) salts. Manganese can exist in various oxidation states thus providing interesting magnetic properties. More specifically, Mn(II) has five unpaired electrons and can give a high ground state spin and Mn(III), being anisotropic, can give high D values. By combining different metal ions, which have versatile magnetic properties and different distributions of

electrons in the atomic orbitals, it should be possible to prepare molecules with larger magnetic anisotropy and higher spin ground states. In order to synthesise such systems a multinucleating ligand with two or more nonequivalent coordination sites should be chosen. Schiff base ligands containing imine and hydroxy groups should be suitable for synthesising heterometallic complexes. Ni(II) ions were chosen along with Mn(II) ions because Ni(II) has significant zero-field-splitting (D) and can give SMMs.⁹⁶ It was possible to obtain homometallic and heterometallic complexes exhibiting slow relaxation of the magnetisation. These complexes, which show SMM behaviour, possess a low spin ground state, but the high D values led to significant energy barrier.

5.1 Characterisation of the Schiff base ligands

The Schiff base ligands from $\mathbf{H}_2\mathbf{L}^1$ to $\mathbf{H}_2\mathbf{L}^6$ were synthesised at room temperature in MeOH by a condensation reaction of a substituted salicylaldehyde with an aromatic amine (1:1 ratio) (see Scheme 5.01). The reaction mixture was stirred for few minutes to give an intense orange solution. After partial evaporation of the solvent, the ligands could be separated from the solution after one or two days. They were characterised by elemental analysis, IR and NMR spectroscopy (see Chapter 7). Isolation of ligands prior to complexation reactions is often useful as it eliminates the presence of side products or the unreacted starting materials leading to pure compounds. In addition information on the structure of metal complexes can be obtained by comparing their IR or NMR spectra to that of the ligands and thus can help in the analysis of the complexes obtained.

In the ^1H NMR spectra of $\mathbf{H}_2\mathbf{L}^1$ ligand (in Figure 5.01), four singlet signals were present with chemical shifts at 3.81, 9, 9.9 and 14 ppm. In addition, there were multiple lines in the region of 6.8 to 7.4 ppm. The singlet at $\delta = 3.81$ ppm corresponds to the methoxy ($-\text{OCH}_3$) hydrogen atoms and the peaks in the region from $\delta = 6.8$ to $\delta = 7.4$ ppm correspond to aromatic protons (Ar-H). The singlet at $\delta = 9$ ppm is characteristic of the hydrogen atom from the imine group ($\text{H}-\text{C}=\text{N}-$). The appearance of this signal and disappearance of the aldehyde

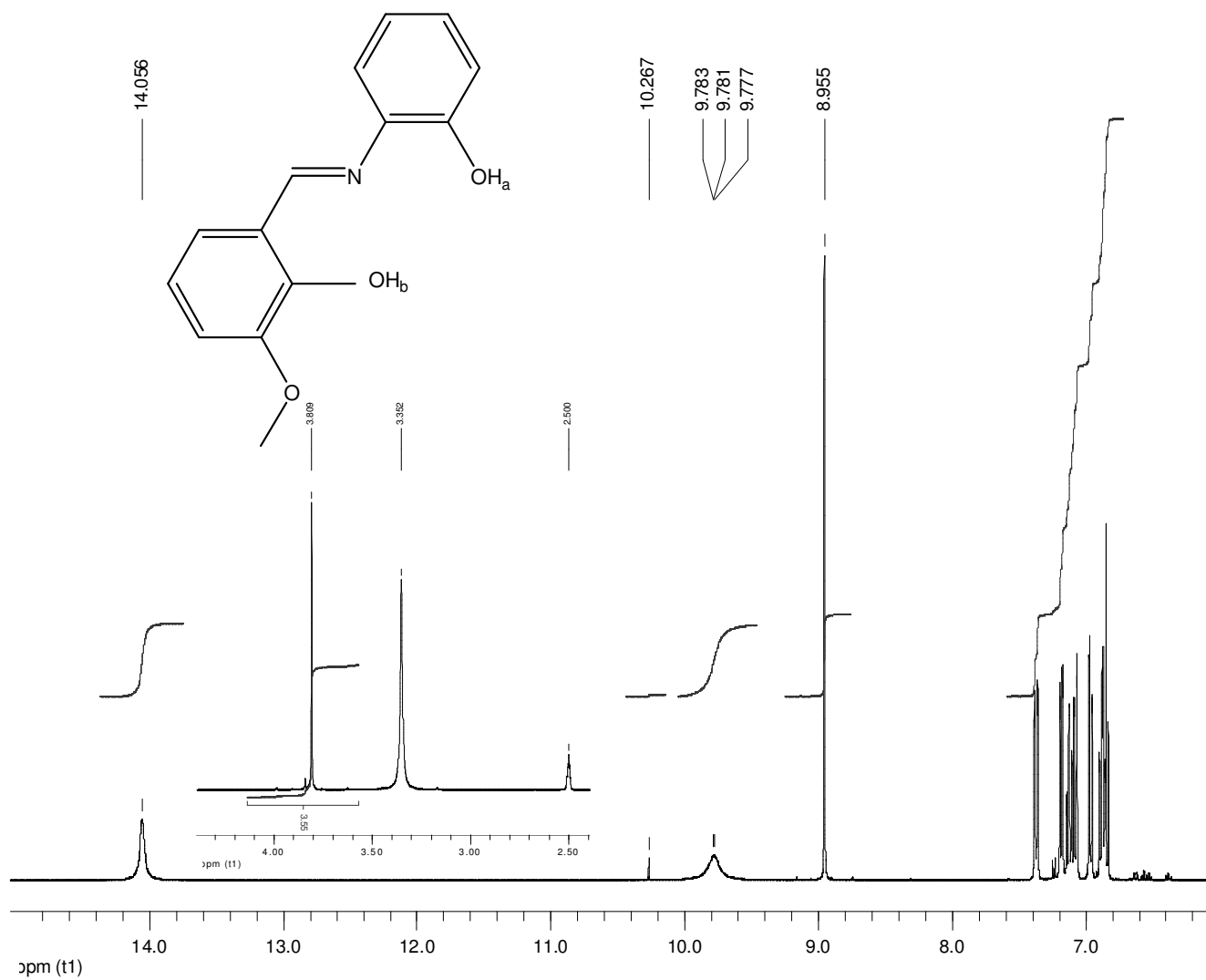


Figure 5.01 $^1\text{H-NMR}$ spectra of the ligand, H_2L^1

signal ($\delta = 10$ ppm) clearly indicates the formation of a Schiff base according to Scheme 5.01. The broad singlet at $\delta = 9.9$ ppm corresponds to the proton of the hydroxy ($-\text{OH}_a$) group, which belongs to the aminophenol part of the Schiff base. The singlet at $\delta = 14$ ppm corresponds to the proton of the hydroxy ($-\text{OH}_b$) group from the salicylaldehyde part of the Schiff base. The higher chemical shift at 14 ppm, and the broadening of the signal is a result of the hydrogen bond formed by the proton of the hydroxy group with the imine nitrogen atom. In the aromatic region of the ^1H NMR spectra, multiple lines indicate spin-spin splitting. For the assignment of the proton signals coming from the two different aromatic rings, the 2D-NMR techniques, $^1\text{H}^1\text{H}$ correlation spectroscopy (COSY) and $^1\text{H}^{13}\text{C}$ heteronuclear correlation (HETCOR) were carried out. Ligands $\mathbf{H}_2\mathbf{L}^2$ to $\mathbf{H}_2\mathbf{L}^6$ were characterized using the same approach mentioned above.

For ligand $\mathbf{H}_2\mathbf{L}^1$, the COSY was carried out in the region from δ 6.8 to δ 7.4 ppm (Figure 5.02). The cross-peaks indicate that proton B is spin-spin coupled to C and A, proton C is coupled to D and B, and proton G is coupled to E and J. In this way, the aromatic protons can be assigned to their respective signals. Further analysis and proof of the structure was obtained from the 2D heteronuclear chemical-shift correlation, $^1\text{H}^{13}\text{C}$ (HETCOR) NMR, indicating the proton-carbon connectivities (Figure 5.03).

The comparisons between some of the NMR spectra of the ligands are shown in Figure 5.04. Although the signals look similar, there are differences in the chemical shifts. This is expected due to the presence of different substituents (CH_3 , OCH_3 , OC_2H_5 , OH) at different positions on the aromatic rings of the ligands. The largest deviation can be seen for ligand $\mathbf{H}_2\mathbf{L}^5$, which is in accordance with the strong electron-accepting behaviour of the OH substituent ($\text{R}_1 = \text{OH}$) of 3-hydroxysalicylaldehyde. Strong influences can also be observed due to the methyl substituent ($\text{R}_3 = \text{CH}_3$) of 4-methylaminophenol in the ligand $\mathbf{H}_2\mathbf{L}^3$. These effects may lead to some modification in the electronic structure of the metal complexes, changing the force and nature of the magnetic interactions.

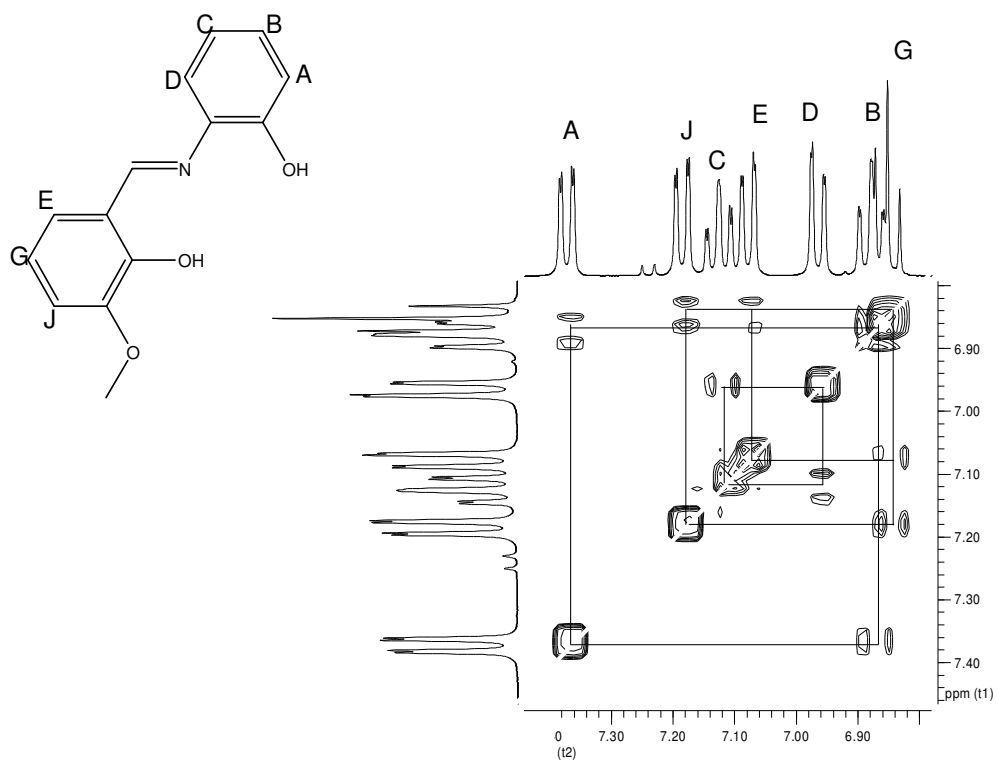


Figure 5.02 COSY 2D ^1H - ^1H NMR for the ligand, H_2L^1 , in DMSO from 6.8 to 7.4 ppm.

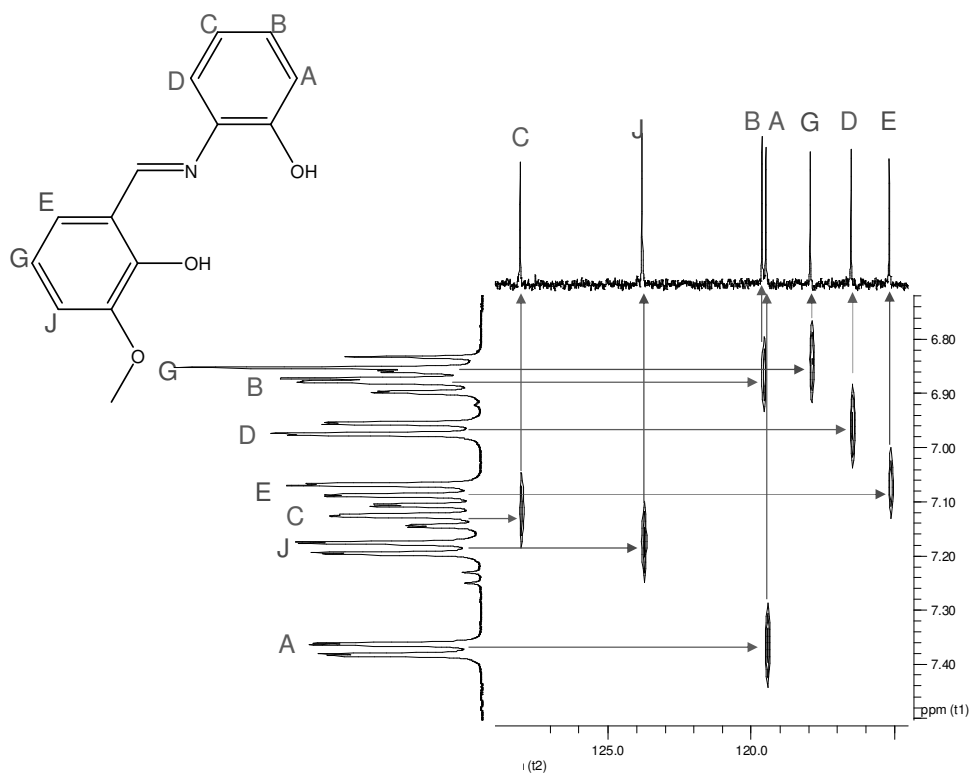


Figure 5.03 HETCOR ^1H - ^{13}C NMR for the ligand, H_2L^1 , in DMSO from 6.8 to 7.4 ppm. .

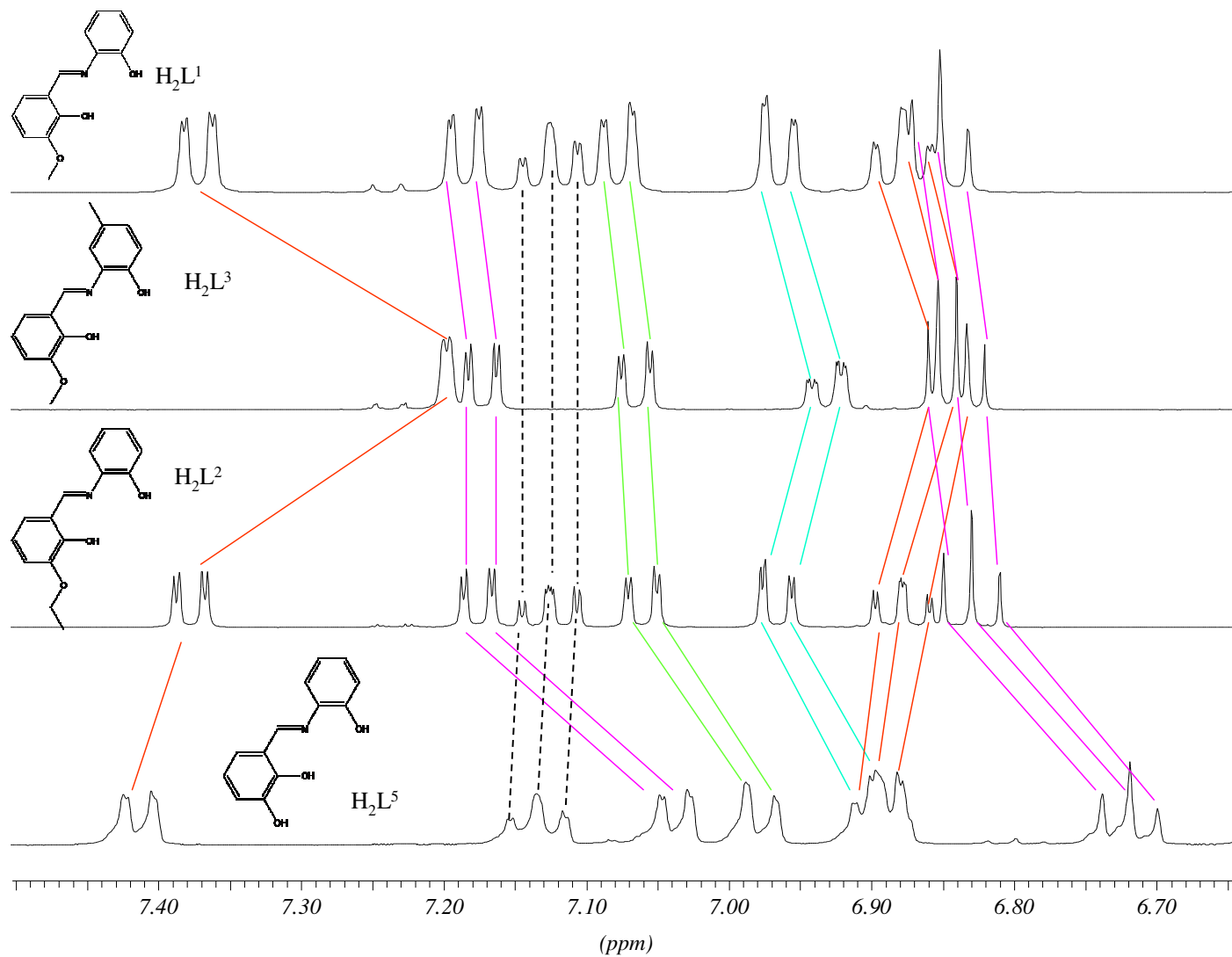


Figure 5.04 Comparisons between the ^1H NMR spectra of the ligands from 6.70 to 7.40 ppm using DMSO as solvent.

5.2 Metal complexes obtained with the Schiff base ligands.

Compounds were obtained via room temperature reactions of a Schiff base ligand and one or more metal salts in methanol. The base used was triethylamine. When a preformed ligand was used, it was first dissolved in methanol, and then the metal salt and base were added. When the ligand was synthesised *in situ*, the aldehyde and the amine were dissolved first in methanol. Completion of the ligand reaction was indicated by the appearance of a characteristic yellow colour to the solution. Only after the colour change were the base and metal salt added.

5.2.1 Structure and magnetic behaviour of $[\text{Mn}^{\text{III}}_2\text{Mn}^{\text{II}}(\text{L}^1)_2(\mu\text{-OAc})_2(\mu\text{-OMe})_2(\text{MeOH})_2]\cdot 2\text{MeOH}$, **17**

The trinuclear Mn complex, $[\text{Mn}^{\text{III}}_2\text{Mn}^{\text{II}}(\text{L}^1)_2(\mu\text{-OAc})_2(\mu\text{-OMe})_2(\text{MeOH})_2]\cdot 2\text{MeOH}$ (**17**), was synthesised from 3-methoxysalicylidene-2-aminophenol (H_2L^1) and Mn(II) acetate in methanol (Figure 5.05). It includes a central octahedral Mn(II) ion, Mn1, located on a crystallographic inversion centre flanked by two tetragonally distorted Mn(III) ions, Mn2. The Mn2 \cdots Mn1 separation is 3.132(5) Å.

The structure is linear with the Mn2-Mn1-Mn2' angle constrained to be 180°. The coordination environment of the central Mn1 is composed of two oxygen atoms (O5, O5') from two bridging acetates, two μ -phenoxo oxygen atoms (O3, O3') from the Schiff base ligand (L^1)²⁻, and two μ -alkoxo oxygen atoms (O4, O4') from two methoxy groups. The Mn1–O bond lengths are in the range of 2.168–2.279 Å and are in accordance with Mn(II)–O distances reported in the literature.⁶⁶ Mn2 is coordinated by the tridentate Schiff base (L^1)²⁻ ligand (N1, O1, O3), a μ -alkoxo oxygen (O4) from a methoxy group, one acetate oxygen (O6), and one methanol molecule (O7). The bond lengths of Mn2 are typical for Mn(III)⁶⁶ and it shows a Jahn-Teller elongation. The average equatorial bond length is 1.922(4) Å, while average axial bond length is 2.250(4) Å and the Jahn-Teller axes of the two Mn(III) centres

are parallel. The methanol molecules present as lattice solvent form hydrogen bonds with the coordinated acetate ($O5 \cdots H$ distance $1.764(3)\text{\AA}$) and methanol ($O21 \cdots H$ distance $1.783(3)\text{\AA}$) molecules. The packing diagram shows strong π - π stacking interactions between the aromatic rings of the two ligand molecules. The shortest distance between the planes of two parallel aromatic rings is about 3.5\AA (Figure 5.06).

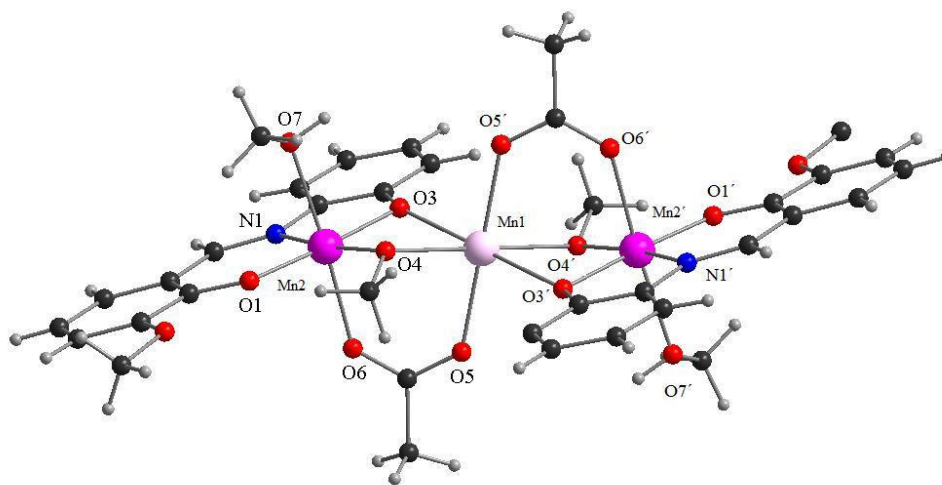


Figure 5.05 Structure of the trinuclear cluster in $[\text{Mn}^{\text{III}}_2\text{Mn}^{\text{II}}(\text{L}^1)_2(\mu\text{-OAc})_2(\mu\text{-OMe})_2(\text{MeOH})_2] \cdot 2\text{MeOH}$, **17**. Colour code: Mn(III), purple; Mn(II), pink; C, black; O, red; N, blue and H, grey.

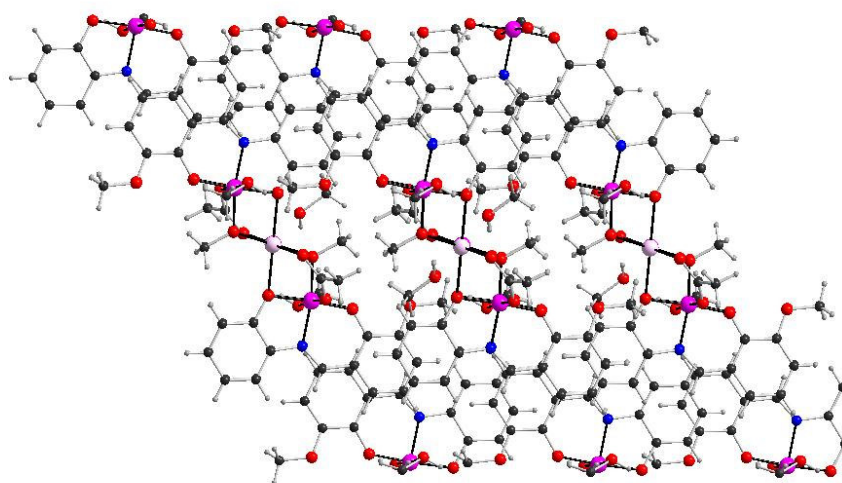


Figure 5.06 Packing diagram for **17**. Colour code: Mn(III), purple; Mn(II), pink; C, black; O, red; N, blue and H, grey.

The magnetic susceptibility of **17** was measured from 300 K to 1.8 K at 1000 Oe and 10000 Oe. At room temperature the χT product is $10.9 \text{ cm}^3\text{K/mol}$ (Figure 5.07). This value is in agreement with the value ($10.4 \text{ cm}^3\text{K/mol}$) expected for the presence of one Mn(II) ($S = 5/2$, $g = 2$) and two $S = 2$ Mn(III) ions ($S = 2$, $g = 2$). Upon decreasing the temperature, the χT product continuously decreases to reach $0.62 \text{ cm}^3\text{K/mol}$ at 1.8 K, indicating dominant antiferromagnetic interactions in the trinuclear complex.

The M versus H measurements were done at low temperatures from 8 to 1.8 K (Figure 5.07). At 7 T, the magnetic moment reaches a value of $3.05 \mu_B$. The absence of true saturation of the magnetisation suggests the presence of magnetic anisotropy and/or low-lying excited states.

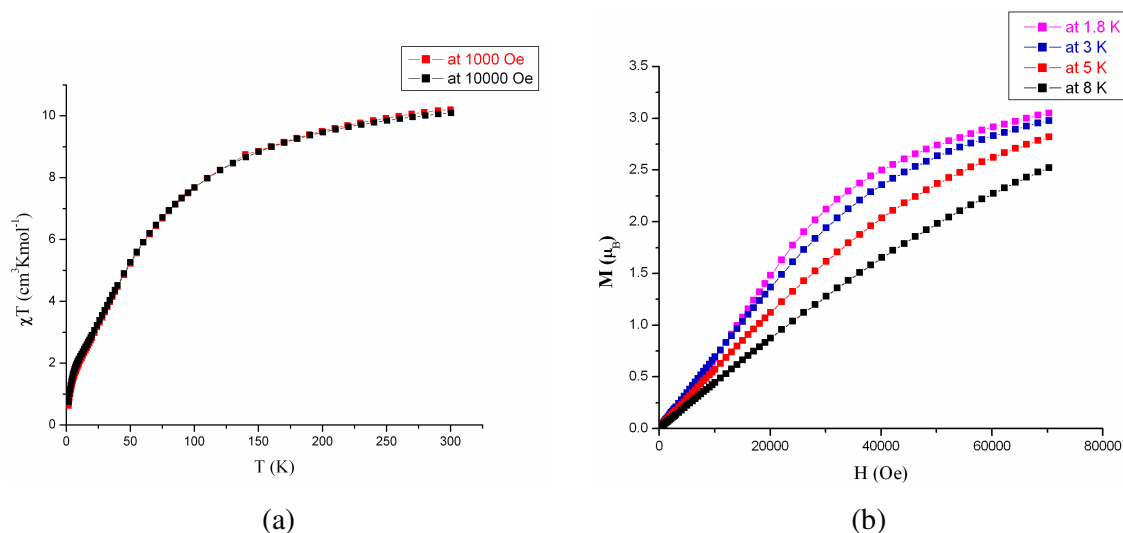


Figure 5.07 (a) Temperature dependence of χT for **17** at 1000 Oe and 10000 Oe.
(b) Field dependence of the magnetisation for **17** from 1.8 to 8 K.

The fitting of the magnetic data for this complex was done using the following Hamiltonian:

$$H = -2J_1(S_{1A}S_2 + S_{1B}S_2)$$

where J_1 is the exchange interaction in the trimer between adjacent Mn(II) and Mn(III) ions; $S_{1A} = S_{1B} = 2$ for Mn(III) and $S_2 = 5/2$ for Mn(II) ions. The parameter for the intermolecular interactions (zJ) was also considered. Fitting the data (Figure 5.08), gave $J_1 = -2.91(6) \text{ cm}^{-1}$,

$zJ = -0.36(6) \text{ cm}^{-1}$ and $g = 2.00$. The energy spectra shows that the lowest spin state is $3/2$. The energy levels, however, can be affected by the zero-field splitting of Mn(III) and the low-lying excited states could be occupied at 1.8 K.

The ac susceptibility measurements were carried out in zero dc field (Figure 5.09). The compound clearly displays in-phase (χ') and out-of-phase (χ'') signals below 3 K with frequency dependence, indicating slow relaxation of the magnetisation. This feature suggests that the compound might be a SMM.

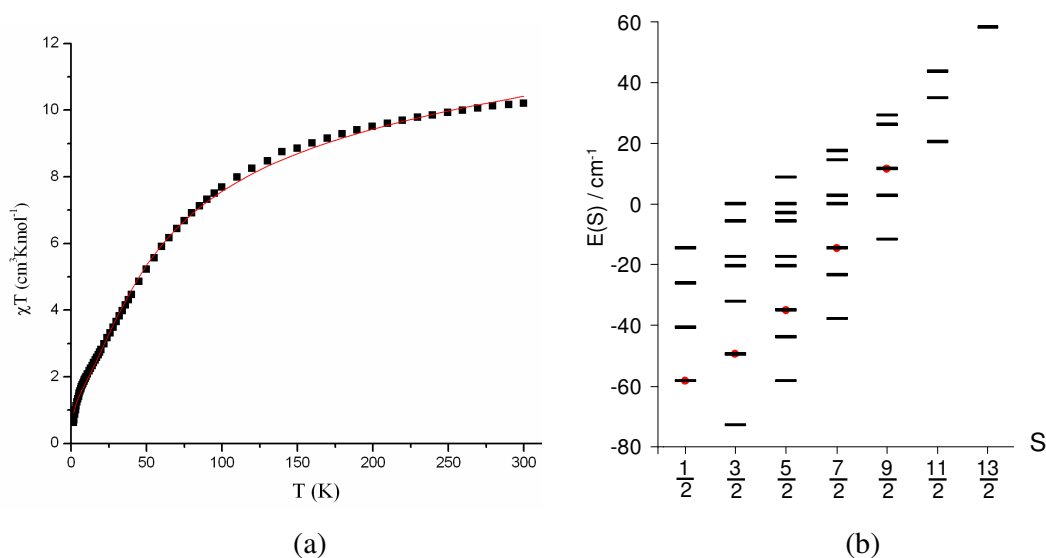


Figure 5.08 (a) Fitting of the χT versus T plot and solid line is the fit. (b) Energy spectrum for **17** and the red points indicate double-degenerate levels.

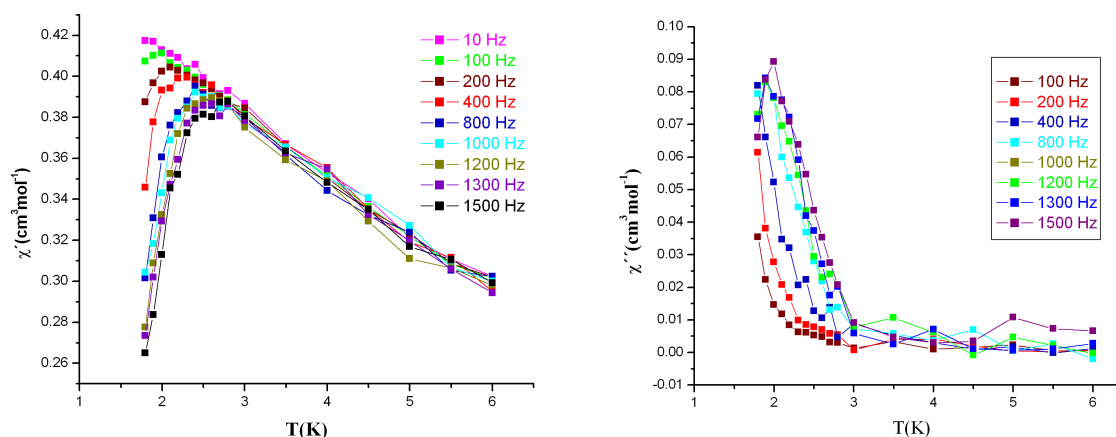


Figure 5.09 Temperature dependence of χ' and χ'' for **17** from 100 to 1500 Hz.

The characteristic time of the relaxation was extracted from the plots of χ'' vs T , and $\ln(\tau)$ versus $1/T$ was plotted. Fitting these data by the Arrhenius law (Figure 5.10), the characteristic SMM energy gap (U_{eff}) was estimated at 12.3 K with a pre-exponential factor (τ_0) of $2.7 \cdot 10^{-7}$ s. Since the exact ground state of the complex is not known, for the estimation of D value further studies (such as high field EPR) are in progress.

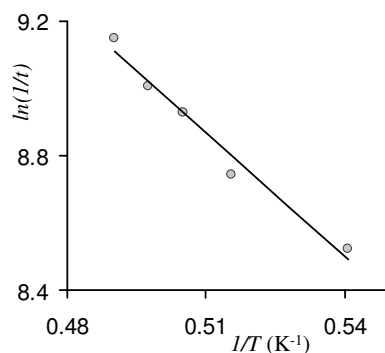


Figure 5.10 Arrhenius Plot of $\ln(\tau)$ versus $1/T$ for **17**.

5.2.2 Structure and magnetic behaviour of $[\text{Mn}^{\text{III}}_2\text{Mn}^{\text{II}}(\text{L}^3)_2(\mu\text{-OAc})_2(\mu\text{-OMe})_2]$, **18**

The trinuclear Mn complex, $[\text{Mn}^{\text{III}}_2\text{Mn}^{\text{II}}(\text{L}^3)_2(\mu\text{-OAc})_2(\mu\text{-OMe})_2]$ (**18**) (Figure 5.11), was synthesised from 3-methoxysalicylidene-(2-amino-4-methylphenol) (H_2L^3) and Mn(II) acetate in methanol. As in compound **17**, there is a central octahedral Mn(II) ion, Mn1, flanked by two Mn(III) ions, Mn2 and Mn2'. In this case, however, the Mn2-Mn1-Mn2' bond angle is $144.55(6)^\circ$ giving rise to a bent structure. In addition, the Mn2 is square pyramidal rather than octahedral.

The coordination environment of the central Mn1 is as in **17**. Mn2 is coordinated by one acetate oxygen (O3), a tridentate Schiff base (L^3)²⁻ ligand (N1, O4, O5) and a μ -alkoxo oxygen (O1) from a methoxy group. The Mn \cdots Mn separation is 3.082(3) Å. The bond lengths of Mn2 are typical for Mn(III),⁶⁶ and it exhibits a Jahn-Teller elongation. The average equatorial bond length is 1.912 Å, while the axial bond length is 2.129(2) Å.

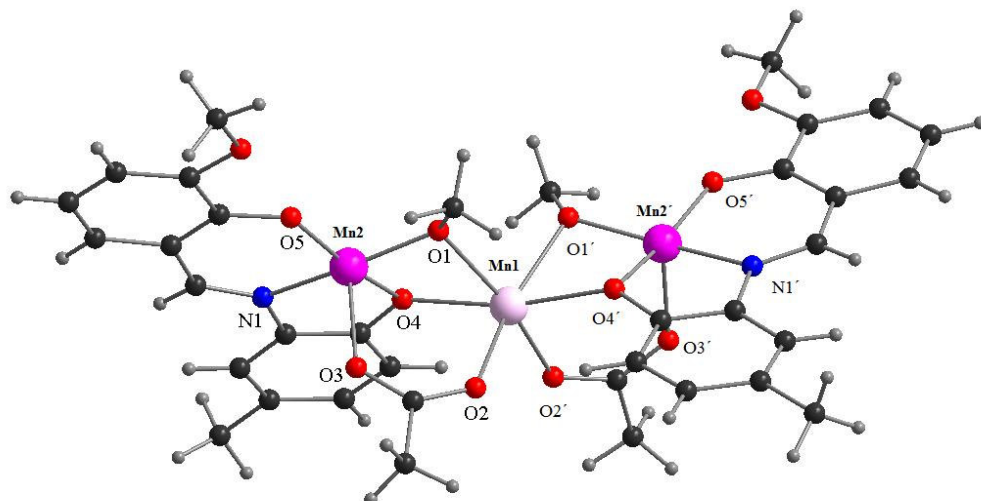


Figure 5.11 Structure of $[\text{Mn}^{\text{III}}_2\text{Mn}^{\text{II}}(\text{L}^3)_2(\mu\text{-OAc})_2(\mu\text{-OMe})_2]$, **18**. Colour code: Mn(III), purple; Mn(II), pink; C, black; O, red; N, blue and H, grey.

The magnetic susceptibility of **18** was measured from 300 K to 1.8 K at 1000 Oe and 10000 Oe. At room temperature the χT product is $8.36 \text{ cm}^3\text{K/mol}$ (Figure 5.12). This value is lower than the value ($10.4 \text{ cm}^3\text{K/mol}$) expected for the presence of one Mn(II) metal ion ($S = 5/2$, $g = 2$) and two $S = 2$ Mn(III) ions ($S = 2$, $g = 2$). Upon decreasing the temperature, the χT product continuously decreases to reach $0.75 \text{ cm}^3\text{K/mol}$ at 1.8 K, indicating dominant antiferromagnetic interactions in the trinuclear complex.

The M versus H measurements were done at low temperatures from 4 to 1.8 K (Figure 5.12). At 7 T, the magnetic moment reaches a value of $3.19 \mu_{\text{B}}$. A true saturation of the magnetisation is absent, indicating the presence of magnetic anisotropy and/or the presence of low-lying excited states, which might be populated when a field is applied.

Fitting the magnetic data using the same symmetrical trimer model as in **17** (Figure 5.13(a)), gave $J_1 = -4.23(2) \text{ cm}^{-1}$, $zJ = 0.67(2) \text{ cm}^{-1}$ and $g = 2.00$. The energy spectra shows that lowest spin state is $3/2$ (Figure 5.13(b)).

The ac susceptibility measurement in zero dc field shows a complete absence of an out-of-phase component above 1.8 K suggesting that there is no slow relaxation present in this compound. This might be due to the bent structure of this trinuclear complex. As a result, the

Jahn-Teller axes are not parallel, and the resultant tensorial sum of the D values decreases.⁹⁷ This can be compared with **17**, where the trinuclear complex has similar coordination environment, but the structure is linear. This leads to the parallel alignment of the Jahn-Teller axes leading to a higher resultant D value. The energy barrier to the thermal relaxation of the magnetisation depends on D , and it increases with the increasing D value. Interestingly, the slight ligand modification affected the structure, as well as the magnetic properties.

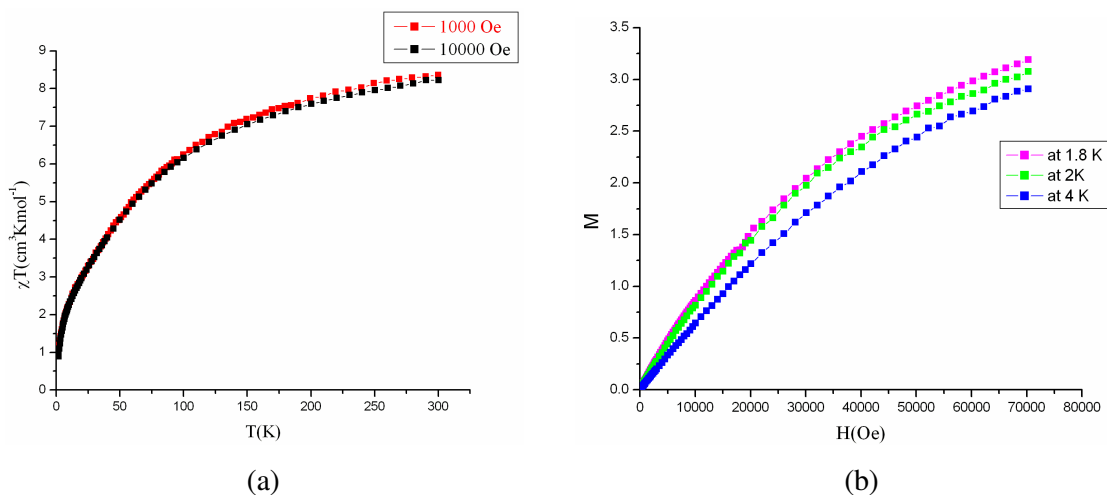


Figure 5.12 (a) Temperature dependence of χT for **18** at 1000 Oe and 10000 Oe. (b) Field dependence of magnetisation for **18** from 1.8 to 4 K.

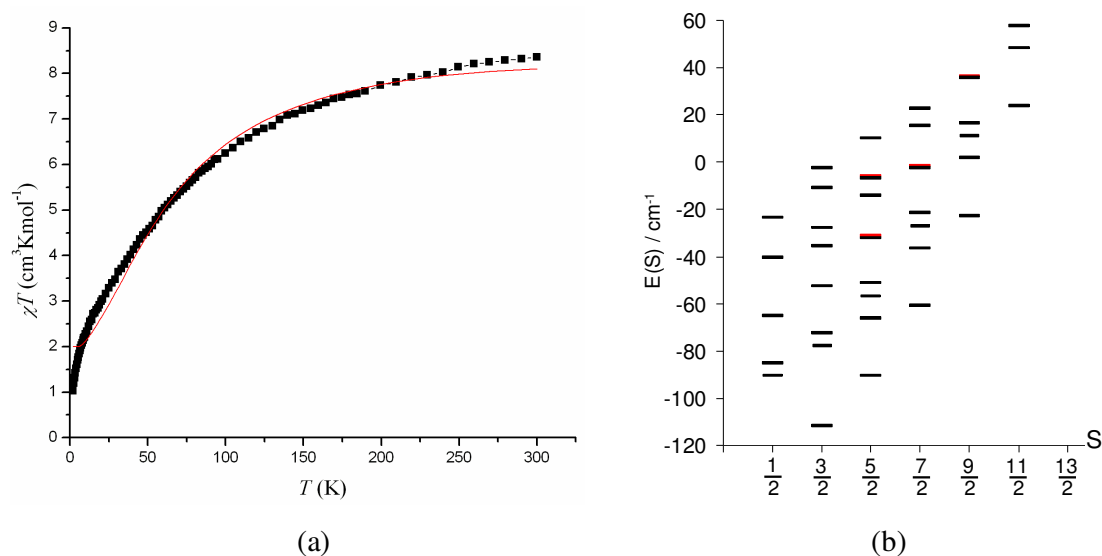


Figure 5.13 (a) Fitting of the χT versus T plot and solid line is the fit. (b) Energy spectrum for **18** and the red points indicate double-degenerate levels.

5.2.3 Structure and magnetic behaviour of $[\text{Mn}^{\text{III}}_2\text{Mn}^{\text{II}}(\text{L}^7)_2(\text{OAc})_4(\text{OH}_2)_2]\cdot\text{MeOH}$, **19**

The reaction of the Schiff base, 3-methoxysalicylidine-2-ethanolamine (H_2L^7 , formed *in situ*), and Mn(II) acetate in methanol gave $[\text{Mn}^{\text{III}}_2\text{Mn}^{\text{II}}(\text{L}^7)_2(\text{OAc})_4(\text{OH}_2)_2]\cdot\text{MeOH}$ (**19**). The molecular structure of **19** comprises of a trinuclear mixed-valence manganese complex (Figure 5.14). This includes a central octahedral manganese, Mn1, flanked by two Mn ions, Mn2 and Mn3. The Mn2-Mn1-Mn3 bond angle is $176.66(4)^\circ$ with the Mn1 \cdots Mn2 separation at $3.499(2)$ Å and the Mn1 \cdots Mn3 separation at $3.512(2)$ Å.

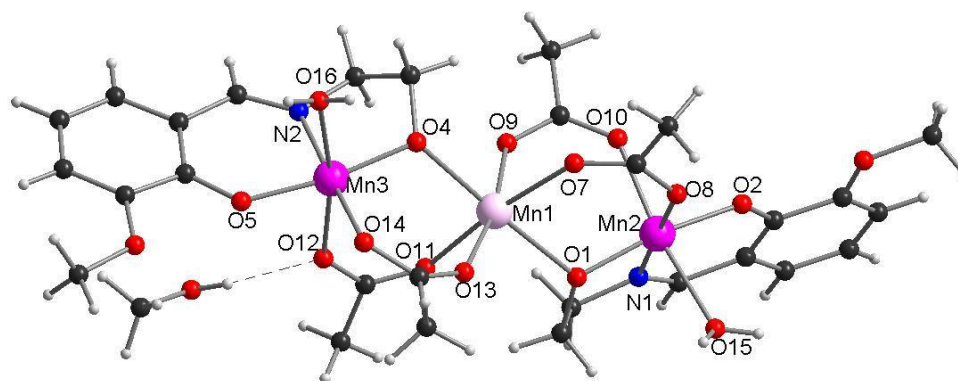


Figure 5.14 Crystal structure of compound $[\text{Mn}^{\text{III}}_2\text{Mn}^{\text{II}}(\text{L}^7)_2(\text{OAc})_4(\text{OH}_2)_2]\cdot\text{MeOH}$, **19**. Colour code: Mn(III), purple; Mn(II), pink; C, black; O, red; N, blue and H, grey. The hydrogen bond is shown by dotted line.

The octahedral coordination environment of the central Mn1 is composed of four oxygen atoms from four bridging acetates (O7, O9, O11, O13) and two μ -alkoxo oxygen atoms (O1, O4) from the Schiff base ligand $(\text{L}^7)^{2-}$. Mn2 and Mn3 are each coordinated by a tridentate Schiff base $(\text{L}^7)^{2-}$ ligand (Mn2: N1, O2, O1 and Mn3: N2, O5, O4), by two oxygen atoms (Mn2: O8, O10 and Mn3: O12, O14) from two bridging acetate groups and by one water molecule. The bond lengths of Mn2 and Mn3 are typical for Mn(III),⁶⁶ and show Jahn-Teller elongation. The average equatorial bond length for Mn2 is 1.932 Å and for Mn3 is 1.934 Å,

while the average axial bond length for Mn2 is 2.232 Å and for Mn3 is 2.243 Å. The Jahn-Teller axes of Mn2 and Mn3 are not parallel, being angled at about 112.5°.

There is one methanol molecule present as lattice solvent. The methanol hydrogen atom forms intramolecular hydrogen bond with acetate oxygen atom (O12...H distance is of 2.016(4)Å). The hydrogen atoms of the coordinated water molecule at Mn(III) in one trinuclear unit form intermolecular hydrogen bonds with an ethoxy oxygen (O...H distance of 2.023(7)Å) and an acetate oxygen (O...H distance of 2.049(8)Å) of another trinuclear unit. This gives rise to a 1D hydrogen-bonded chain (Figure 5.15).

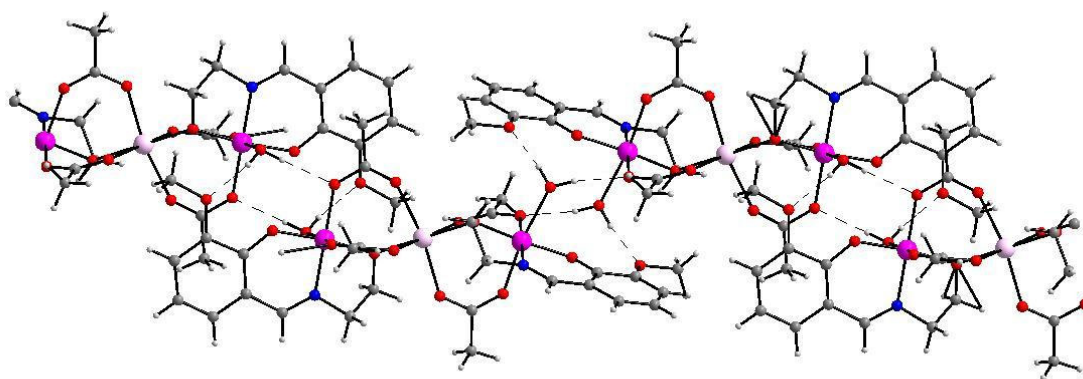


Figure 5.15 Hydrogen-bonded structure of compound **19**.

The magnetic susceptibility of **19** was studied from 300 K to 1.8 K at 1000 Oe and 10000 Oe. At room temperature the χT product at 1000 Oe is 8.22 cm³K/mol, which is lower than the value (10.4 cm³Kmol⁻¹) expected for the presence of one Mn(II) metal ion ($S = 5/2$, $g = 2$) and two $S = 2$ Mn(III) ions ($S = 2$, $g = 2$). Decreasing the temperature, the χT product continuously decreases to reach 0.53 cm³K/mol at 1.8 K, indicating dominant antiferromagnetic interactions in the trinuclear complex (Figure 5.16).

The M versus H measurements were performed from 4 to 1.8 K (Figure 5.16). At 7 T the magnetic moment reaches a value of 3.04 μ_B . A true saturation of the magnetisation is absent, indicating the presence of magnetic anisotropy and/or a field-induced population of

low-lying excited states. Using the the symmetrical trimer model of **17** and **18**, fitting the data gave $J_I = -4.92(2) \text{ cm}^{-1}$, $zJ = -0.87(2) \text{ cm}^{-1}$ and $g = 2.00$ (Figure 5.17(a)). The energy spectra shows that the lowest spin state is $3/2$ (Figure 5.17(b)).

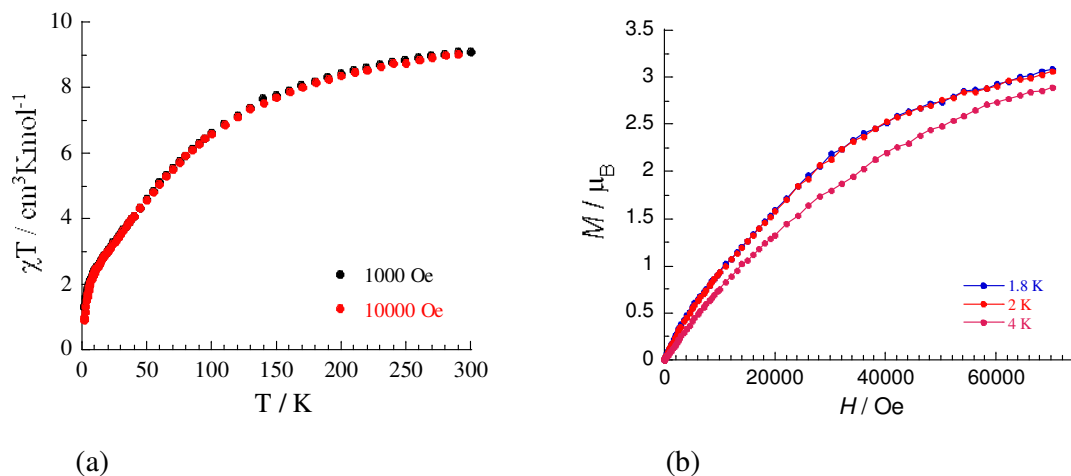


Figure 5.16 (a) Temperature dependence of χT for **19** at 1000 Oe and 10000 Oe. (b) Field dependence of magnetisation for **19** from 1.8 to 4 K.

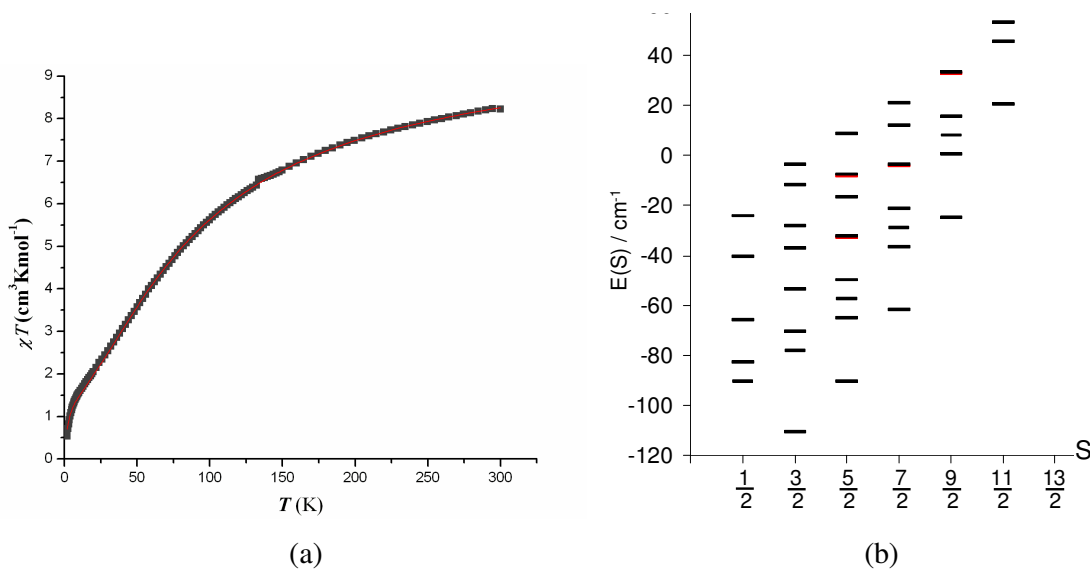


Figure 5.17 (a) Fitting of the χT versus T plot and solid line is the fit. (b) Energy spectrum for **19** and the red points indicate double-degenerate levels.

The complete absence of an out-of-phase component above 1.8 K indicates that the compound does not show slow relaxation. The structure is almost linear as in compound **17**,

but the bridging is different. In this case, one oxo and two carboxylate groups take part in the bridging, while one carboxylate and two oxo groups form the bridges in **17**. It could be possible that the bridging ligands play important role in the magnetic properties and SMM behaviour.

5.2.4 Structure and magnetic behaviour of $[\text{Mn}^{\text{III}}_3(\mu_3\text{-O})(\text{L}^{\text{11}})_3(\text{MeOH})_3](\text{ClO}_4)$, **20**

The reaction of the Schiff base, 3-ethoxysalicylidine-(1-amino-2-propanol) ($\text{H}_2\text{L}^{\text{11}}$, synthesised *in situ*), and Mn(II) perchlorate in methanol gave $[\text{Mn}^{\text{III}}_3(\mu_3\text{-O})(\text{L}^{\text{11}})_3(\text{MeOH})_3](\text{ClO}_4)$, **20**. The structure of **20** has three Mn(III) atoms which form an equilateral triangle with an oxygen atom (O1) in the centre (Figure 5.18). The central μ_3 -oxygen atom is displaced (0.861(3) Å) from the Mn_3 triangular plane.

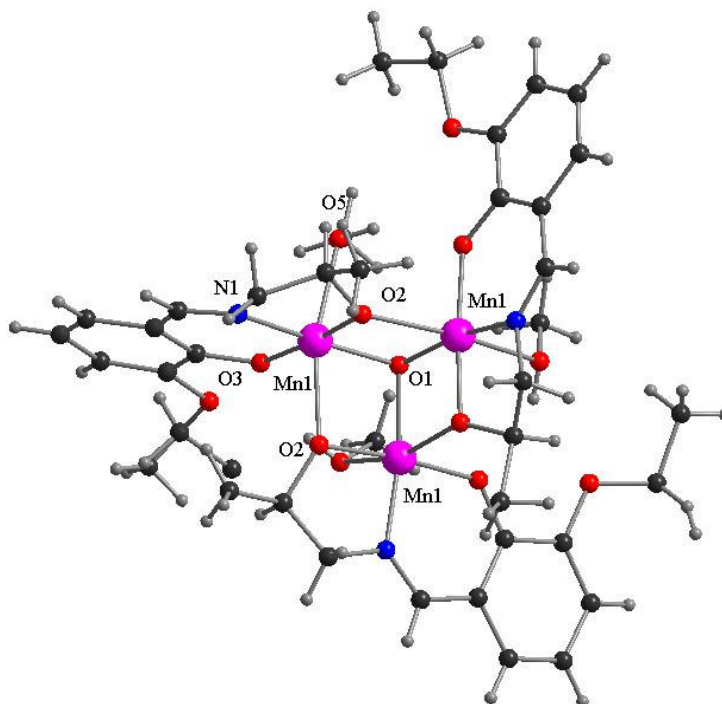


Figure 5.18 Structure of $[\text{Mn}^{\text{III}}_3(\mu_3\text{-O})(\text{L}^{\text{11}})_3(\text{MeOH})_3](\text{ClO}_4)$, **20**. Colour code: Mn(III), purple; Mn(II), pink; C, black; O, red; N, blue and H, grey.

The Mn···Mn distance is 2.968(4) Å. The Mn–(μ_3 -O) bond distance is 1.918(1) Å. Bonding from the tridentate Schiff base (L^{11})²⁻ ligand via N1, O3, O2, one oxygen from methanol molecule (O5), and one μ -alkoxo oxygen (O2) from another Schiff base (L^{11})²⁻ ligand complete coordination at each Mn(III) atom. The average axial bond length of Mn(III) ion (2.256(2) Å) is significantly longer than the average equatorial bond length (1.921(2) Å), and is expected due to Jahn-Teller distortion.

The magnetic susceptibility of **20** was measured from 300 K to 1.8 K at 1000 Oe and 10000 Oe. At room temperature the χT product is 8.69 cm³Kmol⁻¹ (Figure 5.19). This is close to the value (9.00 cm³Kmol⁻¹) expected for the presence of three $S = 2$ Mn(III) ions ($S = 2$, $g = 2$). Upon decreasing the temperature, the χT product continuously decreases to reach 4.97 cm³Kmol⁻¹ at 1.8 K, indicating dominant antiferromagnetic interactions in the trinuclear complex. The M versus H measurements were performed from 8 to 1.8 K (Figure 5.19). At 7 T, the magnetic moment reaches a value of 7.23 μ_B . As seen for compounds **17-19**, a true saturation of the magnetisation is absent in this case also.

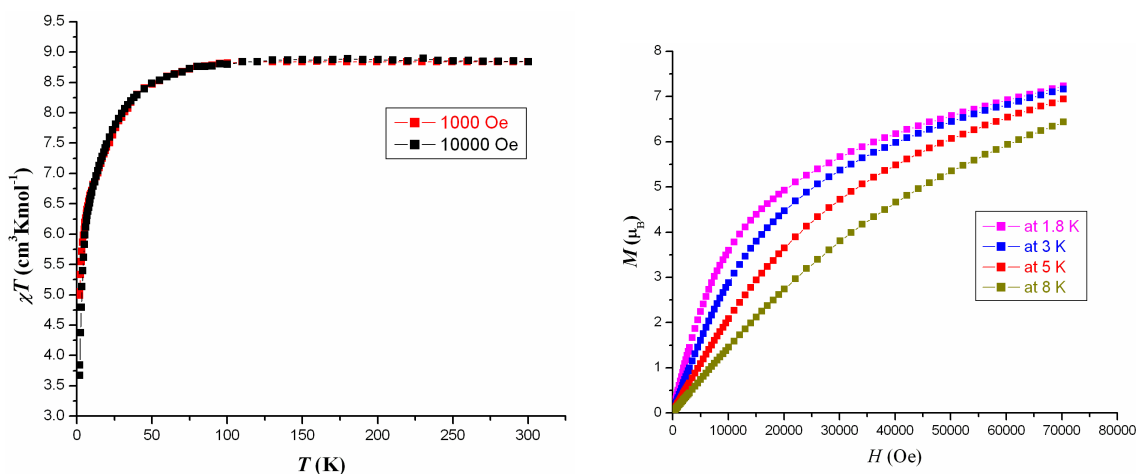


Figure 5.19 (a) Temperature dependence of χT for **20** at 1000 Oe and 10000 Oe.
(b) Field dependence of magnetisation for **20** from 1.8 to 8 K.

The magnetic data for this complex was simulated using the Hamiltonian:

$$H = -2J_{12}(S_1S_2 + S_2S_3) - 2J_{13}(S_1S_3)$$

where J_{12} and J_{13} are the exchange interactions in the triangle between adjacent Mn(III) ions and $S_1 = S_2 = S_3 = 2$ for Mn(III) centres. The theoretical curve ($J_{13} = -0.4 \text{ cm}^{-1}$, $J_{12} = -0.3 \text{ cm}^{-1}$, and $g = 2.0$) and the experimental curve are shown in Figure 5.20(a). The J values indicate presence of antiferromagnetic interactions between the spin carriers. Such behaviour is characteristic for spin frustration in a triangular system. The deviation of the theoretical value below 15 K is due to ZFS (zero-field splitting) contribution. The energy diagram show that the lower spin states ($S = 0$, $S = 1$ and $S = 2$) are very close to each other Figure 5.20(b). The relative distributions of this energy level can be disturbed by ZFS. From the value of χT at 1.8 K, it is expected that two spin states are populated ($S = 2$ and $S = 3$) at this temperature.

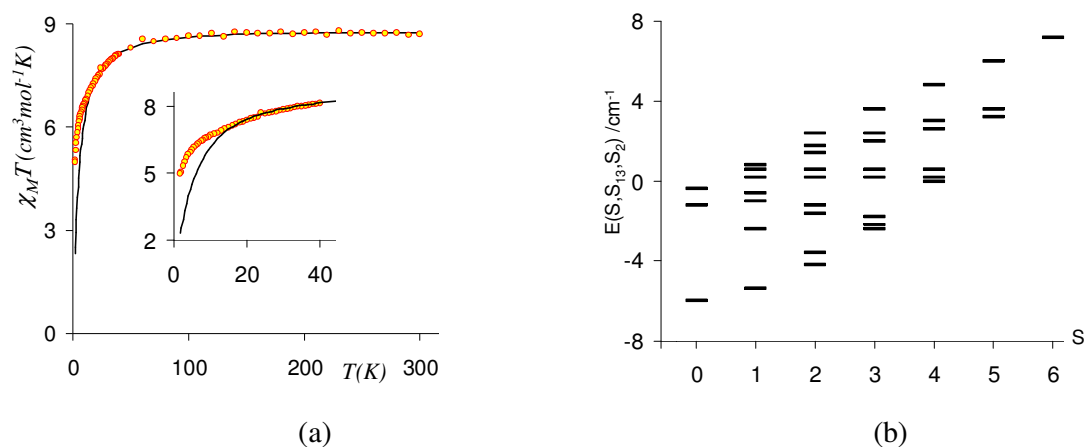


Figure 5.20 (a) χT versus T plot and solid line is the simulation. (b) Energy spectrum for **20**.

5.2.5 Structure and magnetic behaviour of $[\text{Mn}_2^{\text{III}}\text{Ni}_2^{\text{II}}(\text{L}^{14})_4](\text{X})_2$, $\{\text{X} = \text{CH}_3\text{COO}^-$ (**21**), $\text{X} = \text{Cl}^-$ (**22**)}

The complex, $[\text{Mn}_2^{\text{III}}\text{Ni}_2^{\text{II}}(\text{L}^{14})_4](\text{CH}_3\text{COO})_2$ (**21**), was synthesised in methanol by the reaction of manganese and nickel acetates with the Schiff base, salicylidine-(tris-(hydroxymethyl)-aminomethane), which was synthesised *in situ*. The structure of **21** comprises of a face-sharing double cubane core with two missing vertices, composed of two Mn(III) and two Ni(II) ions, as shown in Figure 5.21.

The two Ni(II) and two Mn(III) ions are located at the four corners of the incomplete double-cubane core and are bridged by two μ_2 -alkoxo, two μ_3 -alkoxo and two phenoxo bridges from the Schiff base ligand (L^{14})²⁻. The Mn(III) ions are positioned at the outer vertices of the double-cubane, and the Ni(II) ions are situated on the inner corners. The Mn(III) and Ni(II) ions are doubly bridged forming a dinuclear unit with two oxygen atoms (O2 and O6), and the two symmetrically related dinuclear cores are linked by two phenoxo (O1 and O1') and two alkoxo (O6 and O6') groups by μ_2 - and μ_3 - bridges, respectively.

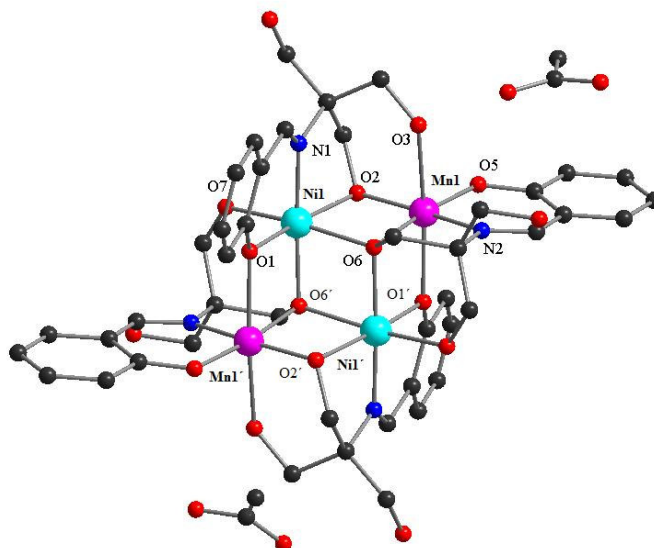


Figure 5.21 Structure of $[\text{Mn}_2^{\text{III}}\text{Ni}_2^{\text{II}}(\text{L}^{14})_4](\text{CH}_3\text{COO})_2$, **21**. Hydrogen atoms were removed for clarity. Colour code: Mn(III), purple; Ni(II), green; C, black; O, red and N, blue.

The Mn(III) ion is Jahn-Teller distorted with octahedral coordination geometry. The equatorial positions are occupied by three oxygen (O2, O5, and O6) and one nitrogen (N2) atoms, and the axial positions have a phenoxo oxygen (O1) and an alkoxo oxygen (O3) atom. The average axial bond length (2.269 Å) is significantly longer than the average equatorial bond length (1.930 Å) as expected for high-spin Mn(III) ions. The Ni(II) ion is also six-coordinate with the equatorial position occupied by four oxygen atoms (O1, O2, O6, O7),

whereas the apical positions are occupied by one nitrogen (N1) and one alkoxo oxygen (O6') atoms. The bond lengths of the Ni(II) ion are longer than those of the Mn(III) ion. Ni(II) ions have coordination bond lengths in the range of 1.974 Å – 2.144 Å. The M···M distances of Mn1···Ni1, Mn1···Ni1', Ni1···Ni1', Mn1···Mn1' pairs are 3.026(9) Å, 3.111(4) Å, 3.188(5) Å and 5.244(1) Å, respectively. The bridging angles between Ni(II) and Mn(III) ions are in the range of 94.43-102.20°, while two Ni(II) ions are bridged by the angle of 99.073(1)°.

The crystal packing of **21** is defined by multiple hydrogen bonds which involve the outer sphere acetate anion and the non-coordinated alcohol groups of the ligand. The hydrogen bonds connect the tetranuclear units forming a 3D hydrogen-bonded network (Figure 5.22).

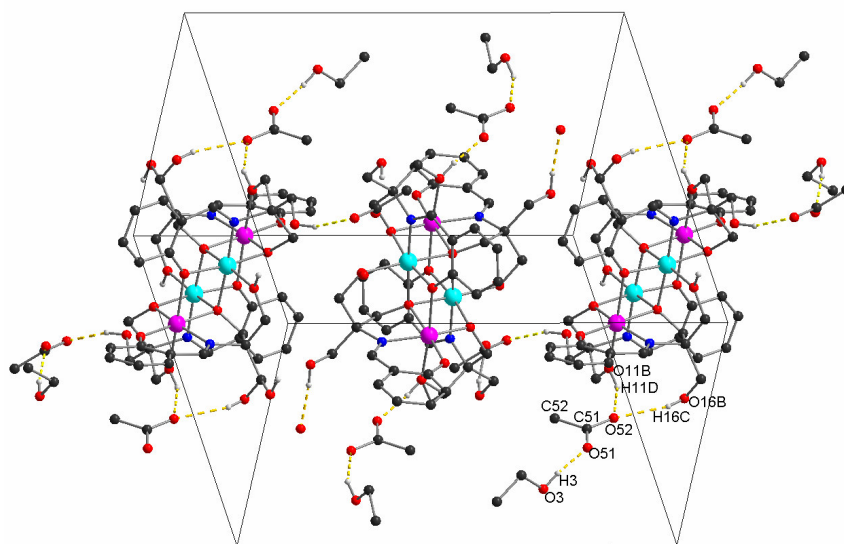


Figure 5.22 Hydrogen bonded 3D network in **21** (hydrogen and some disordered atoms are not shown for clarity).

Complex **22**, $[\text{Mn}_2^{\text{III}}\text{Ni}_2^{\text{II}}(\text{L}^{14})_4](\text{Cl})_2$, was synthesised using a similar reaction as for **21**, but in this case manganese and nickel chlorides were used. It also has the same incomplete double cubane core composed of two Mn(III) and two Ni(II) ions. The coordination environments of Mn(III) and Ni(II) are same as in **21**, but in this case the counter cations are two chloride ions. The M···M distances of Mn1···Ni1, Mn1···Ni1', Ni1···Ni1', Mn1···Mn1'

pairs in **22** are 3.009(2) Å, 3.111(2) Å, 3.144(3) Å and 5.251(5) Å, respectively. The bridging angles between Ni(II) and Mn(III) ions are in the range of 95.17-102.45°, while the two Ni(II) ions are bridged with the angle of 97.826(5)°.

Since the Mn_2Ni_2 core is almost the same in compound **21** and **22**, their magnetic properties are likely to be similar. Magnetic studies on **22** was, however, not possible as the yield was very low and the compound was not pure. The magnetic susceptibility of **21** was measured from 300 K to 1.8 K at 1000 Oe and 10000 Oe (Figure 5.23). At room temperature the χT product is 8.23 $\text{cm}^3\text{K/mol}$ which is in good agreement with the presence of two $S = 2$ Mn(III) ($g = 2$, $C = 3 \text{ cm}^3\text{Kmol}^{-1}$) and two $S = 1$ Ni(II) ($g = 2$, $C = 1 \text{ cm}^3\text{Kmol}^{-1}$) ions. When the temperature is lowered, the χT product continuously decreases to reach 2.05 $\text{cm}^3\text{Kmol}^{-1}$ at 1.8 K indicating the presence of antiferromagnetic interactions among the spin carriers. The field dependence of the magnetisation was performed at 1.8 and 4 K (Figure 5.23). The magnetisation approaches 4 μ_B at 7 T. The absence of magnetisation saturation suggests the presence of magnetic anisotropy, and probably a field-induced population of low-lying excited states in the system.

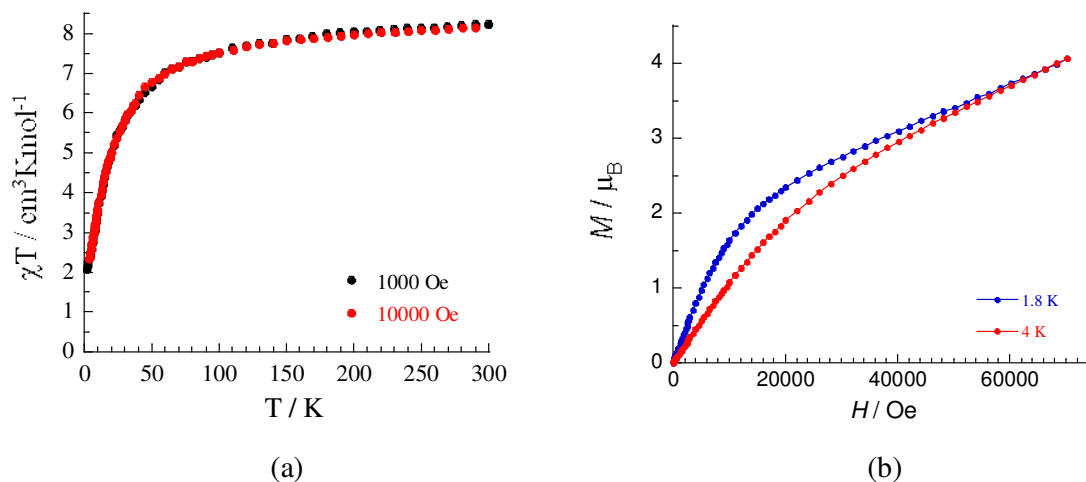


Figure 5.23 (a) Temperature dependence of the χT product for **21** at 1000 Oe and 10000 Oe. (b) Field dependence of the magnetisation for **21** at 1.8 K and 4 K.

The χT (0.1 T) and the magnetisation curves (at 1.8 and 4 K, up to 7 T) were fit using the following Hamiltonian:

$$H = -2J_1(S_1S_3 + S_1S_4 + S_2S_3 + S_2S_4) - J_2(S_3S_4) + D_{Mn}((S_{1z})^2 + (S_{2z})^2) + D_{Ni}((S_{3z})^2 + (S_{4z})^2) + g_{Mn}(S_1 + S_2) \cdot \mathbf{B} + g_{Ni}(S_3 + S_4) \cdot \mathbf{B}.$$

where 1 and 2 are the Mn(III) sites ($S = 2$), and 3 and 4 are the Ni(II) sites ($S = 1$). J_1 is the exchange coupling between the Mn(III) and Ni(II) ions, and J_2 is the coupling between the Ni(II) ions. D_{Mn} and D_{Ni} are the zero-field-splitting (ZFS) values of the Mn and Ni sites, respectively. The g factors were fixed to $g_{Mn} = 2.0$ and $g_{Ni} = 2.2$, which are typical values for the two ions.

The following four fitting scenarios were considered. J_1 and J_2 were always allowed to vary.

- (1) $D_{Mn} = D_{Ni} = 0$
- (2) $D_{Mn} \neq 0, D_{Ni} = 0$
- (3) $D_{Mn} = 0, D_{Ni} \neq 0$
- (4) $D_{Mn} \neq 0, D_{Ni} \neq 0$

The resulting fits for χT were always very good, so they are not shown for all the cases. After consideration of all the scenarios, the fits for the magnetisation curves at 1.8 and 4 K gave some clear conclusions. The curves at 1.8 K are always higher at low fields.

For the first scenario, $D_{Mn} = D_{Ni} = 0$, clear differences are visible in the χT curve at low temperatures (Figure 5.24). The magnetisation curves are poorly reproduced, which is expected considering that both Mn(III) and Ni(II) are generally known to exhibit substantial ZFS. J_1 is found to be in the order of -5 K, while J_2 is zero within the statistical significance.

For the scenario, $D_{Mn} \neq 0$ and $D_{Ni} = 0$, two stable and reproducible fits were obtained, and they are distinguished by $D_{Mn} < 0$ and $D_{Mn} > 0$ (Figure 5.25). The goodness-of-fit is, however, somewhat better for $D_{Mn} < 0$. Since Mn ions are Jahn-Teller elongated D is expected to be negative. J_1 is again found to be in the order of -5 K, while J_2 is very small and negative. In this particular case, the g factor (g_{Ni}) was also allowed to vary freely in the fit, yielding

only slight improvements with $g_{Ni} \approx 2.24$. This shows that fixing the g factor is a reasonable strategy here and that the value considered for the g factor is appropriate.

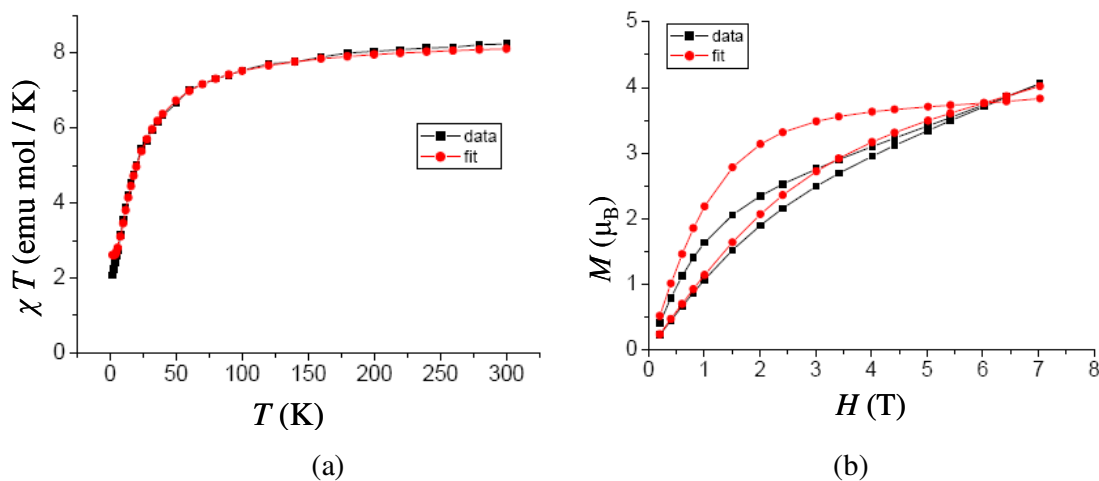


Figure 5.24 (a) Temperature dependence of the χT product for **21**, $D_{Mn}=D_{Ni}=0$.
(b) Field dependence of the magnetisation at 1.8 and 4 K for **21**. $J_1 = -5.4(2)$ K, $J_2 = -1.0(3)$ K and $D_{Mn}=D_{Ni}=0$.

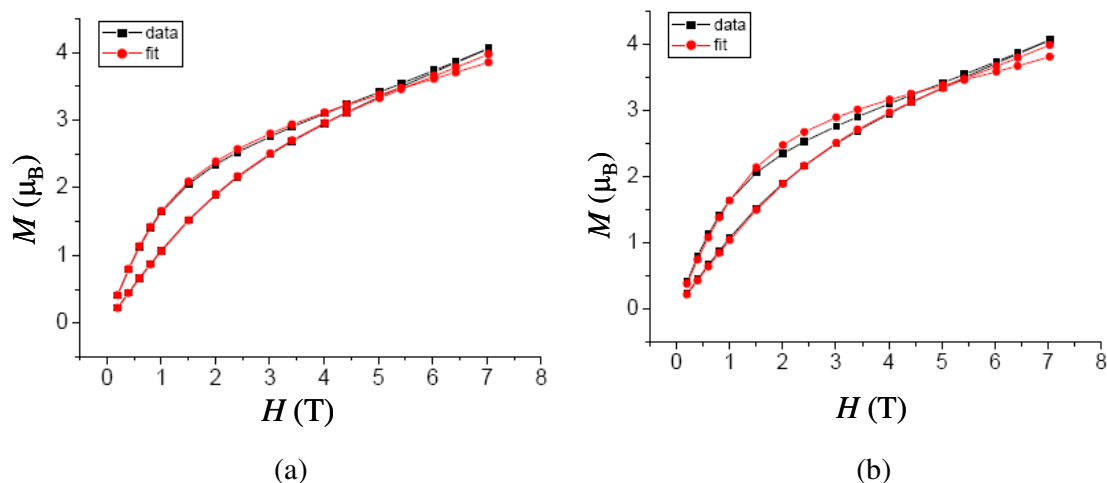


Figure 5.25 Field dependence of magnetisation at 1.8 and 4 K for **21**. (a) $J_1 = -5.18(5)$ K, $J_2 = -1.17(7)$ K, $D_{Mn} = -2.6$ K(1), $D_{Ni} = 0$. (b) $J_1 = -5.17(5)$ K, $J_2 = -1.7(7)$ K, $D_{Mn} = 3.4(2)$ K, $D_{Ni} = 0$.

For the scenario, $D_{Mn} = 0$ and $D_{Ni} \neq 0$, magnetisation curves are poorly reproduced. The values of D_{Ni} are not reasonable and not statistically significant (Figure 5.26). J_1 is again found to be in the order of -5 K, while J_2 is zero within statistical significance.

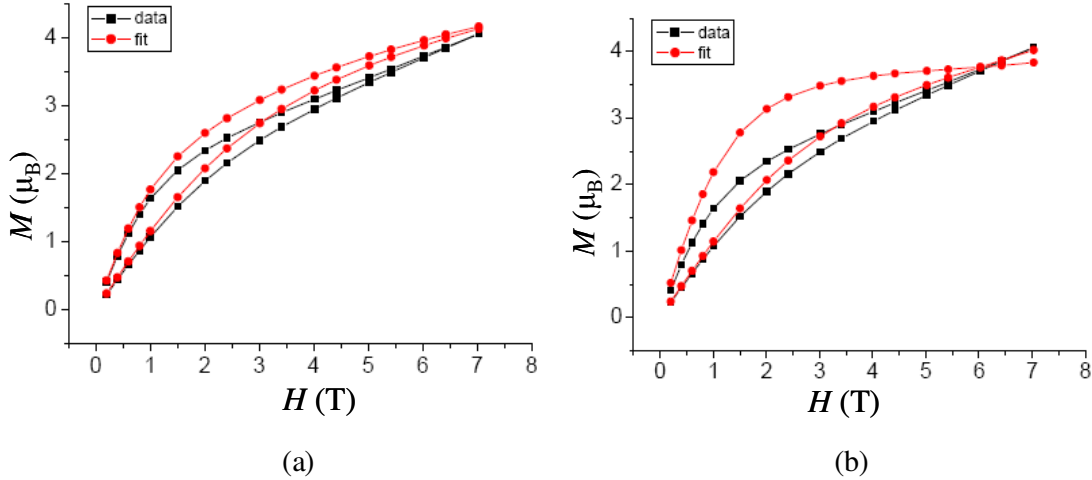


Figure 5.26 Field dependence of magnetisation at 1.8 and 4 K for **21**. (a) $J_1 = -6.5(2)$ K, $J_2 = -2.0(6)$ K, $D_{Mn} = 0$, $D_{Ni} = -73(7)$ K. (b) $J_1 = -5.4(2)$ K, $J_2 = -1(3)$ K, $D_{Mn} = 0$, $D_{Ni} = 1(2)$ K.

For the scenario, $D_{Mn} \neq 0$ and $D_{Ni} \neq 0$, two stable and reproducible fits were obtained (Figure 5.27), which are distinguished by $D_{Mn} < 0$ and $D_{Ni} > 0$ and by $D_{Mn} > 0$ and $D_{Ni} < 0$. These are the best results obtained which is not surprising, considering the fact that the model has the largest number of free parameters. The D values are reasonable in magnitude and are

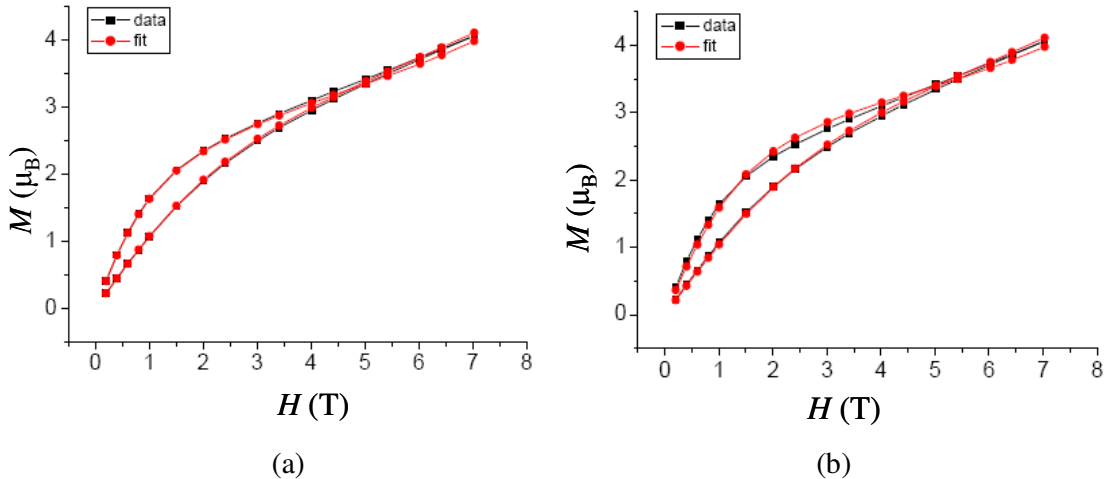


Figure 5.27 Field dependence of magnetisation at 1.8 and 4 K for **21**. (a) $J_1 = -5.3(5)$ K, $J_2 = 0.9(7)$ K, $D_{Mn} = -3.9(2)$ K, $D_{Ni} = 6.2(6)$ K. (b) $J_1 = -5.34(5)$ K, $J_2 = 0.2(8)$ K, $D_{Mn} = 4.1(2)$ K, $D_{Ni} = -7.0(8)$ K.

statistically significant. The goodness-of-fit is somewhat better for the $D_{Mn} < 0$ and $D_{Ni} > 0$ result. J_1 is again found to be in the order of -5 K. J_2 is very small and positive.

The conclusion drawn from the fits were that in all the cases except one, J_1 was found to be in the order of -5 K. Based on the best fit, the final J_1 can be considered to be -5.3(5) K. J_2 always had very small value, was either positive or negative, and thus can be considered close to 0(1) K. The zero-field splitting of Mn(III) cannot be ignored and is important because with $D_{Mn} = 0$ the fits were not good. From these plots, one can not clearly distinguish between positive or negative D_{Mn} , but the goodness-of-fit was slightly better for $D_{Mn} < 0$. The fits were weakly affected by the zero-field splitting of the Ni ion. Considering $D_{Mn} = 0$ gave unreasonable values for D_{Ni} , and inclusion of D_{Ni} did not improve the best-fit curves. Although D_{Ni} values in the order of 6-7 K appear reasonable in the fit of the fourth scenario, the magnitude of the ZFS of the Ni ions cannot be determined reliably.

The ac susceptibility measurements were carried out in a zero dc field. Below 3 K and around 1500 Hz, the compound displays in-phase (χ') and out-of-phase signals (χ''). A frequency dependence of χ' and χ'' signals was also detected (Figure 5.28), which is indicative of a slow relaxation of the magnetisation. This feature suggests that this compound is likely to be a SMM. The weakness of the signal is not surprising considering that the ground state spin of the complex is small.

From the zero-field data, it is not possible to obtain the characteristic relaxation time because there is no clear maximum in the χ'' versus T data above 1.8 K. As a result, a small dc field was applied at 1.8 K in order to remove any fast zero-field relaxation (Figure 5.29). It can be seen that the relaxation of magnetisation is strongly affected by this dc field. The relaxation mode, which was observed above 1500 Hz in a zero dc field, goes down to 58 Hz at 1600 Oe. This type of behaviour strongly suggests that this compound is a SMM, and the zero-field quantum tunneling of the magnetisation is still effective at 1.8 K.

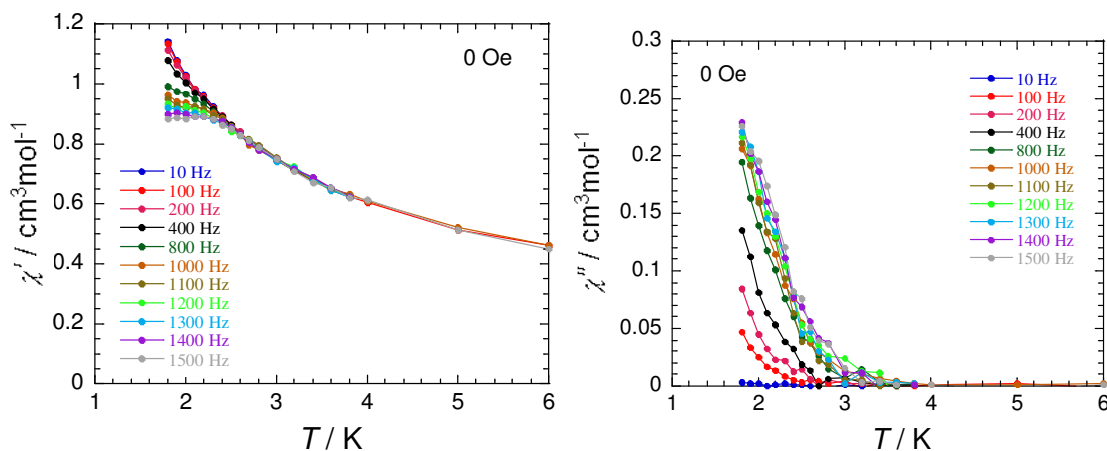


Figure 5.28 Temperature dependence of χ' and χ'' for **21** from 10 to 1500 Hz at zero dc field.

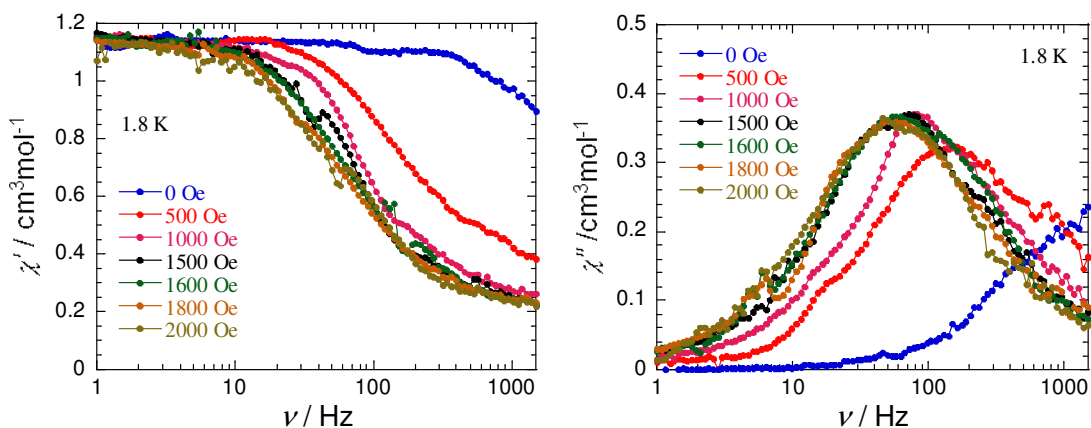


Figure 5.29 Frequency dependence of χ' and χ'' for **21** from 0 to 2000 Oe at 1.8 K.

In order to estimate the relaxation time (τ), ac susceptibility measurements were done at 1600 Oe. A clear maximum can be now detected on the plots of χ'' versus T and χ'' versus ν data (Figure 5.30). The τ versus $1/T$ graph was plotted using the relaxation times obtained from the out-of-phase susceptibility data. Fitting these data by the Arrhenius law, the characteristic SMM energy gap, Δ , was estimated to be 21.1 K with a pre-exponential factor (τ_0) of $1.5 \cdot 10^{-8}$ s (Figure 5.31). If we consider the spin ground state $S_T = 2$, this energy gap will lead to a D/k_B of -5.3 K.

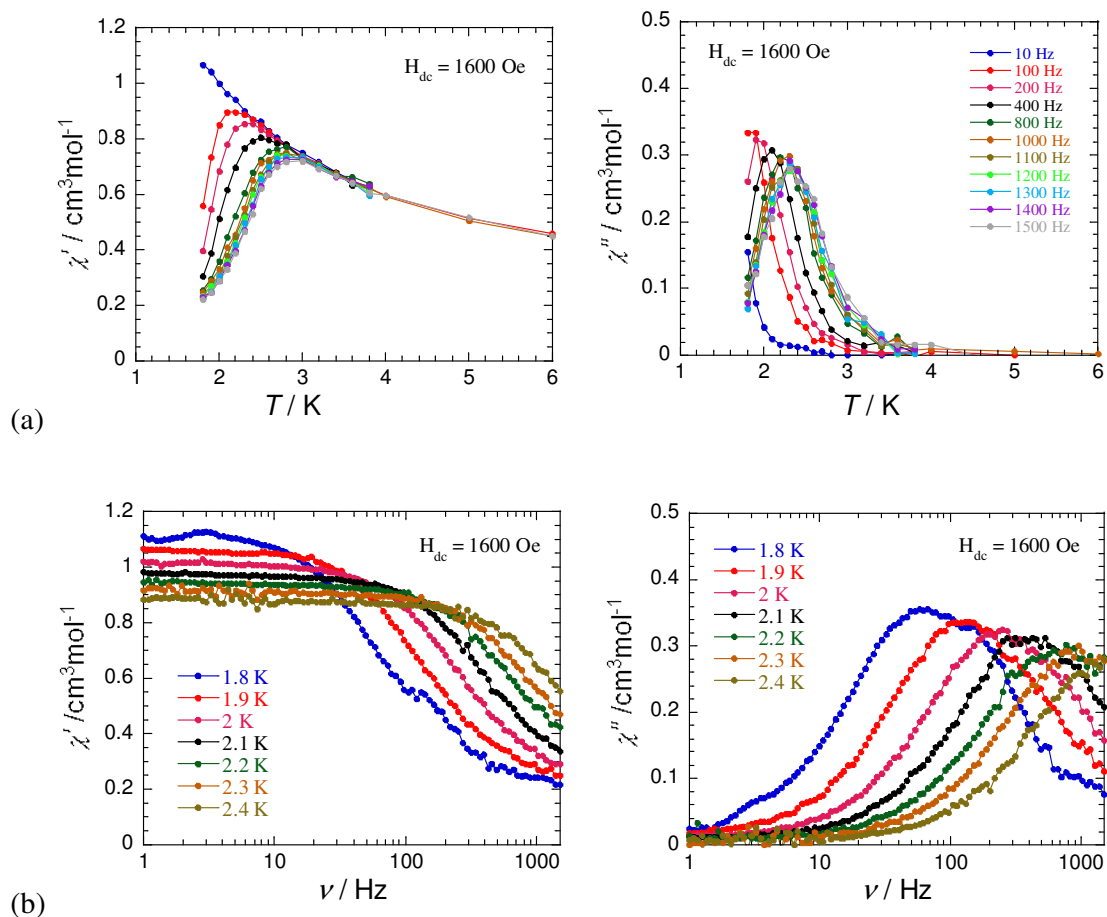


Figure 5.30 (a) Temperature dependence of χ' and χ'' from 10 to 1500 Hz at 1600 Oe dc field. (b) Frequency dependence of χ' and χ'' from 1.8 K to 2.4 K at 1600 Oe, for **21**.

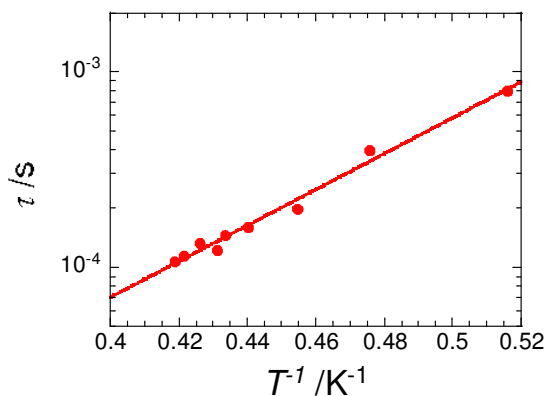


Figure 5.31 Arrhenius plot of τ vs $1/T$, for **21**.

The energy spectra at zero field were also calculated. The energy spectrum in Figure 5.32 was calculated for the parameter set with $J_1 = -5.3$ K, $J_2 = 0$ K, $D_{Mn} = -3.9$ K. The ZFS of Ni was allowed to vary between $D_{Ni} = 0$ and 6 K. It was observed that energy spectra for both the D_{Ni} values were similar. Apparently, the energy spectrum and the ground state, are not much affected by ZFS of the Ni ion. This is the reason that the magnetisation fits were also not affected by D_{Ni} . Figure 5.33 shows the energy spectrum for $J_1 = -5.3$ K, $J_2 = 0$ K, $D_{Mn} = 4.1$ K and $D_{Ni} = 0$ K. For this case too, the energy spectrum is almost independent of the value of D_{Ni} .

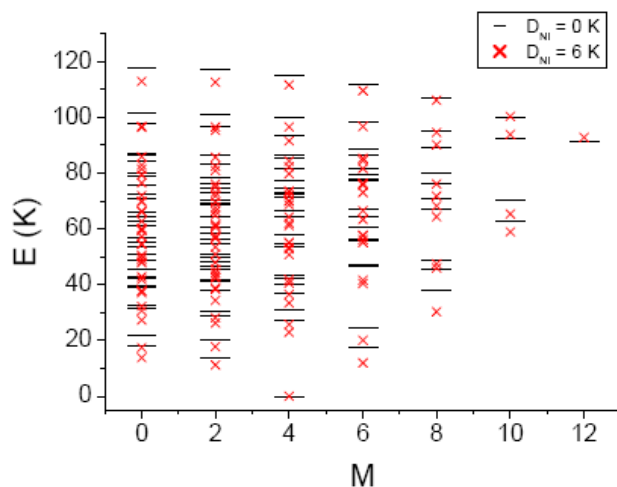


Figure 5.32 Energy spectrum of **21** for $D_{Mn} = -3.9$ K, $D_{Ni} = 0$ or $D_{Ni} = 6$ K.

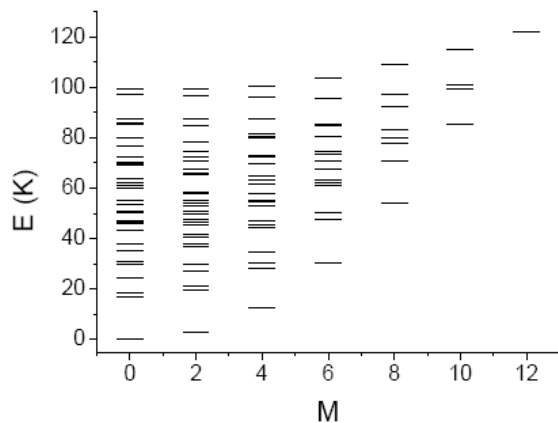


Figure 5.33 Energy spectrum of **21** for $D_{Mn} = 4.1$ K and $D_{Ni} = 0$ K.

For the first case, the ground state is $M = \pm 4$ ($M = 2S$), with an energy gap of about 10 K between the ground state and the next higher-lying state. For the second case, the ground state is $M = 0$, this is so even if a large easy-axis $D_{Ni} = -7$ K is included. Only the negative D_{Mn} scenario is consistent with the observation of a slow magnetic relaxation at low temperatures. The low-lying states can not be characterized by a spin multiplet, and the giant-spin model fails completely. This is because the ZFS parameters are not small compared to the J values, so the giant-spin model does not apply and S -mixing effects are very significant. In fact, the S -mixing is so strong that the concept of multiplets breaks down completely, except for the two lowest $M = \pm 4$ levels, which can be described by an effective spin $-1/2$. In conclusion, **21** has an $S = 2$ spin ground state with a high negative D value ($D/k_B = -5.3$ K), and is a SMM with a magnetisation reversal barrier of $|D|S_z^2 = 21.1$ K.

5.3 Summary

In this chapter, several types of trinuclear mixed-valence manganese complexes **17-20** as well as heteronuclear Mn-Ni complexes **21, 22** have been synthesised with tri-, tetra- and pentadentate Schiff base ligands. It is evident from the deviations in the NMR spectra of the ligands that the electronic environments of the metal complexes are changed by ligand modifications (**17, 18**). The presence of a methyl substituent on the aromatic ring of the ligand **H₂L³**, salicylidene-(2-amino-4-methylphenol), caused a deviation in the chemical shifts compared to the spectra of the ligand without the substituent **H₂L¹**, salicylidene-(2-amino-phenol). Compounds **17** and **18** were synthesized using **H₂L¹** and **H₂L³**, respectively. On comparing their magnetic properties, **17** behaves as a single molecule magnet and **18** does not. The ligand modification led to changes in the structures of the complexes, such that **17** is linear and **18** is bent. The bulkier methyl substituent on the aromatic ring favoured the formation of a bent structure. The SMM behaviour in the linear structure is likely to result from the parallel alignment of Jahn-Teller axes giving higher total anisotropy on the molecule.

The use of aromatic and aliphatic amines gave similar structures in **17** and **19**, but the bridging modes between the metal centres were different giving different magnetic properties. It is also worth noting that using additional bridging ligands along with Schiff base ligands can change the structure, thus compound **19** is linear with bridging acetate groups, whereas in **20** where bridging acetate groups are absent the structure is triangular. Both have antiferromagnetic interactions between the spin carriers, but in **20** there is spin frustration as expected from the triangular structure. In this way, the investigation of a family of complexes can help to compare the effects of small structural variations on magnetic properties.

Heterometallic complexes were targeted because interesting magnetic behaviour can be expected due to the interplay of two different metal ions. Increasing the number of alcohol arms on the aliphatic amines helped to increase the nuclearity and also led to the binding of different metal ions. Compounds **21** and **22**, both with a tetranuclear $\text{Mn}^{\text{III}}_2\text{Ni}^{\text{II}}_2$ core, were synthesised. Magnetic measurements of complex **21** indicate the presence of dominating antiferromagnetic interactions within the heterometallic core. Although it possesses a small ground state spin of $S = 2$, the very high anisotropy ($D/k_B = -5.3$ K) leads to an energy barrier to spin reversal and it behaves as a single molecule magnet. This represents the highest negative D value seen in a cluster compound.⁹⁸ Previously, most efforts had been devoted to the synthesis of compounds with large spin through exchange interactions, which are more predictable than the magnetic anisotropy parameter D . In future however, increasing the magnetic anisotropy in high-nuclearity clusters with a high-spin ground state may be the key in obtaining very high energy barriers. The Schiff base ligands seem to impart high magnetic anisotropy to these complexes and they would be suitable for synthesizing further similar systems. A systematic study of the effect of structural variation on the D values lead to a better understanding of this parameter and may help in synthesising SMMs with larger energy barriers.

Chapter 6: Conclusions

This research has produced a variety of compounds exhibiting a wide range of structural motifs, such as 3D metal organic frameworks and discrete metal clusters. They gave scope to study different magnetic behaviour and helped to establish a magneto-structural correlation.

In Chapter 3, the synthesis, characterisation and magnetic properties of four novel three-dimensional (3D) mixed-valence metal organic frameworks, $[\text{Mn}_3(3\text{-Me-sal})_4(\text{py})_4]$ (**1**), $[\text{Mn}_3(4\text{-Me-sal})_4(\text{py})_4(\text{MeOH})] \cdot (\text{H}_2\text{O})$ (**2**), $[\text{Mn}_3(5\text{-Me-sal})_4(\text{py})_4(\text{H}_2\text{O})_2] \cdot (\text{MeOH})$ (**3**) and $[\text{Mn}_3(3\text{-Me-sal})_4(4\text{-Me-py})_4]$ (**4**), and one coordination polymer $\{[\text{Mn}_2(4\text{-Me-sal})_2(4\text{-Me-py})_2(\text{H}_2\text{O})_2(\text{MeOH})_2][\text{Mn}(4\text{-Me-sal})_2(4\text{-Me-py})_2]\}$ (**5**) were discussed. The compounds were synthesised by room temperature reactions of Mn ions, methyl substituted salicylic acids and coligands. Examining the topology of the 3D frameworks of compounds **1-4** shows that they are based on diamondoid networks, in which each Mn(II) centre is connected to four Mn(III) centres forming a tetrahedral node. The Mn(III) centres form two-fold nodes. While the coordination geometry of Mn(II) varies, that of Mn(III) is always distorted octahedral. The magnetic interactions between Mn(II) and Mn(III) centres are antiferromagnetic inducing a ferrimagnetic long-range order in the 3D network compounds.

In these compounds the coordination environment of the Mn(II) centre plays a very important role in the formation of different structures. It was observed that when Mn(II) is four- (**1**) or five-coordinated (**2**), a 3D diamondoid framework is constructed. For a coordination number of six, the arrangement of the ligands leads to a change in the structural motif of the final compound. In the structures of **1**, **2** and **3**, the diamondoid network, which requires the coordination of four carboxylate oxygens to each Mn(II), could be maintained even with the coordination of one or two additional methanol or water ligands, as they could be accommodated in an octahedral environment for Mn(II). Coordination of two water and two methanol ligands to each Mn(II) in **5** made it impossible for Mn(II) to accommodate four

carboxylates. This resulted in the coordination of only two carboxylates leading to a linear polymer rather than the 3D network. The shape of the diamondoid networks are also affected by the type of ligands at Mn(II) centre. For example, **3** has a flattened diamondoid network due to the *cis* orientation of the water ligands.

Magnetic studies show that there are weak antiferromagnetic interactions between Mn(II) and Mn(III) metal ions in the 1D coordination polymer (**5**). The 3D networks exhibit long-range ferrimagnetic ordering at 7.4 K (**1**), 4.6 K (**2**) and 3.0 K (**3**), which depends on the coordination number (4, 5 or 6) of the Mn(II) centres in the network. As the coordination number of Mn(II) decreases, the blocking temperature increases. This shows that there is a decrease in the magnetic interactions with the increase in bond lengths. The structure of **4** could not be fully refined from the single crystal X-ray diffraction data, but the powder pattern and the space group determination suggested a structural motif similar to **1**. Magnetic properties also reinforced the hypothesis that the structures of **1** and **4** are similar as they have similar blocking temperatures $T_C = 7.4$ K and $T_C = 7.7$ K. Hysteresis effects were observed at low temperature in all 3D compounds, with the coercive fields of 60 Oe, 30 Oe, 100 Oe and 250 Oe for **1**, **2**, **3** and **4**, respectively.

This synthetic strategy was also useful in preparing *3d-4f* heterometallic coordination polymers (**8**, **9**, **10**). $[\text{Fe}_2\text{Ln}(4\text{-Me-sal})_4(2,2'\text{-bipy})_2(\text{OH}_2)_x]^+$ (Ln = Pr, Gd, Dy, $x = 5$ or 6) were the repeating units of these 1D-chain compounds. There is an alternating arrangement of Fe and Ln centres in the chain, and another Fe(III) centre attaches perpendicularly to the Ln ions of the chain. The chelating coligand, 2,2'-bipyridyl, allowed the Fe(III) centres to bridge with only one or two Ln centres, and thus favoured the formation of the 1D chain. The observed decrease of the χT value with decreasing temperature, might be due to antiferromagnetic interactions between Fe-Ln centres, the zero-field splitting of Fe(III), the depopulation of the Stark sublevels level of the anisotropic Ln ions or a combination of these. It was thus difficult to deduce the magnetic interactions between the Fe and Ln ions. Only a few Fe-Ln 1D

coordination polymers are known to date, so these compounds are valuable new examples.⁴¹⁻

⁴² Further study of these complexes will be required to gain a better understanding of the magnetic interactions.

The results in Chapter 4 show that the strategy of varying the metal ions, coligands, solvents and reaction conditions was successful in obtaining a series of compounds for a systematic study of the coordination chemistry of salicylic acid ligands. Linear trinuclear manganese complexes (**13**, **14**) synthesised from methoxy-substituted salicylic acid (3-MeO-salH₂) and pyridine as coligand were similar to the repeating units of the mixed-valence manganese coordination polymers obtained from methyl-substituted salicylic acids described in Chapter 3. It appears that the bulkier methoxy group of 3-MeO-salH₂ prevents further bridging of the Mn(III) centres with the Mn(II) centres of another trinuclear unit. The coordination at each Mn(II) is instead completed by two pyridine molecules, favouring the formation of discrete structures. In these complexes there are antiferromagnetic interactions between the metal centres similar to those observed in the extended system, however, in 3D networks there is a remnant magnetisation which leads to long-range magnetic ordering. Using a bidentate and chelating coligand, 2,2'-bipyridyl, along with 3-MeO-salH₂ and Mn(II) ions, a triangular mixed-valence manganese complex (**15**) was obtained. This shows that variation of the coligands can vary the structure from linear in **13** and **14** to triangular in **15**. All trinuclear mixed-valence manganese complexes had *syn-anti* carboxylate bridging modes and have antiferromagnetic interactions between the spin carriers. The same coligand with Cu(II) ions and 3-MeO-salH₂ gave a linear structure in **16**, with μ -oxo bridges from both carboxylate and phenoxy groups. In this complex, the carboxylate shows two kinds of bridging modes, a *syn-syn* configuration and a μ -oxo bridge by only one of the carboxylate oxygens. These bridging modes favour ferromagnetic coupling in the Cu₃ complex.

Substituted salicylaldimines (Schiff base ligands) produced several trinuclear mixed-valence manganese complexes (**17-20**) and heteronuclear Mn-Ni complexes (**21**, **22**). The

NMR studies of the synthesised Schiff base ligands and a comparison of their spectra were useful in following how ligand modification can change the electronic environment of the metal complexes and in turn can lead to different structures and/or different magnetic properties. This can be well demonstrated in the case of compounds **17** and **18**, synthesised from H_2L^1 , salicylidene-(2-amino-phenol) and H_2L^3 , salicylidene-(2-amino-4-methylphenol), where **17** behaves as a single molecule magnet and **18** does not. The ligand modification also led to changes in the structures of the complexes, such that **17** is linear and **18** is bent. It is likely that the bulkier methyl substituent on the aromatic ring favoured the formation of the bent structure. The SMM behaviour in the linear structure might be due to the parallel alignment of Jahn-Teller axes on the Mn(III) centres giving a higher total anisotropy.

The use of aromatic and aliphatic amines gave linear structures in both **17** and **19**, but the bridging modes between the metal centres were different giving different magnetic properties. Compounds **17-19** were synthesised using mixed ligand systems of salicylaldimines and acetates. Compound **20** was synthesised in the absence of acetate groups and the structure was found to be triangular showing spin frustration effects.

Increasing the number of alcohol arms on the ligand helped in binding more metals, and the use of different metal ions was explored. Compounds **21** and **22**, both with a tetranuclear $\text{Mn}^{\text{III}}_2\text{Ni}^{\text{II}}_2$ core, were synthesised. Magnetic measurements of complex **21** indicate the presence of dominating antiferromagnetic interactions within the heterometallic core. It possesses a small ground state spin of $S = 2$, but has a very high anisotropy ($D/k_B = -5.3$ K) leading to a significant energy barrier, so it behaves as a single molecule magnet. This has the highest negative D value seen in a cluster compound. The Schiff base ligands appear to impart high magnetic anisotropy to these complexes. This may be due to the strong ligand field they induce in the equatorial sites on the Jahn-Teller elongated Mn(III) coordination environment. They are thus highly suitable for synthesising single molecule magnets with high energy barriers.

Chapter 7: Experimental

This chapter presents the syntheses of the reported compounds in addition to various analytical techniques utilised to characterise and investigate the properties of these compounds. All the analytical experiments mentioned were not applied to all of the compounds due to different experimental requirements or stability considerations.

7.1 NMR spectroscopy

^1H NMR and ^{13}C NMR spectroscopy were used to identify the ligands that were synthesized. 2D NMR (COSY) was used to further investigate the ligand structure which could not be completely explained by 1D NMR. The organic ligands were analyzed on the Bruker AC 250 spectrometer at the Inorganic Chemistry Department of the University of Karlsruhe. The deuterated solvents used were DMSO- d_6 and CDCl_3 .

7.2 Elemental analysis

Elemental analysis for C, H and N were carried out at the Inorganic Chemistry Department at the University of Karlsruhe.

7.3 Infra-red spectroscopy

Infra-red spectroscopy is a useful technique for identifying organic ligands and thus helps to verify the presence of organic ligands in the metal-ligand complexes. In addition, it provides a unique fingerprint of the molecule and enables identification of similar structures involving the same ligand.

A small amount of the sample to be measured was ground into a fine powder together with absolutely dry KBr. This was then pressed into a transparent disk while under vacuum using a force of 10 N. Fourier Transform IR measurements were carried out on a Perkin-Elmer Spectrum instrument. The spectra were taken in the normal range between 4000 cm^{-1} to 400 cm^{-1} using 16 scans at a resolution of 4 cm^{-1} .

7.4 X-ray powder diffraction (PXRD)

PXRD was used to deduce the structure of compounds by comparing the spectra of similar systems. As was done for one of the 3D compounds, where a single crystal measurement was not successful, its powder diffraction pattern with other known 3D compounds confirmed its structure.

The samples were ground into fine powder, mounted on a round disk with grease between two plastic sheets and placed on the STOE STADI P X-ray powder diffractometer. The measurements were made using Cu-K α_1 radiation with $\lambda = 1.5406 \text{ \AA}$. The collected data were analysed with the software WinX^{Pow}, which gives plots of the diffraction intensities as a function of the 2θ values.

7.5 X-ray single crystal measurement

The most powerful method for analysing and confirming the structure of molecules is by single crystal X-ray structural analysis. The data were collected at 150 K on a Stoe IPDS II area detector diffractometer or at 100 K on a Bruker SMART Apex CCD diffractometer using graphite-monochromated Mo-K α radiation. The structures were solved using SHELXTL software. The following factors are important while refining the structures. First, the residual factors, R_1 and R_2 are defined as :

$$R_1 = \{ \sum \| F_o \| - \| F_c \| \} / \{ \sum \| F_o \| \}$$

$$wR_2 = \{ \sum [w(F_o^2 - F_c^2)^2] / \sum [w(F_o^2)^2] \}^{1/2}$$

$\| F_o \|$ is the data of the diffraction intensity and background exposure time obtained from the raw data after collection, reduction and correction. $\| F_c \|$ is the corresponding calculated data after structural analysis. $R_1 < 0.05$ normally indicates good structural analysis.

The value w is the weight for each diffraction point and depends on the accuracy with which F_o^2 was measured. It is defined as:

$$w = 1/\sigma^2$$

wR_2 is sensitive to the little differences in the structural analysis, such as the disorder of atoms and the defined H atoms. Normally wR_2 should be lower than 0.15 when the data is reasonable, but 0.2 is still acceptable.

The goodness-of-fit is another important factor for the quality of the structural analysis, and is defined as:

$$S = \{ \Sigma [w(F_o^2 - F_c^2)] / (n - p) \}^{1/2}$$

where n and p are the number of the unique reflections and the number of parameters involved in the refinement, respectively. When S is far from 1.0, it indicates that the weighing scheme could be wrong and should be made better if the collected data is adequate.

7.6 Magnetic Measurements

Magnetic susceptibility measurements were obtained using a Quantum Design SQUID magnetometer MPMS-XL susceptometer. This magnetometer works between 1.8 and 400 K for dc applied fields ranging from -7 to +7 T. Measurements were performed on finely ground polycrystalline samples. Ac susceptibility measurements have been measured with an oscillating ac field of 3.5 Oe and ac frequencies ranging from 1 to 1500 Hz. The magnetic data were corrected for sample holder contributions and for diamagnetic contributions calculated from Pascal's constants.

7.7 Syntheses

All chemicals and solvents used for synthesis were obtained from commercial sources and were used as received without further purification. All reactions were carried out in aerobic conditions.

7.7.1 Ligand Syntheses

7.7.1.1 Preparation of 3-methoxysalicylidene-2-aminophenol ($\mathbf{H}_2\mathbf{L}^1$)

The same procedure was employed to prepare all the ligands ($\mathbf{H}_2\mathbf{L}^n$, $n = 1-6$), and thus only $\mathbf{H}_2\mathbf{L}^1$ is described here in detail. 3-methoxysalicylaldehyde or *o*-vanillin (0.302 g, 2mmol) dissolved in 5ml of methanol was added to another 5 ml methanolic solution of 2-

aminophenol (0.218, 2mmol). The resulting solution was stirred for a few minutes to give a dark orange solution. After filtration, the solution was left to evaporate and in 1-2 days orange crystals can be obtained from the solution. Yield: 75%. Anal. Calcd. for $C_{14}H_{13}NO_3$ (found): C, 69.14 (68.92); H, 5.34 (5.35); N, 5.76 (5.68). 1H NMR (DMSO- d_6 , δ , ppm): 3.81 (s, 3H), 6.83 (t 1H), 6.9 (t, 1H), 6.96 (d, 1H), 7.06 (d, 1H), 7.13 (t, 1H), 7.18 (d, 1H), 7.36 (d, 1H), 9 (s, 1H), 9.9 (s, 1H), 14 (s,1H).

7.7.1.2 Preparation of 3-ethoxysalicylidene-2-aminophenol (H_2L^2)

Yield: 78 %. Calcd for $C_{15}H_{15}NO_3$ (found): C, 70.04 (69.98); H, 5.84 (5.87); N, 5.45 (5.40). 1H NMR (DMSO- d_6 , δ , ppm): 1.3 (t, 3H), 4.05 (s, 2H), 6.83 (t, 1H), 6.9 (t, 1H), 6.97 (d, 1H), 7.06 (d, 1H), 7.14 (t, 1H), 7.17 (d, 1H) 7.38 (d, 1H), 8.85 (s, 1H), 9.9 (s, 1H), 14 (s, 1H).

7.7.1.3 Preparation of 3-methoxysalicylidene-(2-amino-4-methylphenol) (H_2L^3)

Yield: 82%. Calcd for $C_{15}H_{15}NO_3$ (found): C, 70.04 (69.94); H, 5.84 (5.85); N, 5.45 (5.43). 1H NMR (DMSO- d_6 , δ , ppm): 2.24 (s, 3H), 3.81 (s, 3H), 6.83 (t, 1H), 6.86 (t, 1H), 6.94 (d, 1H), 7.06 (d, 1H), 7.18 (d, 1H), 7.20 (d, 1H), 8.94 (s, 1H), 9.6 (s, 1H), 14.1 (s,1H).

7.7.1.4 Preparation of 3-ethoxysalicylidene-(2-amino-4-methylphenol) (H_2L^4)

Yield: 78%. Calcd for $C_{16}H_{17}NO_3$ (found): C, 70.85 (70.78); H, 6.27 (6.28); N, 5.17 (5.12). 1H NMR (DMSO- d_6 , δ , ppm): 1.3 (t, 3H), 4.05 (s, 2H), 2.24 (s, 3H), 6.83 (t, 1H), 6.86 (t, 1H), 6.94 (d, 1H), 7.03 (d, 1H), 7.19 (d, 1H), 7.20 (d, 1H), 8.92 (s, 1H), 9.6 (s, 1H), 14.2 (s, 1H).

7.7.1.5 Preparation of 3-hydroxysalicylidene-2-aminophenol (H_2L^5)

Yield: 65%. Calcd for $C_{13}H_{11}NO_3$ (found): C, 68.12 (68.09); H, 4.80 (4.82); N, 6.11 (6.15). 1H NMR (DMSO- d_6 , δ , ppm): 6.72 (t, 1H), 6.9 (t, 1H), 6.91 (d, 1H), 6.98 (d, 1H), 7.04 (d, 1H) 7.14 (t, 1H), 7.42 (d, 1H), 8.94 (s, 1H), 9.9 (s, 1H), 10.2 (s, 1H) 14.3 (s, 1H).

7.7.1.6 Preparation of 3-hydroxysalicylidene-(2-amino-4-methylphenol) (H₂L⁶)

Yield: 58%. Calcd for C₁₄H₁₃NO₃ (found): C, 69.13 (68.99); H, 5.35 (5.36); N, 5.76 (5.71). ¹H NMR (DMSO-d₆, δ, ppm): 2.25 (s, 3H), 6.72 (t, 1H), 6.85 (t, 1H), 6.91 (d, 1H), 6.95 (d, 1H), 7.02 (d, 1H), 7.25 (d, 1H), 8.95 (s, 1H), 9.9 (s, 1H), 10.2 (s, 1H) 14.2 (s, 1H).

7.7.2 Inorganic Syntheses**7.7.2.1 Preparation of [Mn^{III}₂Mn^{II}(3-Me-sal)₄(py)₄], 1**

MnCl₂·4H₂O (0.079 g, 0.4 mmol) was added to a methanolic solution (20 ml) of 3-Me-salH₂ (0.091 g, 0.6 mmol) and pyridine (130 μl, 1.0 mmol) to give a light yellow solution. The solution was then stirred for 1h followed by the addition of triethylamine (65 μl, 0.5 mmol). A black solution resulted in few minutes. After filtration, slow evaporation of the resulting solution gave black needle-shaped crystals in a few days. The crystals were collected by filtration, washed with cold methanol and air-dried. Yield: 65 mg, 45% based on Mn. Anal. Calcd. for C₅₂H₄₄Mn₃N₄O₁₂ (found): C, 57.17 (57.69); H, 4.01 (4.07); N, 5.07 (5.17). Selected IR data (KBr disc, cm⁻¹): 3425 (b), 2923 (m), 1599 (s), 1576 (m), 1520 (s), 1463 (s), 1446 (s), 1423 (s), 1249 (m), 1082 (m), 875 (m), 760 (s), 698 (s), 630 (m), 439 (b,m).

7.7.2.2 Preparation of [Mn^{III}₂Mn^{II}(4-Me-sal)₄(py)₄(MeOH)]·H₂O, 2

MnCl₂·4H₂O (0.079 g, 0.4 mmole) was added to a methanolic solution (20 ml) of 4-Me-salH₂ (0.091 g, 0.6 mmole) and pyridine (157 μl, 1.6 mmol) to give a light yellow solution. The solution was then stirred for 1h followed by the addition of triethylamine (100 μl, 0.7 mmol). A small amount of white precipitate was formed which then slowly dissolved with further stirring. The resulting solution turned greyish and then black in 1h. After filtration, slow evaporation of the resulting solution gave black crystals in few days. The crystals were collected by filtration, washed with cold methanol and air-dried. Yield: 59 mg, 39% based on Mn. Anal. Calcd. for C₅₃H₅₁Mn₃N₄O₁₄ (found): C, 55.73 (56.14); H, 4.25 (4.50); N, 4.96 (4.94). Selected IR data (KBr disc, cm⁻¹): 3412 (b), 2922 (m), 1599 (s), 1556 (s), 1445 (s), 1325 (s), 1166 (s), 1035 (m), 957 (m), 778 (s), 749 (m), 699 (m), 625 (s).

7.7.2.3 Preparation of $[\text{Mn}^{\text{III}}_2\text{Mn}^{\text{II}}(\text{5-Me-sal})_4(\text{py})_4(\text{H}_2\text{O})_2] \cdot (\text{MeOH})$, 3

$\text{MnCl}_2 \cdot 4\text{H}_2\text{O}$ (0.079 g, 0.4 mmol) was added to a methanolic solution (20 ml) of 5-Me-salH₂ (0.091 g, 0.6 mmol) and pyridine (130 μl , 1.0 mmol) to give a faint pink solution. The solution was then stirred for 1h followed by the slow addition of triethylamine (78 μl , 0.6 mmol). In a few hours, the solution turned black in colour. Filtration and then slow evaporation of the resulting solution gave black crystals after one week. The crystals were collected by filtration, washed with cold methanol and air-dried. Anal. Calcd. for $\text{C}_{53}\text{H}_{52}\text{Mn}_3\text{N}_4\text{O}_{16}$ (found): C, 55.17 (55.35); H, 4.57 (4.53); N, 5.01 (4.87). Selected IR data (KBr disc, cm^{-1}): 3336 (b), 2967 (m), 1618 (s), 1599 (s), 1561 (s), 1543 (s), 1479 (s), 1443 (s), 1420 (s), 1350 (s), 1316 (s), 1231 (s), 1208 (m), 1145 (m), 1067 (m), 1037 (m), 1007 (m), 844 (m), 810 (m), 755 (m), 699 (s), 626 (m), 538 (m), 416 (m).

7.7.2.4 Preparation of $[\text{Mn}^{\text{III}}_2\text{Mn}^{\text{II}}(\text{3-Me-sal})_4(\text{4-Me-py})_4]$, 4

$\text{MnCl}_2 \cdot 4\text{H}_2\text{O}$ (0.079 g, 0.4 mmol) was added to a methanolic solution (20 ml) of 3-Me-salH₂ (0.091 g, 0.6 mmol) and 4-Me-py (118 μl , 1.2 mmole) to give a light yellow solution. After the solution was stirred for 1h, triethylamine (65 μl , 0.5 mmol) was added giving a black solution in a few minutes. After filtration, the solution was slowly evaporated, resulting in black crystals after 2 days. The crystals were collected by filtration, washed with cold methanol and air-dried. Yield: 52 mg. Anal. Calcd. for $\text{C}_{56}\text{H}_{52}\text{Mn}_3\text{N}_4\text{O}_{12}$ (found): C, 58.75 (59.10); H, 4.74 (4.57); N, 4.94 (4.93). Selected IR data (KBr disc, cm^{-1}): 1618 (s), 1599 (s), 1574 (s), 1537 (s), 1462 (s), 1422 (s), 1324 (s), 1249 (s), 1155 (m), 1082 (s), 1023 (m), 876 (s), 812 (s), 762 (s), 695 (m), 536 (m), 439 (m).

7.7.2.5 Preparation of $[\text{Mn}^{\text{III}}(\text{4-Me-sal})_2(\text{4-Me-py})_2\text{Mn}^{\text{II}}(\text{OH})_2(\text{MeOH})_2][\text{Mn}^{\text{III}}(\text{4-Me-sal})_2(\text{4-Me-py})_2]$, 5

$\text{MnCl}_2 \cdot 4\text{H}_2\text{O}$ (0.079 g, 0.4 mmol) was added to a methanolic solution (20 ml) of 4-Me-salH₂ (0.091 g, 0.6 mmol) and 4-Me-py (157 μl , 1.6 mmol) to give a light yellow solution. The solution was then stirred for 1h followed by the addition of triethylamine (100 μl , 0.7

mmol) which gave a black solution in a few minutes. After filtration, the solution was slowly evaporated and black crystals were obtained after 2 weeks. The crystals were collected by filtration, washed with cold methanol and air-dried. Yield: 61 mg, 37% based on Mn. Anal. Calcd. for $C_{58}H_{64}Mn_3N_4O_{16}$ (found): C, 56.15 (56.22); H, 5.12 (5.17); N, 4.48 (4.52). Selected IR data (KBr disc, cm^{-1}): 3417 (b), 2922 (m), 1615 (s), 1563 (s), 1423 (b, s), 1325 (s), 1251 (m), 1170 (s), 1012 (m), 958 (m), 781 (s), 751 (s), 625 (s), 487 (m), 426 (w).

7.7.2.6 Preparation of product 6

$MnCl_2 \cdot 4H_2O$ (0.079 g, 0.4 mmol) was added to a methanolic solution (20 ml) of 5-Me-salH₂ (0.091 g, 0.6 mmol) and 4-Me-py (118 μ l, 1.2 mmol) to give a light pink solution. The solution was then stirred for 1h followed by the slow addition of triethylamine (65 μ l, 0.5 mmol) which gave a black solution in a few minutes. After filtration, the solution was slowly evaporated resulting in black crystals after one week. The crystals were collected by filtration, washed with cold methanol and air-dried. Yield: 48 mg. Elemental analysis: C, 52.05; H, 5.64; N, 4.71. Selected IR data (KBr disc, cm^{-1}): 3410 (b), 2924 (m), 1618 (s), 1582 (s), 1565 (s), 1475 (s), 1443 (s), 1420 (s), 1350 (s), 1324 (s), 1248 (s), 1145 (m), 1070 (m), 1037 (m), 832 (m), 820 (m), 756 (m), 700 (s), 636 (m), 537 (m), 422 (m).

7.7.2.7 Preparation of [(3-MeO-sal)₂MnNa₂·MeOH], 7

$Mn(ClO_4) \cdot 6H_2O$ (0.036 g, 0.2 mmol) was added to a methanolic solution (15 ml) of 3-MeO-salH₂ (0.017 g, 0.1 mmol) and triethylamine (0.013 ml, 0.2 mmol) to give a light yellow solution. After a few minutes, NaN₃ (0.013, 0.2 mmol) dissolved in 5ml H₂O was added slowly followed by stirring for 2h. The resulting black solution was filtered and left to evaporate. After 2 days small black crystals were obtained. The crystals were collected by filtration, washed with methanol and air dried. Yield: 32%. Anal. Calcd. for $C_{18}H_{20}MnNaO_{10}$ (found): C, 45.57 (45.48); H 4.22 (4.25). Selected IR data (KBr disc, cm^{-1}): 3498 (s), 2984 (m), 2932(m), 1596 (s), 1579 (s), 1545 (s), 1476 (s), 1325 (s), 1252 (m), 1208 (m), 1154 (m), 1069 (s), 856 (s), 809 (m), 755 (s), 698 (s), 465 (m), 420 (m).

7.7.2.8 Preparation of $[\text{Fe}_2\text{Pr}(\text{4-Me-sal})_4(\text{2,2'-bipy})_2(\text{OH}_2)_6](\text{NO}_3)_2 \cdot 2\text{MeOH} \cdot 1.5 \text{H}_2\text{O}$, **8**

$\text{Pr}(\text{NO}_3)_3 \cdot 6\text{H}_2\text{O}$ (0.086 g, 0.2 mmol) dissolved in 5 ml of H_2O was added to a methanolic solution (10 ml) of 4-Me-salH₂ (0.122 g, 0.8 mmol) which gave a light yellow coloured solution. To it was added a methanolic solution (10 ml) of $\text{FeCl}_3 \cdot 4\text{H}_2\text{O}$ (0.054 g, 0.2 mmol) and 2,2'-bipy (0.031 g, 0.2 mmol). The colour of the solution changed to purple. After 1h, triethylamine (0.052 ml, 0.4 mmol) was added slowly giving a pinkish purple solution. The solution was filtered and layered with ether. The next day small pinkish purple crystals were obtained. Yield: 55%. Anal. Calcd. for $\text{C}_{55}\text{H}_{64}\text{Fe}_2\text{PrN}_5\text{O}_{24}$ (found): C, 46.04 (46.12); H, 4.24 (4.47); N, 4.81 (4.89). Selected IR data (KBr disc, cm^{-1}): 3446 (b), 2919 (m), 1608 (s), 1558 (s), 1523 (m), 1443 (s), 1423 (s), 1320 (m), 1327 (s), 1249 (s), 1170 (m), 1024 (m), 959 (m), 764 (m), 635 (m), 612 (m), 416 (w).

7.7.2.9 Preparation of $[\text{Fe}^{\text{III}}_2\text{Gd}^{\text{III}}(\text{4-Me-sal})_4(\text{2,2'-bipy})_2(\text{OH}_2)_5]\text{Cl}_{1/2}(\text{NO}_3)_{1/2} \cdot 5\text{H}_2\text{O}$, **9**

A reaction similar to that of **8** was done using $\text{Gd}(\text{NO}_3)_3 \cdot 6\text{H}_2\text{O}$, and by the same layering method pinkish purple crystals were isolated. Yield 62%. Anal. Calcd. for $\text{C}_{52}\text{H}_{60}\text{Fe}_2\text{GdN}_{9/2}\text{O}_{51/2}\text{Cl}_{1/2}$ (found): C, 43.37 (44.24); H, 4.24 (4.26); N, 4.38 (4.47). Selected IR data (KBr disc, cm^{-1}): 3382 (b), 2919 (m), 1607 (s), 1558 (s), 1520 (s), 1444 (s), 1425 (s), 1384 (s), 1249 (s), 1172 (s), 1025 (m), 959 (m), 767 (m), 635 (m), 613 (m), 416 (w).

7.7.2.10 Preparation of $[\text{Fe}_2\text{Dy}(\text{4-Me-sal})_4(\text{2,2'-bipy})_2(\text{OH}_2)_5] \text{Cl}_{1/2}(\text{NO}_3)_{1/2} \cdot 5\text{H}_2\text{O}$, **10**

The reaction of **10** was carried out as in **8** and **9** but using $\text{Dy}(\text{NO}_3)_3 \cdot 6\text{H}_2\text{O}$. With the same layering method, pinkish purple crystals were isolated. Yield: 84%. Anal. Calcd. for $\text{C}_{52}\text{H}_{60}\text{Fe}_2\text{DyN}_{9/2}\text{O}_{51/2}\text{Cl}_{1/2}$ (found): C, 43.49 (43.12); H, 4.13 (4.15); N, 4.29 (4.35). IR (KBr disc, cm^{-1}): 3422 (b), 1607 (s), 1557 (s), 1514 (s), 1443 (s), 1423 (s), 1320 (m), 1250 (s), 1170 (s), 1024 (m), 959 (m), 765 (m), 636 (m), 613 (m), 416 (w).

7.7.2.11 Preparation of $(\text{NH}_4)_3[\text{Mn}^{\text{III}}(\text{3-MeO-sal})_2(\text{MeOH})(\text{H}_2\text{O})]$, **11**

$\text{Mn}(\text{ClO}_4)_2 \cdot 6\text{H}_2\text{O}$ (0.180 g, 0.5 mmol) was added to a methanolic solution (20 ml) of 3-MeO-salH₂ (0.168 g, 1 mmol) and triethylamine (0.130 ml, 2 mmol) to give a yellow solution.

After 1 h, a small amount of precipitate was observed and colour of the solution turned greyish black. The solution was stirred for 2h. The solution was filtered and the filtrate was left to evaporate. Black diamond-shaped crystals were obtained the next day. Yield: 78%. Anal. Calcd. for $C_{23}H_{34}MnNO_{10}$ (found): C, 51.21 (51.19); H, 6.31 (6.34); N, 2.59 (2.56). IR (KBr disc, cm^{-1}): 3435 (b), 2935 (m), 1594 (s), 1546 (s), 1492 (s), 1320 (m), 1248 (s), 1150 (s), 1056 (m), 758 (m), 678 (m), 435 (w).

7.7.2.12 Preparation of $(NH_4)_2[Fe^{III}(3-MeO-sal)_2(OAc)]$, **12**

$[Fe_3(OAc)_6(py)_3](ClO_4)$ (0.186 g 0.2 mmol) dissolved in MeCN (10ml) was added to another MeCN (10ml) solution of 3-MeO-salH₂ (0.101 g, 0.6 mmol) and triethylamine (0.78 g, 0.6 mmol). The resulting solution was red in colour. After stirring for 4 hours, a small amount of precipitate was obtained. The solution was filtered, left to evaporate and in few days deep red crystals suitable for X-ray diffraction were obtained. Yield: 32%. Anal. Calcd. for $C_{30}H_{47}FeN_2O_{10}$ (found): C, 55.30 (55.34); H, 7.22 (7.20); N, 4.30 (4.32). IR (KBr disc, cm^{-1}): 3437 (b), 2926 (m), 1605 (s), 1559 (s), 1517 (s), 1346 (m), 1250 (s), 1156 (s), 1058 (m), 760 (m), 665 (m), 428 (w).

7.7.2.13 Preparation of $[Mn^{II}Mn^{III}_2(3-MeO-sal)_4(py)_6(H_2O)_2] \cdot 4H_2O$, **13**

3-MeO-salH₂ (1.01 g, 6.00 mmol) and $Mn(OAc)_2 \cdot 4H_2O$ (0.5 g, 2.0 mmol) were dissolved in pyridine (10ml) to give a clear yellow solution. The solution was stirred while solid NBu_4MnO_4 (0.15 g, 0.4 mmol) was added in small portions over approximately 10 minutes leading to a black liquor which was layered with an equal volume of petroleum ether. After 2 days dark green crystals, suitable for X-ray diffraction studies was deposited. The crystals were collected by filtration, washed with ether and air-dried. Yield: 72%. Anal. Calcd. for $C_{62}H_{62}Mn_3N_6O_{22}$ (found): C, 52.82 (52.84); H, 5.91 (5.97); N, 4.44 (4.40). Selected IR data (KBr disc, cm^{-1}): 3505 (s), 3461 (b), 2986 (m), 2934 (m), 1594 (s), 1578 (s), 1549 (s), 1474 (s), 1443 (s), 1372 (m), 1348 (m), 1327 (s), 1249 (m), 1206 (m), 1152 (m), 1066 (s), 853 (s), 809 (m), 760 (s), 699 (s), 674 (m), 470 (m), 417 (m).

7.7.2.14 Preparation of $[\text{Mn}^{\text{III}}_2\text{Mn}^{\text{II}}(\text{3-MeO-sal})_4(\text{py})_4(\text{H}_2\text{O})_4]\cdot 4\text{MeOH}$, 14

$\text{MnCl}_2\cdot 4\text{H}_2\text{O}$ (0.079 g, 0.4 mmol) was added to a methanolic solution (20 ml) of 3-MeO-sal (0.101 g, 0.6 mmol) and pyridine (0.202 ml, 1.6 mmol) to give a light yellow solution. The solution was left stirring overnight, and then triethylamine (0.100 ml, 0.7 mmol) was added slowly. In few minutes the solution turned black in colour. The following day black needle-shaped crystals were obtained. The crystals were collected by filtration, washed with cold methanol and air dried. Yield: 64%. Anal. Calcd. for $\text{C}_{54}\text{H}_{60}\text{Mn}_3\text{N}_4\text{O}_{22}$ (found): C, 49.71 (50.54); H, 4.62 (4.68); N, 4.31 (4.36). Selected IR data (KBr disc, cm^{-1}): 3448 (s), 3465(b), 2985 (m), 2932 (m), 1592 (s), 1575 (s), 1542 (s), 1469 (s), 1444 (s), 1366 (m), 1342 (m), 1324 (s), 1237 (m), 1145 (m), 1062 (s), 849 (s), 798 (m), 754 (s), 694 (s), 670 (m), 465 (m), 419 (m).

7.7.2.15 Preparation of $[\text{Mn}^{\text{III}}_2\text{Mn}^{\text{II}}(\text{3-MeO-sal})_4(2,2'\text{-bipy})(\text{H}_2\text{O})_3(\text{MeOH})_2]\cdot 3\text{MeOH}$, 15

$\text{Mn}(\text{OAc})_2\cdot 4\text{H}_2\text{O}$ (0.368 g, 1.5 mmol) was added to a methanolic solution (20 ml) of L^1 (0.168 g, 1 mmol). After 5 min, 2,2'-bipy (0.039 g, 5 mmol) was added to the above solution giving a yellow solution followed by the addition of 1 mmol of triethylamine. The colour of the solution became dark yellow, then light red, and finally black. The following day black crystals suitable for X-ray analysis were obtained. The crystals were collected by filtration, washed with cold methanol and air dried. The crystals lost crystallinity when left in air without the mother liquor for more than 1 week. Yield: 48%. Anal. Calcd. for $\text{C}_{46}\text{H}_{54}\text{Mn}_3\text{N}_2\text{O}_{23}$ (found): C, 47.23 (47.26); H, 4.61 (4.62); N, 2.39 (2.40). Selected IR data (KBr disc, cm^{-1}): 3400 (b), 2925 (m), 1587 (s), 1551 (s), 1480 (s), 1442 (s), 1363 (m), 1335 (m), 1244 (m), 1065 (m), 857 (m), 750 (m), 430 (w).

7.7.2.16 Preparation of $[\text{Cu}_3(\text{3-MeO-salH})_2(\text{3-MeO-sal})_2(2,2'\text{-bipy})_2]$, 16

Crystals were grown by a layering technique involving three-layered solutions in a slender tube with a 0.8cm diameter. The bottom layer was 4 ml of water containing

$\text{Cu}(\text{CH}_3\text{COO})_2 \cdot \text{H}_2\text{O}$ (0.059 g, 0.3 mmol), the middle layer was 4 ml of DMF containing 3-MeO-salH₂ (0.67 g, 0.4 mmol) and the upper layer was 4 ml of methanol containing 2,2'-bipy (0.031 g, 0.2 mmol). Next day green crystals suitable for X-ray diffraction studies were obtained. The crystals were collected by filtration, washed with cold methanol and air dried. It is important that $\text{Cu}(\text{CH}_3\text{COO})_2 \cdot \text{H}_2\text{O}$ was used stoichiometrically, so that the crystals obtained were pure. A slight excess left green precipitate along with the crystals. Yield: 46%. Anal. Calcd. for $\text{C}_{52}\text{H}_{42}\text{Cu}_3\text{N}_4\text{O}_{16}$ (found): C, 53.33 (53.31); H, 3.59 (3.61); N, 4.79 (4.78). Selected IR data (KBr disc, cm^{-1}): 3448 (b), 3064 (m), 2983 (m), 2940 (m), 2836 (m), 1610 (s), 1566 (s), 1465 (s), 1447 (s), 1389 (s), 1373 (s), 1343 (s), 1323 (s), 1250 (s), 1194 (s), 1059 (s), 917 (m), 853 (m), 769 (s), 754 (s), 731 (m), 651 (m), 643 (m) 418 (w).

7.7.2.17 Preparation of $[\text{Mn}^{\text{III}}_2\text{Mn}^{\text{II}}(\text{L}^1)_2(\mu\text{-OAc})_2(\mu\text{-OMe})_2(\text{MeOH})_2] \cdot 2\text{MeOH}$, 17

$\text{Mn}(\text{OAc})_2 \cdot 4\text{H}_2\text{O}$ (0.245 g, 1 mmol) dissolved in methanol (10 ml) was added to a methanolic solution (10 ml) of H_2L^1 (0.122 g, 0.5 mmol). The solution turned brownish black and with further addition of triethylamine (0.130 ml, 1 mmol) it turned completely black in colour. The solution was stirred for 2h at RT, filtered and then left to evaporate. Next day black crystals were obtained. Anal. Calcd. for $\text{C}_{38}\text{H}_{50}\text{Mn}_3\text{N}_2\text{O}_{16}$ (found): C, 48.66 (47.74); H, 5.10 (5.23); N, 2.95 (2.93). Selected IR data (KBr disc, cm^{-1}): 2927 (m), 2816 (m), 1601 (s), 1548 (b,s), 1484 (s), 1429 (s), 1381 (s), 1317 (m), 1298 (m), 1255 (s), 1175 (m), 1108 (m), 1026 (b,m), 831 (m), 735 (m), 539 (m), 439 (w).

7.7.2.18 Preparation of $[\text{Mn}^{\text{III}}_2\text{Mn}^{\text{II}}(\text{L}^3)_2(\mu\text{-OAc})_2(\mu\text{-OMe})_2]$, 18

$\text{Mn}(\text{OAc})_2 \cdot 4\text{H}_2\text{O}$ (0.245 g, 1 mmol) dissolved in methanol (10 ml) was added to a methanolic solution (10 ml) of H_2L^3 (0.122 g, 0.5 mmol). The solution turned brownish black in colour and further addition of triethylamine (0.130 ml, 1 mmol) led to a completely black solution with small amount of black precipitate. The solution was stirred for 2h at RT, filtered and then left to evaporate. The following day black thin needle-shaped crystals were obtained from the solution. Yield: 28%. Anal. Calcd. for $\text{C}_{36}\text{H}_{38}\text{Mn}_3\text{N}_2\text{O}_{12}$ (found): C, 50.53 (50.54); H,

4.44 (4.42); N 3.27 (3.25). Selected IR data (KBr disc, cm^{-1}): 3425 (b), 1574 (s), 1546 (s), 1497 (s), 1416 (s), 1341 (m), 1311 (m), 1258 (m), 1234 (m), 1208 (m), 1106 (m), 1021 (m), 836 (m), 736 (m), 663 (m), 620 (m), 435 (w).

7.7.2.19 Preparation of $[\text{Mn}^{\text{III}}_2\text{Mn}^{\text{II}}(\text{L}^7)_2(\text{OAc})_4(\text{OH}_2)_2] \cdot \text{MeOH}$, 19

The Schiff-base (H_2L^7) was made *in situ* in a methanolic solution (20 ml) of *o*-vanillin (0.158 g, 1 mmol), ethanolamine (0.061 g, 1 mmol), and triethylamine (0.101 g, 1mmol). The solution was stirred for 15 minutes resulting in a pale yellow solution. To this solution $\text{Mn}(\text{OAc})_2 \cdot 4\text{H}_2\text{O}$ (0.245 g, 1.0 mmol) was added with stirring. This reaction was further stirred for 3h at room temperature, then filtered and left to evaporate. The following day brown crystals were obtained. Yield: 64%. Anal. Calcd. for $\text{C}_{29}\text{H}_{42}\text{Mn}_3\text{N}_2\text{O}_{17}$ (found): C, 40.19 (40.70); H, 4.90 (4.91); N, 3.20 (3.27). Selected IR data (KBr disc, cm^{-1}): 3416 (s), 2960 (m), 2925 (m), 2868 (m), 1634 (s), 1590 (s), 1473 (m), 1441 (s), 1417 (s), 1320 (m), 1307 (s), 1245 (s), 1219 (s), 1074 (m), 1025 (m), 966 (s), 860 (m), 738 (m), 614 (m), 592 (m), 538 (m), 454 (m), 417 (w).

7.7.2.20 Preparation of $[\text{Mn}^{\text{III}}_3(\mu_3\text{-O})(\text{L}^{11})_3(\text{MeOH})_3] (\text{ClO}_4)$, 20

The Schiff-base (H_2L^{11}) was made *in situ* in a methanolic solution (20ml) of 3-ethoxysalicylaldehyde (0.152 g, 1.0 mmol), 1-amino-2-propanol (0.075 g, 1.0 mmol) and triethylamine (0.101 g, 1.0 mmol). To this solution was added CaCl_2 (0.222 g, 2.0 mmol). The resulting solution was then added to a second methanolic solution (20ml) of $\text{Mn}(\text{OAc})_2 \cdot 4\text{H}_2\text{O}$ (0.245 g, 1.0 mmol) while stirring at room teperature. The solution was filtered and left to evaporate. Black octahedral crystals were obtained after 1 day. Yield: 88%. Anal. Calcd. for $\text{C}_{39}\text{H}_{57}\text{Mn}_3\text{N}_3\text{O}_{17}\text{Cl}$ (found): C, 40.54 (45.02); H, 5.20 (5.48); N, 3.52 (4.04). Selected IR data (KBr disc, cm^{-1}): 3408 (b), 2975 (m), 2926 (m), 2870 (m), 1626 (s), 1601 (s), 1550 (m), 1466 (m), 1444 (s), 1393 (m), 1300 (s), 1250 (s), 1217 (s), 1180 (m), 1088 (b,s), 1038 (s), 891 (m), 859 (m), 783 (m), 743 (m), 656 (s), 624 (s), 523 (m), 473 (m).

7.7.2.21 Preparation of $[\text{Mn}_2^{\text{III}}\text{Ni}_2^{\text{II}}(\text{L}^{14})_4](\text{CH}_3\text{COO})_2$, 21

The Schiff-base (H_2L^{14}) was made *in situ* in a methanolic solution (20ml) of salicylaldehyde (0.122 g, 1.0 mmol), tris-(hydroxymethyl)aminomethane (0.121 g, 1.0 mmol), and triethylamine (0.101 g, 1.0 mmol). To this solution was added $\text{Ni}(\text{OAc})_2 \cdot 4\text{H}_2\text{O}$ (0.249 g, 1.0 mmol). The resulting solution turned green and then after stirring for 15 min $\text{Mn}(\text{OAc})_2 \cdot 4\text{H}_2\text{O}$ (0.123 g, 0.5 mmol) was added slowly. The solution turned black in colour, and was further stirred for 3h. After filtration, the solution was left to evaporate. Black crystalline needles were deposited after a few days. Yield: 73%. Anal. Calcd. for $\text{C}_{48}\text{H}_{62}\text{Mn}_2\text{N}_4\text{Ni}_2\text{O}_{26}$ (found): C, 43.04 (43.06); H, 4.64 (4.60); N, 4.18 (4.13). Selected IR data (KBr disc, cm^{-1}): 3205 (b), 2914 (m), 2864 (m), 1611 (s), 1542 (s), 1468 (s), 1442 (s), 1298 (s), 1192 (m), 1131 (m), 1020 (s), 922 (w), 658 (m), 676 (m), 520 (m), 452 (w).

7.7.2.22 Preparation of $[\text{Mn}_2^{\text{III}}\text{Ni}_2^{\text{II}}(\text{L}^{14})_4](\text{Cl})_2$, 22

The Schiff-base (H_2L^{14}) was made *in situ* in a methanolic solution (20ml) of salicylaldehyde (0.122 g, 1.0 mmol), tris-(hydroxymethyl)aminomethane (0.121 g, 1.0 mmol) and triethylamine (0.101 g, 1.0 mmol). To this solution was added $\text{NiCl}_2 \cdot 6\text{H}_2\text{O}$ (0.119 g, 0.5 mmol). The resulting solution turned green and then $\text{MnCl}_2 \cdot 4\text{H}_2\text{O}$ (0.098 g, 0.5 mmol) was added slowly. The solution turned black in colour and was further stirred for 3 h. After filtration, the solution was left to evaporate. Black crystals were deposited after 1 week. Yield: 62%. Anal. Calcd. for $\text{C}_{48}\text{H}_{68}\text{Mn}_2\text{Ni}_2\text{N}_4\text{O}_{20}\text{Cl}_2$ (found): C, 43.67 (43.64); H, 5.16 (5.12); N, 4.25 (4.21). Selected IR data (KBr disc, cm^{-1}): 3204 (b), 2920 (m), 2853 (m), 1610 (s), 1540 (s), 1465 (s), 1441 (s), 1293 (s), 1188 (m), 1016 (s), 893 (m), 653 (m), 674 (m), 521 (m), 464 (w).

Chapter 8: Crystallographic data

The crystal structure data for compounds **1-22** are presented here. More detailed information can be found in the cif files on the accompanying CD.

Table 8.01 Crystallographic measurements

	1	2	3	4
Formula	C ₅₂ H ₄₄ Mn ₃ N ₄ O ₁₂	C ₅₃ H ₅₁ Mn ₃ N ₄ O ₁₄	C ₅₃ H ₅₂ Mn ₃ N ₄ O ₁₅	C ₅₆ H ₅₂ Mn ₃ N ₄ O ₁₂
Mr	1081.73	1132.80	1149.81	1192.78
Cryst size[mm]	0.26 x 0.21 x 0.16	0.25 x 0.18 x 0.11		
colour	black	black	black	black
Cryst Syst	tetragonal	tetragonal	monoclinic	tetragonal
Space group	P 4 ₃	I 4 ₁	P 2 ₁ /c	P4 ₃
T[K]	100	100	150	100
<i>a</i> [Å]	18.7991(2)	18.9660(7)	18.888(3)	19.0290(5)
<i>b</i> [Å]	18.7991(2)	18.9660(7)	13.7658(14)	19.0290(5)
<i>c</i> [Å]	13.8136(3)	13.9262(10)	20.054(3)	14.7032(8)
<i>α</i> [deg]	90	90	90	90
<i>β</i> [deg]	90	90	93.780(12)	90
<i>γ</i> [deg]	90	90	90	90
<i>V</i> [Å ³]	4881.81(13)	5009.4(4)	5203.0(13)	5324.1(4)
Z	4	4	4	4
ρ_{calcd} [g cm ⁻³]	1.472	1.502	1.468	
μ (Mo K α) [mm ⁻¹]	0.832	0.817	0.789	
<i>F</i> (000)	2220	2336	2372	
reflns collected	34044	13860	17781	
unique reflns	11063	4687	4704	
<i>R</i> _{int}	0.0213	0.0303	0.1283	
reflns obsd [<i>I</i> > 2 σ (<i>I</i>)]	10556	4452	2867	
parameters/restraints	645/1	348/2	693/6	
GOF on <i>F</i> ²	1.020	1.037	1.038	
<i>R</i> 1 [<i>I</i> > 2 σ (<i>I</i>)]	0.0352	0.0582	0.0856	
w <i>R</i> 2 (all data)	0.0863	0.1424	0.1808	
Larg. residuals [e Å ⁻³]	+1.02/-0.29	+2.41/-0.46	+0.71/-0.60	

	5	7	8	9
Formula	C ₅₈ H ₆₄ Mn ₃ N ₄ O ₁₆	C ₁₈ H ₂₀ MnNaO ₁₀	C ₅₅ H ₆₄ Fe ₂ N ₅ O ₂₄ Pr	C ₅₂ H ₆₀ Cl _{0.5} Fe ₂ GdN _{4.5} O _{23.5}
Mr	1237.95	474.27	1431.72	1410.72
Cryst size[mm]		0.32 x 0.14 x 0.06	0.25 x 0.18 x 0.11	0.21 x 0.15 x 0.05
color	black	black	purple	purple
Cryst Syst	triclinic	monoclinic	monoclinic	monoclinic
Space group	P -1	C 2/c	P 2 ₁ /c	P 2 ₁ /c
T[K]	150	100	100	100
<i>a</i> [Å]	11.8534 (12)	22.064(2)	14.450 (3)	14.7924(5)
<i>b</i> [Å]	12.5635 (14)	8.5408(8)	19.840 (4)	19.4629(6)
<i>c</i> [Å]	19.530 (2)	12.1315(11)	21.930 (4)	22.0420(7)
<i>α</i> [deg]	82.457 (9)	90.00	90	90
<i>β</i> [deg]	83.345 (8)	122.805(2)	105.85(3)	99.995(1)
<i>γ</i> [deg]	85.861 (8)	90.00	90	90
<i>V</i> [Å ³]	2859.0 (5)	1921.5(3)	6048 (2)	6249.6(3)
<i>Z</i>	2	4	4	4
ρ_{calcd} [g cm ⁻³]	1.438	1.639	1.572	1.499
μ (Mo K α) [mm ⁻¹]	0.725	0.766	1.351	1.607
<i>F</i> (000)	1286	976	2928	2864
reflns collected	21350	4727	46099	40580
unique reflns	12060	2162	12890	12755
<i>R</i> _{int}	0.0486	0.0312	0.1248	0.0327
reflns obsd [<i>I</i> > 2 σ (<i>I</i>)]	7513	1706	6763	10006
parameters/restraints	780/14	143/0	734/0	792/49
GOF on <i>F</i> ²	0.979	1.001	1.037	1.024
<i>R</i> 1 [<i>I</i> > 2 σ (<i>I</i>)]	0.0734	0.0368	0.0930	0.0470
w <i>R</i> 2 (all data)	0.1974	0.0770	0.2160	0.1284
Larg. residuals [e Å ⁻³]	+0.77/-1.01	+0.51/-0.37	+1.57/-2.43	+2.48/-0.67

	11	12	13	14
Formula	C ₂₃ H ₃₄ MnNO ₁₀	C ₃₀ H ₄₇ FeN ₂ O ₁₀	C ₆₂ H ₆₆ Mn ₃ N ₆ O ₂₂	C ₅₄ H ₆₀ Mn ₃ N ₄ O ₂₂
Mr	539.45	651.55	1412.03	1281.88
Cryst size[mm]	0.33 x 0.24 x 0.05	0.38 x 0.35 x 0.17	0.29 x 0.21 x 0.031	0.21 x 0.17 x 0.04
color	black	red	greenish black	greenish black
Cryst Syst	monoclinic	monoclinic l	monoclinic	triclinic
Space group	P 2 ₁ /c	P 2 ₁ /c	P 2 ₁ /n	P -1
T[K]	150	150	100	150
<i>a</i> [Å]	13.0949(10)	10.4560(9)	12.8326(6)	9.6054(14)
<i>b</i> [Å]	8.7941(7)	14.5286(9)	16.9338(8)	11.4207(17)
<i>c</i> [Å]	22.1208(19)	11.0919(10)	14.7252(7)	14.352(2)
<i>α</i> [deg]	90	90	90	112.841(11)
<i>β</i> [deg]	100.630(7)	102.817(7)	99.885(1)	103.739(12)
<i>γ</i> [deg]	90	90	90	91.718(12)
<i>V</i> [Å ³]	2503.7(4)	1643.0(2)	3152(4)	1396.3(4)
Z	4	2	2	1
ρ _{calcd} [g cm ⁻³]	1.431	1.317	1.488	1.525
μ(Mo Kα) [mm ⁻¹]	0.583	0.515	0.675	0.753
<i>F</i> (000)	1136	694	1462	663
reflns collected	17321	10790	15699	10088
unique reflns	4822	7069	7047	5825
<i>R</i> _{int}	0.0605	0.0175	0.0271	0.0547
reflns obsd [<i>I</i> > 2σ(<i>I</i>)]	3471	6765	6442	4025
parameters/restraints	328/4	391/1	441/6	390/5
GOF on <i>F</i> ²	0.996	1.094	1.154	0.992
<i>R</i> 1 [<i>I</i> > 2σ(<i>I</i>)]	0.0599	0.0501	0.0628	0.0592
w <i>R</i> 2 (all data)	0.1396	0.1323	0.1397	0.1402
Larg. residuals [e Å ⁻³]	+0.61/-0.91	+0.45/-0.55	+1.13/-1.01	+0.70/-0.89

	15	16	17	18
Formula	C ₄₆ H ₅₄ Mn ₃ N ₂ O ₂₃	C ₅₂ H ₄₂ Cu ₃ N ₄ O ₁₆	C ₃₈ H ₅₀ Mn ₃ N ₂ O ₁₆	C ₃₆ H ₃₈ Mn ₃ N ₂ O ₁₂
Mr	1167.73	1169.52	955.62	855.50
Cryst size[mm]	0.23 x 0.09 x 0.03	0.37 x 0.31 x 0.11	0.14 x 0.06 x 0.03	
color	black	green	black	brown
Cryst Syst	triclinic	monoclinic	triclinic	monoclinic
Space group	P -1	P 2 ₁ /n	P-1	C 2/c
T[K]	150	150	150	200
a [Å]	13.0629(10)	11.0774(12)	9.4051(16)	23.784(3)
b [Å]	13.7564(10)	12.2683(8)	10.1679(17)	8.1517(7)
c [Å]	15.8000(12)	17.8798(17)	12.403(2)	22.069(3)
α [deg]	85.897(1)	90	99.731(12)	90
β [deg]	69.393(1)	94.099(8)	101.448(13)	119.056(14)
γ [deg]	67.905(1)	90	112.202(13)	90.00
V [Å ³]	2456.3(3)	2423.7(4)	1036.6(3)	3740.2(8)
Z	2	2	1	4
ρ _{calcd} [g cm ⁻³]	1.579	1.603	1.531	1.519
μ(Mo Kα) [mm ⁻¹]	0.848	1.383	0.973	1.062
F(000)	1206	1194	495	1756
reflns collected	12885	15299	7193	11086
unique reflns	9933	5130	4304	3349
R _{int}	0.0549	0.0346	0.0259	0.0774
reflns obsd [<i>I</i> > 2σ(<i>I</i>)]	5554	4174	3412	2148
parameters/restraints	690/9	345/0	279/1	244/0
GOF on <i>F</i> ²	0.958	1.008	0.988	1.036
R1 [<i>I</i> > 2σ(<i>I</i>)]	0.0574	0.0520	0.0405	0.0564
wR2 (all data)	0.1256	0.1309	0.0983	0.1605
Larg. residuals [e Å ⁻³]	+ 1.25/-0.50	+ 0.46/-1.11	+ 0.44/-0.78	+ 0.70/-0.36

	19	20	21	22
Formula	C ₂₉ H ₄₂ Mn ₃ N ₂ O ₁₇	C ₃₉ H ₅₇ Mn ₃ N ₃ O ₁₇ Cl	C ₄₈ H ₆₂ Mn ₂ Ni ₂ N ₄ O ₂₆	C ₄₈ H ₆₈ Mn ₂ Ni ₂ N ₄ O ₂₀ Cl ₂
Mr	855.47	1040.15	1338.32	1319.26
Cryst size[mm]	0.25 x 0.18 x 0.11	0.26 x 0.21 x 0.16		0.30 x 0.26 x 0.19
color	black	black	greenish black	greenish black
Cryst Syst	triclinic	trigonal	triclinic	monoclinic
Space group	P -1	R -3	P -1	C 2/c
T[K]	150	100	200	150
<i>a</i> [Å]	10.5589 (13)	16.0482(3)	13.4398(18)	20.559(3)
<i>b</i> [Å]	11.7673 (14)	16.0482(3)	13.4811(19)	24.111(2)
<i>c</i> [Å]	14.7717 (15)	30.7061(12)	18.151(2)	11.880(1)
α [deg]	80.134(2)	90	105.358(15)	90
β [deg]	71.506(3)	90	90.165(15)	109.293(10)
γ [deg]	86.287(2)	120	116.316(15)	90
<i>V</i> [Å ³]	1714.7 (3)	6848.7(3)	2814.9(6)	5520.9(1)
Z	2	6	2	4
ρ_{calcd} [g cm ⁻³]	1.657	1.513	1.579	1.587
μ (Mo K α) [mm ⁻¹]	1.560	0.949	1.186	1.294
<i>F</i> (000)	882	3240	1384	2736
reflns collected	11248	12832	17101	18523
unique reflns	6660	3466	9751	5835
<i>R</i> _{int}	0.0721	0.0300	0.0753	0.0604
reflns obsd [<i>I</i> > 2 σ (<i>I</i>)]	4141	3050	5942	3578
parameters/restraints	474/4	215/18	741/21	361/2
GOF on <i>F</i> ²	1.022	1.020	0.977	0.992
<i>R</i> 1 [<i>I</i> > 2 σ (<i>I</i>)]	0.0854	0.0437	0.0641	0.0631
w <i>R</i> 2 (all data)	0.2179	0.112	0.1508	0.1441
Larg. residuals [e Å ⁻³]	+ 1.26/-1.09	+ 1.01/-0.55	+0.96/-0.76	+0.99/-1.25

Chapter 9: Bibliography

- [1] (a) C. P. Landee, D. Melville, and J. S. Miller in *NATO ARW Molecular Magnetic Materials*, O. Kahn, D. Gatteschi, J. S. Miller, and F. Palacio, Eds., **1991**, *E198*, 395; (b) B. G. Morin, C. Hahn, A. J. Epstein, and J. S. Miller, *J. Appl. Phys.*, **1994**, *75*, 5782; (c) J. S. Miller and A. J. Epstein, *Chemtech*, **1991**, *21*, 168; (d) J. S. Miller, *Adv. Mater.*, **1994**, *6*, 322.
- [2] (a) J. Larionova, O. Kahn, S. Golhen, L. Ouahab, R. Clérac, *J. Am. Chem. Soc.*, **1999**, *121*, 3349; (b) M. Ohba, N. Usuki, N. Fukita, H. Okawa, *Angew. Chem.*, **1999**, *111*, 1911; *Angew. Chem. Int. Ed.*, **1999**, *38*, 1795; (c) J. S. Miller, *Adv. Mater.*, **2002**, *14*, 1105; (d) J. R. Galán-Mascarós, K. R. Dunbar, *Angew. Chem.*, **2003**, *115*, 2391; *Angew. Chem. Int. Ed.*, **2003**, *42*, 2289; (e) H. Miyasaka, H. Ieda, N. Matsumoto, K. Sugiura, M. Yamashita, *Inorg. Chem.*, **2003**, *42*, 3509.
- [3] (a) J. K. Kim; J. M. Lim, Y.-K. Choi, Y. Do, *Angew. Chem. Int. Ed. Engl.*, **1996**, *35*, 998; (b) F. A. Mantner, R. Cortes, L. Lezama, T. Rojo, *Angew. Chem. Int. Ed. Engl.*, **1996**, *35*, 78; (c) H. Miyasaka, N. Matsumoto, H. Okawa, N. Re, E. Gallo, C. Floriani, *J. Am. Chem. Soc.*, **1996**, *118*, 981; (d) W. R. Entley, G. S. Girolami, *Science*, **1995**, *268*, 397.
- [4] (a) G. S. Papaefstathiou, R. Vicente, C. P. Raptopoulou, A. Terzis, A. Escuer, S. P. Perlepes, *Eur. J. Inorg. Chem.*, **2002**, 2488; (b) Y. Kim, D. P. Jung, *Inorg. Chem.*, **2000**, *39*, 1470; (c) E. Lee, Y. Kim, D. Y. Jung, *Inorg. Chem.*, **2002**, *41*, 501; (d) T. F. Liu, H. L. Sun, S. Gao, S. W. Zhang, T. C. Lau, *Inorg. Chem.*, **2003**, *42*, 4792; (e) M.-L. Tong, S. Kitagawa, H.-C. Chang, M. Ohba, *Chem. Comm.*, **2004**, 418; (f) W.-W. Ni, Z.-H. Ni, A.-L. Cui, X. Liang, H.-Z. Kou, *Inorg. Chem.*, **2007**, *46*, 22.
- [5] G. Aromi, S. M. J. Aubin, M. A. Bolcar, G. Christou, H. J. Eppley, K. Folting, D. N. Hendrickson, J. C. Huffman, R. C. Squire, H. L. Tsai, S. Wang, M. W. Wemple, *Polyhedron*, **1998**, *17*, 3005.
- [6] D. Gatteschi, R. Sessoli, J. Villain, *Molecular Nanomagnets*, Oxford University Press, Oxford, **2006**.
- [7] A. L. Barra, P. Debrunner, D. Gatteschi, Ch. E. Schulz, R. Sessoli, *Europhys. Lett.*, **1996**, *35*, 133.
- [8] S. M. J. Aubin, N. R. Dilley, L. Pardi, J. Krzystek, M. W. Wemple, L. C. Brunel, M. B. Maple, G. Christou, D. N. Hendrickson, *J. Am. Chem. Soc.*, **1998**, *120*, 4991.
- [9] S. L. Castro, Z. M. Sun, C. M. Grant, J. C. Bollinger, D. N. Hendrickson, G. Christou, *J. Am. Chem. Soc.*, **1998**, *120*, 2365.
- [10] A. L. Barra, A. Caneschi, A. Cornia, F. F. De Biani, D. Gatteschi, C. Sangregorio, R. Sessoli, L. Sorace, *J. Am. Chem. Soc.*, **1999**, *121*, 5302.
- [11] A. L. Barra, A. Caneschi, D. Gatteschi, D. P. Goldberg, R. Sessoli, *J. Solid State Chem.*, **1999**, *145*, 484.
- [12] J. Yoo, E. K. Brechin, A. Yamaguchi, M. Nakano, J. C. Huffman, A. L. Maniero, L. C. Brunel, K. Awaga, H. Ishimoto, G. Christou, D. N. Hendrickson, *Inorg. Chem.*, **2000**, *39*, 3615.

- [13] J.C. Goodwin, R. Sessoli, D. Gatteschi, W. Wernsdorfer, A.K. Powell, S.L. Heath, A.L. Barra, *J. Chem. Soc. Dalton Trans.*, **2000**, 4702.
- [14] C. Boskovic, E.K. Brechin, W.E. Streib, K. Folting, D.N. Hendrickson, G. Christou, *Chem. Commun.*, **2001**, 467.
- [15] L.F. Jones, E.K. Brechin, D. Collison, M. Helliwell, T. Mallah, S. Piligkos, G. Rajaraman, W. Wernsdorfer, *Inorg. Chem.*, **2003**, 6601.
- [16] E.C. Yang, N. Harden, W. Wernsdorfer, L. Zakharov, E.K. Brechin, A.L. Rheingold, G. Christou, D.N. Hendrickson, *Polyhedron*, **2003**, 1857.
- [17] S. Osa, T. Kido, N. Matsumoto, N. Re, A. Pochaba, J. Mrozinski, *J. Am. Chem. Soc.*, **2004**, 126, 420.
- [18] M. Soler, W. Wernsdorfer, K. Folting, M. Pink, G. Christou, *J. Am. Chem. Soc.*, **2004**, 126, 2156.
- [19] M. Murugesu, M. Habrych, W. Wernsdorfer, K. A. Abboud, G. Christou, *J. Am. Chem. Soc.*, **2004**, 126, 4766.
- [20] C. J. Milios, R. Inglis, R. Bagai, W. Wernsdorfer, A. Collins, S. Moggach, S. Parsons, S. P. Perlepes, G. Christou, E. K. Brechin, *Chem. Commun.*, **2007**, 3476.
- [21] M. Murrie, S. J. Teat, H. Stoeckli-Evans, H.U. Gudel, *Angew. Chem. Int. Ed.*, **2003**, 42, 4653.
- [22] N. Aliaga-Alcalde, R.S. Edwards, S.O. Hill, W. Wernsdorfer, K. Folting, G. Christou, *J. Am. Chem. Soc.*, **2004**, 126, 12503.
- [23] E. C. Sanudo, W. Wernsdorfer, K. A. Abboud, G. Christou, *Inorg. Chem.*, **2004**, 43, 4137.
- [24] G. Chaboussant, R. Basler, H. U. Gudel, S. Ochsenbein, A. Parkin, S. Parsons, G. Rajaraman, A. Sieber, A. A. Smith, G. A. Timco, R. E. P. Winpenny, *Dalton Trans.*, **2004**, 2758.
- [25] C. M. Zaleski, E. C. Depperman, J. W. Kampf, M. L. Kirk, V. L. Pecoraro, *Angew. Chem. Int. Ed.*, **2004**, 43, 3912.
- [26] H. Miyasaka, K. Nakata, K.-I. Sugiura, M. Yamashita, R. Clérac, *Angew. Chem. Int. Ed.*, **2004**, 43, 707.
- [27] H. Oshio, N. Hoshino, T. Ito, M. Nakano, *J. Am. Chem. Soc.*, **2004**, 126, 8805.
- [28] A. Caneschi, D. Gatteschi, N. Lalioti, C. Sangregorio, R. Sessoli, G. Venturi, A. Vindigni, A. Rettori, M. G. Pini, M. A. Novak, *Angew. Chem. Int. Ed.*, **2001**, 40, 1760.
- [29] T. Kajiwara, M. Nakano, Y. Kaneko, S. Takaishi, T. Ito, M. Yamashita, A. Igashira-Kamiyama, H. Nojiri, Y. Ono, N. Kojima, *J. Am. Chem. Soc.*, **2005**, 127, 10150.

- [30] M. Ferbinteanu, H. Miyasaka, W. Wernsdorfer, K. Nakata, K. Sugiura, M. Yamashita, C. Coulon, R. Clérac, *J. Am. Chem. Soc.*, **2005**, *127*, 3090.
- [31] E. Pardo, R. Ruiz-Garcia, F. Lloret, J. Faus, M. Julve, Y. Journaux, F. Delgado, C. Ruiz-Perez, *Adv. Mater.*, **2004**, *16*, 1597.
- [32] N.E. Chakov, W. Wernsdorfer, K.A. Abboud, G. Christou, *Inorg. Chem.*, **2004**, *43*, 5919.
- [33] H. Miyasaka, R. Clérac, K. Mizushima, K. Sugiura, M. Yamashita, W. Wernsdorfer, C. Coulon, *Inorg. Chem.*, **2003**, *42*, 8203.
- [34] R. Clérac, H. Miyasaka, M. Yamashita, C. Coulon, *J. Am. Chem. Soc.*, **2002**, *124*, 12837.
- [35] L. Bogani, C. Sangregorio, R. Sessoli, D. Gatteschi, *Angew. Chem. Int. Ed.*, **2005**, *44*, 5817.
- [36] J.-K. Tang, I. J. Hewitt, N. T. Madhu, G. Chastanet, W. Wernsdorfer, C. E. Anson, C. Benelli, R. Sessoli, A. K. Powell, *Angew. Chem. Int. Ed.*, **2006**, *45*, 1729.
- [37] I. J. Hewitt, J.-K. Tang, N.T. Madhu, R. Clérac, G. Buth, C. E. Anson, A. K. Powell, *Chem. Comm.*, **2006**, *25*, 2650.
- [38] G. Wu, I. J. Hewitt, S. Mameri, Y. Lan, R. Clérac, C.E. Anson, S. Qiu, A.K. Powell, *Inorg. Chem.*, **2007**, *46*, 7229.
- [39] (a) H. Oshio, N. Hoshino; T. Ito, M. Nakano, *J. Am. Chem. Soc.*, **2004**, *126*, 8805; (b) H. Miyasaka, R. Clérac, W. Wernsdorfer, L. Lecren, C. Bonhomme, K. -I. Sugiura, M. Yamashita, *Angew. Chem. Int. Ed.*, **2004**, *43*, 2801; (c) C. Aronica, G. Pilet, G. Chastanet, W. Wernsdorfer, J. -F. Jacquot, D. Luneau, *Angew. Chem. Int. Ed.*, **2006**, *45*, 4659.
- [40] C. Christmas, J. B. Vincent, H.- R. Chang, J. C. Huffman, G. Christou, D. N. Hendrickson, *J. Am. Chem. Soc.*, **1988**, *110*, 823.
- [41] X. S. Tan, J. Chen, Z. N. Chen, P. J. Zheng, W. X. Tang, *Inorg. Chim. Acta* , **1995**, *234*, 27.
- [42] X. S. Tan, J. Sun, C. H. Hu, D. G. Fu, D. F. Xiang, P. J. Zheng, W. X. Tang, *Inorg. Chim. Acta*, **1997**, *257*, 203.
- [43] H. Miyasaka, R. Clérac, W. Wernsdorfer, L. Lecren, C. Bonhomme, K.-I. Sugiura, M. Yamashita, *Angew. Chem. Int. Ed.*, **2004**, *43*, 2801.
- [44] C. Boskovic, R. Bircher, P. L. W. T. -Piggott, H. U. Güdel, C. Paulsen, W. Wernsdorfer, A. - L. Barra, E. Khatsko, A. Neels, H. -S. Evans. *J. Am. Chem. Soc.*, **2003**, *125*, 14046.
- [45] C. J. Milios, A. Vinslava, W. Wernsdorfer, S. Moggach, S. Parsons, S. P. Perlepes, G. Christou, E. K. Brechin, *J. Am. Chem. Soc.*, **2007**, *129*, 2754.
- [46] H. Oshio, M. Nihei, A. Yoshida, H. Nojiri, M. Nakano, A. Yamaguchi, Y. Karaki, Hi. Ishimoto, *Chem. Eur. J.*, **2005**, *11*, 843.

- [47] H. Oshio, M. Nihei, S. Koizumi, T. Shiga, H. Nojiri, M. Nakano, N. Shirakawa, M. Akatsu, *J. Am. Chem. Soc.*, **2005**, *127*, 4568.
- [48] F. E. Mabbs, D. J. Mchin, *Magnetism and Transition Metal Complexes*, Chapman and Hall, **1973**.
- [49] C. J. O'Connor, *Prog. Inorg. Chem.*, **1982**, *29*, 203.
- [50] R. L. Carlin, *Magnetochemistry*, Springer-Verlag, **1986**.
- [51] O. Khan, *Molecular Magnetism*, VCH Publ., Inc., **1993**.
- [52] C. Kittel, *Introduction to Solid State Physics*, 2nd Ed., J. Wiley and Sons, New York, **1953**.
- [53] E. A. Boudreaux, L. N. Mulay, *Theory and Applications of Molecular Paramagnetism*, J. Wiley & Sons, New York, **1976**.
- [54] F. Palacio, *Introduction to Physical Techniques in Molecular Magnetism*, University of Zaragoza, Zaragoza, **1999**.
- [55] (a) G. Aromi' and E. K. Brechin, *Struct. Bonding*, **2006**, 122; (b) G. Christou, D. Gatteschi, D. N. Hendrickson, R. Sessoli, *MRS Bull.*, **2000**, *25*, 66; (c) D. Gatteschi, R. Sessoli, *Angew. Chem., Int. Ed.*, **2003**, *42*, 268; (d) R. Sessoli, D. Gatteschi, A. Caneschi, M. A. Novak, *Nature*, **1993**, *365*, 141; (e) M. N. Leuenberger and D. Loss, *Nature*, **2001**, *410*, 789.
- [56] (a) W. Wernsdorfer, N. A.-Alcalde, D. N. Hendrickson and G. Christou, *Nature*, **2002**, *416*, 406; (b) W. Wernsdorfer, S. Bhaduri, R. Tiron, D. N. Hendrickson and G. Christou, *Phys. Rev. Lett.*, **2002**, *89*, 197201; (c) K. Park, M. R. Pederson, S. L. Richardson, N. A.-Alcalde and G. Christou, *Phys. Rev. B*, **2003**, *68*, 020405; (d) S. Hill, R. S. Edwards, N. A.-Alcalde and G. Christou, *Science*, **2003**, *302*, 1015; (e) R. Tiron, W. Wernsdorfer, N. A.-Alcalde, G. Christou, *Phys. Rev. B*, **2003**, *68*, 140407(R); (f) R. Tiron, W. Wernsdorfer, D. F.-Albiol, N. A.-Alcalde, G. Christou, *Phys. Rev. Lett.*, **2003**, *91*, 27203.
- [57] (a) P. J. Hagrman, D. Hagrman, J. Zubieta, *Angew. Chem. Int. Ed.*, **1999**, *38*, 2639; (b) A. J. Blake, N. R. Champness, P. Hubberstey, W. S. Li, M. A. Withersby, M. Schroder, *Coord. Chem. Rev.*, **1999**, *183*, 117; (c) A. N. Khlobystov, A. J. Blake, N. R. Champness, D. A. Lemenovskii, A. G. Majouga, N. V. Zyk, M. Schröder, *Coord. Chem. Rev.*, **2001**, *222*, 155; (d) M. Eddaoudi, D. B. Moler, H. Li, B. L. Chen, T. M. Reineke, M. O'Keeffe, O. M. Yaghi, *Acc. Chem. Res.*, **2001**, *34*, 319; (e) M. J. Zaworotko, *Chem. Commun.*, **2001**, 1; (f) B. Moulton, M. J. Zaworotko, *Chem. Rev.*, **2001**, *101*, 1629.
- [58] (a) S. R. Batten, R. Robson, *Angew. Chem. Int. Ed.*, **1998**, *37*, 1460; (b) S. R. Batten, *Cryst. Eng. Comm.*, **2001**, *3*, 67.
- [59] Z. Pučeková-Repická, J. Moncol, D. Valigura, T. Lis, M. Korabik, M. Melník, J. Mroziński, M. Mazur, *J. Coord. Chem.*, **2007**, *60*, 2449.
- [60] T. Kido, Y. Ikuta, Y. Sunatsuki, Y. Ogawa, N. Matsumoto, *Inorg. Chem.*, **2003**, *42*, 398.

- [61] (a) A. Bencini, C. Benelli, A. Caneschi, A. Dei, D. Gatteschi, *Inorg. Chem.*, **1986**, 25, 572; (b) A. Bencini, C. Benelli, A. Caneschi, R. L. Carlin, A. Dei, D. Gatteschi, *J. Am. Chem. Soc.*, **1985**, 107, 8128; (c) S. R. Bayly, Z. Xu, B. O. Patrick, S. J. Rettig, M. Pink, R. C. Thompson, C. Orvig, *Inorg. Chem.*, **2003**, 42, 1576.
- [62] (a) C. Benelli, A. Caneschi, D. Gatteschi, O. Guillou, L. Pardi, *Inorg. Chem.*, **1990**, 29, 1750; (b) T. Kido, S. Nagasato, Y. Sunatsuki, N. Matsumoto, *Chem. Commun.*, **2000**, 2113.
- [63] M. Andruk, L. Ramade, E. Codjovi, O. Guillou, O. Kahn, J. C. Trombe, *J. Am. Chem. Soc.*, **1993**, 115, 1822.
- [64] (a) R. Georges, O. Kahn, O. Guillou, *Phys. Rev. B*, **1994**, 49, 3235; (b) S. Wang, Z. Pang, M. J. Wagner, *Inorg. Chem.*, **1992**, 31, 5381.
- [65] (a) O. Guillou, O. Kahn, R. L. Oushoorn, *Inorg. Chim. Acta*, **1992**, 119, 198; (b) O. Guillou, R. L. Oushoorn, O. Kahn, K. Boubekeur, P. Batail, *Angew. Chem. Int. Ed. Engl.*, **1992**, 31, 626; (c) C. Daiguebonne, O. Guillou, M. L. Kahn, O. Kahn, R. L. Oushoorn, K. Boubekeur, *Inorg. Chem.*, **2001**, 40, 176; (d) Z. He, C. He, E. Q. Gao, Z. M. Wang, X. F. Yang, C. S. Liao, C. H. Yan, *Inorg. Chem.*, **2003**, 42, 2206; (e) H. Z. Kou, B. C. Zhou, R. J. Wang, *Inorg. Chem.* **2003**, 42, 7658; (f) B. Zhao, P. Cheng, Y. Dai, C. Cheng, D. Z. Liao, S. P. Yan, Z. H. Jiang, G. L. Wang, *Angew. Chem. Int. Ed.*, **2003**, 42, 934.
- [66] X. S. Tan, J. Chen, Z. N. Chen, P. J. Zheng, W. X. Tang, *Inorg. Chim. Acta*, **1995**, 234, 27.
- [67] H. H. Thorp, *Inorg. Chem.*, **1992**, 31, 1585.
- [68] V. A. Blatov, A. P. Shevchenko, V. N. Serezhkin, *J. Appl. Crystallogr.*, **2000**, 33, 1193.
- [69] X. S. Tan, J. Sun, C. H. Hu, D. G. Fu, D. F. Xiang, P. J. Zheng, W. X. Tang, *Inorg. Chim. Acta*, **1997**, 257, 203.
- [70] (a) C. Janiak, *J. Chem. Soc., Dalton Trans.*, **2000**, 3885; (b) V. Russell, M. Scudder, I. J. Dance, *Chem. Soc. Dalton Trans.*, **2001**, 789.
- [71] R. Georges, J. J. Borrás-Almenar, E. Coronado, J. Curély and M. Drillon, “*Magnetism: Molecules to Materials I*, Wiley-VCH, J.S. Miller and M. Drillon Ed., p. 1-47.
- [72] C. Benelli, D. Gatteschi, *Chem. Rev.*, **2002**, 102, 2369.
- [73] M. L. Kahn, J.-P. Sutter, S. Golhen, P. Guionneau, L. Ouahab, O. Kahn, D. Chasseau, *J. Am. Chem. Soc.*, **2000**, 122, 3413.
- [74] A. Figuerola, C. Diaz, J. Ribas, V. Tangoulis, C. Sangregorio, D. Gatteschi, M. Maestro, J. Mahía, *Inorg. Chem.*, **2003**, 42, 5274.
- [75] A. Figuerola, J. Ribas, X. Solans, M. F.-Bardía, M. Maestro, C. Diaz, *Eur. J. Inorg. Chem.*, **2006**, 1846.
- [76] J. K. McCusker, C. A. Christmas, P. M. Hagen, R. K. Chadha, D. F. Harvey, D. N. Hendrickson, *J. Am. Chem. Soc.*, **1991**, 113, 6114.

- [77] T. Sala, *J. Chem. Soc., Chem. Commun.*, **1978**, 89, 253.
- [78] J. H. Van Vleck, *The Theory of Electric and Magnetic Susceptibility*, Oxford University Press, **1932**.
- [79] K. Kambe, *J. Phys. Soc., Jpn.* **5**, **1950**, 48.
- [80] J. B. Vincent, H. R. Chang, K. Folting, J. C. Huffman, G. Christou, D. N. Hendrickson, *J. Am. Chem. Soc.*, **1987**, *109*, 5703.
- [81] W. H. Crawford, H. W. Richardson, I. R. Wasson, D. J. Hodgson, W. E. Hatfield, *Inorg. Chem.*, **1976**, *15*, 2107.
- [82] P. King, R. Clérac, C. E. Anson, C. Coulon, A. K. Powell, *Inorg. Chem.*, **2003**, *42*, 3492.
- [83] S. M. J. Aubin, M. W. Wemple, D. M. Adams, H.-L. Tsai, G. Christou, D. N. Hendrickson, *J. Am. Chem. Soc.*, **1996**, *118*, 7746.
- [84] G. Christou, D. Gatteschi, D. N. Hendrickson, R. Sessoli, *MRS Bull.*, **2000**, *25*, 66.
- [85] G. Aromí, E. K. Brechin, *Struct. Bonding*, **2006**, *122*, 1.
- [86] R. Sessoli, D. Gatteschi, A. Caneschi, M. A. Novak, *Nature (London)*, **1993**, *365*, 141.
- [87] (a) H. J. Eppley, G. Christou, N. A. Law, V. L. Pecoraro, *Inorg. Synth.*, **2002**, *33*, 61; (b) H. J. Eppley, H.-L. Tsai, N. de Vries, K. Folting, G. Christou, D. N. Hendrickson, *J. Am. Chem. Soc.*, **1995**, *117*, 301; (c) M. Soler, W. Wernsdorfer, K. A. Abboud, J. C. Huffman, E. R. Davidson, D. N. Hendrickson, G. Christou, *J. Am. Chem. Soc.*, **2003**, *125*, 3576; (d) P. Artus, C. Boskovic, J. Yoo, W. E. Streib, L.-C. Brunel, D. N. Hendrickson, G. Christou, *Inorg. Chem.*, **2001**, *40*, 4199; (e) C. Boskovic, M. Pink, D. N. Hendrickson, G. Christou, *J. Am. Chem. Soc.*, **2001**, *123*, 9914.
- [88] (a) S. M. J. Aubin, M. W. Wemple, D. M. Adams, H.-L. Tsai, G. Christou, D. N. Hendrickson, *J. Am. Chem. Soc.*, **1996**, *118*, 7746; (b) J. Yoo, E. K. Brechin, A. Yamaguchi, M. Nakano, J. C. Huffman, A. L. Maniero, L. -C. Brunel, K. Awaga, H. Ishimoto, G. Christou, D. N. Hendrickson, *Inorg. Chem.*, **2000**, *39*, 3615; (c) J. Yoo, A. Yamaguchi, M. Nakano, J. Krzystek, W. E. Streib, L. -C. Brunel, H. Ishimoto, G. Christou, D. N. Hendrickson, *Inorg. Chem.*, **2001**, *40*, 4604; (d) C. Boskovic, K. Folting, J. C. Huffman, D. N. Hendrickson, G. Christou, *Inorg. Chem.*, **2002**, *41*, 5107; (e) C. Boskovic, E. K. Brechin, W. E. Streib, K. Folting, J. C. Bollinger, D. N. Hendrickson, G. Christou, *J. Am. Chem. Soc.*, **2002**, *124*, 3725; (f) E. K. Brechin, C. Boskovic, W. Wernsdorfer, J. Yoo, A. Yamaguchi, E. C. Sañudo, T. R. Concolino, A. L. Rheingold, H. Ishimoto, D. N. Hendrickson, G. Christou, *J. Am. Chem. Soc.*, **2002**, *124*, 9710; (g) E. K. Brechin, M. Soler, J. Davidson, D. N. Hendrickson, S. Parsons, G. Christou, *Chem. Commun.*, **2002**, 2252; (h) A.-L. Barra, A. Caneschi, D. Gatteschi, D. P. Goldberg, R. Sessoli, *J. Solid State Chem.*, **1999**, *145*, 484.
- [89] (a) C. Sangregorio, T. Ohm, C. Paulsen, R. Sessoli, D. Gatteschi, *Phys. Rev. Lett.*, **1997**, *78*, 4645; (b) A.-L. Barra, A. Caneschi, A. Cornia, F. F. deBiani, D. Gatteschi, C. Sangregorio, R. Sessoli; L. Sorace, *J. Am. Chem. Soc.*, **1999**, *121*, 5302; (c) H. Oshio, N. Hoshino, T. Ito, *J.*

Am. Chem. Soc., **2000**, *120*, 2997; (d) J. C. Goodwin, R. Sessoli, D. Gatteschi, W. Wernsdorfer, A. K. Powell, S. L. Heath, *J. Chem. Soc. Dalton Trans.*, **2000**, 1835.

[90] (a) H. Andres, R. Basler, A. J. Blake, C. Cadiou, G. Chaboussant, C. M. Grant, H. U. Güdel, M. Murrie, S. Parsons, C. Paulsen, F. Semadini, V. Villar, W. Wernsdorfer, R. E. P. Winpenny, *Chem. Eur. J.*, **2002**, *8*, 4867; (b) S. T. Ochsenbein, M. Murrie, E. Rusanov, H. Stoeckli-Evans, C. Sekine, H. -U. Güdel, *Inorg. Chem.*, **2002**, *41*, 5133.

[91] W. Wernsdorfer, N. Aliaga-Alcalde, D. N. Hendrickson, G. Christou, *Nature*, **2002**, *416*, 406.

[92] (a) A. Yamaguchi, N. Kusumi, H. Ishimoto, H. Mitamura, T. Goto, N. Mori, M. Nakano, K. Awaga, J. Yoo, D. N. Hendrickson, G. Christou, *J. Phys. Soc. Jpn.*, **2002**, *71*, 414; (b) M. Affronte, J. C. Lasjaunias, W. Wernsdorfer, R. Sessoli, D. Gatteschi, S. L. Heath, A. Fort, A. Rettori, *Phys. Rev. B.*, **2002**, *66*, 064408; (c) M. Murrie, S. J. Teat, H. Stoeckli-Evans, H. U. Güdel, *Angew. Chem.*, **2003**, *115*, 4801.

[93] (a) J.-K. Tang, I. J. Hewitt, N.T. Madhu, G. Chastanet, W. Wernsdorfer, C. E. Anson, C. Benelli, R. Sessoli, A. K. Powell, *Angew. Chem. Int. Ed.*, **2006**, *45*, 1729; (b) J.-P. Costes, S. Sergiu; W. Wernsdorfer, *Dalton Trans.*, **2008**, *14*, 1843; (c) G. Novitchi, J.-P. Costes, J.-P. Tuchagues, L. Vendier, W. Wernsdorfer, *New J. Chem.*, **2008**, *32(2)*, 197.

[94] (a) M. Ferbinteanu, T. Kajiwara, K.-Y. Choi, H. Nojiri, N. Hiroyuki, K. Akio; N. Kojima, F. Cimpoesu, Y. Fujimura, S. Takaishi, M. Yamashita, *J. Am. Chem. Soc.*, **2006**, *128*, 9008; (b) V. Mereacre, A. M. Ako, R. Clerac, W. Wernsdorfer, I. J. Hewitt, C. E. Anson, A. K. Powell, *Chem. Eur. J.*, **2008**, *14*, 3577.

[95] (a) S. L. Castro, Z. Sun, C. M. Grant, J. C. Bollinger, D. N. Hendrickson, G. Christou, *J. Am. Chem. Soc.*, **1998**, *120*, 2365; (b) S. M. J. Aubin, M. W. Wemple, D. M. Adams, H.-L. Tsai, G. Christou, D. N. Hendrickson, *J. Am. Chem. Soc.*, **1996**, *118*, 7746; (c) H. Oshio, N. Hoshino, T. Ito, *J. Am. Chem. Soc.*, **2000**, *122*, 12602; (d) C. Cadiou, M. Murrie, C. Paulsen, V. Villar, W. Wernsdorfer, R. E. P. Winpenny, *Chem. Commun.*, **2001**, 2666; (e) P. L. Feng, C. C. Beedle, C. Koo, W. Wernsdorfer, M. Nakano, S. Hill, D. N. Hendrickson, *Inorg. Chem.*, **2008**, *47*, 3188.

[96] G. Aromí, S. Parsons, W. Wernsdorfer, E. K. Brechin, E. J. L. McInnes, *Chem. Commun.*, **2005**, 5038.

[97] O. Waldmann, *Inorg. Chem.*, **2007**, *46*, 10035.

[98] E. Ruiz, J. Cirera, J. Cano, S. Alvarez, C. Loose, J. Kortus, *Chem. Commun.*, **2008**, 52.

Appendix A: List of compounds

- 1 $[\text{Mn}^{\text{III}}_2\text{Mn}^{\text{II}}(3\text{-Me-sal})_4(\text{py})_4]$
- 2 $[\text{Mn}^{\text{III}}_2\text{Mn}^{\text{II}}(4\text{-Me-sal})_4(\text{py})_4(\text{MeOH})] \cdot \text{H}_2\text{O}$
- 3 $[\text{Mn}^{\text{III}}_2\text{Mn}^{\text{II}}(5\text{-Me-sal})_4(\text{py})_4(\text{H}_2\text{O})_2] \cdot (\text{MeOH})$
- 4 $[\text{Mn}^{\text{III}}_2\text{Mn}^{\text{II}}(3\text{-Me-sal})_4(4\text{-Me-py})_4]$
- 5 $[\text{Mn}^{\text{III}}(4\text{-Me-sal})_2(4\text{-Me-py})_2\text{Mn}^{\text{II}}(\text{OH}_2)_2(\text{MeOH})_2][\text{Mn}^{\text{III}}(4\text{-Me-sal})_2(4\text{-Me-py})_2]$
- 6 Mn - (5-Me-salH₂) - (4-Me-py) product
- 7 $[(3\text{-MeO-sal})_2\text{MnNa}_2 \cdot \text{MeOH}]$
- 8 $[\text{Fe}_2\text{Pr}(4\text{-Me-sal})_4(2,2'\text{-bipy})_2(\text{OH}_2)_6](\text{NO}_3) \cdot 2\text{MeOH} \cdot 1.5 \text{H}_2\text{O}$
- 9 $[\text{Fe}_2\text{Gd}(4\text{-Me-sal})_4(2,2'\text{-bipy})_2(\text{OH}_2)_5]\text{Cl}_{1/2}(\text{NO}_3)_{1/2} \cdot 5\text{H}_2\text{O}$
- 10 $[\text{Fe}_2\text{Dy}(4\text{-Me-sal})_4(2,2'\text{-bipy})_2(\text{OH}_2)_5] \text{Cl}_{1/2}(\text{NO}_3)_{1/2} \cdot 5\text{H}_2\text{O}$
- 11 $(\text{NH}_4)_3 [\text{Mn}^{\text{III}}(3\text{-MeO-sal})_2(\text{MeOH})(\text{H}_2\text{O})]$
- 12 $(\text{NH}_4)_2 [\text{Fe}^{\text{III}}(3\text{-MeO-sal})_2(\text{OAc})]$
- 13 $[\text{Mn}^{\text{II}}\text{Mn}^{\text{III}}_2(3\text{-MeO-sal})_4(\text{py})_6(\text{H}_2\text{O})_2] \cdot 4\text{H}_2\text{O}$
- 14 $[\text{Mn}^{\text{III}}_2\text{Mn}^{\text{II}}(3\text{-MeO-sal})_4(\text{py})_4(\text{H}_2\text{O})_4] \cdot 4\text{MeOH}$
- 15 $[\text{Mn}^{\text{III}}_2\text{Mn}^{\text{II}}(3\text{-MeO-sal})_4(2,2'\text{-bipy})(\text{H}_2\text{O})_3(\text{MeOH})_2] \cdot 3\text{MeOH}$
- 16 $[\text{Cu}_3(3\text{-MeO-salH})_2(3\text{-MeO-sal})_2(2,2'\text{-bipy})_2]$
- 17 $[\text{Mn}^{\text{III}}_2\text{Mn}^{\text{II}}(\text{L}^1)_2(\mu\text{-OAc})_2(\mu\text{-OMe})_2(\text{MeOH})_2] \cdot 2\text{MeOH}$
- 18 $[\text{Mn}^{\text{III}}_2\text{Mn}^{\text{II}}(\text{L}^3)_2(\mu\text{-OAc})_2(\mu\text{-OMe})_2]$
- 19 $[\text{Mn}^{\text{III}}_2\text{Mn}^{\text{II}}(\text{L}^7)_2(\text{OAc})_4(\text{OH}_2)_2] \cdot \text{MeOH}$
- 20 $[\text{Mn}^{\text{III}}_3(\mu_3\text{-O})(\text{L}^{11})_3(\text{MeOH})_3](\text{ClO}_4)$
- 21 $[\text{Mn}_2^{\text{III}}\text{Ni}_2^{\text{II}}(\text{L}^{14})_4](\text{CH}_3\text{COO})_2$
- 22 $[\text{Mn}_2^{\text{III}}\text{Ni}_2^{\text{II}}(\text{L}^{14})_4](\text{Cl})_2$

Appendix B: List of organic compounds

- H₂L¹** 3-methoxysalicylidene-2-aminophenol
H₂L² 3-ethoxysalicylidene-2-aminophenol
H₂L³ 3-methoxysalicylidene-(2-amino-4-methylphenol)
H₂L⁴ 3-ethoxysalicylidene-(2-amino-4-methylphenol)
H₂L⁵ 3-hydroxysalicylidene-2-aminophenol
H₂L⁶ 3-hydroxysalicylidene-(2-amino-4-methylphenol)
H₂L⁷ 3-methoxysalicylidene-2-ethanolamine
H₂L⁸ 3-ethoxysalicylidene-2-ethanolamine
H₂L⁹ 3-hydroxysalicylidene-2-ethanolamine
H₂L¹⁰ 3-methoxysalicylidene-(2-propanolamine)
H₂L¹¹ 3-ethoxysalicylidene-(2-propanolamine)
H₂L¹² 3-hydroxysalicylidene-(2-propanolamine)
H₂L¹³ salicylidene-(2-amino-2-methyl-1,3-propanediol)
H₂L¹⁴ salicylidene-(tris-(hydroxymethyl)-aminomethane)
H₂L¹⁵ 3-methoxysalicylidene-(2-amino-2-methyl-1,3-propanediol)
H₂L¹⁶ 3-methoxysalicylidene-(tris-(hydroxymethyl)-aminomethane)
H₂L¹⁷ 3-ethoxysalicylidene-(2-amino-2-methyl-1,3-propanediol)
H₂L¹⁸ 3-ethoxysalicylidene-(tris-(hydroxymethyl)-aminomethane)

Appendix C: List of abbreviations

Ln	lanthanide
3-Me-salH ₂	3-methylsalicylic acid
4-Me-salH ₂	4-methylsalicylic acid
5-Me-salH ₂	5-methylsalicylic acid
4-Me-py	4-methylpyridine
Me	methyl
py	pyridine
Ph	phenyl
MeOH	methanol
MeCN	acetonitrile
DMF	dimethylformamide
DMSO	dimethylsulfoxide
mg	milligram
ml	millilitre
mmol	millimole
IR	infrared
NMR	nuclear magnetic resonance
EPR	electron paramagnetic resonance
SQUID	super-conducting quantum interference device
ac	alternating current
dc	direct current
D	zero-field splitting parameter
K	kelvin
Oe	oersted
<i>H</i>	field
Hz	hertz
<i>M</i>	magnetisation
<i>T</i>	temperature
T	tesla
<i>T_b</i>	blocking temperature
<i>T_c</i>	critical temperature
h	hour
χ	molar magnetic susceptibility
χ'	in-phase magnetic susceptibility
χ''	out-of-phase magnetic susceptibility
μ_B	bohr magneton
U_{eff}	effective energy barrier
cm ³	cubic centimetres
b	broad
d	doublet
t	triplet
s	singlet (NMR), strong (IR)
m	multiplet (NMR), medium (IR)
w	weak
MOFs	metal organic frameworks
SMM	single molecule magnet

Appendix D: List of figures

Figure 1.01	Substituted Salicylic acids used as ligands	4
Figure 1.02	Salicylaldimine (Schiff base) ligands used in this research	4
Figure 1.03	Structure of $[\text{Mn}_9\text{O}_4(\text{OOCPh})_8(\text{sal})_4(\text{salH})_2(\text{py})_4]$. Plots of (χ_m) and (μ_{eff}) versus temperature	5
Figure 1.04	Structure of the infinite chain of $[\text{Mn}_4(\text{sal})_4(\text{H}_2\text{O})_4(\text{py})_8][\text{salH}]_2 \cdot 4\text{py}$	6
Figure 1.05	Structure of (a) the mononuclear anion, $[\text{Mn}(\text{sal})_2(4\text{-Me-Py})_2]$ (b) the trinuclear cation, $[\text{Mn}_3(\text{sal})_2(\text{salH})_2(\text{H}_2\text{O})_4(4\text{-Me-Py})_6]$	7
Figure 1.06	Structure of $[\text{Mn}_2(\text{sal})_2(\text{im})_2(\text{CH}_3\text{OH})_2]$ $[\text{Mn}(\text{sal})_2(\text{Py})_2]$	7
Figure 1.07	(a) Dinuclear manganese complex, $[\text{Mn}_2(\text{saltmen})_2(\text{ReO}_4)_2]$, (b) Plot of out-of-phase ac susceptibility versus frequency	8
Figure 1.08	(a) Tetranuclear manganese complex, $[\text{Mn}_4\text{X}_4\text{L}_4]$, (b) Plot of out-of-phase susceptibility versus temperature for C	9
Figure 1.09	Molecular structure of $[\text{Mn}^{\text{III}}_6\text{O}_2(\text{Et-sao})_6(\text{O}_2\text{CPh}(\text{Me})_2)_2(\text{EtOH})_6]$	10
Figure 1.10	(a) Structure of $[\text{Mn}^{\text{III}}\text{Cu}^{\text{II}}\text{Cl}(\text{5-Br-sap})_2(\text{MeOH})]$ (b).Plot of in-phase and out-of-phase ac susceptibility versus temperature	11
Figure 1.11	Structure of $[\text{Mn}^{\text{III}}_2\text{Ni}^{\text{II}}_2\text{Cl}_2(\text{salpa})_2]$ and hysteresis loop at 0.55 K	12
Figure 1.12	An example of 2D ^1H - ^1H COSY spectra	16
Figure 1.13	(a) The plot of χT and $1/\chi$, as a function of temperature for paramagnetic, ferromagnetic, antiferromagnetic and ferrimagnetic materials	20
Figure 1.14	The plot of χ as a function of temperature for paramagnetic, ferromagnetic, antiferromagnetic and ferrimagnetic materials	20
Figure 1.15	Plot of energies of the microstates in a $S = 10$ system	22
Figure 1.16	An example of ac susceptibility measurements as a function of temperature at different frequencies, and as a function of frequency at different temperatures	23
Figure 3.01	Structure of the different salicylic acid ligands	27
Figure 3.02	Structure of the various coligands	28
Figure 3.03	The asymmetric unit of $[\text{Mn}^{\text{III}}_2\text{Mn}^{\text{II}}(3\text{-Me-sal})_4(\text{py})_4]$, 1 and its packing diagram	29
Figure 3.04	A diagram of the diamondoid network motif for compound 1	30
Figure 3.05	Temperature dependence of the χT product for 1	31
Figure 3.06	Temperature dependence of χ for 1	32

Figure 3.07	Field dependence of the magnetisation for 1 from 1.8 to 8 K; hysteresis loop at 2 K	32
Figure 3.08	Temperature dependence of χ' and χ'' for 1	33
Figure 3.09	The asymmetric unit of $[\text{Mn}^{\text{III}}_2\text{Mn}^{\text{II}}(4\text{-Me-sal})_4(\text{py})_4(\text{MeOH})]\cdot\text{H}_2\text{O}$, 2 and its packing diagram	36
Figure 3.10	The diamond fragment and the network of compound 2	36
Figure 3.11	Temperature dependence of the χT product for 2	37
Figure 3.12	Temperature dependence of χ for 2 at 1000 Oe and 10000 Oe	37
Figure 3.13	Field dependence of the magnetisation from 1.8 to 7 K and hysteresis loop at 2 K	38
Figure 3.14	Temperature dependence of χ' and χ'' for 2 from 100 to 1000 Hz	38
Figure 3.15	The asymmetric unit of $[\text{Mn}^{\text{III}}_2\text{Mn}^{\text{II}}(5\text{-Me-sal})_4(\text{py})_4(\text{H}_2\text{O})_2]\cdot(\text{MeOH})$, 3 and its packing diagram	39
Figure 3.16	The flatter diamond fragment and the network of compound 3	40
Figure 3.17	(a) Temperature dependence of the χT product for 3 at 1000 Oe. (b) Temperature dependence of χ for 3 at 1000 Oe	41
Figure 3.18	Temperature dependence of χ' and χ'' for 3 from 100 to 1500 Hz	41
Figure 3.19	Field dependence of the magnetisation from 1.8 to 4 K, and hysteresis loop at 1.8 K (right), for 3	41
Figure 3.20	Powder pattern for 1-4	42
Figure 3.21	(a) Temperature dependence of the χT product for 4 at 1000 Oe, (b) Temperature dependence of χ for 4 at 1000 Oe	43
Figure 3.22	Field dependence of the magnetisation from 2 to 5 K and hysteresis loop at 1.8 K (right), for 3	43
Figure 3.23	Temperature dependence of χ' and χ'' for 4	44
Figure 3.24	(a) Structure of the chain, $[\text{Mn}^{\text{III}}(4\text{-Me-sal})_2(4\text{-Me-py})_2\text{Mn}^{\text{II}}(\text{H}_2\text{O})_2$ $(\text{MeOH})_2]^+$, (b) Structure of the mononuclear anion, $[\text{Mn}^{\text{III}}(4\text{-Me-sal})_2(4\text{-Me-py})_2]$, in 5	45
Figure 3.25	A view along the [1 0 0] direction of the unit cell of the 3D supramolecular network in 5	47
Figure 3.26	Temperature dependence of the χT product for 5	48
Figure 3.27	(a) The Curie-Weiss plot for 5 , (b) Temperature dependence of the χT product for 5 from 1.8 to 300 K	49

Figure 3.28	(a) Field dependence of the magnetisation for 5 , (b) M versus H/T plot for 5 from 1.8 to 7 K	49
Figure 3.29	Part of the structure of the 1D polymer, $[\text{MnNa}_2(3\text{-MeO-sal})_2(\text{MeOH})_2]$, 7	51
Figure 3.30	The repeating unit, $[\text{Fe}_2\text{Pr}(4\text{-Me-sal})_4(2,2'\text{-bipy})_2(\text{OH}_2)_6](\text{NO}_3)_3 \cdot 3\text{MeOH}$, of the 1D chain in 8	52
Figure 3.31	Structure of the 1D chain of compound 8	53
Figure 3.32	Temperature dependence of χT for 8 at 1000 Oe and 10000 Oe	55
Figure 3.33	(a) Field dependence of magnetisation, (b) M versus H/T , for 8 from 2 to 5 K	55
Figure 3.34	The repeating unit, $[\text{Fe}_2\text{Gd}(4\text{-Me-sal})_4(2,2'\text{-bipy})_2(\text{OH}_2)_5]\text{Cl}_{1/2}(\text{NO}_3)_{1/2} \cdot 5\text{H}_2\text{O}$, of the 1D chain in 9	56
Figure 3.35	Structure of the 1D chain of compound 9	57
Figure 3.36	(a) Temperature dependence of χT product for 9 (b) The Curie-Weiss plot for 9 from 1.8-300 K	58
Figure 3.37	(a) M versus H , (b) M versus H/T , for 9	58
Figure 3.38	Temperature dependence of χT product for 10	59
Figure 3.39	(a) M versus H , (b) M versus H/T , for 10	60
Figure 4.01	The ligand, 3-methoxysalicylic acid (3-MeO-salH ₂)	63
Figure 4.02	Structure of $(\text{NHEt}_3)[\text{Mn}^{\text{III}}(3\text{-MeOsal})_2(\text{MeOH})(\text{H}_2\text{O})]$, 11	64
Figure 4.03	Packing diagram of compound 11	64
Figure 4.04	Structure of $(\text{NHEt}_3)_2[\text{Fe}^{\text{III}}(3\text{-MeOsal})_2(\text{OAc})]$, 12	65
Figure 4.05	Molecular structure of $[\text{Mn}^{\text{II}}\text{Mn}^{\text{III}}_2(3\text{-MeOsal})_4(\text{py})_6(\text{H}_2\text{O})_2] \cdot 4\text{H}_2\text{O}$, 13	66
Figure 4.06	Temperature dependence of the χT product for 13	67
Figure 4.07	The Curie-Weiss Plot for 13	68
Figure 4.08	Field dependence of the magnetisation for 13 , from 1.85 K to 10 K	68
Figure 4.09	Temperature dependence of the χT product (fitting) for 13	69
Figure 4.10	Structure of $[\text{Mn}^{\text{III}}_2\text{Mn}^{\text{II}}(3\text{-MeO-sal})_4(\text{Py})_4(\text{H}_2\text{O})_4] \cdot 4\text{MeOH}$, 14	70
Figure 4.11	Hydrogen-bonded structure of compound 14	71
Figure 4.12	Temperature dependence of the χT product for 14	72
Figure 4.13	Temperature dependence of the χT product (fitting) for 14	72
Figure 4.14	Field dependence of the magnetisation for 14 at 1.8 K	73
Figure 4.15	Structure of the trinuclear cluster, $[\text{Mn}^{\text{III}}_2\text{Mn}^{\text{II}}(3\text{-MeO-sal})_4(2,2'\text{-bipy})(\text{H}_2\text{O})_3(\text{MeOH})_2]$, in 15	74

Figure 4.16	Temperature dependence of the χT product for 15	76
Figure 4.17	Field dependence of the magnetisation for 15	76
Figure 4.18	Temperature dependence of the χT product (fitting) for 15	77
Figure 4.19	Structure of $[\text{Cu}_3(3\text{-MeO-salH})_2(3\text{-MeO-sal})_2(2,2'\text{-bipy})_2]$, 16	78
Figure 4.20	The two carboxylate bridging modes in compound 16	78
Figure 4.21	Temperature dependence of the χT product for 16	80
Figure 4.22	Temperature dependence of the χT product (fitting) for 16	81
Figure 4.23	(a) Field dependence of the magnetisation for 16 (b) The plot of M versus H with the fitting	81
Figure 5.01	$^1\text{H-NMR}$ spectra of the ligand, H_2L^1	86
Figure 5.02	COSY 2D $^1\text{H}^1\text{H}$ NMR for the ligand, H_2L^1	88
Figure 5.03	HETCOR $^1\text{H-}^{13}\text{C}$ NMR for the ligand, H_2L^1	88
Figure 5.04	Comparisons between the ^1H NMR spectra of the ligands	89
Figure 5.05	Structure of the trinuclear cluster in $[\text{Mn}^{\text{III}}_2\text{Mn}^{\text{II}}(\text{L}^1)_2(\mu\text{-OAc})_2(\mu\text{-OMe})_2(\text{MeOH})_2]\cdot 2\text{MeOH}$, 17	91
Figure 5.06	Packing diagram for 17	91
Figure 5.07	(a) Temperature dependence of χT for 17 , (b) Field dependence of the magnetisation for 17 from 1.8 to 8 K	92
Figure 5.08	(a) Fitting of the χT versus T plot (the fit) for 17 (b) Energy spectrum for 17	93
Figure 5.09	Temperature dependence of χ' and χ'' for 17 from 100 to 1500 Hz	93
Figure 5.10	Arrhenius Plot of $\ln(\tau)$ versus $1/T$ for 17	94
Figure 5.11	Structure of $[\text{Mn}^{\text{III}}_2\text{Mn}^{\text{II}}(\text{L}^3)_2(\mu\text{-OAc})_2(\mu\text{-OMe})_2]$, 18	95
Figure 5.12	(a) Temperature dependence of χT for 18 (b) Field dependence of magnetisation for 18	96
Figure 5.13	(a) Fitting of the χT versus T plot (the fit) for 18 (b) Energy spectrum for 18	96
Figure 5.14	Structure of $[\text{Mn}^{\text{III}}_2\text{Mn}^{\text{II}}(\text{L}^7)_2(\text{OAc})_4(\text{OH}_2)_2]\cdot \text{MeOH}$, 19	97
Figure 5.15	Hydrogen-bonded structure of compound 19	98
Figure 5.16	(a) Temperature dependence of χT for 19 (b) Field dependence of magnetisation for 19	99
Figure 5.17	(a) Fitting of the χT versus T plot (b) Energy spectrum for 19	99
Figure 5.18	Structure of $[\text{Mn}^{\text{III}}_3(\mu_3\text{-O})(\text{L}^{11})_3(\text{MeOH})_3](\text{ClO}_4)$, 20	100

Figure 5.19	(a) Temperature dependence of χT for 20 , (b) Field dependence of magnetisation for 20	101
Figure 5.20	(a) χT versus T plot and solid line is the simulation, (b) Energy spectrum for 20	101
Figure 5.21	Structure of $[\text{Mn}_2^{\text{III}}\text{Ni}_2^{\text{II}}(\text{L}^{14})_4](\text{CH}_3\text{COO})_2$, 21	102
Figure 5.22	Hydrogen bonded 3D network in 21	104
Figure 5.23	(a) Temperature dependence of the χT product for 21 , (b) Field dependence of the magnetisation for 21	105
Figure 5.24	(a) Temperature dependence of the χT product, (b) Field dependence of the magnetisation at 1.8 and 4 K for 21 , $D_{\text{Mn}}=D_{\text{Ni}}=0$	107
Figure 5.25	Field dependence of magnetisation for 21 , $D_{\text{Mn}} \neq 0$ and $D_{\text{Ni}} = 0$	107
Figure 5.26	Field dependence of magnetisation for 21 , $D_{\text{Mn}} = 0$ and $D_{\text{Ni}} \neq 0$	108
Figure 5.27	Field dependence of magnetisation for 21 , $D_{\text{Mn}} \neq 0$ and $D_{\text{Ni}} \neq 0$	108
Figure 5.28	Temperature dependence of χ' and χ'' for 21	110
Figure 5.29	Frequency dependence of χ' and χ'' for 21	110
Figure 5.30	(a) Temperature dependence and (b) Frequency dependence of χ' and χ'' , for 21	111
Figure 5.31	Arrhenius plot of τ vs $1/T$, for 21	111
Figure 5.32	Energy spectrum of 21 for $D_{\text{Mn}} = -3.9$ K, $D_{\text{Ni}} = 0$ or $D_{\text{Ni}} = 6$ K	112
Figure 5.33	Energy spectrum of 21 for $D_{\text{Mn}} = 4.1$ K and $D_{\text{Ni}} = 0$ K	112

Appendix E: List of schemes

Scheme 5.01	Schematic representations of the reactions to produce the Schiff base ligands	84
--------------------	---	----

Appendix F: List of tables

Table 3.01	Critical temperature (T_C), coupling constant (J) between Mn(II) and Mn(III) and coercive field (H_c), for 1 , 2 , 3 and 4	35
Table 8.01	Crystallographic measurements	132

Acknowledgements

It is a great pleasure for me to express my sincere thanks and heartfelt gratitude to my supervisor, Prof. A. K. Powell for her excellent guidance, constant encouragement, constructive criticism, and continuous support throughout the course of this work. I am grateful to her for giving me the liberty of thought and work.

I would like to take this opportunity to express my sincere gratitude to Dr. Chris Anson for collecting and solving the crystallographic data presented in this work. I would also like to thank him for giving me valuable suggestions throughout my research work. Many thanks to Dr. Rodolphe Clérac and Dr. Oliver Waldman for magnetic interpretation of the compounds in this work. Thanks to Dr. Ghenadie Novitchi for his help and advice in the synthesis and NMR spectra of the ligands. I am very thankful to him for helping me to increase my understanding of magnetism. I would like to thank Dr. Yanhua Lan for performing the SQUID measurements of all the compounds and for their magnetic studies. My special thanks to Dr. Lianne Beltran for being a great friend and mentor, whose suggestions enabled me to present my results in the best possible way. Many thanks to Dr. George E Kostakis for giving useful tips while writing my manuscripts and giving me more insight on MOFs.

I am thankful to Getraud Amschlinger for all her help in both official as well as unofficial works. Thanks to Rolf Lehman for solving any technical problems with the instruments and for being there whenever I needed him. I will never forget the lovely discussions with H. Henke and his garden parties. At Universität Karlsruhe, I thank Dr. Matern and Dr. H. Berberisch for measuring NMR spectra. Thanks to Fr. S. Lude for providing elemental analysis, Fr. G. Kuhn and Frau S. Böcker for their help in chemical stores.

I would like to thank all the group members for helping and giving me friendly suggestions. Thanks to Sanjit and Suparna for all their help during my stay at karlsruhe. Thanks to Frederick for all the hilarious moments and helping me to make shelves in my fumehood. Thanks to Julia and Kartik for helping me in my difficult moments.

Finally, I would like to thank my husband, Dr. S. K. Ghosh for his continuous support and encouragement. My parents and my brother for having faith and confidence on me, which helped me to reach wherever I am today.

Curriculum Vitae

Name: Sudarshana Mukherjee

Date of Birth: 26 September 1981

Place of birth: Varanasi, India

Marital Status: Married

Nationality: Indian

Education

- | | |
|------|---|
| 1997 | Indian certificate of secondary education (High School), St. John's School, Varanasi, India |
| 1999 | Indian School Certificate (Senior Secondary), St. John's School, Varanasi, India |
| 2003 | B.Sc. in Chemistry, Banaras Hindu University (B.H.U), Varanasi |
| 2005 | M.Sc. in Chemistry, Indian Institute of Technology (IIT), Roorkee, India. |
| 2008 | PhD from University of Karlsruhe, Germany, under Prof. A. K. Powell. |

FELLOWSHIPS AND AWARDS:

- Junior Research Fellowship of Council of Scientific and Industrial Research, New Delhi.
- Dr. A.N. Khosla medal for obtaining highest CGPA in M.Sc /M.Tech science courses.
- Seema Jain scholarship for obtaining highest CGPA in MSc at IIT, Roorkee.
- Summer Project Fellowship from **INDIAN ACADEMY OF SCIENCES** for 3 months, May – July (2004)
- Certificate of Merit for standing First in Chemistry in B.Sc (Chemistry Hons.) in 2003.

WORKING EXPERIENCE IN CHEMISTRY:

- Summer project at **IIT Kanpur** under Prof. P.K.Bharadwaj (Inorganic Chemistry Department) from May 2004 to July 2004,
- M.Sc Project at **IIT Roorkee** (4th semester) under Dr. R. K. Peddinti, worked on organic synthesis, January 2005- April 2005.
- Project Assistant (CSIR-JRF) at **IIT Kanpur** under Prof. S. Sarkar (Inorganic Chemistry Department), July 2005-January 2006.
- Teaching assistantship in the quantitative practical classes of diplom students at University of Karlsruhe.

Publications:

Influence of Water Ligands on Structural Diversity: From a 1D Linear Coordination Polymer to 3D Ferrimagnetic Diamondoid Metal-Organic Frameworks. *Cryst. Growth & Design, in press.*

Synthesis, structures and magnetic properties of trinuclear $\text{Mn}_2^{\text{III}}\text{Mn}^{\text{II}}$ and tetranuclear $\text{Mn}_2^{\text{III}}\text{Ni}_2^{\text{II}}$ complexes using Schiff base ligands. *Manuscript under preparation.*

Synthesis and magnetic properties of heterometallic Fe-Ln coordination polymers. *Manuscript under preparation.*

Conferences and meetings attended:

- (1) QuEMolNa Meeting at Valencia, Spain, 24-26 April 2006. (oral presentation)
- (2) European Conference on Molecular Magnetism (ECMM) at Tomar, Portugal, 15-19 October 2006. (poster presentation)
- (3) QuEMolNa Meeting at Paris, France, 18-20 May 2007. (oral presentation)
- (4) QuEMolNa Meeting at Modena, Italy, 18-20 April 2008. (oral presentation)
- (5) Karlsruhe-Strasbourg bilateral meetings on progress in Supramolecular Chemistry at Strasbourg, France, June 9th 2008. (oral presentation)